UNIVERSITÀ
DEGLI STUDI
DI PADOVA

Sede Amministrativa: Università degli Studi di Padova

Dipartimento di Scienze Chimiche

CORSO DI DOTTORATO DI RICERCA IN SCIENZA E INGEGNERIA DEI MATERIALI E DELLE NANOSTRUTTURE

XXX CICLO

ADVANCED MATERIALS FOR SOLID OXIDE FUEL CELLS INNOVATION: REVERSIBLE AND SINGLE CHAMBER SOLID OXIDE FUEL CELLS, FRONTIERS IN SUSTAINABLE ENERGY

Coordinatore: Ch.mo Prof. Giovanni Mattei

Supervisore: Prof.ssa Antonella Glisenti

Dottorando: Andrea Bedon

Abstract

The energy transition is changing the way we use, convert and store energy for all our purposes. It is a process driven by an increased acknowledgement of the relevant consequences of the current heavy use of fossil energy sources, and it is not clear where it will lead. Several technologies have been proposed as the best choice for the future of energy. Among them, Solid Oxide Fuel Cells (SOFCs) deserve a considerable attention. They are high temperature devices able to convert a variety of fuels (hydrogen, methanol, hydrocarbons, etc.) into electrical energy, with efficiencies that reach 90% when coupled with a heat recovery system. They can also be operated reversibly as Solid Oxide Electrolysis Cells (SOECs) and store electrical energy as fuels, so they can easily absorb the fluctuations of renewable energy production and save the energy until it is needed. Because of the high temperature of operation, they do not require noble metals. The SOFC technology is not mature yet for a large scale diffusion, but there is an intensive research towards this target. One of the main drawbacks of SOFCs is the short device life compared to the high costs, due to premature degradation of some cell components. This work of thesis is an attempt to increase economic convenience of SOFCs, by researching more stable materials and by decreasing the device costs. Particular attention has been devoted to find materials that are suitable for operation in reversible cells and Single Chamber cells (SC-SOFCs), two highly innovative variants of the basic SOFCs. A particular approach for the design of new materials has been proposed, consisting in coupling a Mixed Ionic Electronic Conductive (MIEC) substrate with an active phase, specifically chosen to obtain the properties desired for the respective application. The LSGF perovskite ($La_{0.6}Sr_{0.4}Ga_{0.3}Fe_{0.7}O_3$) has been synthesized and fully characterized as the MIEC substrate. Then, it has been impregnated with cheap manganese and iron oxide, and the two different nanocomposites were studied in depth. Their activity as fuel cell electrodes has been tested, and very interesting performance of the iron composite as cathode and the manganese composite as anode has been recorded. A fuel cell based on LSGM electrolyte, with LSGF composite electrodes has been fabricated and successfully tested. The high homogeneity of this cell, that features very similar

materials both as electrode and electrolyte, should prevent the formation of any insulating phase, and the nickel-free anode avoids problems related to nickel coarsening, so a higher durability of the device is guaranteed. LSGF has been tested as an electrode material for symmetric reversible cells, and promising results were obtained. A fully selective cathode material has been designed from $Ca_2FeAl_{0.95}Mg_{0.05}O_5$ brownmillerite, that has been impregnated with iron oxide. Decent performances were obtained, in spite of the relevant cheapness of the used elements. Preliminary results indicate that such a material could be used to operate SC-SOFCs without the extensive fuel losses that current state-of-the-art material cause.

Summary

1 Introduction

ENERGY AWARENESS: THERE IS MORE THAN WE SEE

WHAT A FUEL CELL EXACTLY IS AND HOW IT WORKS

THE MATERIALS FOR FUEL CELLS: A BIG CHALLENGE (BUT WE DON'T HAVE FEAR)

AMBITIOUS PERSPECTIVES FOR AN ENVIRONMENTALLY FRIENDLY TECHNOLOGY

Energy has always been a central issue in every human civilization, and by now almost everybody is in some way familiar with the terms *energy source* and *energy production*. At this point, it is worthful to mention that, for a more precise understanding of the matter, it would be more accurate to speak about energy *conversion* instead of *production*; the principle of conservation of energy states energy cannot be created nor destroyed, thus the whole problem is reduced to a matter of converting efficiently energy around us to a form suitable for our purposes. Indeed, we are continuously surrounded by energy: photons light is made of contain radiant energy, the movement of air that we call wind and the movement of water that we call tide bring kinetic energy with themselves, the inner layers of our planet are hotter than the crust and heat is another form of energy, water falls from the sky and from the mountains because of its gravitational energy. Then, we can further expand the boundaries of our energetic playground beyond the everyday experience: everything that exists in the universe is made of atoms kept together by chemical energy, atoms that are energy themselves, as relativistic physics teach us. In other words, energy is everywhere (or, more precisely, energy is everything), but not all the forms energy can assume are equivalent, and some are easier to exploit than others.

Under this point of view, the abundance of a certain form of energy can be only a secondary factor. We can consider, as an example for this purpose, solar energy: our planet receives a hugely massive amount of energy from the sun, around $3 \cdot 10^{24}$J[1] every year, a striking value, particularly if compared with world energy consumption, that consists more or less of $6 \cdot 10^{11}$J[2]. Nonetheless, it has been more convenient for more than two centuries to dig fossils out from the deep of Earth's crust than

exploiting close at hand light energy. In fact, solar energy has become convenient with respect to fossil fuel only a few years ago[3], after 60 striving years of technological advancement since the first silicon solar cell was proposed[4]. The key factor that led to this apparent paradox is the conversion method itself: it is easy to burn something and to use the pressure of generated steam to produce movement, but it is very difficult to extensively perturb a system using only light photons (which have, frankly speaking, only modest energy).

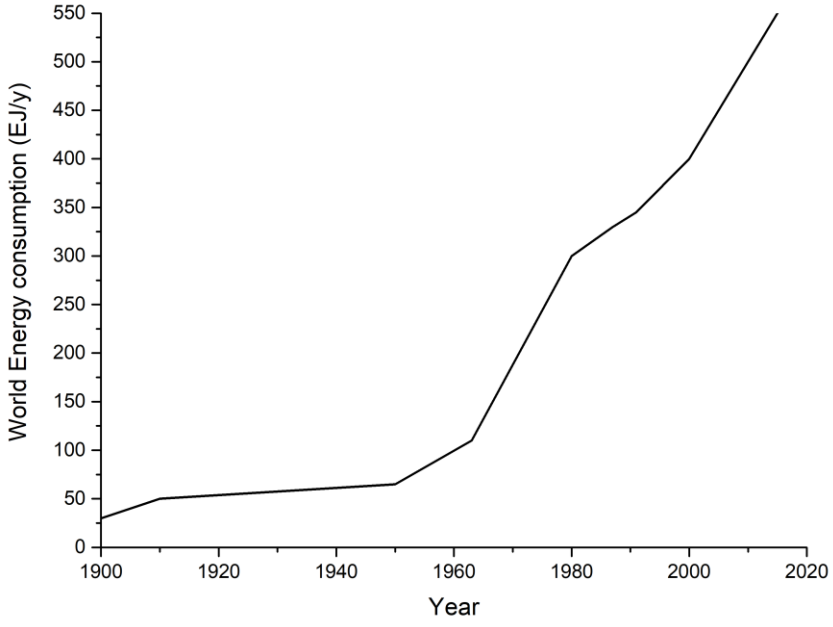

Figure 1.1 World Primary Energy consumption per year since 1900.[5][2]

So, the real crucial point is the development of fast and efficient methods to convert energy, as it has been along the whole human history. It is possible to easily realize than every significant advancement in human technology, that corresponded also to an improvement of living condition, can be related to the rise of better methods to convert energy; it would be clearly presumptuous to state a direct correlation between new energy conversion technologies and improvement of living conditions, but it is a fact that only with an easier availability of higher powers some progresses could have been possible[6]. The increase of the mere power output has been the main and almost unique goal for almost the whole human history, while some kind of awareness about the consequences of the ways we use to convert energy arose only in relatively recent times. The extent of the exploitation of the energy sources before the industrial revolution was not sufficient to affect significantly living

conditions on a global scale, and in general pollution was only one among various other problems impacting on human health[7]; nonetheless, locally damages stemming from human activities have been found to be relevant long before that time[8], [9]. But, since the beginning of the industrial revolution, energy demands have grown with an increasing rate (see Figure 1.1 World Primary Energy consumption per year since 1900.[5][2]); thus, side effect have been magnified too, to the current situation in which they directly influence world equilibria.

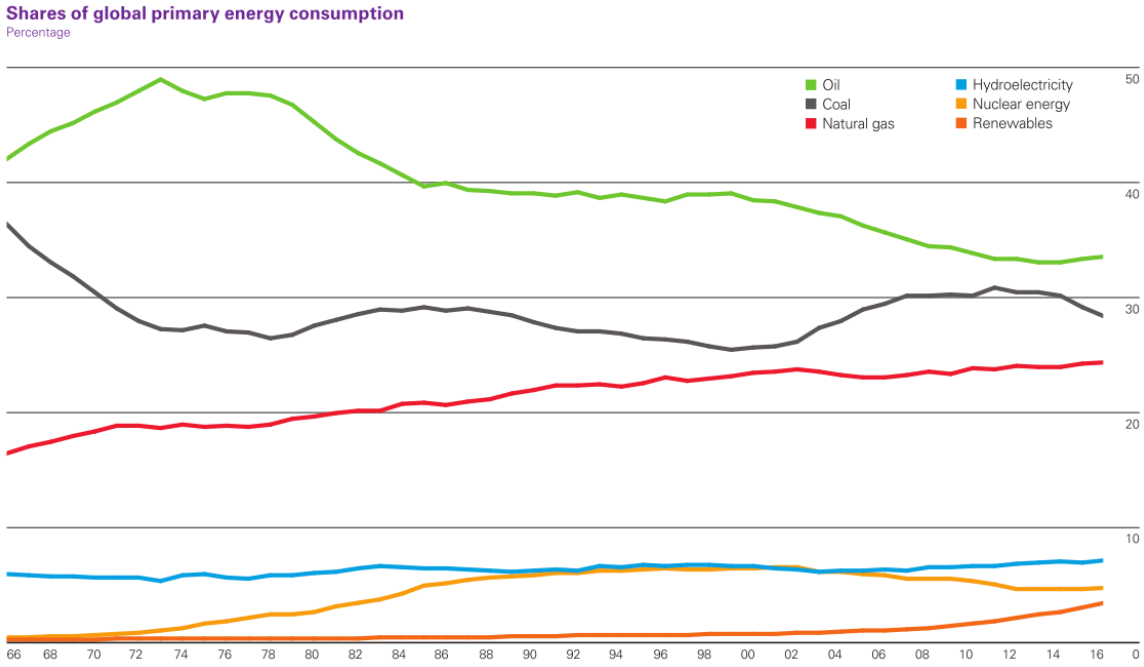

Figure 1.2 Shares of global primary energy consumption. Biomass in included in renewables. From [2].

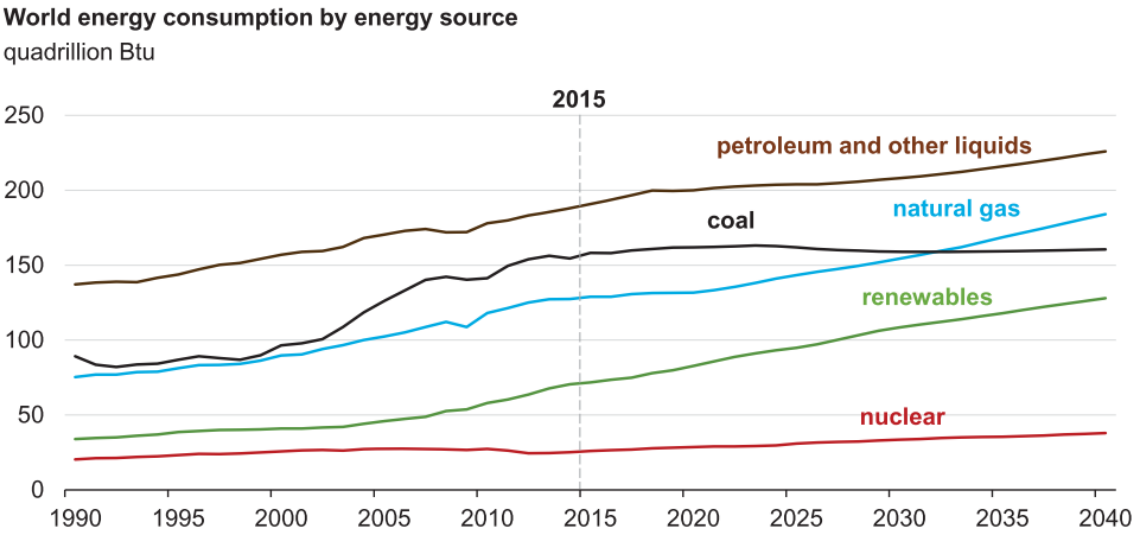

Figure 1.3 World energy consumption by energy source. From [10].

1.1 Not all energy sources are the same

Currently used sources of energy are rather well varied, but fossil fuels (oil, coal and natural gas) accounts for around 85% of the total demand (Figure 1.2). Among these, only coal is currently not increasing (Figure 1.3) after years of growth caused mainly by Chinese reliance on this source[10]. The use of oil and natural gas will probably steadily grow in the next years, in spite of the politic attempts to limit reliance on fossil fuel. Good news is that renewables are the fastest growing energy source and are swiftly gaining shares among the other sources, but they will not be able to considerably replace traditional sources nor in the medium neither in the long term. This also means that we are going to deal with the same fossil fuels related issues for several decades; including not only the most famous greenhouse effect, but also other important consequences on human health and environment in general. At this point, it is important to stress that often is considered only the mere fuel burning, and all the other less evident steps of the fuel supply chain (extraction, refinery and supply at a first stage) are neglected in spite of their importance; it is evident that for a comprehensive understanding the full-cycle impact must be acknowledged instead[11], [12].

Fossil fuels impact on the environment since they are taken out from the soil. Coal mining affects air diffusing toxic gases as SO_2 and NO_2 as well as heavy metal particulate[13]: the heavy metal particulate reaches also water where it harms aquatic life[14]; in addition, mine fires are often associated to mining facilities due to natural causes and human errors and pose an additional danger related to coal extraction[15]. When coal is extracted with surface mining, extensive areas of natural habitat are destroyed[16], leaving in the long term a poor soil unable to sustain the restoration of the previous ecosystem. Natural gas extraction, in particular when carried out with so-called *fracking*, raises some extremely serious concerns regarding the sustainability of this source that should theoretically be cleaner than its fossil counterparts. The development of fracking has been a real breakthrough in the natural gas industry, and has made available for the extraction reserves that could not be considered previously; it consists in pumping a high-pressure fluid (mostly water with some appropriate additives) that fractures particular gas containing rocks

named *shales* (hence the name *shale gas* for the natural gas extracted with this technique)[17]. Together with natural gas, several other toxic materials are extracted by the water flow posing a risk of contamination for both groundwater and surface water[18]. Oil and gas offshore extraction impacts on surrounding water with the discharge of alkylphenols and polyaromatic hydrocarbons during routine operation; in addition, accidental spills of oil and chemicals further contribute to the damage of the marine environment[19]. Similarly, onshore facilities strongly impact on water quality due to routine contamination and spills. In both the cases, they significantly contribute to global warming because of the release of greenhouse gases[20]. In general, the extraction of every kind of fossil fuel represents, with its own peculiarities, a threat for biodiversity[21].

Oil refining, necessary to obtain common used fuels as gasoline, diesel and kerosene from crude oil, impacts on the environment too[22]. Refineries release to the atmosphere toxic and greenhouse gases as NO_x, SO_x, NH_3, aldehydes, particulate and hydrocarbons[23]; their effluents contain toxic chemicals including oils, greases, phenols, sulphides, NH_3, particulate, cyanides, nitrogen compound and heavy metals[24]; also a great amount of solid waste is produced, including inert waste (wood, demolished materials, scrap materials, paper and construction materials), garbage and hazardous wastes consisting in exhausted catalysts made of heavy metals, tank bottom sludges and residues from wastewater treatment and petroleum process units[25], in addition they suffer from the risk of spills that affect every facility managing hazardous chemicals. Spills and leaks from pipelines exist and are a great concern especially for natural gas[26]: some study suggests that up to 9% of managed gas could be lost in the atmosphere, greatly eroding the advantage of this source compared to oil and coal under an environmental point of view[27]. For this purpose it is useful to mention that a single molecule of methane as the same global warming potential of 25 molecules of CO_2 over a 100 years span[28].

Then it comes the point the fuel is really used and combustion products are released to the environment. Power plants require very high amount of water, obtained by the deviation of surrounding rivers impacting on the ecosystems that relied on them. Under this point of view, coal is considered the dirtiest fossil fuel,

nevertheless it is far from being an obsolete energy source[29]; moreover, in developing country, where still used as an common energy source in houses, it is a major danger for people health[30], [31]. The main pollutants produced by coal and liquid fuels derived from oil are CO_2, NO_x, SO_x, ozone and particulate (carbonaceous and with heavy metals)[15], [32] that contaminates air, water (including seas, oceans, rivers) and the soil. Natural gas, as already mentioned, is cleaner because its combustion releases lower amounts of contaminants per unit of energy obtained, although small leakages easily brings us to the same level in terms of greenhouse effect, given CH_4 power in this sense[26].

The range of consequences the release of these substances brings is very wide, roughly summarizing, they boost the greenhouse effect, impact negatively on human health and damages the ecosystems. There are various ways pollution affects human health, this depends also on the variety of toxic chemical compounds are released in air. Pollutants in the air can be divided in four categories: gaseous pollutants, persistent organic pollutants, heavy metals and particulate[33], of these, only for the persistent organic compounds the use of fossil sources is not to blame. Gaseous pollutants, NO_x, SO_x, CO, ozone, and the so-called VOCs (Volatile Organic Compounds, a group including benzene and similar molecules), mainly affect respiratory system. They are able to create irritations, worsen the effects of existing diseases, reduce lung function and are able to induce asthma, emphysema and lung cancer. CO and benzene penetrate the cardiovascular system where CO reduces the ability of blood to transfer oxygen, and benzene can spread all over the organism and exert its well-known toxic and carcinogenic effects. Heavy metals are spread in the air by combustion of fuels which contain them as impurities, mainly coal, but also liquid fuels. They are dangerous because they tend to bioaccumulate, until they reach dangerous concentrations inside the body. Heavy metals are neurotoxic (especially lead and mercury), irritate respiratory system, strongly affect cardiocirculatory system, induce kidney damage and can increase the risk of kidney cancer. Particulate pose a risk for the entire organism, as the finer they are the more they penetrate inside the organism; they mainly affect respiratory and cardiocirculatory system, increasing the risks of lung cancer, atherosclerosis, heart ischemia, etc.[34]. Damage to

ecosystems is less evident, as it is mainly related to fuels extraction and processing, and has been described previously in the paragraph.

1.2 Climate change and greenhouse effect

The greenhouse effect is probably the most known concern related to air pollution, it receives wide interest also during public debates because, through the global warming intimately associated to it, it is potentially able to drastically modify the environment of our entire planet in the long term, and this transition is hardly reversible[35]. The first scientist to quantify how CO_2 molecules in the atmosphere can increase ground temperature was Svante Arrhenius in 1896[36], although it was not until 1901 that the atmosphere was compared to a greenhouse, a definition we owe to Swedish meteorologist Nils Ekholm[37]. In the following decades the studies moved forward to today's knowledge of the precise energy budget between the Sun, the Earth and the surrounding space. The mechanism implicated is the absorption of infrared radiation by molecules composing atmosphere. Earth surface is heated by solar radiation, and emits a black body radiation according to Planck's law, that can be estimated with the following equation, derived from the Planck's law itself:

$$B_\lambda(\lambda, T) = \frac{2hc^2}{\lambda^5} \frac{1}{e^{\frac{hc}{\lambda k_B T}} - 1} \quad (1)$$

B is the spectral radiance (power per unit of area), h is the Planck's constant, c is the speed of light, λ is the wavelength of the radiation, k_B is the Boltzmann constant and T the body absolute temperature. As Figure 1.4 shows, solar radiation, simply represented by the black body radiation of an object at 6000K, heats Earth's surface that re-emits some energy at much higher wavelengths as its own black body radiation; this infrared radiation is dispersed in space in planets with no atmosphere, but in our case the atmosphere exists so a part of the energy is actually retained by some gases that compose it. These chemical species, defined as *greenhouse gases*, are transparent to incoming solar radiation and let it reach Earth's surface, but are able to collect part of the rebounded energy through the excitation of their molecular vibration modes, in an analogy with the glass of a greenhouse[38] (although, at a certain point, this name is misleading, as greenhouses keep their temperature not allowing hot air flee outside, instead of retaining black body radiation).

The most important natural greenhouse gas in our atmosphere is water, followed by carbon dioxide, methane, the oxides of nitrogen and ozone. In addition, fluorinated gases, all of artificial origin, have been found to have a tremendous impact to the atmosphere; they have the greenhouse potential of thousands to tens of thousands CO_2 molecules, according to EPA (US Environmental Protection Agency). The greenhouse effect is a natural process, and it is fundamental in keeping stable Earth's surface temperature; nonetheless, the increase in greenhouse gases concentration increases also the fraction of energy retained by the planet unbalancing the whole energy budget. The contribution of every factor to the heat balance (see Figure 1.5 for a graphical summary) has been carefully estimated and weighed inside what has been found to be an extremely complex system in which many contributions can exert different and in case conflicting effects. These include positive feedbacks and mitigating effect, that sometimes could lead to counterintuitive result. Only few know, for example, that a sudden shut off of all fuel combustions in the planet would result in an immediate increase of Earth's temperature, due to the fall of light-reflecting particulate atmospheric concentration, that is estimated to mask around 45% of the global warming greenhouse gases would cause[39].

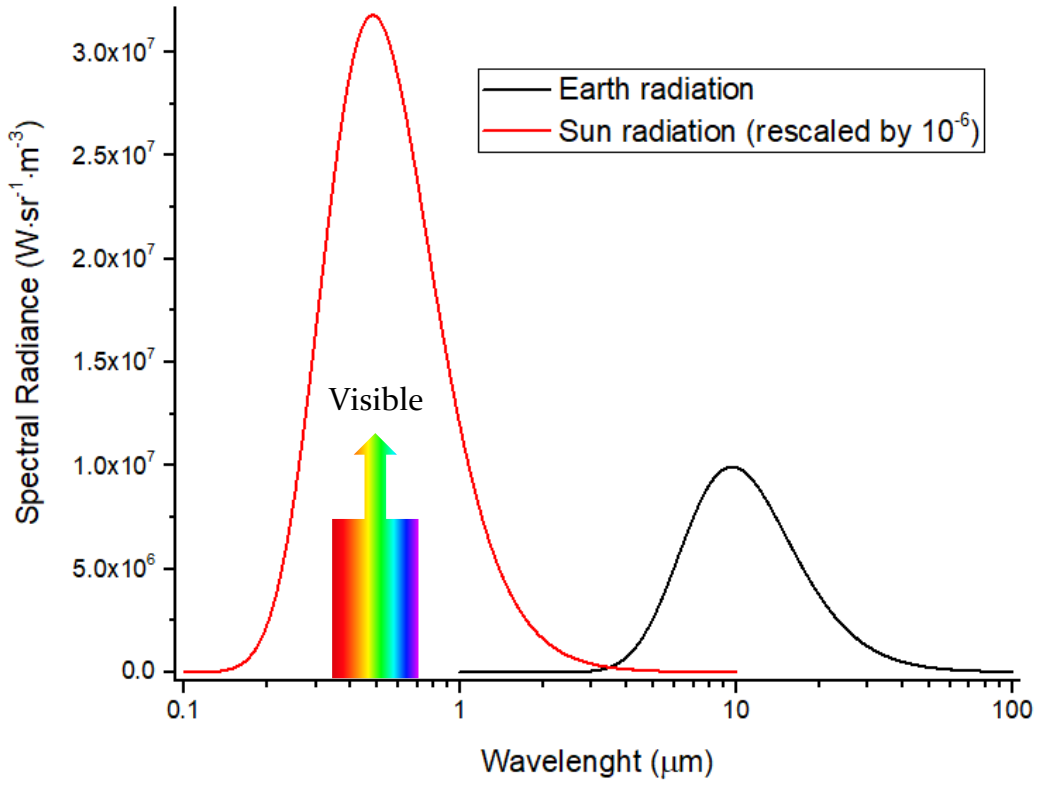

Figure 1.4 Comparison between solar radiation received and emitted by Earth.

Clouds are involved in climatic regulation as they reflect light away from the planet, so it is suspected that the warming, reducing the cloud amount, should trigger a positive feedback, but the issue is still largely debated in scientific community[40]–[43]. Water, being the most important greenhouse gas, is involved in a feedback itself[44]; an comprehensive and robust model predictive of water behaviour in climate change is still under development, but current data already suggest this feedback is strong and not negative[45]. Ice reflects light, and the loss of frozen areas on the planet increases heating due to the higher amount of light being absorbed by the surface; this is called sea ice-albedo feedback, it is positive, too, so able to further accelerate warming[46]–[49].

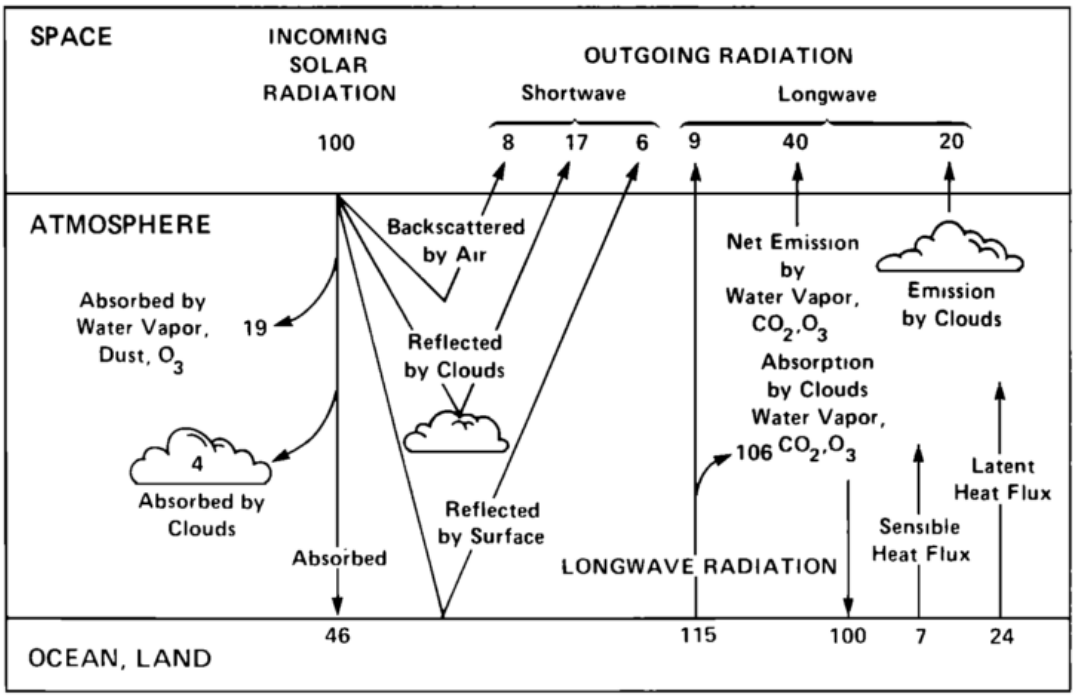

Figure 1.5 Diagram of the main components of Earth's energy balance. From [38].

There has been and still there is a great effort in the scientific community for the determination of the impact of climate change on the planet and on human society. It has been assessed that the process is already at place, it will make sea level rise, heat and acidify the oceans, increase global temperature, melt glaciers and ice sheets, overturn most of the ecosystems, impact on human health, alter the hydrological cycle, affect crop yield, etc...[50], [51]. The consensus among the scientific community that the climate change is in act and it is caused by human activity is unanimous[52]: it has been determined that 97-98% of researchers on this field supports the position

of the Intergovernmental Panel on Climate Change and the most prominent experts are concentrated in this same group, rather than the denying one[53]. Nonetheless, public opinion seems to have only little awareness of these figures, and it is often misled by biased and partisan reports of the authorities[54]. The substantial failing of scientific communication in building a correct consciousness on this topic is currently matter of debate in the scientific community, along with the strategies to restore a factual knowledge[55]. The issue is of primary importance, because the current bias in public is driving the global powers to politics potentially able to upset the entire planet, and is a big challenge for today's science[56].

1.3 Improvement of current technology

The range of possibilities to tackle the problems outlined in the previous paragraphs is extremely wide. A first solution is to reduce the consumption of current sources by improving the efficiency of the processes, which is not very high if some combustion is involved. Carnot's law poses a first insuperable limit for every energy conversion process that involves the production of heat as an intermediate stage, it is expressed by the equation:

$$\eta = 1 - \frac{T_2}{T_1} \quad (2)$$

Where T_1 is the temperature in kelvin degrees of the hot reservoir, and T_2 is the temperature in kelvin degrees of the cold reservoir. T_2 is usually fixed as it corresponds to room temperature, and it is in general around 300K. Aiming to the highest efficiency possible we should raise the hot reservoir temperature (which can be roughly defined as the temperature produced by the combustion) as high as possible, but there are obvious technical limitations to the attainment of very high temperatures. For example, a coal power plant injects steam vapours at a temperature of 673K, so the maximum ideal efficiency would be around 55%. Unfortunately, real devices are far from perfection, and the actual efficiency is normally even lower. According to EIA[57], in 2015 the average efficiency of power plants in the U.S.A. was 33% for coal, 32% for oil and 43% for natural gas. Internal combustion engines for automotive, which cannot benefit from heat recovery generators and operate on a smaller scale, in general attain efficiencies between 20-30%. When they are coupled

to batteries as in hybrid vehicles this value significantly increases but cannot gain more than a further 10%. The current most efficient car is the Prius, for which Toyota declares an efficiency of 40%. In August 2017 Mazda unveiled it will start to sell from 2019 new compression-ignition engines with an efficiency up to 30% higher than previous engine[58], so they would probably be able to reach an overall efficiency close to 40%; therefore, it could be estimated that a hybrid car with such an engine could boast an efficiency between 40% and 50%. This is indeed a great step forward for internal combustion engine, that was almost deemed dead prior this announcement. In any case, summarizing current and future state, it is evident it will not be possible to exceed a 50% efficiency with any conversion method that involves combustion. So, the replacement of thermal combustion with other devices able to attain higher efficiencies is at this point desirable, considering how much of the total energy we are currently wasting.

1.4 Fuel cells

Fuel cells, which are also the main topic of this thesis, can be a great help in fulfilling the task of reducing the environmental impact of our energy sources. A fuel cell is an electrochemical device, in principle very similar to a battery. As batteries, it has an anode and a cathode separated by an electrolyte, an is able to produce electrical energy under the same principle of a battery. But, unlike normal batteries, energy is not stored inside the electrodes, and fresh reactants can endlessly be supplied to the cell. Fuel cells are not closed systems, because they exchange continuously mass with the environment. This means also that, unlike batteries, fuel cell can operate indefinitely, being limited only by their degradation or the depletion of reactants reserves. A scheme of a fuel cell is presented in Figure 1.6, representing a Solid Oxide Fuel Cell, which is also the type of fuel cell studied during this thesis. The operating principle is very simple: hydrogen at one side is oxidized and oxygen at the other side is reduced, and the circuit is closed by the conduction of oxygen ions towards the anode. Here, they combine with oxidized hydrogen to form water that is expelled as a by-product. All the other fuel cells are similar in terms of operation, the main difference is the species conducted through the electrolyte and the side where water is formed. The different types of fuel cells are described in the following

paragraphs. Being electrochemical devices, fuel cells are not bounded by thermodynamical limits expressed by Carnot's law. Clearly, this does not mean they can easily reach near 100% efficiencies, but they do not suffer from a first flaw that cuts performances by 25% even before starting to design the device. The efficiency of a fuel cell depends on its type (there are more than one, as we are going to examine shortly), but never goes below 60% even in the worst case. Hydrogen is the main fuel used in fuel cell, and in general is considered a clean energy source as its combustion produces only water. Nonetheless, on Earth there is no hydrogen in the form of H_2, because the molecule is too light to be held by Earth's gravitational force, so the current main source of hydrogen is the reforming of fossil fuels, which implies the release of greenhouse gases. However, the combined efficiency of a reforming process and a fuel cell is higher than the one of a common combustion processes. So, fuel cells, indeed, are an immediate solution to environmental problems, although it is not appropriate to claim the use of hydrogen is *zero emission* (of greenhouse gases). In any case, as described in the following paragraphs, methods to obtain fully renewable fuels are under development.

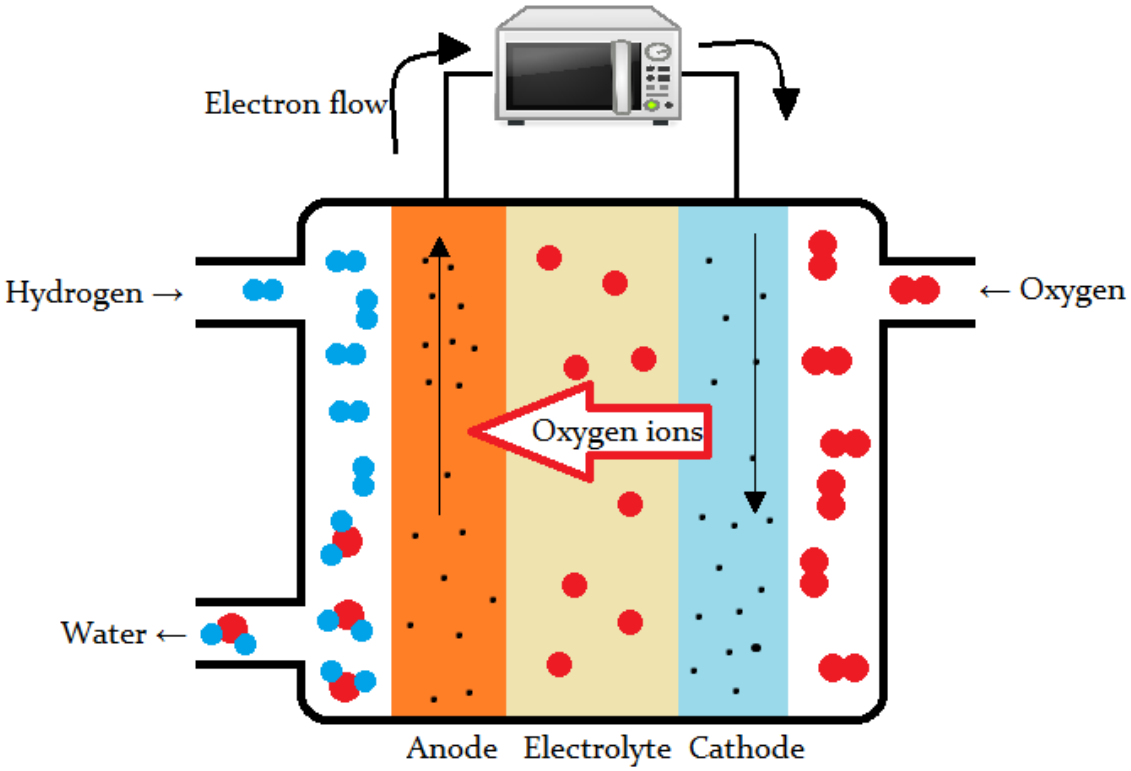

Figure 1.6 Scheme of a hydrogen fuelled Solid Oxide Fuel Cell. Of course, fuel cells can feed other than microwave ovens.

1.4.1 Brief history of the fuel cells

The idea of a cell able to produce electrical energy from a chemical reaction without carrying out a combustion is not new at all. Their history dates back to around 1840, when German chemist Friedrich Schoenbein discovered the operation principle and English William Robert Grove examined and studied the first phenomenon attributed to a fuel cell[59]. He submerged two platinum electrodes in sulphuric acid on one side and in separated hydrogen and oxygen on the other side, and was able to observe a flow of current between them (Figure 1.7). Given their early discovery, fuel cells can be considered the first device for electrical energy conversion invented by man. Base research on fuel cells proceeded during the XIX century without producing anything suitable for practical use; indeed, it must be considered that at that time electricity were a phenomenon interesting for the scientific studies, but was not a relevant energy source yet. Towards the end of the century interest in electricity started to raise, and the earlier power plants began to be designed and built, with the first coal power plant being opened in 1882 in London. From the 1920s the fuel cells started to assume the shape they have today. First came the molten carbonate fuel cell, from the experiments of William Jacques and Emil Baur, and more or less a decade after the Alkaline Fuel Cell (AFC) and the Solid Oxide Fuel Cell (SOFC) were designed for the first time, respectively by Thomas Francis Bacon[60] and Emil Baur/Hans Preis[61]. The first SOFC already employed a mixed oxide of zirconium and yttrium, a material that still is the state-of-the-art under the name of YSZ; this could give a first clue about how difficult is to find efficient pure ionic conductors at high temperatures.

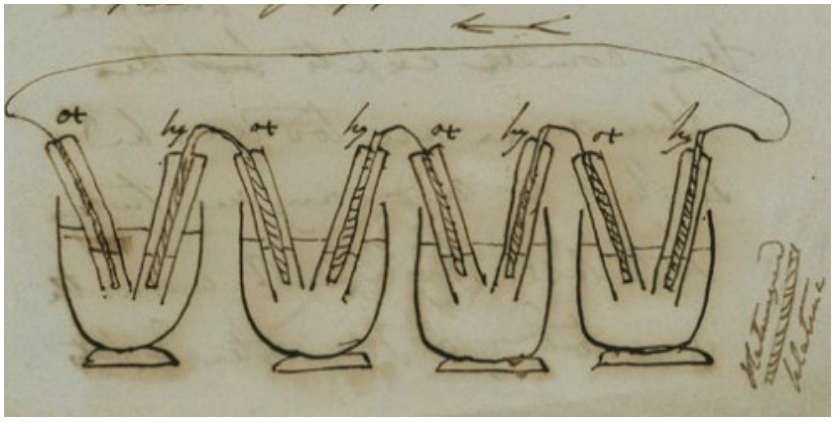

Figure 1.7 The first ever scheme of a fuel cell, drawn by Sir William Robert Grove in 1842. The original letter addressed to Michael Faraday is conserved at the Royal Institution in Mayfair, London.

The alkaline fuel cell was the first to obtain a decent success outside the scientific entourage. Compared to other fuel cell types, an alkaline fuel cell is simpler and cheap, so the technology of 60s' and 70s' found easier to employ it, rather than other more complex cells, for the production of electrical energy. In the appropriate contexts, these cells obtained a remarkable outcome. In the second half of the twentieth century, more than some notable example of use of alkaline fuel cells has been recorded. A tractor based on AFCs manufactured by Allis Chalmer was produced from 1959, in the same years scientist Karl Kordesch equipped its Austin A40 with an AFC and six hydrogen tanks positioned over the roof[62] (Figure 1.8), and in 1966 General Motors produced its Electrovan completely fuelled by AFCs, although it has always been used inside the General Motor properties, and in any case the machine did not prove to be very reliable[63]. Alkaline fuel cells were extensively used by NASA in programs Apollo and Space Shuttle, as they were acknowledged as a reliable, efficient technology able also to supply potable water as a valuable by-product[64]. In effect, it was not a problem at all for NASA to supply hydrogen as a fuel for its mission, but it would have been for extensive terrestrial uses; probably this is why AFCs did not experience the same success in everyday life, they found their best niche in the spatial mission, but given the easy availability of other fuels there was no more room for them at that time.

In the meanwhile, in the fifties Grubbs and Niedrach conceived the first Polymer Electrolyte Membrane Fuel Cell (PEMFC), a technology that was going to become the most diffused today[65], [66]; in the first prototypes a polystyrene based membrane were used as electrolyte between Ni electrodes activated by platinum black. The phosphoric acid fuel cell was invented in 1961 by Elmore and Tanner, completing the range of types of fuel cells we know today. The invention and release into commerce of PTFE and in particular of the PTFE derivative Nafion® by DuPont was a turning point for PEMFCs, because the introduction of membranes based on it, that happened in the seventies, has allowed the operation without dehydration of the membrane at higher temperatures, up to 100°C [67].In 1962 there was another step for the SOFCs, when Weissbart and Ruka modified the YSZ electrolyte of the previous cells to the form we use today[68].

Then, the following years until today have been devoted to the optimization of the cell, towards an economic sustainability that is being reached only in these years, after slightly less than two centuries from their invention. A more comprehensive report about the history of these devices can be found in [69].


Figure 1.8 Left: an Allis Chalmer AFC fuelled tractor. Right: the AFC fuelled Austin A-40 of Karl Kordesch.

1.4.2 Fuel cells thermodynamic

The chemical reaction at the base of a fuel cell is a very simple reaction:

$$2H_2 + O_2 \rightarrow 2H_2O$$

As for any reaction, the heat enthalpy can be calculated from the enthalpies of formation of the reactants and products.

$$\Delta_r H^{\ominus} = \Delta_f H^{\ominus}{}_{liquid}(H_2O) - \frac{1}{2}\Delta_f H^{\ominus}(O_2) - \Delta_f H^{\ominus}(H_2) = -286\ kJ/mol \quad (3)$$

The result is the simple standard enthalpy of formation of water, as both oxygen and hydrogen have zero standard enthalpy of formation by definition. The negative sign of the final enthalpy indicates the reaction is exothermic, this is an expected result because the reaction in fact is a combustion. Similarly, it is possible to calculate the standard entropy of formation.

$$\Delta_r S^{\ominus} = S^{\ominus}{}_{liquid}(H_2O) - \frac{1}{2}S^{\ominus}(O_2) - S^{\ominus}(H_2) = -0.1633\ kJ/(mol\ K) \quad (4)$$

And then the standard free Gibbs energy:

$$\Delta_r G^{\ominus} = \Delta_r H^{\ominus} - T\Delta_r S^{\ominus} = -237.34\frac{kJ}{mol} \quad (5)$$

The entropy is a figure of how much of the free Gibbs energy is irreversibly lost, so it is possible to define a first efficiency for the fuel cell, as the ratio between enthalpy (energy that can be really used) and Gibbs free energy (total energy in the reaction). This is called *Gibbs efficiency*. The calculation from data shown here is easy, but purely hypothetical (as also others shown in this section), because no fuel cell operates at 25°C.

$$\eta_G(25°C) = \frac{\Delta_r G^{\ominus}}{\Delta_r H^{\ominus}} = 0.83 \quad (6)$$

Since $-\Delta_r G = nFE$ (5), it is possible to calculate the standard electromotive force of the cell, that is:

$$\Delta_{rev} E\ (25°C) = \frac{-\Delta_r G^{\ominus}}{nF} = 1.23V \quad (7)$$

Both reaction enthalpy and reaction entropy changes with temperature, and their variation is related to heat capacities of the chemical species. In particular:

$$\left(\frac{\partial \Delta_r H^{\ominus}}{\partial T}\right)_p = \Delta_r C_p \quad \left(\frac{\partial \Delta_r S^{\ominus}}{\partial T}\right)_p = \frac{\Delta_r C_p}{T} \quad (8)$$

And the variation of the free Gibbs energy is:

$$\left(\frac{\partial \Delta_r G^{\ominus}}{\partial T}\right)_p = \Delta_r S^{\ominus} \quad (9)$$

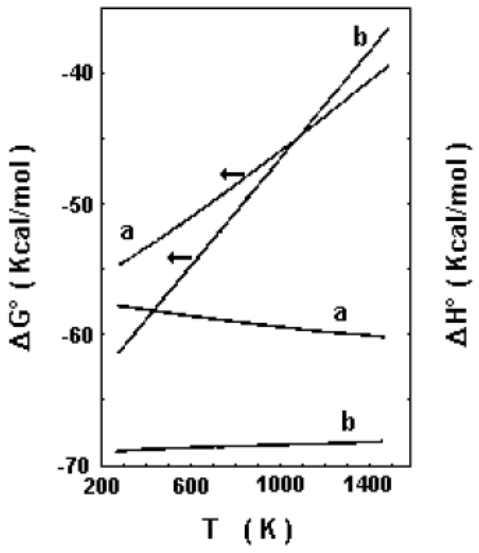

Figure 1.9 Variations of standard free Gibbs energy and enthalpy depending on temperature for oxidation of H2 (a) and CO (b)

In Figure 1.9 it is possible to see how thermodynamical functions for hydrogen oxidation vary at higher temperature. In general, free Gibbs energy increases and enthalpy slightly decreases. This determines an overall decrease of the Gibbs efficiency.

The potential calculated with equation 6 in ideal conditions corresponds to the *Open Circuit Voltage* (OCV), often called also *Open Circuit Potential*. The ratio between the actual OCV of a cell and the ideal one defines a second efficiency called *voltage efficiency:*

$$\eta_V = \frac{\Delta V}{\Delta_{rev} E} \quad (10)$$

The loss of potential is caused by resistances internal to the cell, that at first approximation can be described as:

$$R_{tot} = R_0 + R(i) \quad (11)$$

R_o is the part of resistance that does not depend on current intensity, and R(i) is the part that does. In case R(i) is small and neglectable it is possible to express the voltage loss as the product $R_o \cdot I$. Hence equation 10 becomes:

$$\eta_V = \frac{\Delta_{rev} E - R_0 I}{\Delta_{rev} E} = 1 - \frac{R_0 I}{\Delta_{rev} E} \quad (12)$$

In practical terms R_o represents the ohmic loss, caused by the electrolyte, and often corresponds to the higher resistance impacting on cell operation. R(i) on the other hand is the activation polarization, it is more evident when cell operates close to the OCV, so, at small overpotentials, and can be therefore represented with a Tafel equation.

$$\eta = b \cdot ln \frac{i}{i_0} \quad (13)$$

Note that in this case η is the overpotential and not the efficiency. i_o is the exchange current and i the current. From the Butler-Volmer equation we know that the parameter b can be expressed as:

$$b = \frac{RT}{\alpha n F} \quad (14)$$

Where R is the universal gas constant, T the absolute temperature, F the Faraday constant, n the electron exchanged in the process and α the charge transfer coefficient. R and F are constants, n is defined for this process whatever the cell is, and T is related to cell operating conditions. α is the only factor influenced by the material, and is related to the catalytic performance of the electrode. The electrode influences also i_0, so an electrode able to transfer charges easily hence with a high exchange current avoids loss of efficiency.

A third efficiency is related to fuel consumption, and can be defined as the ratio between the fuel the cell if fed with and the fuel the cell actually consumes. So, the total cell efficiency is the product of the Gibbs efficiency, the voltage efficiency and the fuel consumption efficiency:

$$\eta_{TOT} = \eta_G \cdot \eta_V \cdot \eta_F \quad (15)$$

At a first glance it could be apparent that a higher temperature is always detrimental for the efficiency, as the Gibbs efficiency decreases if temperature is high. In reality, the temperature is hidden inside the voltage efficiency with a completely opposite effect: activation processes are easier and in general internal resistances are lower. At the end, SOFCs are the most efficient fuel cells, even more efficient than low temperatures PEMFCs. These theoretically can carry on the reaction in conditions closer to the reversibility, but in fact lose more energy in moving electrons and chemical species because of the low temperature. Another factor must be considered when evaluating the efficiency of fuel cell: the calculation previously described accounts only for the efficiency considering the electrical energy immediately generated by the cell. The coupling with heat recovery systems, able to retrieve energy the cell disperse as heat, can significantly increase overall efficiency. Such systems are able to convert up to 80%-90% of energy, much more than the simple fuel cell alone and than any other energy conversion system.

1.4.3 Fuel cell types

Fuel cells in general are defined on the basis of their electrolyte (Figure 1.10, Table 1.1). Each electrolyte then entails specific working conditions, and electrodes along with all the other cell components are designed on that basis. A different electrolyte means also a different chemical species is carried through it, and this determines the

electrode where water formation takes place. For example, PEMFCs have a protonic electrolyte taking H^+ ions from the anode to the cathode, so water is formed at the cathode. The contrary happens with a SOFC, its electrolyte is an anionic conductor that brings oxygen from the cathode to the anode and this time water forms at the anode.

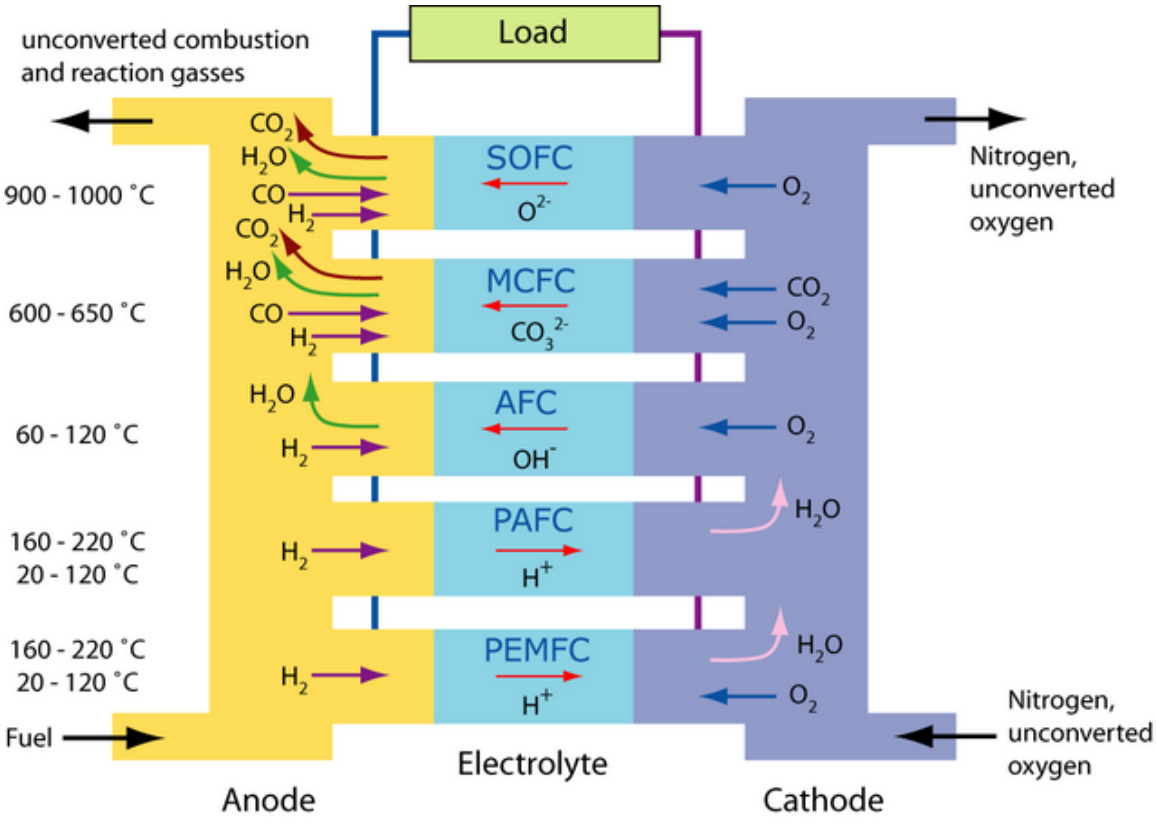

Figure 1.10 Summary of mechanisms of the different types of fuel cells. Source: University of Cambridge.

Fuel cell type	Common electrolyte	Operating temperature	Typical Stack Size	Electrical Efficiency (LHV*)	Applications	Advantages	Drawbacks
Polymer Electrolyte Membrane (PEM)	Perfluorosulfonic acid (PFSA)	<120°C	<1kW-100kW	60% direct H_2 40% reformed fuel	• Backup power • Portable power • Distributed generation • Transportation • Specialty Vehicles	• Solid electrolyte reduces corrosion and electrolyte management problems • Low temperature • Quick start-up and load following	• Expensive catalysts • Sensitive to fuel impurities
Alkaline (AFC)	Aqueous potassium hydroxide in a porous matrix, or alkaline polymer membrane	65°C-220°C	1-100 kW	60%	• Military • Space • Backup power • Transportation	• Wider range of stable materials allows lower cost components • Low temperature • Quick start-up	• Sensitive to CO2 in fuel and air • Electrolyte management (aqueous) • Electrolyte conductivity (polymer)
Phosphoric Acid (PAFC)	Phosphoric acid soaked in a porous matrix	150°C-200°C	5–400 kW, 100 kW module	40%	• Distributed generation	• Suitable for CHP • Increased tolerance to fuel impurities	• Expensive catalysts • Long start-up time • Sulphur sensitivity
Molten Carbonate (MCFC)	Molten lithium, sodium, and/or potassium carbonates, soaked in a porous matrix	600°C-700°C	300 kW–3 MW, 300 kW module	50%	• Electric utility • Distributed generation	• High efficiency • Fuel flexibility • Suitable for CHP • Hybrid/gas turbine cycle	• High temperature corrosion and breakdown of cell components • Long start-up time • Low power density
Solid Oxide	Yttria stabilized zirconia	700°C-1000°C	1kW-2MW	60%	• Auxiliary power • Electric utility • Distributed generation	• High efficiency • Fuel flexibility • Solid electrolyte • Suitable for CHP • Hybrid/gas turbine cycle	• High temperature corrosion and breakdown of cell components • Long start-up time • Limited number of shutdowns

*Table 1.1 Comparison between different fuel cells. Table mainly taken from https://energy.gov/eere/fuelcells/comparison-fuel-cell-technologies. At the web page are also available efficiency references to actual cells. *: Low Heating Value*

Polymer Electrolyte Membrane Fuel Cells (PEMFC, PEFC, or simply PEM)

Polymer Electrolyte Membrane fuel cells are for sure the fuel cells it is easier to encounter during everyday life. All the hydrogen vehicles are fed by a PEMFC, except a SOFC prototype by Nissan, and it is already possible to hop on a PEMFC bus in different cities: London, Aberdeen, Milan, Cologne, Bolzano (Figure 1.12), Hamburg are some examples considering only Europe. The success of this fuel cell is probably related to its flexibility: it occupies only small volumes, it is easily scalable (there are both PEM fuelled buses and drones), all the components are in a solid phase (Figure 1.11), it is compact and robust and it requires only minimum maintenance. The semi-reaction in a PEMFC are the following:

$2H_2 \rightarrow 4H^+ + 4e^-$ (anode)

$O_2 + 4H^+ + 4e^- \rightarrow 2H_2O$ (cathode)

Both water and heat are produced during operation, and their management must be accurate to prevent cell drying/flooding. Drying is avoided with the use of humidified gases, while the risk of flooding is more challenging because of the high amount of generated water, and in general requires a very accurate optimization of water balance inside the cell[70].

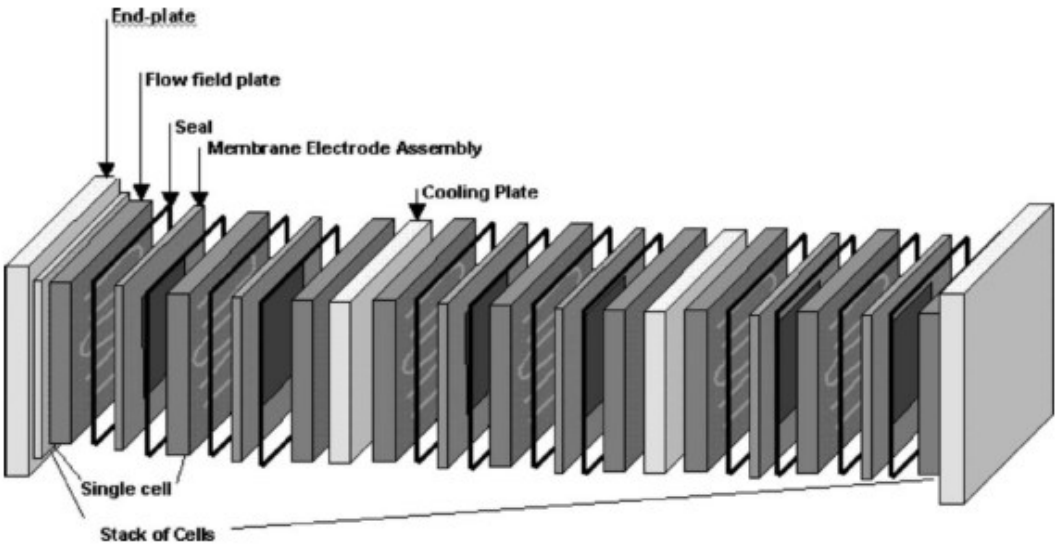

Figure 1.11 Stack of a PEM fuel cell. From [71].

The electrolyte in PEMFCs is a humidified membrane, able to transport only protons. Perfluorosulfonic acid is the most common material for PEMFC electrolytes, because it provides both a chemical/mechanical high stability and a good protonic conductivity. It consists of a polytetrafluoroethylene backbone with $O\text{-}CF_2\text{-}CF_2$ like side chain and sulfonic acid (SO_3^-) groups at the end of the side chains that provide the conduction properties[71]. A carbon black layer improves gas diffusion into the electrodes. Both cathode and anode are made of catalyst platinum deposited on carbon black, and therefore represent the most expensive component of this cell. This catalyst in reducing condition is highly susceptible of CO poisoning even if this chemical is present only in traces[72], so utilized fuel must be purified. The requirement of a very clean gas makes complicated the use of fuels generated by biomasses. Several projects plan to produce environmentally-friendly fuels from this source in the future[73], but they would be unsuitable for PEMFCs, because they often contain remarkable amounts of CO and sulphur impurities. Other than this, the presence of platinum brings a more serious problem potentially able to make impossible a global diffusion of PEMFCs; platinum is a scarce metal simply it is not enough: it has been calculated that the entire global resources would not be able to sustain a 500 million vehicles fleet (the size of European Union's + United States's) for more than 15 years[74]. For this reason, there has been a huge effort in reducing the amount of platinum required for every cell by improving technology and using alloys with other metals[75], as well as in finding a substitute for this precious metal, a research that has been unsuccessful, at least until now[76].

Figure 1.12 PEM fuel cell bus in Bolzano, Italy

A particular version of the PEMFC is the Direct Methanol Fuel Cell (DMFC). DMFCs operate at 130°C with liquid methanol as fuel, which is easier than hydrogen to store and manage, not being a gas. Adjective *direct* means there is no reformer, but methanol is directly fed to the anode. However, efficiencies are low (40%) and electrodes need a high amount of noble metal to catalyse direct oxidation of methanol.

Alkaline Fuel Cells (AFC)

In alkaline fuel cells the electrolyte is an alkaline solution, typically a water solution of KOH. The conduced species is $(OH)^-$, from the cathode to the anode. The electrolyte is contained into a solid matrix, the electrodes are a composite system in which PTFE supports carbon black and the catalyst. The catalyst can be chosen from a range of metals, not necessarily noble. Nickel in particular, and silver in second place, are the most used electrodes; platinum is suitable too, although its high cost discourages its use when other cheaper material work fairly[62]. Electrodes are enveloped by hydrophobic PTFE layers that allow gas diffusion. The semi-reactions taking place at the electrodes are:

$2H_2 + 4OH^- \rightarrow 4H_2O + 4e^-$ (anode)

$O_2 + 2H_2O + 4e^- \rightarrow 4OH^-$ (cathode)

Water is a by-product and must be removed, because its accumulation causes a dilution of the electrolyte that makes it lose its conductivity for OH^-. The cell produces also heat, and its management is necessary to avoid evaporation of the electrolyte. Due to the alkaline environment, CO_2 is poisonous for the cell because it reacts with basic electrolyte and forms K_2CO_3[77]. Due to the sensibility of the electrolyte to water and CO_2, two electrolyte designs, static and mobile, can be implemented to avoid loss of performances of the cell. Static electrolytes are enclosed between the electrodes, and in fact they are just like any other fuel cell electrolyte. Cells with static electrolyte have controlled water evaporation at the anode and must be used with pure oxygen or purified air, because there is no way to remove CO_2 once it reaches the cell. Cells with mobile electrolyte are continuously replenished with new electrolyte, whose composition is hence kept always fixed. This solution complicates the system, because it needs an electrolyte reservoir, some pumps and a

higher distance between electrodes to allow the flow. The overall performance of AFCs is good, they are among the most efficient fuel cells, because of the low temperature and the alkaline environment that favourites the reaction, and are the cheapest ones. Their power density can be compared to more diffused PEMFC as well as their life, but probably the complications related to the electrolyte induced industries to choose PEMFCs for low temperature applications, they are more expensive because of platinum but their management is considerably easier. In any case, AFCs could represent a good substitute for PEMFC in case platinum supply becomes a problem.

Phosphoric Acid Fuel Cell (PAFC)

PEMFCs had sulfonic acid groups bound to a solid matrix to provide protonic conduction. In a PAFC the principle is the same, the electrolyte is an acid and conducts proton, but the electrolyte is liquid, made of pure phosphoric acid. This cell must operate around 200°C to achieve a sufficient ionic conduction, and is therefore defined as an Intermediate Temperature fuel cell, between low temperature (AFC, PEMFC) and high temperature (MCFC, SOFC) ones. Phosphoric acid melting temperature is 40°C, so cell start up could be a problem. The electrodic reactions are the same of a PEMFC:

$2H_2 \rightarrow 4H^+ + 4e^-$ (anode)

$O_2 + 4H^+ + 4e^- \rightarrow 2H_2O$ (cathode)

PAFCs electrodes are Pt on carbon, like PEMFC, and the same concerns related to platinum abundance apply to them. The carbon black gas diffusion layer must be hydrophobic, so it is usually immersed in a PTFE solution. Due to the higher temperature, platinum catalyst is not as sensible to CO poisoning as in PEMFCs, so fuel does not require purification. Water budget must be taken in consideration during design, as it can dilute the electrolyte. A PAFC is big and heavy, not particularly flexible and the presence of concentrated phosphoric acid entails relevant hazards. Because of these important drawbacks, today PAFCs use is limited only to some stationary application.

Molten Carbonate Fuel Cell (MCFC)

A MCFC has a liquid electrolyte made of molten carbonates contained into a solid matrix. To keep the electrolyte in the liquid state, operating temperature is fixed at 650°C, so these cells belong to the High Temperature fuel cells group. The first MCFCs used as electrolyte a mixture of Li_2CO_3/K_2CO_3, over the time also a Li_2CO_3/Na_2CO_3 mixture has been developed having the advantage of being less aggressive towards the Ni of the electrodes. The matrix is usually made of γ-$LiAlO_2$. CO_3^{2-} is the chemical species transported by the electrolyte, from the cathode to the anode, and the semi-reactions taking place at the electrodes are:

$$2H_2 + 2CO_3^{2-} \rightarrow 2H_2O + 2CO_2 + 4e^- \text{ (anode)}$$

$$O_2 + 2CO_2 + 4e^- \rightarrow 2CO_3^{2-} \text{ (cathode)}$$

Carbon dioxide is recycled at the anode and re-used at the cathode. This cell can operate also with hydrocarbons as fuel because reforming can happen at the anode, generating syngas ready to use for the electrochemical reaction. Indeed, a common feeding for MCFCs is a methane/water mixture. Electrodes are Ni-based; the cathode is NiO and the anode is a Ni cermet. For MCFCs, CO is a fuel and does not produce any poisoning. They are completely tolerant also to CO_2, so air directly from atmosphere can be used. MCFCs drawbacks are related with the high operative temperature causing fast materials deterioration[78] and a low flexibility of the device, used only for stationary applications[79].

1.4.4 Solid Oxide Fuel Cell (SOFC)

SOFCs are ceramic cells with a solid oxide as electrolyte (see Figure 1.6). Their operating temperature is the highest of all the fuel cells and spans between 700°C and 1000°C, with prototypes working also at lower temperatures down to 500°C; they obviously are among the High Temperature Fuel Cells. In these cells, oxygen is reduced at the cathode, incorporated in the crystalline lattice of the electrolyte as O^{2-}, and is conducted to the anode jumping from oxygen vacancy to oxygen vacancy though the lattice. The semi-reactions at the electrodes are:

$$2H_2 + 2O^{2-} \rightarrow 2H_2O + 4e^- \text{ (anode)}$$

$$O_2 + 4e^- \rightarrow 2O^{2-} \text{ (cathode)}$$

The O^{2-} species is a very large and hindering ion, and its conduction is not easy as due to its size it can easily get stuck; this is the reason why SOFCs operate at such high temperatures. SOFCs are robust devices: they can work with a very wide range of fuels (hydrocarbons, alcohols, etc.) without being subjected to poisoning. SOFCs efficiencies are high, electrical efficiency (the efficiency considering only electrical power) normally reaches 60%[80]; SOFCMAN in China holds current efficiency record, having declared it is developing a stack with 94.3% fuel consumption and 72.5% electrical efficiencies at 700°C, very close to maximum attainable values[81]. Co-generation systems for heat recovery can be easily associated to SOFCs, and allow to raise overall efficiency to more than 90%[80].

For SOFCs, mechanical stability is problematic more than for the other types of fuel cells. Because of the high temperatures, they can be made only of ceramic materials, whose mechanical properties are modest. In particular, ceramics are brittle and easily crack when subjected to mechanical stress, which can arise simply because of a different Thermal Expansion Coefficient (TEC) of the cell components. Commercial SOFCs are highly engineered towards the more accurate uniformity of the TEC possible, in order to minimizes stresses, during cooling/heating cycles, that could lead to cell failure. It is easily understandable that the choice of which cell component provides mechanical support is critical. Early cells used a supporting thick electrolyte. This geometry provides the simplest fabrication, as it is sufficient to press some electrolyte powder into a pellet and to fire it at high temperature; then, anode and cathode are deposited on the sides of the cell by means of tape casting or screen printing. The electrolyte is a dense layer, so it is able to provide a decent mechanical stability. Unfortunately, an *electrolyte supported cell* has a serious drawback that deeply weakens its performance: for the cell economy, the electrolytic layer can be represented as a purely resistive element, so its resistance is directly proportioned to its thickness.

The need of reducing electrolytes thickness led to other two variants of the SOFC: μ-SOFCs and anode supported SOFCs. The so-called *μ-SOFCs* are SOFC cells in which the thickness of every component is reduced to the maximum possible extent. Their thickness is lower than 1 μm, and in general the electrolyte is still supporting, but it

is able to fulfil this task only because the electrodes are even thinner. μ-SOFCs are fabricated with successive depositions of layers with Ultra High Vacuum techniques (UHV, mainly: sputtering, Atomic Layer Deposition, Pulsed Laser Deposition)[82], [83]. Given the accuracy of the deposition and the perfection of the layers created with the mentioned techniques, the performances normalized by area of these cells are outstanding compared to macroscopical cells, but the high costs related to the used techniques, an intrinsic fragility for the extreme thinness and a difficult scalability make difficult a large-scale application of these devices.

A simpler way to reduce the thickness of the electrolyte is to designate another layer for the mechanical support, this is what an *anode supported* fuel cell does. However, the anode is an active layer which interacts with the gas phase and must therefore be porous, the thickness and porosity of the anode are then a compromise between the mechanical properties and a sufficient gas diffusion inside the electrode. Often, the anode is prepared in two stages: first, some anode powder is pressed to obtain a denser thick substrate able to provide mechanical support, then the functional anode layer, more porous, is deposited with tape casting. The obtained anode is fired, then a layer of dense electrolyte is deposited with tape casting and the cell is fired again. Finally a third tape casting deposition is done for the cathode and the cell is fired a last time[84]. A supporting cathode is theoretically possible, but it is avoided because the reduction of oxygen taking place at it is the most difficult reaction the cell must carry on, and it can be considered the real *rate determining step* of the whole process. Hence, to fabricate a supporting thick cathode would mean to slow reaction speed, and decrease significantly the cell power.

Electrolyte materials

First SOFCs used YSZ (Yttria Stabilized Zirconia) as electrolyte, this material today is still in use and far from being obsolete. It has a decent ionic conductivity, and no electronic conductivity up to 1500°C. In addition, it is cheap and its components are abundant. Common zirconia (ZrO_2) would face two phase transitions during heating: from monoclinic to tetragonal at 1170°C and from tetragonal to cubic (fluorite) at 2370°C. The addition of yttria stabilizes the fluoritic structure also at lower temperatures, hence the name *yttria stabilized zirconia*. Yttria presence

generates also oxygen vacancies in the crystalline structure, which are fundamental for the ionic conduction, according to the reaction:

$$Y_2O_3 \rightarrow 2Y'_{Zr} + 3O_O^x + V_O^{\bullet\bullet}$$

The stabilization with scandium instead of yttrium further improves conduction because of the very similar radius between Sc^{3+} and Zr^{4+} cations. Unfortunately, this system possesses a high amount of ordered and metastable phases and this leads to a general instability, as the formation of undesired phases also during operation is common[85]. Because of this, YSZ is still the most used electrolyte material in SOFCs.

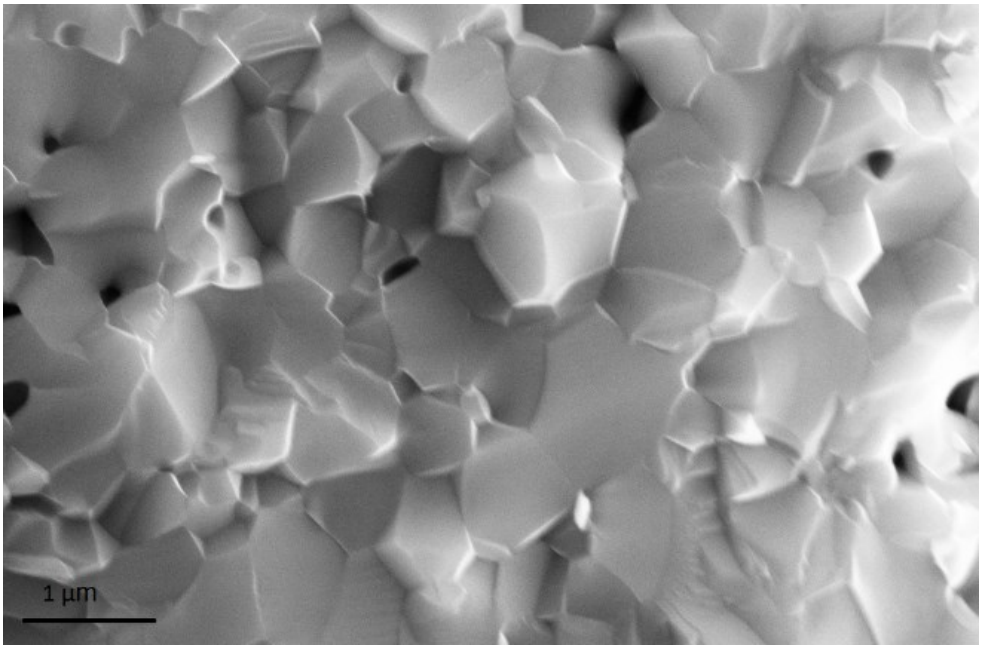

Figure 1.13 SEM picture of the section of a thick CGO electrolyte.

Ceria is another oxide with fluoritic structure. Oxygen vacancies in ceria are generated, analogously with zirconia, with the doping with proper metal cation. The most common substitution is with gadolinium, to form Gadolinium Doped Ceria (GDC), sometimes called also Ceria Gadolinium Oxide (CGO), Figure 1.13:

$$Gd_2O_3 \rightarrow 2Gd'_{Ce} + 3O_O^x + V_O^{\bullet\bullet}$$

Samarium is another common dopant, the oxide obtained is named Samarium Doped Ceria (SDC). Both gadolinium and samarium are lanthanides with valence 3+, so the equation shown above is valid also for samarium doping. Ce^{4+} has an ionic radius is very similar to Sm^{3+}, and this makes the conductivity obtained with samarium the best cerium oxide can reach. In oxidizing condition ceria is a pure ionic

conductor, but Ce^{4+} is easily reduced to Ce^{3+} when oxygen partial pressure decreases, and this brings some electronic conduction to the material. The presence of electronic conduction is undesired, because it short-circuits the electrodes and decreases available potential and therefore efficiency. For this reason, cells with ceria electrolyte should not be operated at temperatures above 600°C[86]; so, ceria is the best choice for Intermediate Temperature SOFCs[87] (i.e.: SOFCs designed to operate below 600°C).

The third SOFC electrolyte examined here, $La_{0.8}Sr_{0.2}Ga_xMg_{1-x}O_3$ is the less common, and is a perovskite, instead of a fluorite as the previous two. In general, Ga based perovskites are predominantly ionic conductors, and almost all possible combination of elements leading to a gallium perovskite have been studied. At the end, $La_{0.8}Sr_{0.2}Ga_xMg_{1-x}O_3$ (named also LSGM, x is usually 0.9 or 0.8) was found to be the best compromise in terms of cost, stability and performance. At high temperatures (>650°C) LSGM conductivity outperforms both CGO and YSZ (Figure 1.14). The presence of magnesium increases the amount of oxygen vacancies, according to the following equation:

$$2MgO \rightarrow 2Mg'_{Ga} + 2O_O^x + V_O^{\bullet\bullet}$$

One of the reason LSGM is not very diffused is it has a compatibility problem with nickel, which is the catalyst material of almost all the SOFCs and close to La-containing perovskites can form ionic insulating phase $LaNiO_3$. LSGM in reducing atmosphere at 800°C has been found to lose gallium from the surface on the long term due to evaporation [88], [89], because of a relatively high GaO partial pressure in that condition. This strongly limits application of the material at high temperature; in any case the GaO partial pressure decreases exponentially with temperature so at lower temperature Ga evaporation is in fact negligible[86]. An accurate experimental assessment of the maximum safe temperature for LSGM use currently lacks. Finally, it must be stressed that, since LSGM has so far remained only of scientific interest on a lab scale, the problem of avoiding Ga evaporation has never been really tackled.

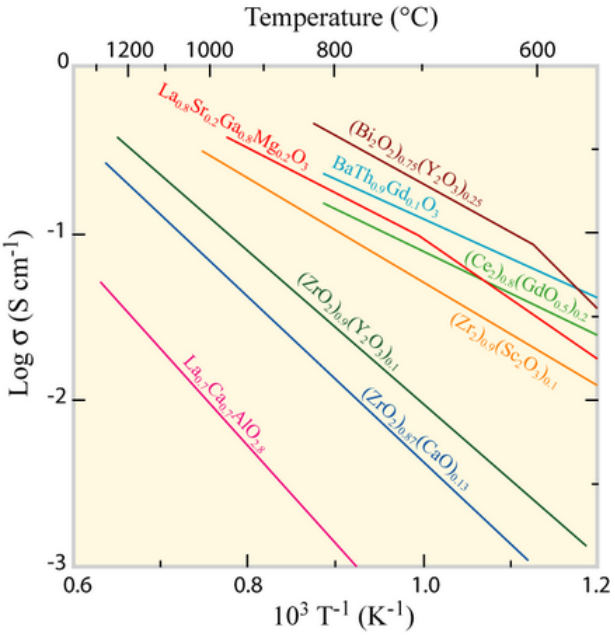

Figure 1.14 Ionic conduction of different electrolyte materials for SOFCs. From [86].

Anode materials

SOFCs are high temperature devices, so they do not need noble metals to catalyse reactions. The standard anode catalyst is nickel, which is cheap and in SOFC conditions show a good activity. The anode is in form of a cermet, of nickel particles deposited on a ceramic backbone made of the same material of the electrolyte (so, generally CGO and YSZ). Its preparation begins with the mixing of NiO and YSZ or CGO in the appropriate amounts, this powder is then used to prepare the anode, the reduction from NiO to Ni is carried out with hydrogen on the complete cell, during an activation procedure. The anode, as any electrode, must be an electronic conductor, so nickel must be in a sufficient amount to allow electronic percolation in the entire volume of the cermet. On the other hand, nickel is a catalyst so its superficial area is very important, and an excessive amount of it would lead to the formation of bigger particles with loss of active surface; in fact, anodes with too much nickel show metallic behaviour. An optimal ratio between volumes of nickel and YSZ/CGO is important to have electrically conductive and catalytically active anodes, and is located between a 30%-40% of Ni and 60%-70% of YSZ or CGO. The granulometry of the YSZ/CGO powder is very important to obtain an appropriate porosity in the final electrode. Porosity must be sufficient to allow an easy gas diffusion inside the electrode, but not too much, in that case it would be difficult for Ni to create electronic percolation pathways. Ni cermet anodes do not possess mixed

conductivity, so hydrogen oxidation can take place only where the gas phase that contains H_2, the Ni catalyst and the YSZ/CGO that brings the oxygen meet. These interface zones are very important because the anodic reaction can happen only here, and are named Triple Phase Boundaries (TPBs). For a Ni cermet anode, it is good to have TPBs as large as possible. So, Ni cermets are very complicated systems, in which a lot of parameters can be varied, from the granulometry of the used powders to the synthesis (temperature, times, ratios Ni/solid oxide), affecting several characteristics of the final material. This systems, in particular the classic Ni/YSZ cermet, has been extensively studied and several reports are available[90], [91].

Even if nickel cermet anodes are the standard for current SOFCs, they have some flaws, so that they cannot be considered the optimal solution for this application. At 800°C, metallic nickel has a $16{\cdot}10^{-6}$ K^{-1} TEC[92], while YSZ has 10 K^{-1}[93]. Nickel particles are subjected to slow degradation because of the aggregation of Ni particles that leads to progressive loss of active surface (hence, also triple phase boundary is lost), and fast more disruptive degradation due to RedOx cycles they can be subjected to, during operation, for a variety of reasons[94](Figure 1.15). Nickel tends to cover itself with carbon when catalysing the oxidation of organic compounds, and the process is irreversible; this relegates the SOFCs practically to the only use of hydrogen as fuel, because hydrocarbons, methanol or ethanol would lead to anode deactivation. This is probably the biggest limit of a nickel anode, as for several contexts the use of hydrogen is impractical, due to its low energy density and difficult supply. In addition, several artificial photosynthesis methods for the production of fuels are able to synthesize directly methanol or other carbon containing chemicals from CO_2, and a high efficiency device as a SOFC is would be an incomparable match for them.

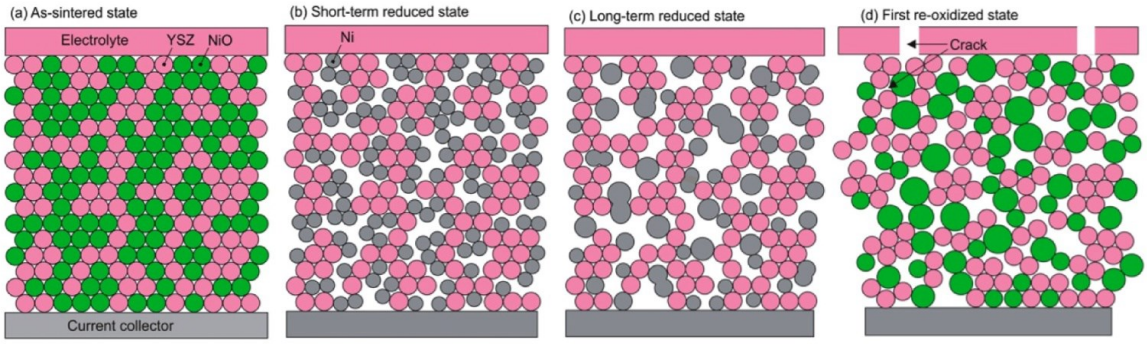

Figure 1.15 Coarsening and disruptive expansion of Ni in a cermet following a RedOx cycle. From [94].

Cathode materials

A cathode material for a SOFC must be stable in oxidizing conditions at high temperatures, and must be an electronic conductor. The best materials for this task are some perovskites, which have also the advantage of being Mixed Ionic Electronic Conductors (MIEC). The mixed conductivity allows a great simplification of the electrode, in such a material the oxygen can be absorbed anywhere on the surface, because the catalyst is also ionic and electronic conductor. There is no more triple phase boundary at least in a restrictive sense as it was in cermet electrodes, and all the surface of the cathodic material can be considered active. In reality, actual process is more complicated than this, because oxygen reduction is a very complex chemical reaction, that involve several steps and that can happen via different routes.

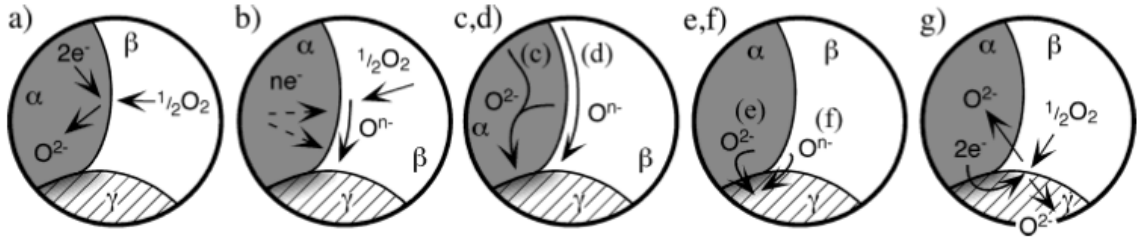

Figure 1.16 Some mechanisms for oxygen reaction in a SOFC cathode. α is the cathode, β is the gas phase and γ is the electrolyte. From [95].

In Figure 1.16 there are some hypotheses of how the reaction can take place at a SOFC cathode. Oxygen reduction can be summarized in general as composed of three main steps: O_2 is adsorbed on the electrode, the molecule is split and reduced (not necessarily in this order) and O^{2-} ions reach the electrolyte. How, precisely, these steps happen and which intermediate steps, among all the ones shown in the figure, are present or not, is not entirely clear. Not all of these mechanisms are available for all the electrodes, for example, a), c) and e) need a mixed ionic electronic cathode material, as SOFC cathodes, indeed, are. But even if the cathode is a MIEC there is a competition between the surface path (b-d-f) and the bulk path (a-c-e). The choice between them depends on a variety of factors, including the perovskite ionic conductivity of the perovskite, the distance from the electrolyte and the electrode morphology; in any case, there is sufficient agreement that for materials with rather high ionic conduction, as the perovskites used as cathodes, the bulk path cannot be neglected. Thus, there is no real TPB, rather, a more complicate interaction that

involves all the surface but it is still influenced by how and where cathode and electrolyte are connected. It is not clear also which one, of the many represented in Figure 1.16, is the rate determining step, although it seems there is no real rate determining step, but the reaction is co-limited by more than one step. This means also that probably the speeding up of any of the steps would result in a faster overall reaction. For an extensive explanation, we refer to Adler's review[95].

Most used cathode materials are LSM ($La_{0.6}Sr_{0.4}MnO_3$), LSC ($La_{0.6}Sr_{0.4}CoO_3$), LSCF ($La_{0.6}Sr_{0.4}Co_{0.2}Fe_{0.8}O_3$) and BSCF ($Ba_{0.5}Sr_{0.5}Co_{0.8}Fe_{0.2}O_3$). All of these materials are also MIEC, and in general the better is the mixed conduction the best the cathode behaves. All strontium containing cathodes have a compatibility issue with YSZ, because at high temperature they easily form $SrZrO_3$, which is an insulating phase. This can be avoided with the deposition of a CGO buffer layer so there is no contact between the perovskite and YSZ[96]. In general, cobaltates show the highest activity, but cobalt significantly increases the TEC so there are problems of thermal expansion matching, leading to cracks on the long term. BSCF has very good performances, but its poor stability makes it unsuitable for industrial purposes. LSM compared to the other cathodes has lower performances, but its high stability and its cheapness keep it among the most used materials.

Single Chamber Solid Oxide Fuel Cells (SC-SOFCs)

A particular architecture, available for SOFCs, is the Single Chamber one (SC)[97]. SC-SOFCs have no physical separation between the anode and the cathode, and both the electrodes are immersed in the same atmosphere. This has several advantages[98], especially for small devices. The obtainment of an effective sealing at high temperature is complicated, and tight connections between the cell and the other sealing elements can be the source of tensions leading to failures. For Single Chamber devices, cell design becomes more compact, and in general fabrication is easier.

After start-up, SC-SOFCs can operate without external heating, because the direct oxidation between fuel and oxygen is exothermal and can sustain autonomously the cell, at expense of a fraction of efficiency. The main drawbacks are the low efficiency due to parasitic reactions, which are desirable only if the heat produced by them is

exactly the amount needed for self-sustainment (all the extra heat corresponds to loss of efficiency) and the risk of explosion related to the presence of fuel and oxygen in the same mixture. For safety reasons, SC-SOFCs are fed only with methane and rarely with hydrogen; methane at the anode is subjected to partial oxidation and the syngas produced is the real fuel[99].

Anodes are made of nickel, which is able to operate under methane because the presence of oxygen in the atmosphere prevents its passivation by carbon deposition. Since both the oxidant and the fuel are present at both the electrodes, the selectivity of electrode materials for the respective electrochemical reaction is critical, and has been the main restrain to a large diffusion of these devices. In fact, no fully selective materials have been found (indeed, all SOFC cathode perovskites catalyse methane oxidation), so the electrical efficiencies of SC-SOFCs have always remained extremely low, below 5%. In reality, there has been no particular research about specific materials for SC-SOFCs, as the tested cells were always prepared with electrodes taken from current SOFC technology, attempting only to optimize the cell towards better performances. Today, the SC-SOFCs are being abandoned by research, due to a lack of significant results in research involving these devices. In this thesis, an attempt to revive attention on SC-SOFCs has been done, with the study of a cathode material potentially able to raise efficiency towards more economically sustainable amounts.

The operating principle of a SC-SOFC is shown in Figure 1.17. A fuel rich gas mixture is used to promote only partial oxidation at the anode, so syngas is formed and used for the electrochemical reaction. The cathode is not able to catalyse the partial oxidation, so in principle it should ignore methane and use only oxygen. Flows are divided sending only 25% at the anode to recuperate the imbalance in fuel composition, so each electrode can consume 100% of its reactant (stoichiometric mixture would be CH_4:O_2=1:2). The lack of selectivity at the cathode determines the oxidation of fuel at its side, causing a great loss of efficiency.

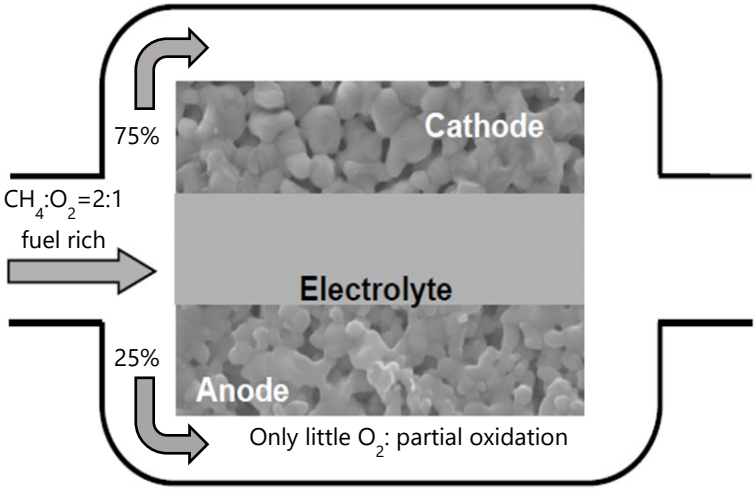

Figure 1.17 A Single Chamber SOFC.

1.5 Perovskites

As explained in the previous paragraph, most of the materials used as cathodes are perovskites, and a consistent part of the research on new SOFC materials is focussing on them. So, it could be useful to offer a deeper insight on this interesting class of materials.

Perovskites are a class of crystalline solids with a ABX_3 brute formula, in which A and B are cations, and X is an anion. In the most of the cases, and always in the field of fuel cells, the anion is oxygen so the formula can be written as ABO_3. X can be also a halogen, as it happens for the hybrid perovskites that are gaining attention for solar cells; however, only inorganic oxide perovskites are useful for our purposes, so we will consider only them in the following paragraph.

A perfect perovskite has a cubic symmetry, as shown in Figure 1.18. At the centre of the primitive cell, a B cation is surrounded by an octahedra of oxygen atoms. A cubic cage of eight A cations encloses every oxygen octahedra. As evidenced by Figure 1.18 A, in fact every A cation is placed inside a very large void formed at the centre of a cube of B cations and to occupy all the volume must have a large radius. Indeed, A cations are often alkaline earth metals, or lanthanides. B cations are smaller, and often determine chemical and physical properties of the perovskites, while A cations tune them, other than influencing stability[100]. The perovskites are flexible structure, they are able to accommodate almost the entirety of the periodic table inside their structure, provided that the ratios between the atomic radii are suitable for the

formation of a stable structure. The constraints are mainly geometric, and the stability of a structure can be roughly predicted with the Goldschmidt tolerance factor:

$$t = \frac{r_A + r_O}{\sqrt{2}(r_B + r_O)}$$

Where r_A is the ionic radius of the A cation, r_B is the ionic radius of the B cation and r_O is the ionic radius of oxygen. If t>1, the perovskite is hexagonal or tetragonal, if 0.9<t<1 the perovskite is cubic (the ratio between the cations is ideal), if 0.71<t<0.9 the perovskite is orthorhombic, with t<0.71 the crystals assumes different structures.

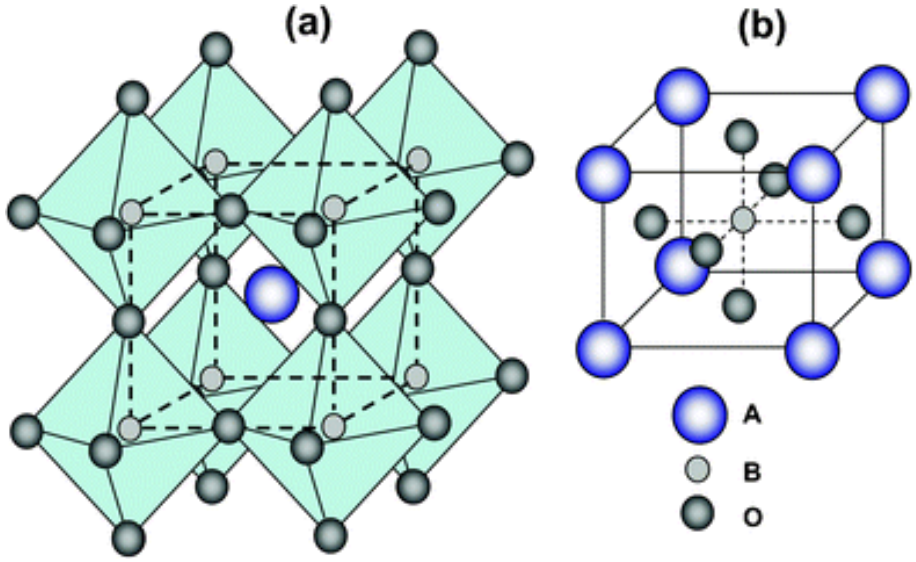

Figure 1.18 Crystalline structure of a perovskite. A: evidencing the octahedra formed by O atoms. B: primitive cell. From [101].

The Goldschmidt tolerance factor provides an indication of the most probable structure for a specific composition, but it is not an absolute rule. Depending of ambivalent oxidation states (which means cations have radii hardly predictable), oxygen vacancies and particular interaction between atoms the actual structure sometimes differs from the predicted one.

The three oxygen atoms carry a total -6 oxidation state, so the sum of the A and B cations must balance this to obtain charge neutrality. From this assumption it is possible to distinguish different classes of perovskites depending on the charges A and B cations have. III-III perovskites are the most common, including $LaMnO_3$, $LaCoO_3$ and in general all the perovskites with a lanthanide as A cation. II-IV

perovskites include the ones with alkaline earth metal A cations: $SrTiO_3$, $SrFeO_3$, $BaTiO_3$, etc. I-V perovskites are more known for physical and optical properties, the most famous ones are niobates as $KNbO_2$ and tantalates as $KTaO_3$. These categories are not strict at all, it is possible to combine elements with different oxidation states to confer new properties to the perovskites or to push some element to a more desired oxidation states.

The electronic conductivity of the perovskites depends on B cations. If they have a redox couple (as, for example, Fe^{2+}/Fe^{3+}, Co^{3+}/Co^{4+} and $Mn^{2+}/Mn^{3+}/Mn^{4+}$) electronic conduction is possible, via the overlapping d orbitals of B cations. The cation has to be in the suitable condition to change its oxidation state to be able to conduce: $CaTiO_3$, as an example, is an insulator because titanium cannot move from its 4+ oxidation state. Perovskites are mostly semiconductors, although some with metallic behaviour exist[102]. The stable perovskitic crystalline structure provides a robust scaffold for ionic conduction, O^{2-} ions can move from vacancy to vacancy through the crystalline structure of the material. Ionic conductivity is directly influenced by the amount of oxygen vacancies the material has.

Perovskites can accommodate more than one type of cation for each A/B site. This offers plenty of possibilities for the design of new innovative materials. It is not uncommon to find perovskites with two cations for each site, the already mentioned LSCF is an example. There are various reasons this is done. Catalytic activity of a perovskite can be enhanced by different A cations, for example often strontium addition in a III-III perovskite has this effect at the expense of the stability. Alkaline earth metals in a III-III perovskite have also the effect of increasing oxygen vacancies for ionic conductivity: if the B cation cannot easily increase its oxidation state to counterbalance the lost positive charge, electroneutrality is maintained by removing some oxygen atoms from the lattice. Alkaline metals, given their only +1 oxidation state, push to oxygen vacancies formation even more strongly, but due to their small size they tend to be tolerated in the perovskitic structure only if in limited amounts. This peculiar ability of the perovskites to lose oxygen without affecting the crystalline structure is sometimes recalled in the compound formula, where the stoichiometric coefficient of oxygen in perovskites can be indicated as $3-\delta$, to account for the oxygen

vacancies formed to maintain electroneutrality. New B cations can be introduced to add new properties to a perovskite, as for example electronic conductivity or catalytic activity. Sometimes the association of two particular B cations improves the performance of a material, due to some cooperative effect, at a level higher than the one each of the cations could reach singularly. The B cations influence also the stability of the material, so the addition of a proper species can increase the material stability, as Ga does in $LaFeO_3$.

Perovskite are ceramic materials, and under air are stable until high temperatures, in general at least 1200-1300°C. However, low pO_2 can swiftly lead to their degradation. If a cation is reduced below the oxidation state the perovskite can tolerate the material degrades, and most metallic cations occupying the B site are reduced below 3+ oxidation state (the minimum for a B site cation) between 600 and 1000°C, which correspond to the operating temperature of a SOFC. Because of this, they are not employed at the anodic side, even if they could be active also as electrocatalysts for oxidation reactions.

1.6 Energy transition and new possibilities

A more radical but already happening process is a shift from traditional fossil sources to cleaner ones. At the present moment, it is still unclear where the present energy transition will lead, although the involvement of renewable sources, mainly solar energy, seems to be the focal point of the new system. Renewable energy sources are subjected to a physiological variability in power output depending on factors beyond our control (solar energy is influenced by daytime, wind energy by the weather, etc.) and peaks of power production do not correspond necessarily to peaks of demand. So, it becomes necessary to provide also some energy storage system, able to stockpile the excess of production until demand surpass production. Currently, with fossils being the main source, this problem does not exist, because they can be tuned to match the energy demand. In case fossil generate power can be reduced when renewable production increases, and renewable sources never reach or exceed the demand. But if the main sources are renewable, as it will hopefully be in some years, the extra energy must be stored.

1.6.1 Batteries

The easiest way to store electrical energy is batteries. This technology, Li-ion batteries in particular, has received wide attention in the last years thanks to important advancements; as the most evident but not the only one, they are the core element of electric cars, including famous Tesla supercars. The use of batteries for the storage of renewable energy excess is already a reality, even if at its first stages. In 2017 Mitsubishi opened in Kyushu (Japan) the largest battery energy storage system, employing its NaS batteries with a total capacity of 1.1TJ/300MWh and a maximum power of 50MW[103]. Tesla itself on November 2017 has delivered in Jamestown, Australia, the world largest Li-ion battery storage facility with a capacity of 465GJ/100MWh and a maximum power of 100MW[104]. On a smaller size, it is already possible to purchase specific products for the storage of the excess of energy from a photovoltaic panel on a domestic scale.

1.6.2 Electrolysers and SOECs

Batteries are probably the most at hand choice for the storage of power, but they are not the only one. Another possibility is to store energy not in the form it was obtained (electrical), but to transform it in something easier to store and manage, as a fuel. The conversion into a fuel has various benefits: a fuel is easier to store, can be directly used in already existing technologies, has a very high energy density, in general is more flexible, which is an advantage that must not be underestimated. Indeed, when we talk in general about energy demand we sum up a lot of necessities, environments and uses that are extremely diversified if compared singularly, and every one of them has found its best solution in the current scenario. This is why there are so many energy sources and so many ways to use them. An airplane requires high amount of energy with the minimum weight possible, houses have plenty of small ready to use devices that must be fed with a clean energy source (nobody wonders why there are gasoline lawn mowers and electrical dishwashers, and not the contrary), heavy industries use a lot of energy so they need when possible a cheap source, electronics devices use small amount of energy packed in the smallest volume possible and must be shut on/off in the matter of seconds.

So, for some contexts electricity is the best choice, for some others it is not, and this is where fuels found application. Often this happened for energy density reasons, and for these cases one can expect it would be preferable to still have fuels also in the future. At least, as long as batteries do not reach the same performances as energy; but they still have not, in spite of the huge and surprising development of the last years, even if compared to the centennial internal combustion engine technology.

Electrolysis allows to convert electricity into fuels, it is a process known since centuries and already commonly used for small scale hydrogen production. In the last years, the development of fuel cells, as some kind of side effect, is boosting also the development of electrolysis for fuel production. The device for fuel production from electricity and electricity from fuel is essentially the same, i.e. a fuel cell that operates with a potential applied is the starting point for building an electrolyser. Traditionally, water electrolysis can be carried out in two ways, by means of an alkaline electrolyser (conventional setup with liquid electrolyte) or a Polymer Electrolyte Membrane, which makes the device analogous to a PEM fuel cell. Efficiency for these two techniques are similar, around 60%. PEM electrolysers can be twice as expensive compared to alkaline one, in part because they require platinum electrodes, but they should reach higher efficiencies in shorter times given their less developed stage[105]; maximum theoretical efficiency for PEM electrolysers is 94%, although this is only a purely speculative value[106].

A third way to convert electricity into fuel, that is currently under development but with very promising premises are the Solid Oxide Electrolysis Cells (SOECs), which stand to Solid Oxide Fuel Cells (SOFCs) the same way the PEM electrolysers stand to the PEM fuel cells. A SOEC works at high temperatures (≥800°C) and thank to this the reaction is less impeded than it is for the low temperature devices. It does not require platinum, but the costs are still high because of a more complicated fabrication technique. On the other hand, there are two major valuable advantages. SOECs already tested were able to reach much higher efficiencies than their low temperature counterparts: their energy-conversion efficiency can even surpass 100% in some operation mode due to the possibility to use heat from other processes as a source of energy[107][108]. Second, SOECs are able to co-electrolyse water and carbon

dioxide, producing syngas (H_2 + CO)[109], in other words they can be used for large scale conversion of atmospheric CO_2 into a useful chemical; this process today is already possible by means of dry reforming[110]–[113], but requiring methane as a reactant, while a SOEC only needs water (some argue also methane is a greenhouse gas, so it could be removed from the atmosphere[114] hence the reforming would not use any fossil fuel, but the 1.8ppm methane concentration[115] would make this process hardly economically sustainable). Moreover, syngas produced by SOECs can be converted to hydrocarbons via a Fischer-Tropsch process[116], [117]. Hypothetically, it would be already possible today to produce methane, which is a common used fuel, with completely sustainable processes by coupling a renewable energy source to a SOEC and a Fischer-Tropsch reactor; current estimation is the first fuel from solar production prototypes should be presented within a decade[118].

A common objection to the production of carbon containing fuels and to the continuation of their use is the subsequent emission of CO_2, that would further increase greenhouse effect. At this purpose it is important to stress that the real issue is the release of carbon that was trapped under the soil, but the use of carbon that already is in the atmosphere does not alter the carbon budget; similarly, the use of fuels generated from crops (the so-called biofuels) is cleaner than extracted fuels because no new carbon is introduced in the atmosphere[119].

First prototypes of cell stacks beyond the lab scale have already been proposed[120], although there are still significant problems of durability due to excessive anode degradation[121]. Very interesting is the possibility to operate the same cell alternatively in the *fuel cell* mode and in the *electrolyser* mode, analogously to a secondary battery that can be discharger and recharged. Such a device is called *reversible* SOFC and is already studied and developed[122], because it would allow both an easy storage of energy excess from renewable and an efficient re-conversion to electrical energy when needed. A SOEC would greatly benefit from the switching between the two modes, because this mode of operation has been found to significantly reduce the long term degradation of the cell[123].

In the challenge for the energy storage system of the future, batteries have an unquestionable advantage in terms of development stage, compared to electrolysers,

However, they still have drawbacks that will make difficult for them to gain an exclusive supremacy as the only energy storage devices. As Figure 1.19 shows, their energy density is low compared with fuel cells, which on the other hand fail when high powers are needed. Regarding mobile application, recharge times are another drawback for batteries: a 50 litres fuel tank contains around 1.7GJ of gasoline and is filled in a minute, so the fuel pump supplies a power of about 29MW in form of liquid fuel. Regardless of how fast could be the charging of a battery, it is very difficult to transfer such high powers from the electrical grid, at least at a domestic scale; actually, recharging columns for electrical cars that can be already found in some cities can supply up to 7kW of power. To combine energy density and power density, probably the best solution is to build hybrid devices, that could benefit from both the advantages of the fuel cells and the batteries[124].

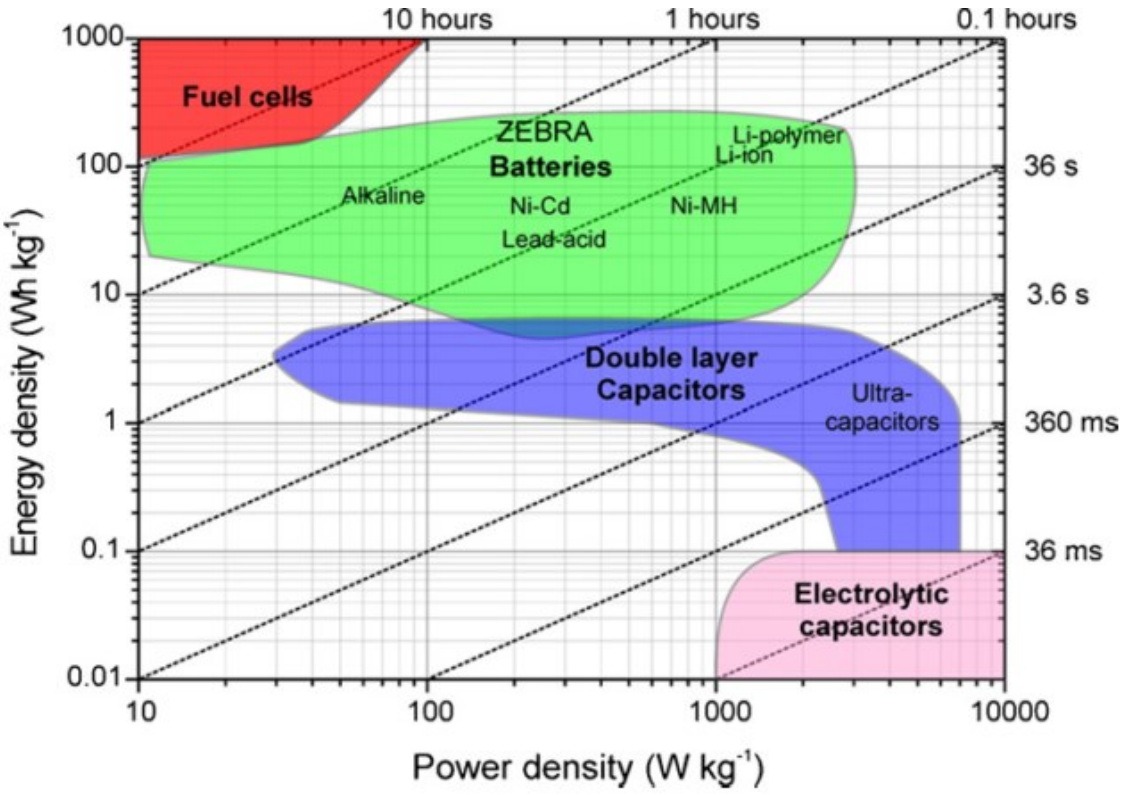

Figure 1.19 Ragone plot of different energy storage technologies. Dashed lines indicate characteristic times. From [124].

1.6.3 Artificial photosynthesis

Compared to batteries and electrolysers, artificial photosynthesis is more distant in the future. Nonetheless, the great efforts in this research field and the encouraging results allow to speculate that in 10-20 years we will be able to synthesize fuels from

solar energy without an electrical intermediate, as plants normally do[118]. Clearly, not every fuel can be produced. The reactants at our disposal are atmospheric gases, so H_2O and CO_2. H_2O can be split to obtain hydrogen, and CO_2 can be reduced, in this case the easiest product would be methanol. These fuels would be renewable, because obtained from solar energy, and fully sustainable. Fuel cells would allow an efficient exploitation of artificially photosynthesized fuels, thus can be a bridge between old fossil fuels and new renewable ones as they are compatible with both. This way fuel cells can ease the energy transition, mitigating the technological gap from the current situation to a new sustainable one.

1.7 Thesis outline

This thesis aimed to the development of new materials for Solid Oxide Fuel Cells. A precise approach has been adopted throughout the work: to combine the characteristics of more phases to obtain the desired properties. So, nanocomposites specific for each application have been designed, featuring a MIEC substrate and a catalytically active phase supported by it. In particular, the formation of a cooperative effect between the two phases, able to catalyse the desired reaction at a sufficient speed without the need of noble metals, has been pursued. One of the main flaws of SOFCs is the relatively short life of the device compared to the costs, and the most severe degradation happens at the cathodes; more stable cathodes could help in making most economically sustainable devices. For this reason, the first focus has been the cathode. A MIEC substrate has been selected on the basis of the best stability as a first criterion, and of the highest conductivity as the second. The $La_{0.6}Sr_{0.4}Ga_{0.3}Fe_{0.7}O_3$ perovskite (LSGF) turned out to be the best choice, for its high chemical stability and its fair mixed conductivity. In chapter 2 the synthesis of LSGF has been carefully studied, including the assessment of its resistance against reducing conditions. In chapter 3 LSGF has been functionalised with iron and manganese oxides. The so-obtained nanocomposites have been extensively characterized, and tested as SOFC cathodes in symmetrical cells for Electrochemical Impedance Spectroscopy (EIS) measurements; interesting performances emerged in particular from the composite of LSGF and iron oxide. In chapter 4, LSGF has been studied as a material for reversible symmetrical cells, hence a cell able to operate as both a SOFC

and a SOEC with identical anode and cathode. The cell was supported on a LSGM electrolyte, a perovskite very similar to LSGF; the great uniformity of the whole cell should guarantee a reduced materials degradation and a longer device life. During the experiments, LSGF was found to lack catalytic activity when at the negative electrode, and was impregnated with small amounts of palladium. EIS data and polarization curves were collected for the cell in both fuel cell and electrolysis operation mode. Results confirmed the successful operation of the device as a reversible cell. In chapter 5, the nanocomposite LSGF with manganese oxide, after unsatisfying results as cathode during symmetrical cell measurements, was studied as anode in EIS tests; manganese oxide was found to effectively enhance the activity of LSGF for this application. So, a cell with the composites of LSGF as electrodes (iron oxide at the cathode and manganese oxide at the anode) was prepared on a LSGM electrolyte, and tested in a variety of fuels. Results are promising especially when hydrocarbons are used. In chapter 6 a specific material for the cathodes of SC-SOFCs was designed, synthesized, characterized and tested. The target was the fabrication of a highly efficient SC-SOFC, even if efficiency came at great expense of power output. A very cheap MIEC brownmillerite, $Ca_2FeAl_{0.95}Mg_{0.05}O_5$ (CFA), was selected for its very low catalytic activity towards methane oxidation, with the purpose of being completely selective for oxygen electroreduction. Some CFA samples were also impregnated with iron oxide, in an attempt to replicate the beneficial effect observed on LSGF. Impedance tests on a symmetric CFA cells were carried out to measure its resistance as a cathode, then complete SC-SOFCs with a CFA cathode were prepared and tested, and their power output and cathode selectivity were measured. Cathode materials present several similarities with high temperature ceramic membranes for oxygen separation. In chapter 7 the same materials developed in chapter 3 have been tested also for oxygen semi-permeation

2 On the synthesis of $La_{0.6}Sr_{0.4}Fe_{0.7}Ga_{0.3}O_3$

THE DEVELOPMENT AND OPTIMIZATION OF A NEW SYNTHESIS
THE INVESTIGATION OF THE EFFECT OF SYNTHESIS PARAMETERS
AN ACCURATE STUDY ON THE STABILITY AND REVERSIBILITY
SCALABILITY OF THE PREPARATION PROCEDURE

2.1 Introduction

The research on Mixed Ionic Electronic Conducting (MIEC) materials is intense. Materials with ionic and electronic conductivity have been first applied as electrodes in solid oxide fuel cells (SOFCs)[125]. The addition of the ionic conductivity to a pure electronic conducting electrode increases the efficiency, because the electrochemical reaction is no longer restricted to TPB areas and more mechanisms of oxygen reduction are possible, as outlined in chapter 1. Mixed ionic electronic conductors are not exclusive of SOFCs [126]–[130], as they found another extensive application in oxygen separating dense membranes [131]–[137] (see chapter 7). Moreover, in electrochemistry it is possible to use an EMF (electromotive force) sensor based on MIECs[138].

Various MIEC materials have been investigated in the past years [131], [139], [140]: among them fluorites and perovskites, the most promising ones belonging to the second category. Perovskites have attracted a growing interest during the last years in different technological fields, mainly due to their robust crystalline structure that can easily be modified in order to introduce new properties or to tune/enhance existing ones. A perovskite, as explained in chapter 1, is defined as a solid with ABX_3 formula[141]: A and B are cations and X is an anion, most of the times oxygen, but in some case also a halogen [142]. The great flexibility of this class of materials led to a great diversification of the applications[131], [143]–[146] and to the development of increasingly complex formulations. Manganese and cobalt based perovskites are, at

the state of the art, among the best performing materials for application as cathode in SOFCs and dense membranes[139], [147]–[149]. Nonetheless their stability is poor, in particular in low p_{O_2} atmospheres. Another perovskite, (La, Sr)(Fe, Ga)O_3 (LSGF)[150], has only sligthly lower performances, but seems to exhibits an excellent chemical stability. Its oxygen semi-permeation is high, around 10^{-8}mol·cm^{-1}·s^{-1} [151]. Strontium and gallium insertion in general enhances the oxygen transport properties and catalytic activity, although an excessive amount of Sr is known to destabilize the material, in addition gallium seems to enhance chemical stability in reducing conditions[151], although a complete study about the behaviour of the material in such conditions has never been performed. The composition exhibiting the best compromise between activity and stability, has been identified in $La_{0.6}Sr_{0.4}Ga_{0.3}Fe_{0.7}O_3$[139], hence this is the only considered composition in this work.

Synthesis procedure and conditions can deeply affect the properties of perovskites, in particular of doped perovskites. Solid state reactions are widely used for the synthesis of iron based perovskites[152], [153]. Nevertheless, this reaction route requires high temperature, at least 1100°C, and can yield distorted rhombohedral perovskites[152] so potentially affecting conductivity and stability. Wet chemistry procedures, such as Pechini[154] or citrate[155] methods, are powerful in allowing to obtain pure perovskitic phases also at lower temperature. The synthesis herein proposed combines elements from the citrate[156], [157] and the citrate-nitrate auto-combustion [158] methods. The developed procedure is easier and cheaper than original citrate route, due to the avoidance of any extra step between the gel formation/combustion and the final calcination (Figure 2.1). Furthermore, in general, combustion methods allow obtaining better results with lower calcination temperatures[159]. Synthesis have been optimized in the same practical perspective, trying to develop a procedure as easy and fast as possible, without sacrificing the reproducibility and the purity of the final phase. To this purpose several synthesis parameters have been investigated and the obtained powder was characterized by means of X-Ray Photoelectron Spectroscopy (XPS), X-Ray Diffraction (XRD), Temperature Programmed Reduction (TPR), Scanning Electron Microscopy (SEM), Energy Dispersive X-Ray (EDX) Analysis. Attention was paid to the consequences of

the modification of some synthesis parameters, in order to provide some guidance about the possible adjustments depending on the final purpose of the material.

Once defined and optimized the preparation procedure another important task is stability. In this chapter the stability and behaviour of the LSGF under reducing conditions are also studied. To the best of our knowledge the stability of LSGF was examined in literature only under very particular conditions (i.e. at 900°C in 3% CH_4 atmosphere for 24h)[151]. In the present case both the stability under reducing conditions (for hydrogen and at temperatures between 800°C and 1000°C) and the reversibility of the changes occurred during reduction have been investigated. In particular, variations in synthesis parameters have been studied in terms of behaviour under reducing condition, and the stability of samples obtained by using different preparation parameters has been compared.

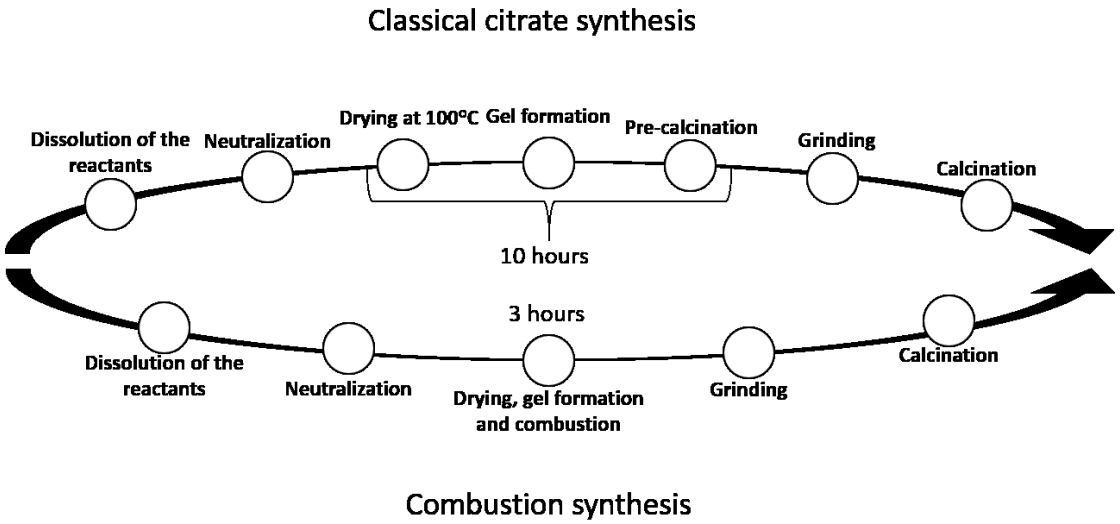

Figure 2.1 Comparison between the steps required for a combustion synthesis and a classical citrate synthesis, highlighting the greater simplicity of the first one.

2.2 Material and methods

2.2.1 Materials

Fe (Sigma-Aldrich, chips, 99.98%), gallium acetylacetonate (Strem Chemicals, 99.99%), strontium nitrate (Carlo Erba, 98%), lanthanum oxide (Sigma-Aldrich, 99.9%), nitric acid (Sigma-Aldrich, 66%), and citric acid monohydrate (Sigma-Aldrich, 99%).

2.2.2 Synthesis

As mentioned, $La_{0.6}Sr_{0.4}Fe_{0.7}Ga_{0.3}O_3$ powder was synthesized optimizing a method intermediate between citrate and the citrate-nitrate auto-combustion [156]–[158]. Several parameters have been systematically changed in order to understand their effect on the chemical and physical properties of the compound; the prepared powders are summarized in Table 2.1. Stoichiometric amounts of the reactants were dissolved separately. Iron chips were dissolved in a concentrated solution of nitric acid heated at 50°C. Lanthanum oxide and gallium acetylacetonate were dissolved in concentrated nitric acid. The amount of nitric acid is in excess with respect of the minimum quantity needed for the dissolution of the reactants. This excess has a deep effect on the final product, as will be discussed in the following paragraphs. We have examined the range from 3 to 6.5ml of nitric acid per gram of product at steps of 0.5ml/g (corresponding respectively to 0.68ml/mol to 1.13ml/mol, with steps of 0.11ml/mol). These limits have been selected on the basis of our experience in the previous syntheses. Strontium nitrate is dissolved in water, and citric acid is added in a molar ratio 1.9:1 with respect to the total amount of cations. The different solutions were mixed in a single beaker, obtaining a very dark purple one with a pH below 0. An aqueous solution of ammonia was added drop by drop until the pH is neutralized. To ensure a good uniformity of the heating in the whole volume and to contain all the material produced during the following step, the solution was transferred to a large beaker (3 litres for a 5-grams synthesis) and heated at 260°C on a plate. The heat treatment caused the evaporation of the excess of ammonia and water and a sticky gel was obtained. After the complete evaporation of water, the gel began to swell and the organic fraction auto-ignited, causing the combustion of the entire gel. A very porous dark brown solid formed by the combustion, occupying more than half the beaker. The solid was grinded and finally calcined for 6 hours at temperatures between 800 and 900°C in order to investigate the effect of calcination temperature: a black powder was finally obtained. Scalability of this method within the lab scale was tested, syntheses were carried out for final product weights ranging from 0.5g to 5g. The synthesis carried out with HNO_3 = 4.5ml/g followed by calcination at 900°C was repeated several times in order to verify the reproducibility.

Some similar procedure[160] suggests to stir the solution overnight after the neutralization with ammonia. To verify this indication, we have split one reaction batch in two parts, burning the first one immediately after while waiting under stirring until the following day for the other.

2.2.3 Characterization

The XPS measurements were carried out with a Perkin Elmer Φ 5600ci Multi Technique System. The spectrometer was calibrated by assuming the binding energy (BE) of the Au 4f7/2 line to be 84.0eV with respect to the Fermi level. Both extended spectra (survey - 187.85eV pass energy, 0.5eV·step^{-1}, 0.05s·step^{-1}) and detailed spectra (for La 3d, Fe 2p, Ga 2p, Sr 3d, O 1s and C 1s – 23.50eV pass energy, 0.1eV·step^{-1}, 0.1 s·step^{-1}) were collected with a standard Al Kα source working at 250W. The standard deviation in the BE values of the XPS line is 0.10eV. The atomic percentage, after a Shirley-type background subtraction [161], was evaluated by using the PHI sensitivity factors[162]. The peak positions were corrected for the charging effects by considering the C 1s peak at 285.0eV and evaluating the BE differences [163].

The XRD analyses were performed with a Bruker D8 Advance diffractometer with Bragg-Brentano geometry using a Cu Kα radiation (40kV, 40mA, λ = 0.154nm). The data were collected at 0.03° at a counting time of 10 s/step in the (2θ) range from 10° to 90°. The crystalline phases were identified by the search-match method using the JCPDS database. The structure and lattice parameters of the powders were determined with great accuracy by Rietveld's powder structure refinement analysis of XRD data, by using the MAUD (Material Analysis Using Diffraction) software, which applies the RITA/RISTA method as developed by Wenk et al.[164] and Ferrari and Lutterotti[165]. The Rietveld's method has given a reasonable fit of the diffraction profiles (Rwp < 5%). The required crystallographic data were taken from ICSD[166].

Temperature Programmed Reduction (TPR), and BET specific surface area measurements were performed with an Autochem II 2920 Micromeritics, equipped with a Thermal Conductivity Detector (TCD). The TPR measurements were carried out in a quartz reactor by using 50mg of sample and heating from RT to 900°C at 10°Cmin^{-1} under a constant flow of H_2 5% in Ar (50ml·min^{-1}). TPR samples were previously outgassed with He (50ml·min^{-1}) at room temperature.

In BET measurements 100mg of sample were used; before measurement the sample was treated at 350°C under a constant flow of He (50ml·min^{-1}); each surface area value is the result of three consecutive measurements.

Field emission-scanning electron microscopy and EDX measures were carried on a Zeiss SUPRA 40VP. Morphological and EDX analysis were carried out setting the acceleration voltages at 20kV.

2.3 Results and discussion

2.3.1 Chemistry of the solution before the gel formation

The solution of precursors shows a quite heterogeneous behaviour in the different batches. We investigated some aspects, mainly related to colour changes and precipitations. The dark purple colour of the solution before the addition of ammonia is due to the formation of the complex [Fe(acac)$_3$]: Fe(III) in presence of β-dichetons forms neutral complexes characterized by strong absorptions [167] (consistently, the same effect replicates adding only gallium acetylacetonate to the iron solution, whereas no colour change is noticed if gallium nitrate is used).

As mentioned, ammonia solution was added to the precursors' solution in order to increase the pH. With increasing pH the solution gets gradually lighter and undergoes some colour changes, that are not replicated systematically every batch, and that appear unrelated to synthesis parameters. In any case, the solution reaches a yellow colour at a neutral pH independently on the specific history. The yellow colour, due to the presence of Fe(III), is reached after different stirring time but these differences are not evident anymore during the following step of water evaporation and do not seem relevant for the synthesis.

The effect of pH on the preparation procedure was also investigated by carrying out several syntheses with different final pH. A pH between 6.5 and 7 is sufficient for a correct complexation of the cations. At pH=6.50, the addition of the ammonia solution induces the precipitation of a metastable fine brownish powder that is completely re-dissolved in some hours. Further basification, until pH 10, in contrast, induces the faster re-dissolution of the precipitate without any significant effect on the final product. This phenomenon is not always exactly repeatable, as the

precipitate was observed to dissolve at different pH values between 9.5 and 10.5. Moreover, the dissolution is never immediate, rather, it is gradual, and it seems that a higher pH has the only effect to speed it. This precipitate is hydrate iron oxide, which is normally soluble in acids and strong basis. Sometimes the precipitation is not observed at all, and it has not been possible to identify one or more parameters involved in this process. This particular behaviour can be related to the complexity of the solution, and kinetic effects should be involved. During basification, when NH_4OH droplets are mixed in the solution, local conditions may differ strongly from equilibrium. It is possible that for some of these conditions, precipitation of some species is favoured; in this case, nucleation happens and can trigger further nucleation around, inducing a complete precipitation, even if for the most stable thermodynamic state at equilibrium aqueous complexed cations are expected. Such a state would be metastable, hence conversion to the most stable state is slowed by kinetic and takes several hours to happen: a higher pH favours the kinetic, reducing the time from hours to minutes. It is probable that the mechanism involves citric acid, which favours the formation of iron complexes, more stable than iron oxides but whose kinetic of formation is apparently slow.

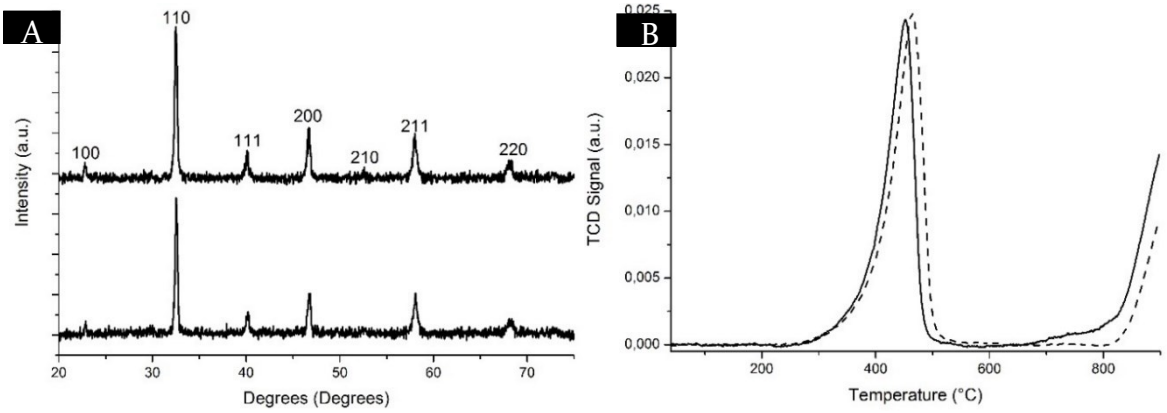

Figure 2.2 Comparison between samples obtained from a solution thermally treated immediately after neutralization (lower profile in XRD and dashed line in TPR) and from a solution stirred overnight (upper profile in XRD and solid line in TPR). A: XRD profiles (49-0285-JCPDS). B: TPR profiles.

As reported in the experimental part, the compound was prepared both starting from a solution thermally treated immediately after the addition of the ammonia solution and after a prolonged stirring, to verify if the different methodology produces different results. The results of the measurements carried out on the sample stirred overnight and immediately burn does not reveal any significant difference. The

superficial area measured by BET is the same (9m²/g) and XRD and TPR show the same profile (Figure 2.2).

2.3.2 Effect of the nitric acid amount

The quantity of nitric acid used at the beginning of the procedure to dissolve metallic cations directly affects the power of the combustion, as it influences the amount of ammonium nitrate formed. The same effect would be obtained by using only minimum amounts of acid to dissolve solid and by adding later the missing ammonium nitrate as another reactant. So, variations in the synthesis determined by its amount are not directly related to its chemistry; rather, a different amount of nitric acid requires a different amount of ammonium hydroxide to reach pH neutrality, so at the end it determines how much ammonium nitrate forms in the solution. The purpose of ammonium nitrate, which is a strong oxidant used also in explosives, is, above all, to ignite homogeneously the gel and to sustain the combustion properly; in fact, it is used as a mere propellent. Apart from the dissolution of metallic cations and the formation of ammonium nitrate, nitric acid has no other role.

Sample	$HNO_3 \gtrless$ 4.5ml/g	Combustion	Calcination T (°C)	Superficial Area (m^2/g)	Colour in graphs
#1	>	Complete	900	9	black
#2	>	Complete	850	-	orange
#3	>	Complete	800	11	blue
#4	<	Incomplete	900	9	red
#5	<	Incomplete	800	18	olive

Table 2.1 Summary of the most significant samples studied.

We have performed different syntheses with different volumes of nitric acid, in order to identify the minimum amount of acid required and its effects on the combustion. Such effects were then related to the chemical and morphological properties of the obtained powder and how they changed depending on combustion. As mentioned, the range from 3ml per gram of product to 6.5ml per gram of product at steps of 0.5ml/g was investigated. The threshold between a complete effective combustion and an incomplete one, was identified to be 4.5ml of nitric acid per gram of product. When the amount of nitric acid is below this amount, the gel combustion

starts on the base of the beaker and is not able to reach the surface and to burn all the material, leaving an external crust of not-combusted gel. This last fraction of the material can be recovered with another treatment at 400°C for some hours. Anyway, this extra step can be easily avoided with a complete combustion. Characterizations of powders with < 4.5ml/g of nitric acid, has been carried out on the combusted fraction. Above 4.5ml/g the combustion starts at the surface of the gel and spreads from that point to the rest of the material. Higher amounts of nitric acid result in more violent combustions[158], with higher temperatures reached, and in this way at the end a solid with thinner branches is obtained. From these considerations it can be argued that the combustion is complete only above 4.5ml/g, therefore the indication "complete/incomplete" combustion can be considered equivalent to "above/below" 4.5ml/g.

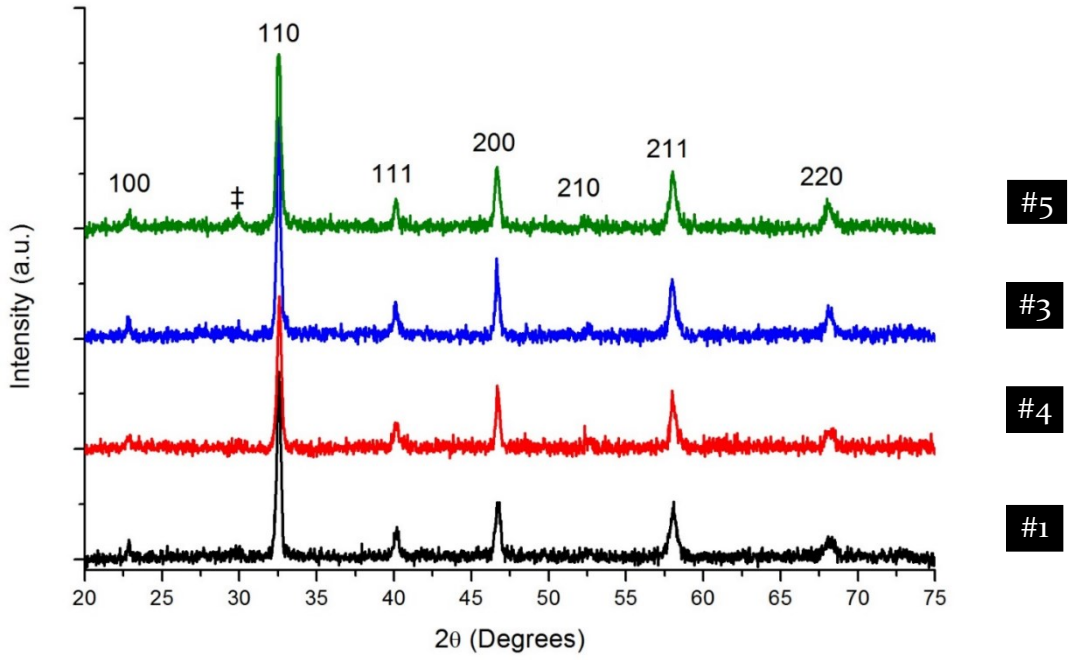

Figure 2.3 XRD spectra. The reflections are indexed on the basis of the 49-0285-JCPDS file for the rhombohedral perovskite. ‡ is a reflection that can be assigned to $LaSrGa_3O_7$ (45-0637-JCPDS).

The incomplete combustion is not only a matter of reaction not reaching completion. When complete combustion is not reached, the temperature at which the combustion happens is lower than the "complete combustion" case; so, the combusted fraction after an incomplete combustion represents how the final material would be if the whole combustion was carried out at a lower temperature. So, indirectly, the character of combustion, complete or incomplete, is an indication of

the most suitable temperature for a better synthesis. The quality of samples with incomplete combustion can be higher than the one of the samples with complete combustion, this means that the temperature of the complete combustion is excessive. In this case a better quality could be obtained with a combustion at lower temperature. This can be achieved through an adjustment of the synthesis parameters, it is necessary to create the suitable conditions for the combustion not to stop at a certain point even if the temperature is lower. For example the fuel/oxidant ratio can be modified, a different complexant can be used, or a suitable propellent can be added. Measurements on samples with "incomplete combustion" aim to assess this issue, verifying if a milder combustion could be beneficial. In fact, only their combusted fraction was analysed, while the non-combusted part of the gel has not been considered in the characterizations.

XRD analysis (Figure 2.3) does not show significant differences between a complete and a non-complete combustion, underlying the significant role played by calcination. In all the cases after calcination the typical peaks of the perovskitic phase are observed. The structure of the perovskite has a slight rhombohedral distortion as evidenced by the splitting, barely detectable, of some peaks, as predicted for the same perovskite without gallium [100], and contrary to what reported for LSGF[168]. Lattice parameters are summarized in Table 2.2. No other significant reflection can be detected: only a minor signal at 30°, assigned to traces of $LaSrGa_3O_7$. This phase is observed to form independently on reaction condition, it does not affect the materials behaviour and it appears not to interact with the other phases.

SAMPLE	STRUCTURE	A(Å)	C(Å)
#1	Rhombohedral	5.508(0.001)	13.425(0.007)
#3	Rhombohedral	5.511(0.001)	13.421(0.003)
#4	Rhombohedral	5.509(0.001)	13.398(0.003)
#1 (REDUCED 800°C)*	Rhombohedral	5.560(0.001)	13.680(0.003)
#1 (REDUCED 900°C)*	Rhombohedral	5.539(0.002)	13.547(0.011)

*Table 2.2 Lattice parameters and cell volume for different samples. *: see paragraph 2.3.4.*

TPR turned out to be complementary to XRD to reveal differences between samples. In effect, all the samples whose TPR profiles are reported in Figure 2.4 have the same identical XRD profile, so the higher sensitivity of TPR could be helpful in finding the differences between the samples. Visually, at the end of TPR measurement the powders turn from the original black colour to a brown one. The response of TPR is related to iron atoms, no one of the other elements (lanthanum, strontium and gallium[169]) is reduced in the sampled temperature interval. In the profile of the sample #1 a peak is evident between 300°C and 500°C; this signal is attributed to the reduction $Fe^{4+} \rightarrow Fe^{3+}$ [170]. At temperature higher than 800°C the reduction of Fe^{3+} begins[171], and terminates at temperatures well above instrumental maximum. From the area of the first peak is also possible to calculate the fraction of Fe^{4+} atoms in the sample, which results to be 1/3 of the total iron atoms. With this value, it is possible to calculate the Goldschmidt tolerance factor for this material, that results exactly 1. This value would account for a cubic structure without any distortion, but from XRD we know that this is not the case. The tolerance factor is based only on geometrical considerations, and it is not rare to find an actual structure not corresponding to it; this simply means there are other interactions in the crystalline cell that counterbalance the geometrical constraints. The TPR profiles of the samples #2, #3 and #4 have more minor signals. The presence of the extra peaks, that are observed in the samples obtained using lower amounts of nitric acid or treated at lower temperature, means some iron atoms is in an environment different from the standard LSGF perovskite. The sample #4, beside the peak at 400°C shows some broad signals between 500°C and 700°C. This profile is similar to the one of $LaFeO_3$[172], so these odd signals can be indicative of the presence of iron cations (Fe^{3+}) not coordinated to gallium and/or strontium, this coordination does not guarantee the same stabilization of the ideal LSGF structure, hence reduction of Fe^{3+} is moved up 200°C. The area of these signals is less than 5% of the main peak and the amount of atoms responsible for this small signal can be estimated from the curve area to be 1.5% of the total iron atoms. As already mentioned no additional phases are observed by means of XRD; this means that the iron present in $LaFeO_3$-type environment is amorphous (but, given the high calcination temperature, this appears to be unlikely) or highly dispersed. Summarizing, the sample #1 appears to be the purest and the

most homogeneous, whereas other sample show some signals related to some kind of heterogeneity. No significant differences have been observed when using amounts of nitric acid higher than 4.5ml/g on the basis of TPR and XRD measurements.

The atomic compositions obtained by means of XPS and EDX are summarized in Table 2.3, whereas in Table 2.4 the corresponding atomic ratios are compared. The synthesis with complete combustion and calcination at 900°C was repeated several times in order to verify the reproducibility. As a general consideration it can be observed that the compositions obtained by means of EDX are very similar to the nominal ones, with the exception of the sample obtained after treatment at 800°C instead that 900°C in which a higher Fe/Ga atomic ratio is observed. The surface composition, in contrast, shows interesting differences as a function of the synthesis conditions. Beside the higher percentage of oxygen, which is a consequence of the presence of hydroxyl and carbonate surface terminations, several segregation phenomena are observed as a function of the amount of nitric acid. The comparison between sample #1 and #4 clearly indicates that the Fe/Ga atomic ratio is lower than the nominal one for the sample prepared with HNO_3 < 4.5ml/g whereas slightly higher in the sample in which the combustion is complete (HNO_3 >4.5ml/g). In general, the tendency of a surface segregation of the A cations is observed, as the sum of La and Sr concentration is always higher than the sum of Fe and Ga. However, this segregation differs as a function of the amount of nitric acid. The ratio between Sr and La is completely different from the stoichiometry, with Sr segregating at the surface, in all the samples made with an amount of nitric acid ≥ of 4.5ml/g. If there is not enough nitric acid (sample #4), Sr appears to segregate less at the surface, where in fact its abundance is only slightly higher than the stoichiometric one.

Focussing on sample #1, the analysis of the single elemental peaks (Figure 2.5) confirms our expectations. Oxygen shows two components, the one at lower binding energy (528.8eV) corresponding to the oxygen in the perovskite, the other one (531.5-531.7eV) due to the presence of hydroxyl and carbonate species. It is interesting to observe that slightly higher BE values (at about 529.5eV) have been observed in a similar compound ($LaFe_{1-x}Ga_xO_3$-type) not doped with Sr[171]. Lanthanum 3d peak shows the expected multiplet splitting, the separation between the 5/2 and 3/2

components being in agreement with the presence of lanthanum oxides. The presence of the shake-up contributions at 837.8 and 854.5eV is characteristic of La(III). Finally, the La $3d_{5/2}$ peak position (833.5-833.6eV) is characteristic of this element in perovskites. Focussing on the Sr 3d peak, the fitting procedure suggests the presence of two overlapping doublets and thus of different strontium compounds. In detail, the first contribution ($Sr3d_{5/2}$ at about 132.0-132.5eV) is compatible with Sr(II) in perovskite. A second contribution at about 133.6-133.8eV is due to Sr(II) in $SrCO_3$[173], [174]. This result is in line with the lower Sr surface segregation and suggests that Sr surface segregate as a consequence of its tendency to interact with CO_2 to form carbonate species. Gallium peak is positioned at 1117.9-1118.1eV, as expected for Ga(III) in a similar perovskite structure[171]. Fe2p peaks at about 710eV and 723eV match the expectation for Fe(III) in perovskites. Slightly higher BE (around 710.5eV) have been observed on a $LaFe_{1-x}Ga_xO_3$-type perovskite not containing Sr.[171]. The comparison between the XPS spectra obtained for the samples with and without complete combustion (#1 and #4, respectively) evidences some interesting difference. In the $La3d_{5/2}$ signal, as an example, the broader peak at 834eV suggests the presence (#4) of lanthanum hydroxide species (LaOOH). Another interesting difference can be observed in the Sr3d spectral region: in the sample with incomplete combustion, in fact, the contribution due to $SrCO_3$ (133.6eV) is less evident than in the other cases. This suggests that the Sr-segregation is favoured by temperature.

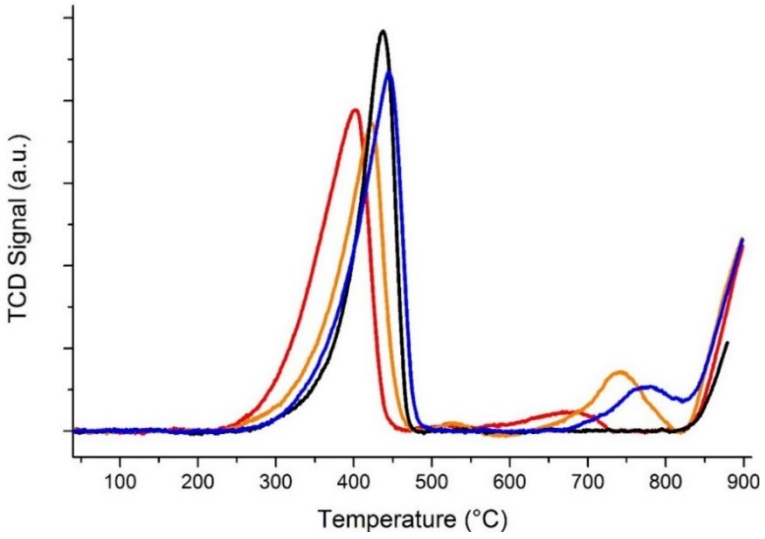

Figure 2.4 TPR profiles of different $La_{0.6}Sr_{0.4}Fe_{0.7}Ga_{0.3}O_3$ powders after calcination. Signal measured by the Thermal Conductivity Detector (TCD) of the instrument is reported. Black: sample #1 (HNO_3>4.5ml/g, calcination 900°C). Orange: sample #2 (HNO_3>4.5ml/g, calcination 850°C). Blue: sample #3 (HNO_3>4.5ml/g, calcination 800°C). Red: sample #4 (HNO_3<4.5ml/g, calcination 900°C).

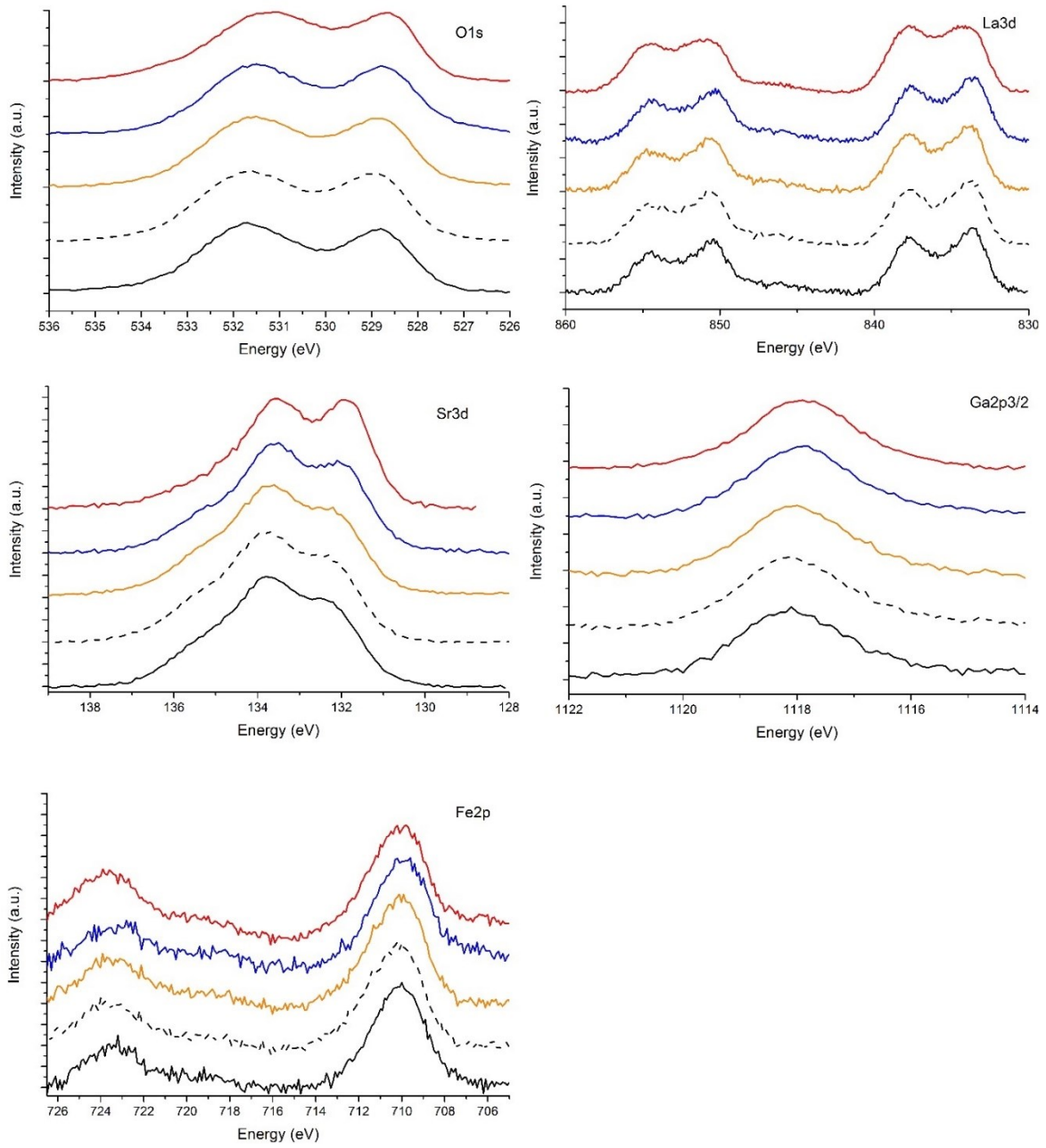

Figure 2.5 XPS peaks of various samples. Black: sample #1 (HNO_3>4.5ml/g, calcination 900°C). Orange: sample #2 (HNO_3>4.5ml/g, calcination 850°C). Blue: sample #3 (HNO_3>4.5ml/g, calcination 800°C). Red: sample #4 (HNO_3<4.5ml/g, calcination 900°C). Black dotted line refers to a sample obtained following the conditions of sample #1 but for a different amount (5g) synthesis.

		EDX			XPS		
	Nominal	Sample #1	Sample #3	Sample #4	Sample #1	Sample #3	Sample #4
La	12.0	13.2	12.6	12.5	4.4	4.7	7.9
Sr	8.0	7.6	7.7	7.6	13.3	9.4	6.2
Fe	14.0	15.0	14.9	15.0	8.1	6.9	7.6
Ga	6.0	6.2	5.1	6.2	3.1	4.1	4.5
O	60.0	58.0	59.7	61.4	71.3	74.9	73.8

Table 2.3 Composition (at. %) obtained by means of EDX and XPS (surface specific) analysis. Samples 1, 3 and 4 as in Table 2.1. The composition of sample 1 is an average of the samples of the three black lines in Figure 2.5. The nominal composition, obtained from the weighted amounts is also reported for comparison.

		EDX			XPS		
	Nominal	Sample #1	Sample #3	Sample #4	Sample #1	Sample #3	Sample #4
Sr/La	0.7	0.6	0.6	0.6	3.0	2.0	0.8
Fe/Ga	2.3	2.4	2.9	2.4	2.6	1.7	1.7
(Sr+La)/(Ga+Fe)	1.0	1	1	1	1.6	1.3	1.2

Table 2.4 Atomic ratios obtained by means of EDX and XPS (surface specific) analysis. Samples 1, 3 and 4 as in Table 2.1. The data of sample 1 are an average of the samples of the three black lines in Figure 2.5. The nominal ratios, obtained from the weighted amounts are also reported for comparison.

From the SEM images (Figure 2.6) it is possible to estimate roughly the dimension of the particles. The particles obtained with 4.5ml/g of HNO_3 and treatment at 900°C have a diameter of about 200 to 400nm. It can be observed that with decreasing amount of nitric acid and decreasing calcination temperature the dimension of the particles tends to decrease. Sample #3 and #4 have smaller particles of similar size (100-200nm), but it seems that the complete combustion with reduced calcination temperature allowed to obtain a more open porosity, compared to the non-complete combustion and higher calcination energy. Probably, a higher temperature during combustion induces the nucleation of bigger crystallites with a more compact arrangement, this results in a close porosity even if calcination is carried out in milder conditions. On the contrary, a lower temperature during combustion forms smaller particles with more open morphologies, then the calcination at 900°C pairs up the size of the particles, but does not change the different porosity. An incomplete combustion and a reduced calcination temperature together result in a significantly

reduced particle size, of some tens of nanometres; hence, a synthesis with a milder combustion and a calcination carried out at 800°C should be taken in consideration if superficial area is critical for the considered application.

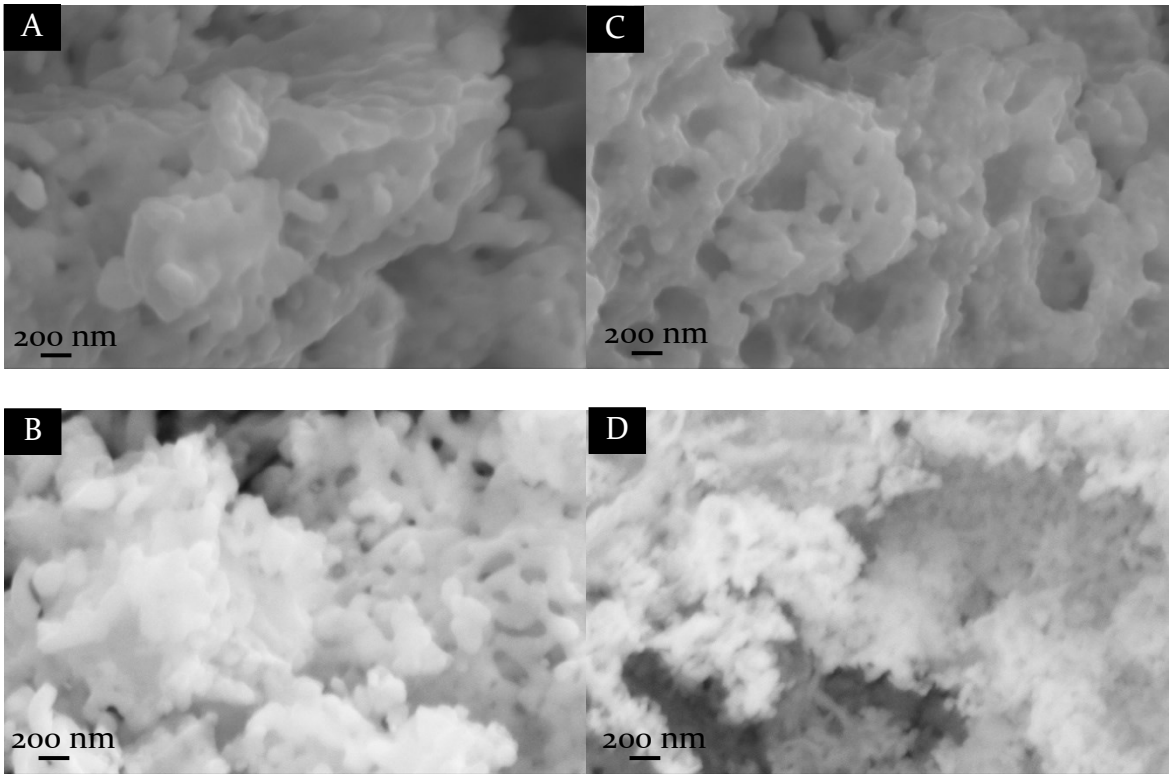

Figure 2.6 A: sample #1 (HNO_3>4.5ml/g, calcination 900°C). C: sample #3 (HNO_3>4.5ml/g, calcination 800°C). B: sample #4 (HNO_3<4.5ml/g, calcination 900°C, combusted fraction). D: sample #5 ((HNO_3<4.5ml/g, calcination 800°C, combusted fraction).

A first effect of the combustion is the removal of the organic fraction that acts as a fuel during the combustion. The combustion, despite the high temperature, does not remove entirely this fraction, as a weight loss is also observed after the calcination. There is a correlation between the amount of nitric acid and the residual impurities (measured as weight loss after calcination): with increasing nitric acid the residue decreases (due to higher temperature the combustion consumes a higher amount of organic fraction). The weight loss is around 15% with 4.5ml/g of nitric acid and calcination at 900°C.

The scalability of the synthesis was also tested. This method yields well reproducible results in the whole examined range, from 0.5 g to 15g of final product, and no significant difference has been noticed: regarding scalability, XPS, XRD and TPR do not reveal any difference between samples of different batches.

2.3.3 Effect of the calcination temperature

Calcination temperature has different effects on the final material. In general, it is good to keep it as low as possible, so the treatment is cheaper in terms of consumed energy and it is easier to achieve high surface area. High temperatures are employed to maximize purity and eliminate secondary phases, but have the side effect of activate major aggregation between particles, whose growing limits surface area and can be detrimental for catalytic/electrocatalytic applications. This effect is clear in this work, as can be seen from the SEM images of Figure 2.6.

In order to optimize the thermal treatment, calcination treatments have been carried out at temperatures between 800°C and 900°C. No significant differences have been observed among XRD patterns of the samples calcined at different temperatures. The TPR analysis (Figure 2.4) shows that samples treated with more than 4.5ml/g of nitric acid and calcined at temperatures lower than 900°C have some extra peaks (different from the ones observed on the sample obtained using different amounts of nitric acid and calcined at 900°C). The TPR curves obtained for the samples prepared using 4.5ml/g of nitric acid and treated at 800 and 850°C (#3 and #2), show a signal between 700°C and 800°C. The comparison with literature reveals that this profile is similar to the one of the perovskite without strontium, $LaGa_{0.3}Fe_{0.7}O_3$[171]. The area of these peaks is 17% of the main peak (6% of the total iron atoms).

The peaks previously described disappear only when calcination is carried out at least at 900°C, thus we consider this temperature as the minimum temperature necessary for a complete chemical and structural uniformity. This puts some constraint to the management of the superficial area. From BET measurements (Table 2.1), it results that a treatment at 900°C limits the superficial area at 9m²/g, while calcination at 800°C potentially would allow to reach 18m²/g. In any case, for some applications a phase pure enough that XRD shows only the reflection of the principal phase is sufficient, so the decision to lower calcination temperature in order to obtain higher superficial areas could be appropriate. However, in this case a rethought of the combustion step should be done, as it has been showed that both a high calcination temperature and a powerful combustion concur in aggregating particles. So, a mean

to carry out a milder combustion that reaches completion should be found, as described in the previous paragraph.

The XPS spectra of the samples calcined at different temperature (#1 and #3 – Figure 2.5) do not reveal any significant differences from the qualitative point of view.

In some previous paper [160], [175] it was reported that the formation of the perovskitic phase happens entirely during the combustion, and that this process would leave only minimum amounts of organic fractions, consequently the aim of the calcination would be in this case only the removal of the residues; they report a weight loss of only 0.16% at 900°C, two orders of magnitude lower than the one determined in the present work. The XRD pattern (Figure 2.7A) of the powder before the calcination is characterized by a low signal to noise ratio, probably also consequently to the presence of un-burnt residual organic fraction (Figure 2.7A). Nonetheless, the peaks of the perovskite structure are visible, suggesting that, despite the impossibility to determine the composition of the sample from these measurements, the perovskite phase is already formed. Also TPR results are very different with respect to those obtained for the calcined powders. The profile (Figure 2.7B) obtained before calcination is completely different from the ones of the calcined samples. A large number of peaks is overlapped in the whole temperature interval and it is difficult to resolve all of them. The profile is clearly very different from the calcined product, probably a part of the signals is caused by residual carbon which was not completely eliminated by the combustion. However, the two broad peaks at about 400-500°C and over 800°C observed in Figure 2.4, characteristic of the desired perovskitic phase, are already visible. The XRD and TPR results confirm, thus, the formation, at least partial, of the perovskite phase before calcination. Nonetheless, it has been already shown (Figure 2.4) the calcination temperature influences the TPR profile, suggesting that the treatment has consequences going beyond the mere combustion of the organic undesired fraction. Hence, the calcination appears to imply also an adjustment of the composition, that reaches the complete purity only after this process.

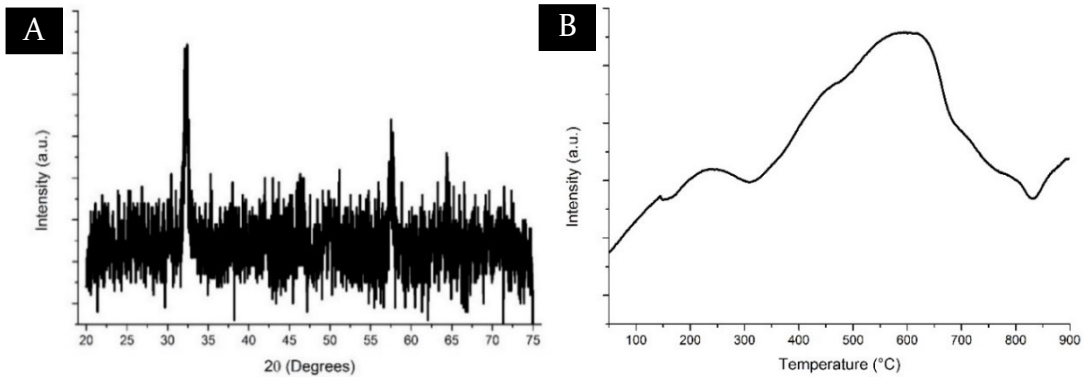

Figure 2.7 A: complete combustion, before calcination, background removed. B: TPR profile of a sample before calcination.

2.3.4 Stability of the material in reducing environments

Among all the MIEC materials, (La, Sr)(Ga, Fe)O_3 is addressed as one of the most chemically stable, in particular in reducing environments. Stability under reducing atmosphere is one of the main flaws for perovskites, and the use of materials with high stability even when pO_2 is low is fundamental is some cases. For example, in case of membranes for oxygen purification, one side of the membrane, the one from which oxygen is released, is forcibly under a reduced pO_2 pressure. SOFC electrolytes too, have the cathodic side under air but the anodic one under methane/hydrogen. SOFC anodes are always subjected to a reducing atmosphere, and it would be very interesting to exploit perovskites catalytic activity also for this process, a use that has been limited, indeed, by the poor stability of the material in these conditions. Our investigation on LSGF aimed to define the maximum working temperature of the material in a reducing atmosphere. Samples prepared following the procedure defined for sample #1 were reduced in H_2/Ar 5% atmosphere up to 800°C, 900°C and 1000°C. XRD was performed on the reduced samples to compare their behaviour at different temperatures and how they were affected (Figure 2.8A). In all the three patterns, the peaks of the perovskite are maintained, but they are shifted towards lower angles. This shift is compatible with the partial iron reduction: the Fe^{4+} cations are reduced to bigger Fe^{3+} cations, leading to a small expansion of the cell (see Table 2.2). The XRD profile of the sample reduced at 800°C is identical to the one before reduction, except for the shifted peaks. In the pattern of the sample reduced at 900°C only a slight difference can be observed: a small peak (underlined by the red circle) appears at 31°. This signal can be assigned to a $LaSrGaO_4$ phase. This phase becomes

significantly more evident in the pattern of the sample reduced at 1000°C. In addition, signals of metallic iron appear at 45° and 65°.

In order to verify the reversibility and resistance to the reduction, the samples reduced at 800°C and 1000°C (all of them prepared with #1 protocol: nitric acid amount > 4.5ml/g, calcination temperature 900°C), were re-oxidized, by means of a treatment at 900°C for 4 hours in atmosphere O_2 /Ar 10%. The powder reduced at 800°C completely recovers the original XRD profile (Figure 2.8B), all the peaks shift back at their original position. The powder reduced at 1000°C recovers the exact profile of the as-synthesized material, too. The perovskite peaks shift to their original position, so the perovskite has restored its original cell size; the peaks of metallic iron and $LaSrGaO_4$ completely disappear; from these results, the formation of the new phases can be considered completely reversible. Figure 2.8D shows the results of the TPR measurement, the original profile of sample #1 is also shown for comparison. The profile obtained for both the powders after the re-oxidation is similar to the original, as it shows the $Fe^{4+} \rightarrow Fe^{3+}$ peak at 450°C. This peak is slightly sharper than the original one, suggesting that the repeated treatments at high temperature have favoured the homogenization of the size of the crystallites. For both the samples, the one reduced at 800°C and the one reduced at 1000°C, the area of the $Fe^{4+} \rightarrow Fe^{3+}$ peak is equal to the original one after synthesis; so, during the oxidation the iron atoms that reached oxidation state 4+ correspond to the initial amount of the as-synthesized material, there is a full recovery of the original features. This could be expected for the sample reduced at 800°C, which did not undergo major degradation, but is a result far more significant for the sample reduced at 1000°C, in which the perovskite phase was partially destroyed.

The behaviour with respect to reduction of samples prepared with different procedures (different calcination temperature, samples #1, #3, different amount of nitric acid, sample #4) was tested as well. They were reduced at 1000°C, and subsequently re-oxidized in order to compare the results. As already mentioned, samples #3 and 4 differ with respect to sample #1 for the presence of poorly intense TPR signals between 500 and 800°C, whereas no difference in the XRD patterns have been revealed. After the reduction/oxidation treatments, TPR does not show

significant differences between the three samples (Figure 2.8E). The profiles are similar, furthermore, they completely lack minor features between 500°C and 800°C that were observed after the synthesis (Figure 2.4). After the TPR, that corresponds also to a reduction treatment at 1000°C, a XRD measurement was done to highlight the consequences of the different synthesis parameter after one cycle of reduction, oxidation and reduction (Figure 2.8C). No difference can be found between the three profiles, with $LaSrGaO_4$ and metallic iron peaks appearing with similar intensities in all the three XRD profiles; moreover, the result is exactly the same observed after the first reduction. So, it appears that the perovskite during the reduction/oxidation cycle is able to arrange itself towards the most stable structure and fixes, in case, some already existing defect. This is probably what happened to the minor impurities that could be observed after syntheses with lower amount of nitric acid or after calcination at temperatures lower than 900°C and that are not observed anymore after these cycles. Therefore, in principle syntheses can be carried out also at milder conditions and in a less accurate and cheaper way if the material is destined to be submitted to oxidation/reduction cycles; a single cycle of reduction/oxidation, in fact, can be implemented to achieve the maximum purity and obtain a perfect LSGF phase.

Summarizing, up to 800°C in reducing atmosphere, the reduction does not affect the perovskitic structure: the original TPR profile is obtained again after a treatment of in oxygen atmosphere and no changes are observed in the XRD pattern. This temperature is not casual; indeed, it is related to the behaviour of the material in reducing atmospheres, as no atoms changes its oxidation state to values incompatible with the perovskitic structure. Up to 800°C the reduction involves only the Fe^{4+} atoms, that around 500°C are reduced to Fe^{3+}, which is can be still easily accommodated inside a perovskitic structure, so no significant structural modification is observed. Above the 800°C temperature, the reduction of Fe^{3+} to lower oxidation states, that are not compatible with the perovskite anymore, begins. The appearance of the impurity peak of $LaSrGaO_4$ indicates that during the reduction of Fe^{3+}, the atoms came out of the cell leaving the other elements, with their oxidation state not affected, free to form alone another oxide phase. Iron atoms gathered and formed a new metallic phase, this is confirmed by the presence of Fe^0 peaks in the XRD patterns. All of these iron atoms are restored in the original state during the

subsequent step of oxidation. The material after oxidation recovers the exact amount of Fe^{4+} atoms it had before the reduction, confirming the tendency of this material to be regenerated, and that the amount of 1/3 of iron as Fe^{4+} is strongly preferred for stability reasons. In any case, the resistance to several cycles has not been tested, and further work is needed in order to determine whether reversibility of reduction is complete or decays after some cycle.

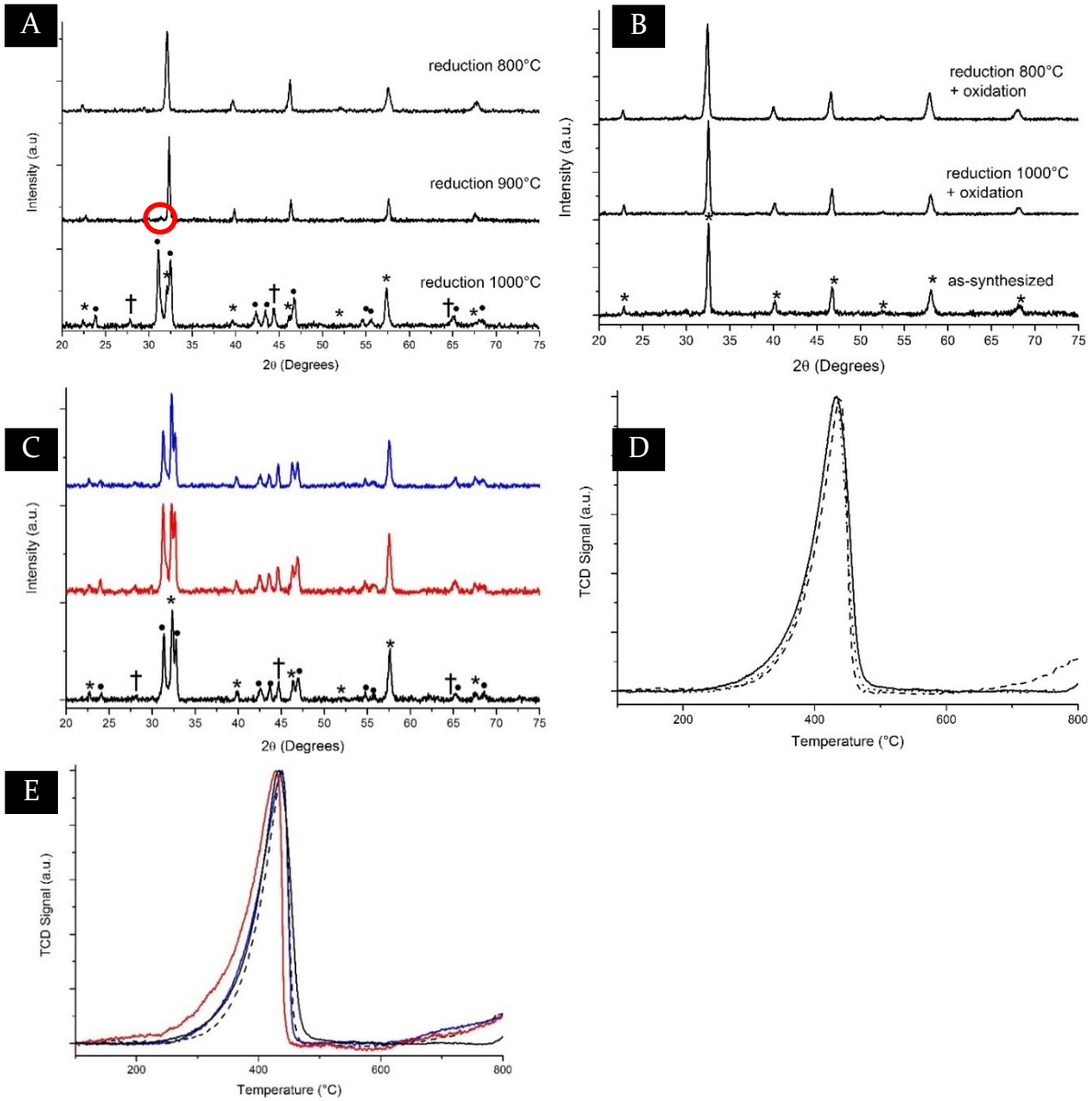

*Figure 2.8 XRD and TPR profiles. Legend for XRD peaks *: perovskite, •: $LaSrGaO_4$, †: metallic iron. A: XRD patterns of samples #1, after reduction at different temperatures. The reduction temperature is shown near the respective profile. B: XRD patterns of samples #1, after reduction at different temperatures and oxidation. The reduction temperature is shown near the respective profile. C: XRD patterns of different samples reduced at 1000°C, oxidized and reduced at 1000°C. Black: sample #1, blue: sample #3, red: sample #4. D: TPR profiles of samples #1 reduced at different temperatures and re-oxidized. Solid: sample #1, as-synthesized (for reference), dashed: reduction at 1000°C, dotted: reduction at 800°C. E: TPR profiles. Black solid: sample #1, as-synthesized (for reference), dashed: sample #1 reduced until 1000°C and re-oxidized, blue: sample #3 reduced until 1000°C and re-oxidized, red: sample #4 reduced until 1000°C and re-oxidized.*

The results reported here suggest that up to 800°C the material is reasonably stable, and operating below this value guarantees complete stability against all reducing condition applied in this study.

As a general consideration, the behaviour depicted in this work is not expected to change radically with other reducing agents. In particular, the material is expected to keep its self-recovering ability also if the reduction was carried out with a reducing agent different from hydrogen. In presence of carbon (i.e. whether the reducing agent is CO or CH_4) strontium can form the stable phase $SrCO_3$ that is not observed in this work because no carbon reductant was used. Temperatures for reduction of different states of iron may change in this case, probably being shifted upwards due to the lower reducing power; in a less aggressive atmosphere, it is thus reasonable that the material would be able to withstand even higher temperatures than the ones demonstrated in the present case, in which hydrogen is used as reductant.

2.4 Conclusions

In this chapter, we have successfully synthesized $La_{0.6}Sr_{0.4}Ga_{0.3}Fe_{0.7}O_3$ with a simple, controllable and easily scalable wet chemistry route: preparation with amounts from 0.5 to 15g have been carried out and the obtained results demonstrated the high reproducibility of the method. We have investigated several parameters of the synthesis, setting the minimum amount of nitric acid at 4.5ml per gram of product for a complete combustion, and the minimum calcination temperature at 900°C for a completely pure phase. The calcination temperature limits the superficial area, that is useful in particular for catalytic purposes, to $9 m^2/g$. Calcination temperature can be lowered if minor impurities are tolerated or whether the material will undergo cycles of reduction/oxidation, in this case the perovskite auto-arranges towards the complete purity and the BET specific surface area is about twice. Investigations on the powders prior to calcination indicated that after the combustion the perovskitic phase have already been formed, but persists a massive organic fraction that requires a temperature treatment for its removal. The resistance of the material to the reduction was tested between 800 and 1000°C, and the obtained results outline an exceptional resistance to reduction compared to the other perovskites: operation of the material in hydrogen atmospheres at 800°C leads only to minor structural

modification. This, joint to the peculiar ability of this perovskite to recover the original structure after a simple oxidation treatment, makes it particularly suitable for applications even in very reducing atmospheres. No differences of stability have been observed as a function of the different preparation conditions.

3 Tuning functionality through nano-composition: MO_x (M=Mn and Fe)+ LSGF as electrodes in Solid Oxide Fuel Cells

NANOCOMPOSITES: A FLEXIBLE MEAN FOR TUNING THE PROPERTIES OF A MATERIAL

THE DISCOVERY OF UNEXPECTED AND VERY COMPLEX INTERACTIONS ON THE SUBSTRATE

AN ACCURATE INVESTIGATION OF THE NEW PROPERTIES

EIS INVESTIGATIONS OF THE PREPARED MATERIALS AS SOFC CATHODES

3.1 Introduction

The accurate selection of the element constituting a perovskite can confer new properties to the material[176], modify existing ones [177] or stabilize desired phases[178]. Most of the currently employed perovskite-based materials result from an elaborate optimization process. In this work, a different modification technique has been studied: functionalization through nanocomposition. The properties and behaviour of the nanocomposites and of the pristine perovskite have been compared with the aim of developing and optimizing a performant cathode to be used in SOFCs. After a detailed investigation, the effect on material properties of the thermal treatments, carried out to obtain the final button cell, has been correlated with the electrochemical performance of the materials. Finally, the catalytic activity in a model reaction as methane oxidation was studied with the aim of developing symmetric SOFCs directly fed with fuels different than hydrogen, such as methane or biogas.

The perovskite $La_{0.6}Sr_{0.4}Ga_{0.3}Fe_{0.7}O_3$ (LSGF) derives from simpler $LaFeO_3$: the addition of Sr pushes Fe atoms to oxidation state 4+ and induces the formation of oxygen vacancies increasing electronic and ionic conductivity, whereas gallium

increases the stability towards reducing and chemically aggressive environments[150], [151]. LSGF is already known for its catalytic activity towards methane oxidation[179] (this is a common feature among ferrites[170], [180]) and it is studied as a material for dense membranes to be applied in oxygen purification, or in membrane reactors (for methane partial oxidation reactors, as an example)[139], [181]. Catalytic activity was related to the Fe-redox couple and to oxygen mobility. Application of LSGF as a SOFC cathode has already been proposed, especially coupled with LSGM as electrolyte[182], [183] to avoid the formation of insulating phases at the interfaces (with electrolyte and interconnect). Some problem related to thermal expansion during a phase transition at intermediate temperature could however arise[184]. Because of the interesting catalytic and conductivity properties, the potential uses of LSGF are wide, covering different fields from catalysis to energy production and storage.

Impregnation[185] is a process commonly used to enhance the performances of a material, and consists in depositing a new phase on an existing substrate from a drying solution: the solution evaporates, and the solid precursor deposits on the substrate. Often, the impregnated phase contains a noble metal, which most of the times is indeed the real active phase of the material, while the substrate gives mainly mechanical strength; a notable example of this is Pt impregnated on carbon in Polymer Electrolyte Fuel Cells[71] and in general automotive catalysts, on inert [186]–[188] but also on active [189] substrates. It is possible to distinguish between a wet and a dry impregnation[190], whether the used precursors solution is in excess (wet) or has a limited volume corresponding to the porosity of the substrate (dry). In this case, wet impregnation has been chosen because it allows to easily control the amount of deposited phase on powder substrates.

In this chapter, simple iron and manganese oxides are deposited, by wet impregnation, on LSGF, a support which is not inert but catalytic and electrocatalytically active, with the aim of improving the SOFC's electrode performance. The choice of non-noble, cheap impregnated phases is driven by the need of avoiding or limiting the use of expensive and/or critical elements (CRM)[191].

Beside economic reasons, Fe and Mn oxides have been chosen because of their catalytic activity[192]–[198].

The impregnated LSGF powders (named LSGF + FeO_x and LSGF + MnO_x) has been studied by means of X-Ray Diffraction (XRD), Temperature Programmed Reduction (TPR), X-Ray Photoelectron Spectroscopy (XPS) and Energy Dispersive X-Ray Analysis (EDX). The surface modification subsequent to the oxide deposition have been studied also by means of N_2 adsorption isotherms and SEM. The nanocomposites have been tested in catalytic activity towards methane oxidation. In previous works LSGF has been already tested in oxygen excess condition[179]; during these tests, an excess of methane has been used, in order to assess materials selectivity also in conditions where partial oxidation would be favoured. The effect of impregnation on electrocatalytic properties has been studied using the nanocomposite materials as SOFC cathodes in symmetrical electrolyte (CGO – cerium 90% gadolinium 10% mixed oxide) supported cells. CGO has been chosen to easily compare results with other materials' performances, considered the only limited literature available on LSGM. Since deposition of electrodes involves treatment at high temperatures potentially able to modify the LSGF composite, the powders (both LSGF and impregnated LSGF ones) have been treated under the same conditions and thoroughly examined to monitor closely any modification of the material consequent to each preparation step. In particular the XRD vs temperature investigation allowed to monitor the structural behaviour of the nanocomposites during the thermal treatment necessary for the SOFC preparation.

3.2 Experimental

3.2.1 Synthesis

Synthesis of the powders

The supporting perovskite has been synthesized by means of a solid combustion synthesis route[199]. A solution of the cations to be deposited is prepared (using manganese(II) acetate for the MnO_x composite and iron(II) acetate for the FeO_x composite). The supporting powder is added to the solution, and the mixture is kept under stirring for 24h; the amount of cation (Mn(II) or Fe(II)) vs. supporting perovskite was selected to obtain 10%mol deposition. The obtained suspension is then

mildly heated, avoiding boiling, until the solvent is completely evaporated; the resulting powder is treated at 550°C to remove the organic fraction. The powders were also treated at 1000 and 1100°C, the same temperatures used to prepare the SOFC.

Cell preparation

Cells for EIS measurements are electrolyte supported and prepared by screen printing the LSGF based material to be tested on both sides of a CGO pellet (diameter 20mm, thickness 1.4mm). The pellet was prepared by pressing the CGO powder (GDC10-TC, Fuel Cell Materials) and treating the so-obtained pellet at 1350°C for two hours. A perovskite ink was prepared by mixing LSGF powder with a fraction of CGO powder, and adding binder V400 (ESL, commercial) and solvent T4O4 (ESL, commercial) to adjust viscosity. The ink deposition is carried out by means of a screen printing machine. The layer is then dried in an oven at 100°C for 15 minutes. Two layers on each side of the CGO pellets were printed this way. The symmetrical cell is treated at 1000°C and 1100°C to ensure a good electrical contact between the electrolyte and the electrodes. Treatments at temperatures lower than 1000°C have been found not to be sufficient to ensure enough mechanical stability to the electrodic layer. Finally, a gold grid is printed from a gold ink (8880-H, ESL, commercial) on both the electrodes, and the cell is treated a last time at 850°C for two hours.

3.2.2 Characterization

XRD

The XRD analyses at high temperature were performed with a Bruker D8 Advance diffractometer with Bragg-Brentano geometry using a Cu Kα radiation (40kV, 40mA, λ =0.154nm) equipped with a high temperature chamber HTK16 (Anton Paar) and a scintillation detector preceded by a graphite monochromator. Working power is 1600W. The room temperature XRD analyses were performed with a Siemens D5000 diffractometer equipped with a rotating platinum sample holder and a scintillation detector preceded by a graphite monochromator. The data were collected at 0.03° in the (2θ) range from 10° to 70°. The crystalline phases were identified by the search-match method using the JCPDS database.

SEM

Field emission-scanning electron microscopy and EDX measures were carried on a Zeiss SUPRA 40VP. Morphological and EDX analysis were carried out setting the acceleration voltages at 20kV.

TPR

Temperature Programmed Reduction (TPR) and oxygen Temperature Programmed Desorption (O_2-TPD) were performed with an Autochem II 2920 Micromeritics, equipped with a Thermal Conductivity Detector (TCD). The measurements were carried out in a quartz reactor by using 50mg of sample and heating from RT to 900°C at 10°C min^{-1} under a 50ml·min^{-1} constant gas flow. Used gas mixture was H_2 5% in Ar for TPR and Ar for O_2-TPD. TPR samples were previously outgassed with He (50ml·min^{-1}) at room temperature. O_2-TPD samples were previously fully oxidized at 900°C under pure O_2 for 2 hours. Measured gas volumes were determined calibrating the TCD with proper standards, and then converted to the molar amount reported in the Tables 2 and 3. An ESS Evolution mass quadrupole was used to check only oxygen was released during O_2-TPD measurements.

N2 adsorption isotherms

Nitrogen adsorption isotherms were measured at 77K with a Micromeritics ASAP 2020 plus instrument. Superficial area by BET model has been calculated from adsorption curves.

XPS

The XPS measurements were carried out with a Perkin Elmer Φ 5600ci Multi Technique System. The spectrometer was calibrated by assuming the binding energy (BE) of the Au $4f_{7/2}$ line to be 84.0eV with respect to the Fermi level. Both extended spectra (survey - 187.85eV pass energy, 0.5eV·$step^{-1}$, 0.05s·$step^{-1}$) and detailed spectra (for La 3d, Fe 2p, Ga 2p, Sr 3d, Mn 2p, O 1s and C 1s – 23.50eV pass energy, 0.1eV·$step^{-1}$, 0.1s·$step^{-1}$) were collected with a standard Al Kα source working at 250W. The standard deviation in the BE values of the XPS line is 0.10eV. The atomic percentage, after a Shirley-type background subtraction [161], was evaluated by using the PHI sensitivity factors [162]. The peak positions were corrected for the charging effects by considering the C 1s peak at 285.0eV and evaluating the BE differences [200].

Powder Catalytic tests

For the catalytic tests, 0.2g of the powder were placed in the middle of a vertical quartz tube, sustained by a quartz wool support underneath. The sample temperature was measured by means of a thermocouple positioned inside the reactor as close as possible to the powder. The tube was placed inside a furnace, and a gas mixture (30l/h, 20% CH_4, 10% O_2, 70% N_2) was flushed through the sample in upward direction. The reaction products were monitored at the outlet of the set-up by an on line micro gas chromatograph (SRA Instruments microGC3000). The calibration was done using standard gases containing known concentrations of the components.

EIS

In order to evaluate the performances of the materials for SOFC operation, Electrochemical Impedance Spectroscopy (EIS) tests were performed on the following symmetrical cells: LSGF/CGO/LSGF, FeO_x + LSGF/CGO/FeO_x + LSGF and MnO_x + LSGF/CGO/MnO_x + LSGF. The applied excitation voltage is 10mV.

Impedance of the cell was measured under air (normal operating condition for a double cell SOFC cathode); furthermore, cells after the first measurement were subjected to a mild reducing treatment under 20% CH_4+10% O_2 at 600°C for 1 hour, and then the measurement was repeated to assess any variation in activity. Data were collected with Solartron 1286 Electrochemical Interface and Solartron 1255 Frequency Response Analyzer devices.

3.3 Results and discussion

3.3.1 Room Temperature XRD

X-Ray Diffraction has been employed to carefully monitor any structural variation in samples before, during and after all the treatments described in this work to prepare the symmetrical cells. XRD patterns of the impregnated powders have been compared with the one of the as-synthesized LSGF, in order to identify any new phase formation or modification.

Before the deposition (Figure 3.1) LSGF shows the typical perovskitic pattern, and traces of a $LaSrGa_3O_7$ phase impurity (weak signal at 30°) already observed in previous works[199]. No pattern modification is observed after the deposition of manganese

oxide or of iron oxide. This can be due to the high dispersion or to the low amount of the deposited phases. The only difference concerns the small signal at 30°, whose intensity strongly decreases after the deposition of the oxides (Mn oxide, in particular), often completely disappearing.

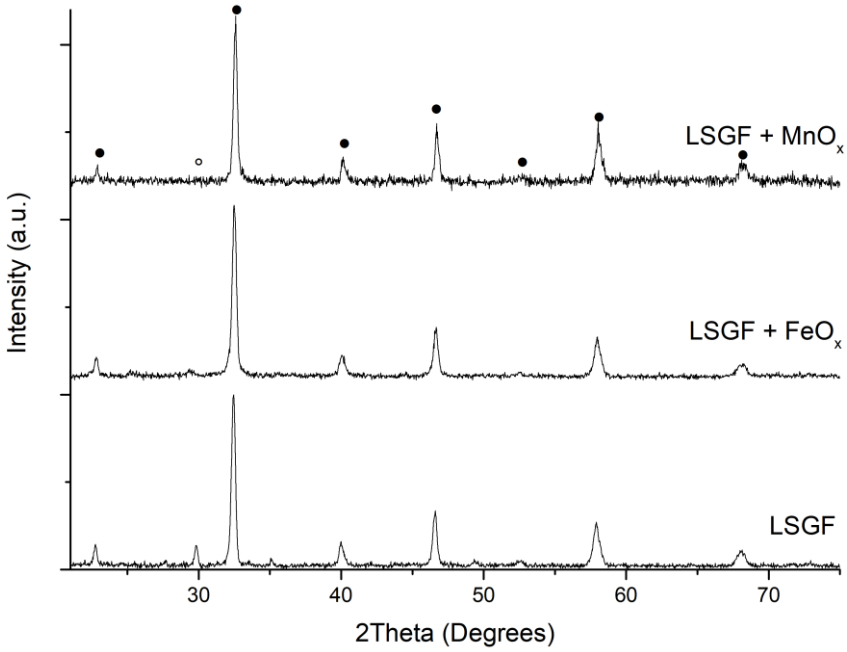

Figure 3.1 XRD pattern of LSGF before and after the deposition of the oxides. ●: LSGF, rhombohedral, JPCDS 04-016-7460; ○: $LaSrGa_3O_7$, melilite, tetragonal, JPCDS 00-045-0637.

3.3.2 XRD VS. Temperature

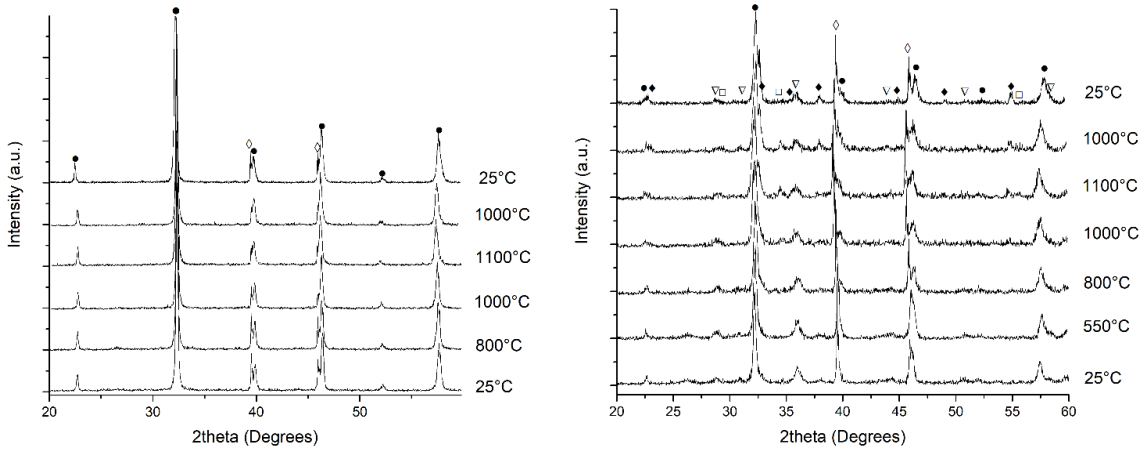

Figure 3.2 XRD patterns of LSGF + MnO_x. Left: 10% mol. composite during temperature treatment from 25°C (lowest pattern) to 1100°C and then back to 25°C (highest pattern). ●: LSGF, rhombohedral, JPCDS 04-016-7460; ◊: Pt (substrate), cubic, JPCDS 00-004-0802. Right: 30% mol. composite during temperature treatment from 25°C (lowest pattern) to 1100°C and then back to 25°C (highest pattern). ●: LSGF, rhombohedral, JPCDS 04-016-7460; □: Mn_3O_4, cubic, JPCDS 04-002-5633; ▽: Mn_3O_4, hausmannite, tetragonal, JCPDS 04-007-1841; ♦: Mn_2O_3, bixbyte, cubic, LPCDS 00-041-1442; ◊: Pt (substrate), cubic, JPCDS 00-004-0802.

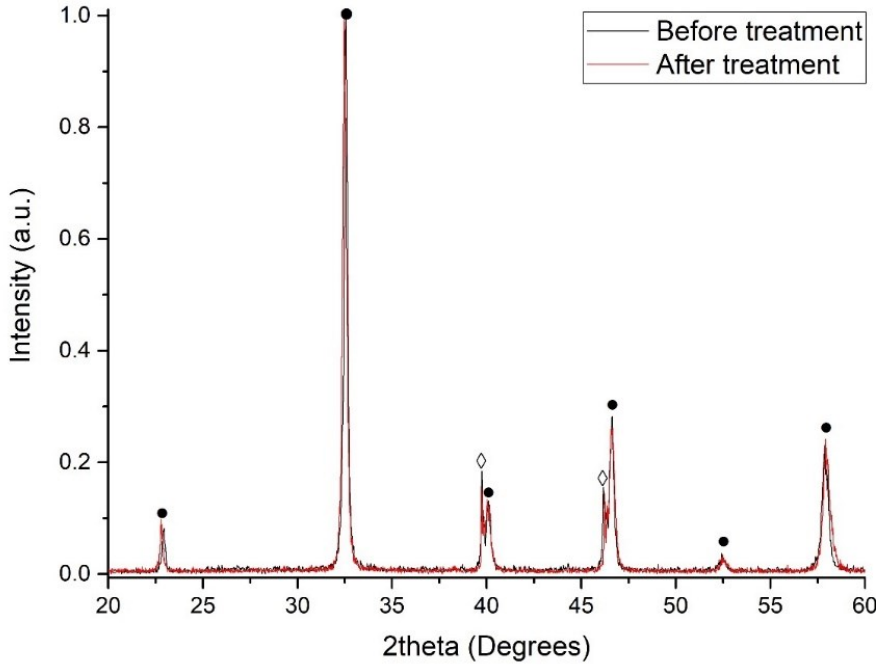

Figure 3.3 XRD patterns obtained (at RT) for LSGF + MnO_x (10% mol.) before and after the thermal treatment at 1100°C. ●: LSGF, rhombohedral, JPCDS 04-016-7460; ◊: Pt (substrate), cubic, JPCDS 00-004-0802.

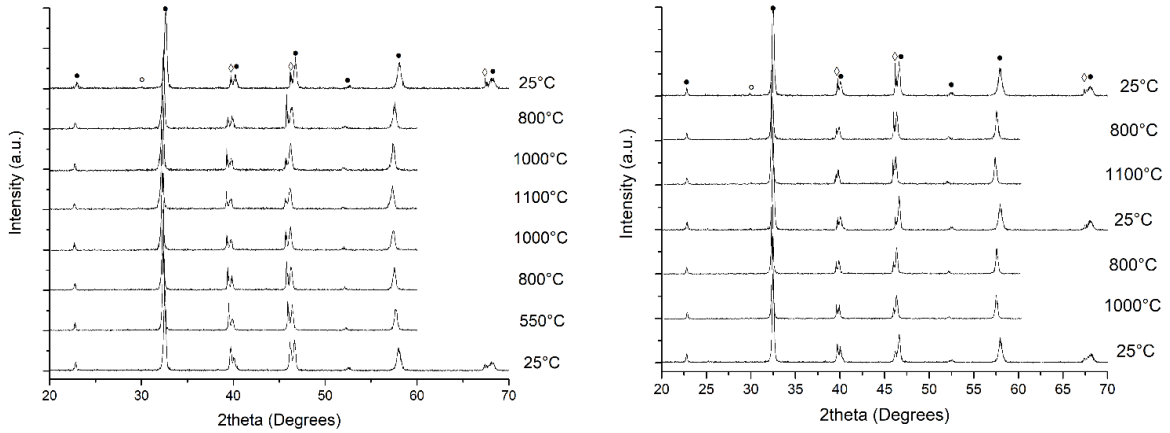

Figure 3.4 XRD patterns of LSGF + FeO_x. Left: 10 % mol. composite during heating, from 25°C (lowest pattern) to 1100°C and cooling (highest pattern). ●: LSGF, rhombohedral, JPCDS 04-016-7460; ○: $LaSrGa_3O_7$, melilite, tetragonal, JPCDS 00-045-0637; ◊: Pt (substrate), cubic, JPCDS 00-004-0802. Right: 30% mol. composite during the following thermal treatment: 25°C (lowest pattern) -1000°C-25°C-1100°C-25°C (highest pattern). ●: LSGF, rhombohedral, JPCDS 04-016-7460; ○: $LaSrGa_3O_7$, melilite, tetragonal, JPCDS 00-045-0637; ◊: Pt (substrate), cubic, JPCDS 00-004-0802.

A series of XRD measurements on composite powders has been performed in situ during heating from 25°C to 1100°C. The aim is to study the behaviour of the material and to monitor any modifications undergone by the electrode powders while preparing the SOFC. This result is obtained by simulating the treatments the material is subjected to, during the preparation of the fuel cell. In order to overcome the poor detectability of Mn and Fe oxide phases, the same test has been carried out, beside

on the 10% mol composited, also on composites with a higher amount of deposited oxides (30% mol).

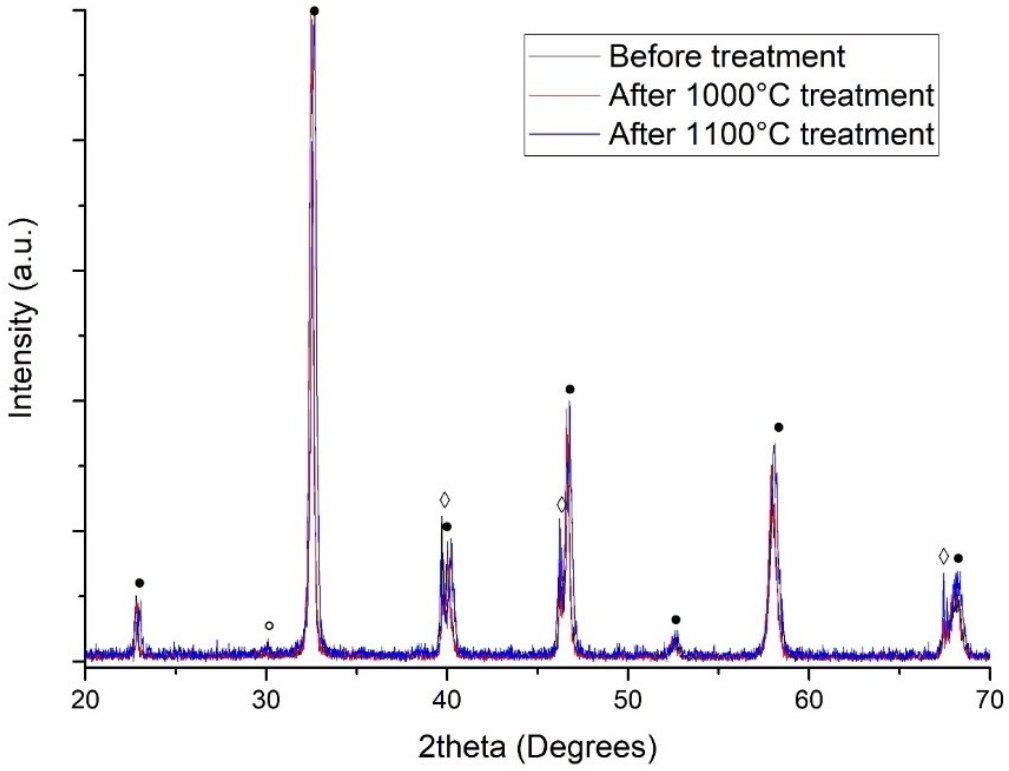

Figure 3.5 XRD pattern obtained, at RT, for LSGF + FeO_x (10% mol.) before and after the 1000°C and 1100°C thermal treatments. ●: LSGF, rhombohedral, JPCDS 04-016-7460; ○: $LaSrGa_3O_7$, melilite, tetragonal, JPCDS 00-045-0637; ◊: Pt (substrate), cubic, JPCDS 00-004-0802.

A more complex protocol was used for LSGF + FeO_x samples, which consisted in heating at 1000°C, cooling at RT, heating at 1100°C and finally cooling at RT. This choice is driven by the need to better understand the differences caused by the thermal treatment at 1000 and 1100°C. Interesting differences, in fact, are observed between the electrochemical behaviour of the two nanocomposites at these temperatures.

Measurements performed during in situ treatments remark the stability of the LSGF phase: no variation in its signals is detected during the whole process. This is true in particular for the MnO_x composite (Figure 3.2 and Figure 3.3). The Fe composite is subjected only to a small increase of the signals of the $LaSrGa_3O_7$ secondary phase (Figure 3.4).

Composites with 30% oxide concentration have been prepared with the specific purpose of enabling a more accurate study of the behaviour of the deposited phase

during the thermal treatments. Unfortunately, even with 30% concentration, only the manganese composite showed reflections of the deposited oxide, while the iron composite pattern was unchanged from 10% sample. Hence, the only XRD vs temperature patterns for 30% nanocomposites reported here are the ones for the manganese impregnation. It has been decided not to further increase FeO_x concentration until its reflection were visible because at too high concentrations the result could not be considered representative of the 10% composite which is the aim of this study.

The temperature protocol on the 30% MnO_x composite (Figure 3.2) was analogous to the ones on samples with 10% oxide concentration. The 25°C pattern before temperature treatment, noteworthy, shows the presence of a Mn_3O_4 haussmannite phase which is reported to normally form in bulk only above 1000°C[167] whereas the sample has been treated only at 550°C in the present work; the presence of the perovskitic phase plays probably a role in stabilizing phases that would form at higher temperatures. This could be of some interest because Mn_3O_4 itself is studied for its catalytic activity[201], [202]. Manganese oxide peaks are also characterized by some broadness, an indication that the size of the crystallites is small; the high dispersion could be a reason for the absence of MnO_x signals in the 10% composite pattern. Similar considerations hold for FeO_x.

Above 1000°C, during heating, the signals of the pristine haussmannite phase Mn_3O_4 decrease in intensity. At the same temperature, two new manganese phases appear: Mn_2O_3, normally forming below 1000°C, and a cubic Mn_3O_4. During the cooling phase, no further modification of the reflexes of the haussmannite is observed, while the ones associated with Mn_2O_3 continue to increase and the cubic Mn_3O_4 disappears. Between the 1000°C patterns collected while cooling and heating the only differences are the appearance of the Mn_2O_3 phase and an increase in intensity of the cubic Mn_3O_4 phase. Meanwhile, no other manganese phase is observed to decrease or disappear. It is possible that these manganese atoms come from the perovskite itself, which has incorporated them during heating. In fact, XPS quantitatives (paragraph XPS, EDX characterization) indicate that there is some interaction between LSGF and overlaying manganese oxide. XRD data prove that this

interaction, that comprises exchange of atoms and phase variations of the manganese oxides, is continuous; the LSGF and MnO_x phases respond jointly at every temperature and show a complex behaviour. It is possible that a similar phenomenon happens also in the composite with 10% MnO_x, although the insufficient intensity of the signals did not allow to observe it directly.

Measurement on LSGF + FeO_x samples recorded while heating to 1000°C, cooling and re-heating at 1100°C aimed to identify any phase variation that could explain unexpected ASR (Area Specific Resistance) values measured by EIS (see paragraph 3.3.10 EIS). Comparison between XRD patterns during and after the thermal treatments (Figure 3.4) does not evidence any major differences, thus it can be assumed that no observable phase variation happens between 1000°C and 1100°C. Figure 3.5 compares directly the patterns determined after the thermal treatments at 1000 and 1100°C with the one before: the only difference being a small shift toward higher angles of the after-1100°C profile. One interesting feature is the stability of the $LaSrGa_3O_7$ reflection at 30°, that does not increase in intensity after the second treatment; this means it had already reached its equilibrium amount thus it is not expected to further increase with aging. This is important because it excludes a progressive increase of this parasitic phase during operation, potentially harming integrity of the main LSGF phase.

3.3.3 SEM on powders

SEM images obtained before and after the deposition of the oxides do not show any difference (Figure 3.6). EDX and XPS measurements, described in paragraph XPS, EDX characterization, however clearly indicate that oxides are deposited on the surface; the comparison of the XPS, EDX, XRD, and SEM results supports the hypothesis that the oxide are deposited in a highly dispersed form on the perovskite surface.

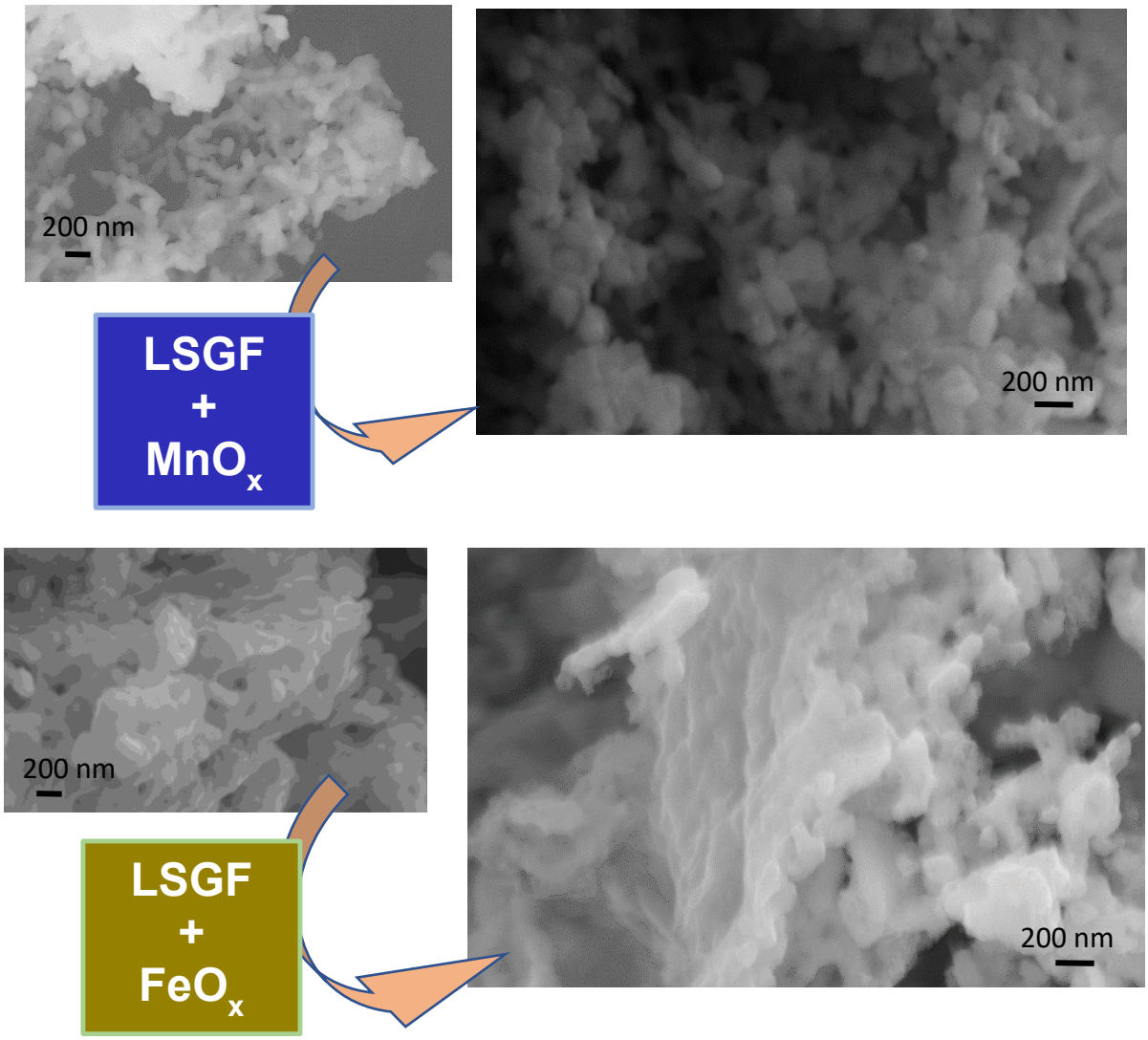

Figure 3.6 Up: SEM pictures before and after deposition of manganese oxide. Down: SEM pictures before and after deposition of iron oxide

3.3.4 N_2 isotherms

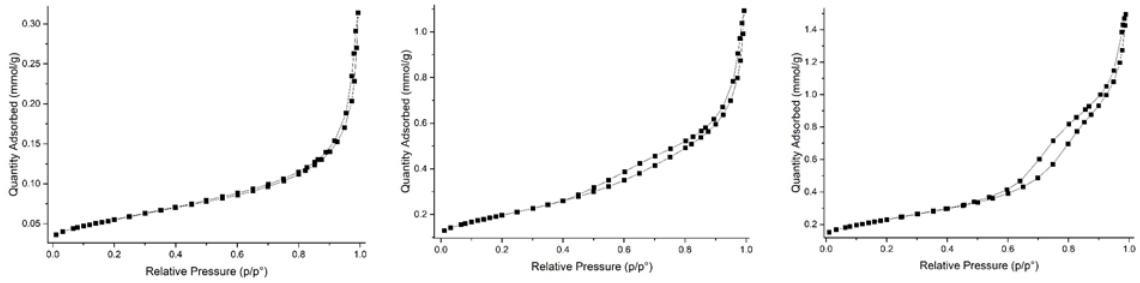

Figure 3.7 Left: N_2 isotherm of LSGF. Center: N_2 isotherm of LSGF + MnO_x. Right: N_2 isotherm of LSGF + FeO_x

The comparison of the N_2 isotherms of LSGF and of the Mn and Fe nano-composites (Figure 3.7) indicates a strong modification of the powders after the impregnation process, as expected in case of a good deposition of the oxides on the

perovskitic substrate. Superficial area increases, from 4.4m²/g measured for the pure LSGF perovskite, to 15.9m²/g for the MnO_x composite and to 18.5m²/g for the FeO_x composite; also the shape of the isotherms differs suggesting a different morphology. The LSGF perovskite shows a type II isotherm, along with a very low superficial area. The deposition of the oxide causes, beyond the increase in the superficial area, a transition of the isotherm towards type IV, that can be related to the formation of mesoporosities in which adsorbed N_2 gas can condensate leading to the typical hysteresis[203]. Type IV shape is more evident in LSGF + FeO_x, while in LSGF + MnO_x the curve still resembles type II with a principle of hysteresis. The hysteresis can be classified as type H_3, which is associated to the presence of slit-shaped pores[204]. The formation of the mesoporosity is a consequence of the iron oxide deposition and is determined by the deposition technique and by the interactions between the substrate and the deposited phase.

Sample		La	Sr	Fe	Ga	O	Mn	La/Sr	(Fe+Ga)/La	(Fe+Ga)/(La+Sr)	Fe/Ga	(Fe+Mn)/Ga
LSGF	Nominal	12.0 (30.0)	8.0 (20.0)	14.0 (35.0)	6.0 (15.0)	60.0		1.5	1.7	1.0	2.3	
	XPS	4.4 (15.2)	13.3 (46.0)	8.1 (28.0)	3.1 (10.7)	71.3		0.3	2.5	0.6	2.6	
	EDX	13.2 (31.4)	7.6 (18.1)	15.0 (35.7)	6.2 (14.8)	58.0		1.7	1.6	1.0	2.4	
LSGF 1000°C	XPS	4.3 (17.8)	11.4 (47.3)	5.6 (23.2)	2.8 (11.6)	75.9		0.4	2.0	0.5	2.0	
LSGF 1100°C	XPS	6.2 (24.3)	9.2 (36.1)	7.0 (27.5)	3.1 (12.2)	74.6		0.7	1.6	0.7	2.3	
LSGF + MnO_x	Nominal	12.0 (29.3)	8.0 (19.5)	13.0 (31.7)	6.0 (14.6)	60.0	2.0 (4.9)	1.5	1.6	1.0	2.2	2.5
LSGF + MnO_x	XPS	3.3 (11.7)	4.6 (16.3)	5.6 (19.8)	3.7 (13.1)	71.7	11.1 (39.2)	0.7	2.8	1.2	1.5	4.5
	EDX	11.7 (29.2)	7.1 (17.7)	13.6 (33.9)	5.4 (13.5)	59.9	2.3 (5.7)	1.6	1.6	1.0	2.5	2.9
LSGF + MnO_x 1000°C	XPS	6.2 (22.0)	6.5 (23.0)	7.5 (26.6)	7.0 (24.8)	71.7	1.0 (3.5)	1.0	2.3	1.1	1.1	1.2
LSGF + MnO_x 1100°C	XPS	4.7 (18.4)	10.3 (40.2)	5.1 (19.9)	4.8 (18.8)	74.4	0.7 (2.7)	0.5	2.1	0.7	1.1	1.2
LSGF + FeO_x	Nominal	12.0 (29.3)	8.0 (19.5)	15.0 (36.6)	6.0 (14.6)	60.0		1.5	1.8	1.1	2.5	
LSGF + FeO_x	XPS	8.3 (29.2)	5.5 (19.4)	13.1 (46.1)	1.5 (5.3)	71.8		1.5	1.8	1.1	8.7	
	EDX	13.1 (31.8)	6.5 (15.8)	16.4 (39.8)	5.2 (12.6)	59.2		2.0	1.6	1.1	3.2	
LSGF + FeO_x 1000°C	XPS	4.8 (23.3)	6.8 (33.0)	6.6 (32.0)	2.4 (11.7)	79.4		0.7	1.9	0.8	2.8	
LSGF + FeO_x 1100°C	XPS	3.7 (18.4)	8.9 (44.3)	5.9 (29.4)	1.6 (8.0)	79.9		0.4	2.0	0.6	3.7	

Table 3.1 Composition (at. %) of LSGF, LSGF + MnO_x and LSGF + FeO_x composites as measured by means of XPS and EDX. The nominal composition obtained by the weighted amounts are reported for comparison. The composition (at. %) considering only cations is inside brackets.

3.3.5 XPS, EDX characterization

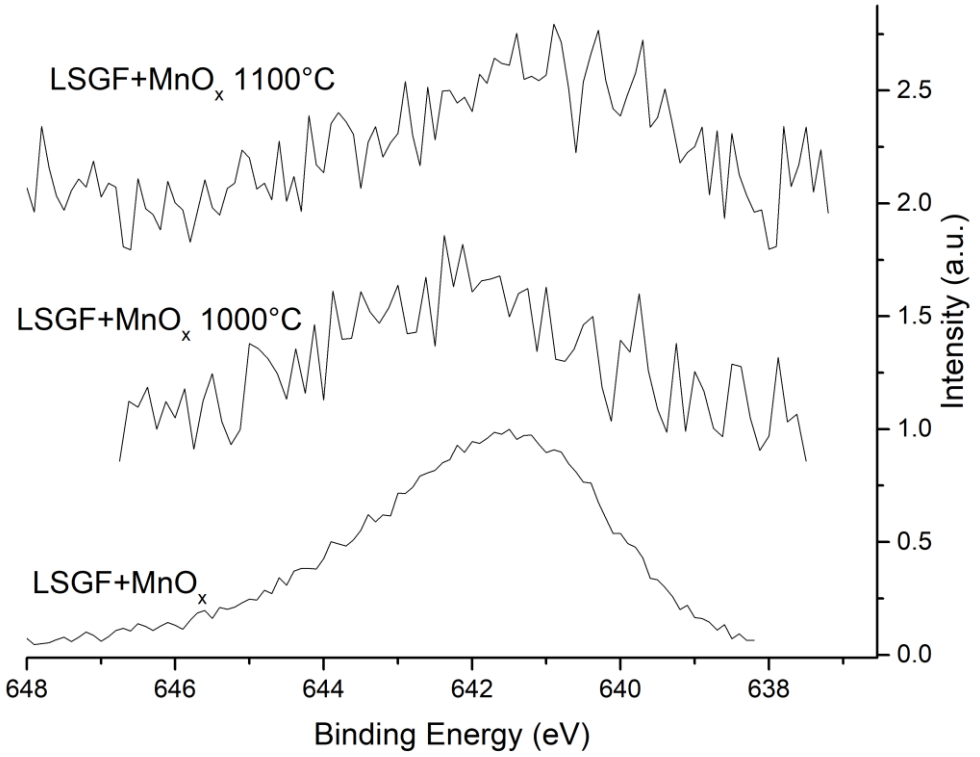

Figure 3.8 XPS spectra of Mn2p3/2 peak of LSGF+MnOx treated at different temperatures.

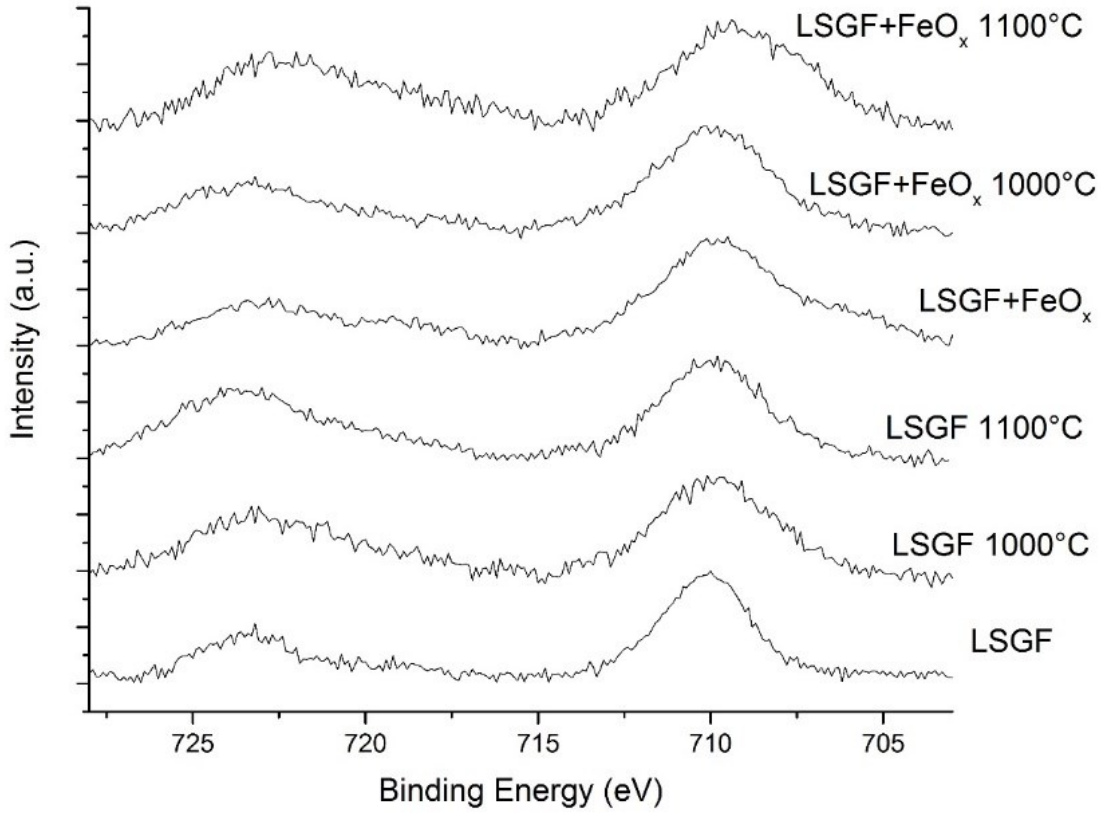

Figure 3.9 XPS spectra of Fe2p peak of LSGF+FeOx treated at different temperatures.

In Table 3.1 the atomic compositions obtained by XPS and EDX are summarized.

LSGF

The XPS atomic composition reveals the Sr surface segregation. The comparison with the EDX atomic composition, which is more similar to the nominal one, confirms that the segregation is a superficial phenomenon. The thermal treatment causes the increasing diffusion of lanthanum toward the surface. The Fe/Ga atomic ratio is always near to the nominal one.

LSGF + MnO_x and LSGF + FeO_x

Both in the case of LSGF + MnO_x and LSGF + FeO_x, the oxide phase is deposited on the surface of the perovskite and no significant diffusion inside the perovskite is observed in the as prepared composite; this is proved by the Fe/Ga and (Fe+Mn)/Ga atomic ratios. Composites show a more complex behaviour when heated at 1000°C or more: deposited cations diffuse into the perovskite and their XPS concentration decrease. Another effect that iron and manganese depositions have in common is the inversion of the tendencies of A-site cations to segregate when heating: in the pure LSGF with increasing temperature lanthanum segregates to the surface and tend to replaces strontium, whereas in the composites these behaviours are switched. It is interesting that manganese seems to expel gallium from the inner to the surface: the at% of Ga increases, whereas it was expected an opposite effect due to the perovskite surface covering by manganese oxide.

In the LSGF + MnO_x composite, the position of Mn2p peaks (see Figure 3.8) is interpreted with an oxidation state intermediate between +2 and +3. This is consistent with the presence of Mn_3O_4 that has been indicated by XRD and TPR.

Variations of binding energy of iron oxides depending on oxidation state are very small, so a clear recognition of the phase from the only XPS spectrum is very difficult. In the case of LSGF + FeO_x (see Figure 3.9) it is possible to observe the appearance of shoulders at binding energies lower than the perovskite ones. This confirms the presence of a FeO phase, as already outlined by TPR.

The $LaSrGa_3O_7$ secondary phase

The behaviour showed by this phase is tricky. In LSGF, it is visible by XRD and its reflections were not broad enough to suspect it has nano-sizes. Segregation on the surface seems unlikely because XPS does not detect any abundance of Ga on the surface compared with bulk. Data described so far would suggest the presence of a separated phase instead of an impurity in LSGF particle, but from SEM (see paragraph Cells) it is not possible to distinguish any phase separations. This secondary phase disappears when some simple oxide (Fe or Mn) is deposited, after a treatment at only 550°C. This is a very low temperature for this kind of reactions, also considering that $LaSrGa_3O_7$ abundance at the beginning is remarkable, and especially because the phase seems, from XRD reflections' sharpness, quite bulky. It was tested that temperature alone is not able to trigger disappearance, so there must be some interaction between the deposited phase and $LaSrGa_3O_7$, which, for this reason, must have some contact with the surface. A possible explanation to all these seemingly contradictory data is the formation of particular $LaSrGa_3O_7$ structures within LSGF particles, that emerge on the surface. This way, the phase could reach the surface and interact with FeO_x/MnO_x without increasing XPS Ga abundance or being clearly detected by SEM.

3.3.6 TPR

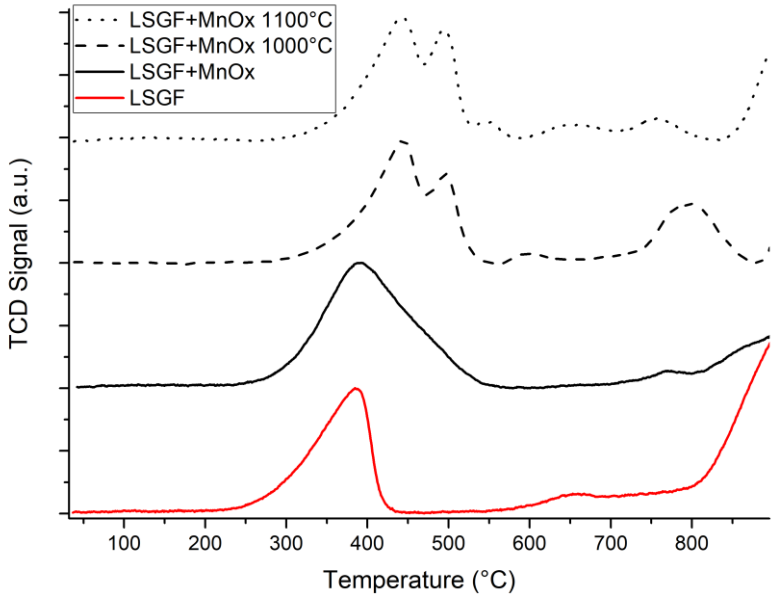

Figure 3.10 TPR profiles of LSGF + MnO_x treated at different temperatures. In red, the profile of LSGF before the deposition is shown for comparison.

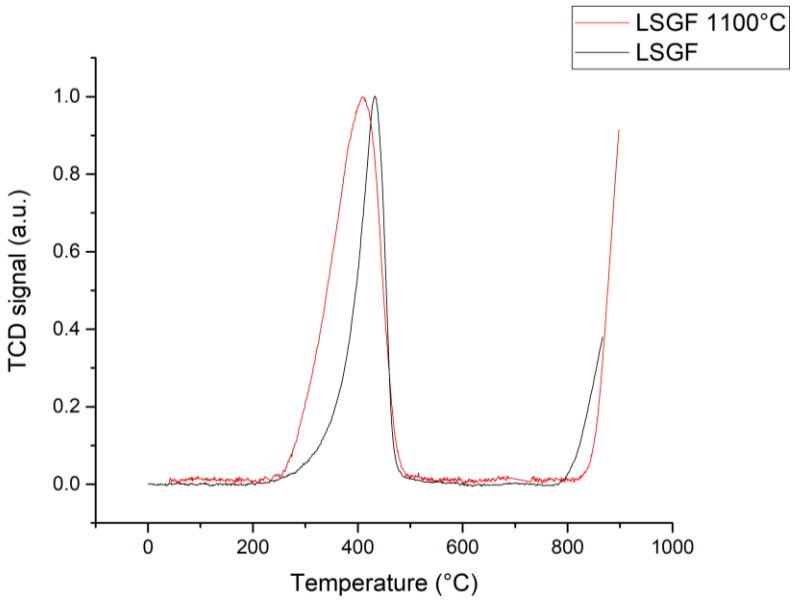

Figure 3.11 Comparison between TPR results of LSGF as-synthesized and LSGF treated at 1100°C.

SAMPLE	400°C	500°C	800°C
LSGF, ANY TREATMENT BETWEEN 900-1100°C	115	0	0
	400°C	500°C	800°C
THEORETICAL LSGF + 10% MN3O4	145		0
LSGF + MNOX	150		Traces
LSGF + MNOX 1000°C	100	35	40
LSGF + MNOX 1100 °C	55	35	5
	400°C	500°C-700°C GROUP OF 3 PEAKS	800°C
THEORETICAL LSGF + 10% FEO	115	0	100
LSGF + FEOX	120	0	110
LSGF + FEOX 1000°C	115	40 (1.5+19+19)	0
LSGF + FEOX 1100 °C	100 (30+70)	15 (1.5+7+7)	Traces
LSGF + FEOX 1000°C 10% O2	110	40	0

Table 3.2 Hydrogen consumption for main peaks in Figure 3.10, Figure 3.11 and Figure 3.12 (mmol/mol of perovskite). In the LSGF + MnO_x sample the peaks are not resolved enough to allow an estimation of their area, hence their total area is reported instead. Brackets indicate deconvolution of groups of peaks.

Figure 3.10 shows the TPR profile of the LSGF powder. The main item is the $Fe^{4+} \rightarrow Fe^{3+}$ reduction, that happens between 300°C and 500°C[170]; at 800°C iron reduction to lower oxidation states begins, ending above 1000°C so it is only partially visible in this measurement. As also reported in the previous chapter, this corresponds to a Fe(IV) abundance of 1/3 of all the iron atoms. This profile does not change with treatment at temperatures up to 1100°C (see Figure 3.11), so modifications observed during measurements on impregnated oxides should be attributed to the presence of the impregnated atoms. The comparison of the TPR profiles of the nanocomposites and of the supporting LSGF, allows to go deeper into the interaction between supported oxide and supporting perovskite.

Samples with manganese oxide show a number of signals superimposed to the LSGF ones. Stobbe et al. report that reducibility of manganese oxides has been found to significantly depend on particles' specific surface area [205]. In general, MnO_2 showed almost a one-step reduction to Mn(II) around 500°C, whereas Mn_2O_3 showed a clear two step reduction (around 300 and 400°C): from Mn_2O_3 to Mn_3O_4 and then to MnO. The reduction of Mn_3O_4 in hydrogen (ranging from 450 to 500°C) is influenced by the preparation procedure and the degree of crystallinity, being higher in highly crystalline materials. Kapteijn et al.[206], in contrast observed a two-step reduction for MnO_2 (the reduction temperature of Mn^{4+}, 331–351°C, being lower than that of Mn^{3+}, 443–526°C) [207].

TPR profiles of LSGF + MnO_x treated at different temperatures are reported in Figure 3.10, and Table 3.2 summarizes the H_2 consumptions determined for the different peaks. The signal at 400°C is attributed to the $Fe^{4+} \rightarrow Fe^{3+}$ reduction whereas those at 500°C and 800° are related to manganese. The as-prepared LSGF + MnO_x sample shows a broad shoulder superposed to the reduction $Fe^{4+} \rightarrow Fe^{3+}$ of the perovskite iron. Hydrogen consumption of this peak is estimated (by subtracting the expected 115 mmol/mol consumption for the perovskite contribution determined in the unsupported LSGF, from the total area) to be around 35 mmol/mol. According to Figure 3.2 the manganese oxide is deposited as Mn_3O_4, and the $Mn^{3+} \rightarrow Mn^{2+}$ reduction of this phase to MnO is compatible with the calculated area. Also the temperature supports this hypothesis being in the range already mentioned for Mn(III) reduction.

No signal indicating further reduction to Mn^0 is observed in the examined temperature interval. After the treatment at 1000°C the area of the $Fe^{4+} \rightarrow Fe^{3+}$ transition at 400°C of the perovskite slightly decreases (Fe^{4+} fraction is now 29%), while the intensity of the peak at 500°C assigned to manganese $Mn^{3+} \rightarrow Mn^{2+}$ does not seem to be modified. Now this $Mn^{3+} \rightarrow Mn^{2+}$ peak can represent, other than the Mn_3O_4 contribution, a Mn_2O_3 fraction that was indicated to form by XRD measurements and another fraction of Mn^{3+} that can have entered inside the perovskitic lattice. A new peak at 800°C appears, suggesting the further reduction of manganese: $Mn^{2+} \rightarrow Mn^0$. The area of this peak is slightly less than half the one expected for the complete reduction of all deposited manganese and this indicates that only a portion of Mn(II) is reduced. Literature data indicate, at this temperature, the reduction of Mn(II) cations present inside the perovskitic lattice[207], so probably in this sample only half of the total deposited manganese atoms are inside the perovskite lattice. The absence of any peak before 400°C excludes the presence of Mn^{4+}. TPR data, as a whole, indicate that part of the manganese is penetrated inside the perovskite cell, but do not give particular information about where the other half of manganese atoms has gone. After 1100°C treatment, the perovskitic $Fe^{4+} \rightarrow Fe^{3+}$ 400°C peak further decreases (Fe^{4+} fraction, calculated from peak area, is 16%), the area of the manganese peak at 500°C is maintained whereas that of the peak at 800°C strongly decreases. This suggests that manganese atoms that were previously in the perovskitic structure could have been expelled from it. Nonetheless, the $Fe^{4+} \rightarrow Fe^{3+}$ variation implies the joint effect of temperature and that manganese presence has modified again bulk LSGF. Though, it is not clear where manganese is actually located after the treatments, because it disappears from TPR measurements. In other perovskites the ability of Mn to segregate as a defect in Sr vacancies and at grain boundaries with oxidation state 2+ is reported[208]. This behaviour would also explain why so much strontium is found to segregate at the surface, and why its reduction does not appear in the TPR curve (in that +2 state it would overlap with Fe^{3+} reduction at 800°C). Furthermore, this accommodation for manganese would not impact on XRD reflections, and in fact no modification of the position of LSGF is observed in all LSGF + MnO_x samples.

The results of TPRs in LSGF + FeO_x materials are shown in Figure 3.12 and the volume of H_2 consumed for each peak is summarized in Table 3.2. In the profile of as-

prepared LSGF + FeO_x the peak at 400°C is broadened with respect to LSGF but the H_2 consumption is very similar. Literature data report that the reduction of bulk iron oxide by hydrogen usually proceeds through the following steps: Fe_2O_3 to Fe_3O_4 to FeO to Fe, the reduction to metallic iron being complete below 1000°C [209], [210].

The peak at 800°C can, thus, be assigned to the $Fe^{2+} \rightarrow Fe^0$ reduction of the deposited oxide, the area of this peak is consistent with this interpretation, being only slightly larger than the calculated one for this case. The small shoulder at 750°C can be assigned to a small $LaGa_{0.3}Fe_{0.7}O_3$ impurity[171]. The profile measured after the 1000°C treatment shows one main peak between 300°C and 500°C ($Fe^{4+} \rightarrow Fe^{3+}$ atoms of the perovskite) and a group of three small peaks between 500°C and 750°C (area ratios 1:15:15, see arrows in the Figure), whereas the peak at 800°C disappears. This result suggests some phase or morphological transformation happened, and caused the disappearance of the FeO phase, whose reduction at 800°C is not visible anymore.

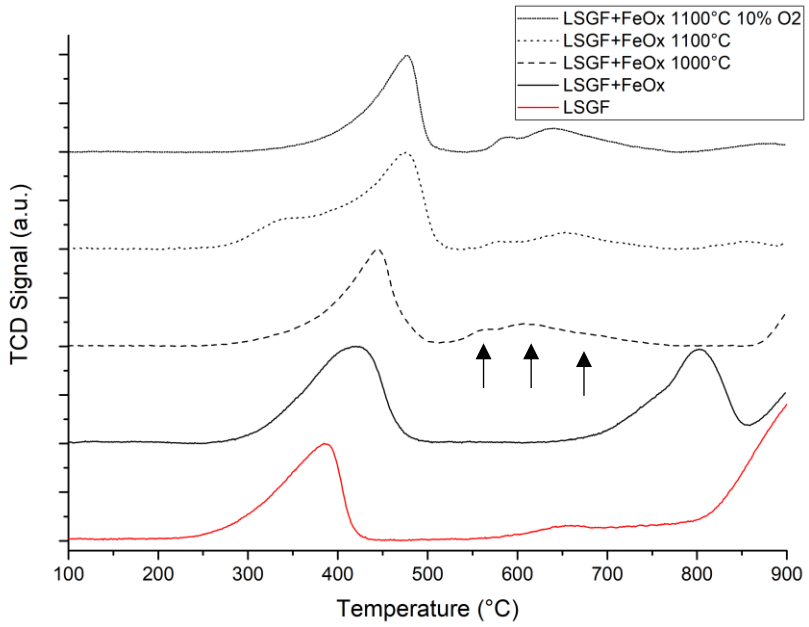

Figure 3.12 TPR profiles of LSGF + FeO_x treated at different temperatures. In red, the profile of LSGF before the deposition is shown for comparison.

The inclusion of these iron atoms as Fe(III) into the perovskite shifts their reduction at higher temperatures out of the measuring interval. XPS measurements indicates a significant segregation of Sr at the surface, this fact, together with the high concentration of iron, could have induced the formation of a $SrFeO_3$ phase, or similar at the surface. $SrFeO_3$ is reported to be reduced completely between 400°C and 600°C with two non-resolved peaks[211], similarly to the group of peaks observed at 500°C-

700°C but shifted of 100°C. In addition, $SrFeO_3$ XRD reflections would be overlapped to the ones of LSGF. After the treatment at 1100°C the signal at 400° is split into two peaks, of area respectively 30 mmol/mol (around 350°C) and 70 mmol/mol (around 470°C). The second and third peaks of the group between 500°C and 700°C lose more than half of their areas, but they keep the same 1:1 ratio: therefore, they are two steps of reduction of a same phase, that could be $SrFeO_3$ as previously proposed. The decomposition of this phase, due to the relevant segregation of strontium at the surface, could be at the origin of the 350°C peak phase. Regrettably, due to the high number of elements in the sample, precise identification of new phases is extremely difficult; moreover, the reduction temperature is greatly affected by particles' dimension so high dispersion, also confirmed by the absence of XRD signals, could be a cause of the low reduction temperature. In addition to the new phases, some changes must have been induced also on the perovskite, because the $Fe^{4+} \rightarrow Fe^{3+}$ peak area decreases. It has been observed that it is possible to avoid the modifications described above if the treatment is carried out at 1100°C with a controlled 10% O_2 atmosphere (instead of air). Interestingly, in this case the material is able to retain the same TPR curve of the 1000°C treatment suggesting that the changes are related to the oxidizing atmosphere.

3.3.7 O_2-TPD

O_2 TPD is an effective tool to examine oxygen mobility in ceramic materials. Results of O_2 TPD measurements obtained after the thermal treatment at 1000 and 1100°C for LSGF and LSGF + MO_x samples are compared in Figure 3.13, and the amount of oxygen released is summarized in Table 3.3. The mass quadrupole detected oxygen was the only species in the carrier stream at the instrument outlet. All the curves show an oxygen release that begins at 200°C-250°C and does not end until 1000°C.

Conventional separated α and β oxygen peaks (respectively, surface and lattice oxygen), cannot be distinguished, instead the two types of oxygen produce two broad not completely resolved signals. This behaviour is in accordance with other literature data for (La,Sr) ferrites, which describe an uninterrupted release without any resolvable peak in the same interval of temperatures[212], and seems exclusive of this particular composition: ferrites with elements such as Ni[213], Bi[212], Ca[214],

Ba[215], [216], Co[217] or without La[180] tend to desorb oxygen with more defined peaks.

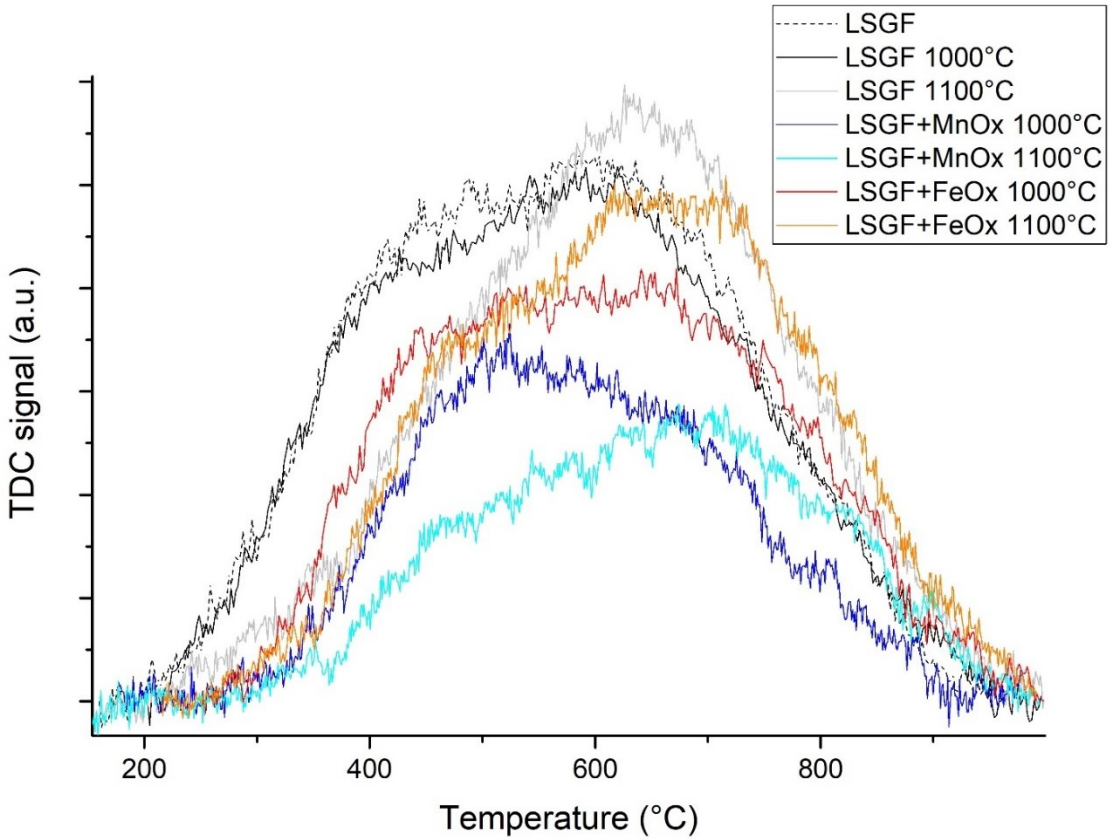

Figure 3.13 O_2 desorption of the tested samples

	900°C*	1000°C	1100°C
LSGF	52	48	46
LSGF + MnO_x		26	19
LSGF + FeO_x		41	42

*Table 3.3 Amount per mole of desorbed oxygen during O_2-TPD measurement (mmol/mol of perovskite). *: 900°C is the calcination temperature of LSGF during its synthesis.*

Gallates have a single small desorption signal peaked around 650°C[218], so it appears that LSGF retains characteristics of ferrites rather than gallates. However, peaks tend to be shifted at higher temperatures probably for a stabilizing effect from gallium. Oxygen exchange properties of this material are attributed to the ability of B-site cation Fe to easily shift between +3 and +4 oxidation states, and have been found to be related to the amount of Sr-doping and completely reversible [219]. As reported elsewhere[214], [220], the perovskite accommodates extra charge of the

substitution of tri-valent La with bi-valent Sr in three ways: oxidation of Fe^{3+} to Fe^{4+}, hole formation or creation of oxygen vacancies. Both the Fe^{4+} and oxygen vacancies formation are reported for $La_xSr/Ca_{1-x}FeO_3$ perovskites[221].

Data on our sample seem to suggest that the profile is the sum of two broad peaks, centred respectively around 500°C and 700°C. Increase of calcination temperature at 1000°C has only little effect on pure LSGF. After the treatment at 1100°C, in contrast, a significant decrease of the contribution at around 400°C and increase of the signal around 650°C are observed. This behaviour can be related to the desorption of slightly bonded surface active oxygen species (α-oxygen) and the increment of oxygen mobility and exchange capability (β-oxygen desorption from lattice)[180], [222]. The superficial LSGF α-oxygen concentration, calculated from experimental superficial area, is close to $1{\cdot}10^{15}$ atoms/cm², compatible with an oxygen monolayer[221]. The presence of Fe and Mn, the latter in particular, induces changes in oxygen desorption. In LSGF + FeO_x the FeO_x deposition causes the decrease of both α and β-oxygen species; this decrease can be also due to the surface covering after deposition. The increment of treatment temperature causes the increment of the contribution around 700°C, due to the lattice oxygen desorption, that get similar to the one of supporting LSGF; this behaviour can be related to the diffusion of FeO inside the perovskite with the formation of mixed valence phases. In LSGF + MnO_x the decrease of oxygen desorption is more severe, particularly when considering the lattice oxygen. The increasing temperature induces the decrease of the signal around 450-500°C so suggesting that a lower amount of oxygen active species desorbs from the surface.

It is possible to find some correlation between the results of these tests and the TPR's ones and, in particular, with the TPR signals related to the reduction $Fe^{4+} \rightarrow Fe^{3+}$: the variations in H_2 consumption corresponding to this process follow the same trend of the ones of O_2 release during O_2 TPD. The interaction between LSGF and the deposited phases induced small modifications in the perovskite, that, regarding TPR and O_2-TPD measurements, can be evaluated in terms of ability to accommodate Fe^{4+} atoms and oxygen vacancies. Focusing on the amount of adsorbed/desorbed species (H_2 during TPR and O_2 in O_2-TPD) LSGF + FeO_x shows a behaviour similar to the supporting LSGF. The formation of perovskitic phases with different stoichiometry,

proposed in the previous paragraph, could explain why oxygen exchange properties are only little affected. On the other hand, in LSGF + MnO_x the amounts of oxygen desorbed are lower; in addition, this sample shows increasingly less intense TPR signals after the thermal treatments at 1000°C and 1100°C. The amount of Fe^{4+} and oxygen vacancies is generated to balance charge neutrality when Sr, limited to oxidation state +2, is in the perovskitic structure. So, a decrease of both the concentrations of Fe^{4+} and oxygen vacancies can be consistent with XPS results about strontium. This element segregates on the surface, as it happened with FeO_x, but this time it does not find high iron concentrations. Instead, there is a consistent amount of gallium, so no perovskite phase is possible. The progressive depletion of strontium, triggered in some way by manganese, explains the TPR and O_2-TPD results.

3.3.8 Catalytic tests

Literature data[179] report that, under oxygen excess, methane conversion starts below 400°C. Figure 3.14 shows the results of the catalytic tests on LSGF and its composites. In the present case, with fuel excess, LSGF begins to convert methane abruptly at 440°C and reaches instantaneously almost completion. This causes an increase of 75°C in sample temperature compared with blank, and this is why in Figure 3.14 there are no intermediate points between 400°C and 525°C. At 525°C, a residue of 0.7% of O_2 was detected. Even with excess of fuel, LSGF is highly selective towards complete oxidation: only 0.5% of H_2 was measured at 670°C, and CO was below 1%.

The behaviour of the composite with manganese is interesting: at 440°C a transient activation of 5-10 minutes is observed, and after that activity totally ceases. During the transient activation period, oxygen consumption is estimated around 20-30% and temperature increases to 460°C. After this, only small signs of activity (<5%) are detected until 530°C. The presence of activity within the same onset temperature suggests the incomplete coverage of the LSGF surface that could be responsible of this activity. Then the catalytic activity observed from 530-550°C could also be caused by MnO_x itself. It is possible that the transient temperature increase due to combustion, triggered rearrangement in the MnO_x phase, leading to inactivation of the LSGF surface; then no activity is observed until onset temperature for MnO_x is

reached. It is important to remind that both LSGF and manganese oxides are considered catalysts for methane oxidation[179], [223], [224]. Further work is in course to better understand the catalytic behaviour of this composite, but the capability of manganese to diffuse toward the supporting perovskite giving rise to different phases, surface and behaviour with respect to H_2 and O_2 is evident. Overall catalytic activity is lower than bare LSGF, oxygen consumption at 600°C is only 80%. Composite with FeO_x begins to be convert CH_4 at 450°C, and then the activity increases slowly and almost linearly with temperature, reaching 67% at 680°C. The lower reactivity with respect to methane oxidation could be related to the decrease of the surface active oxygen species revealed by O_2-TPD. Different oxidation mechanisms, in fact, are usually considered to be relevant at different temperatures: at lower temperatures (lower than 400-500°C) supra-facial mechanisms involving oxygen active surface species (probably necessary for reactants activation) seem to be preferred whereas oxidation mechanisms requiring bulk oxygen mobility can be relevant only at rather high temperature. In general, the deposition of iron and manganese oxides on the perovskite surface effectively modified catalytic activity towards methane, although in different ways: MnO_x after the "transient activation" probably covers and substitutes LSGF activity, while coverage of FeO_x is incomplete thus leaving some active LSGF surface exposed. Increased mesoporosity as indicated by N_2 isotherms in LSGF + FeO_x sample can be the cause of the residual exposition of the perovskite to the atmosphere. Moreover, it has to be considered that the Fe^{4+} to Fe^{3+} reduction is completed at higher temperature in the LSGF + MnO_x and LSGF + FeO_x confirming a lower reducibility.

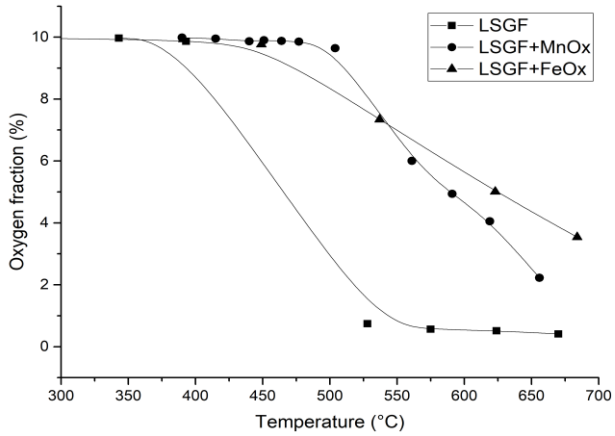

Figure 3.14 Catalytic tests on LSGF and LSGF composites: oxygen fraction determined as a function of temperature, for the LSGF before and after the deposition of the oxides.

3.3.9 Cells

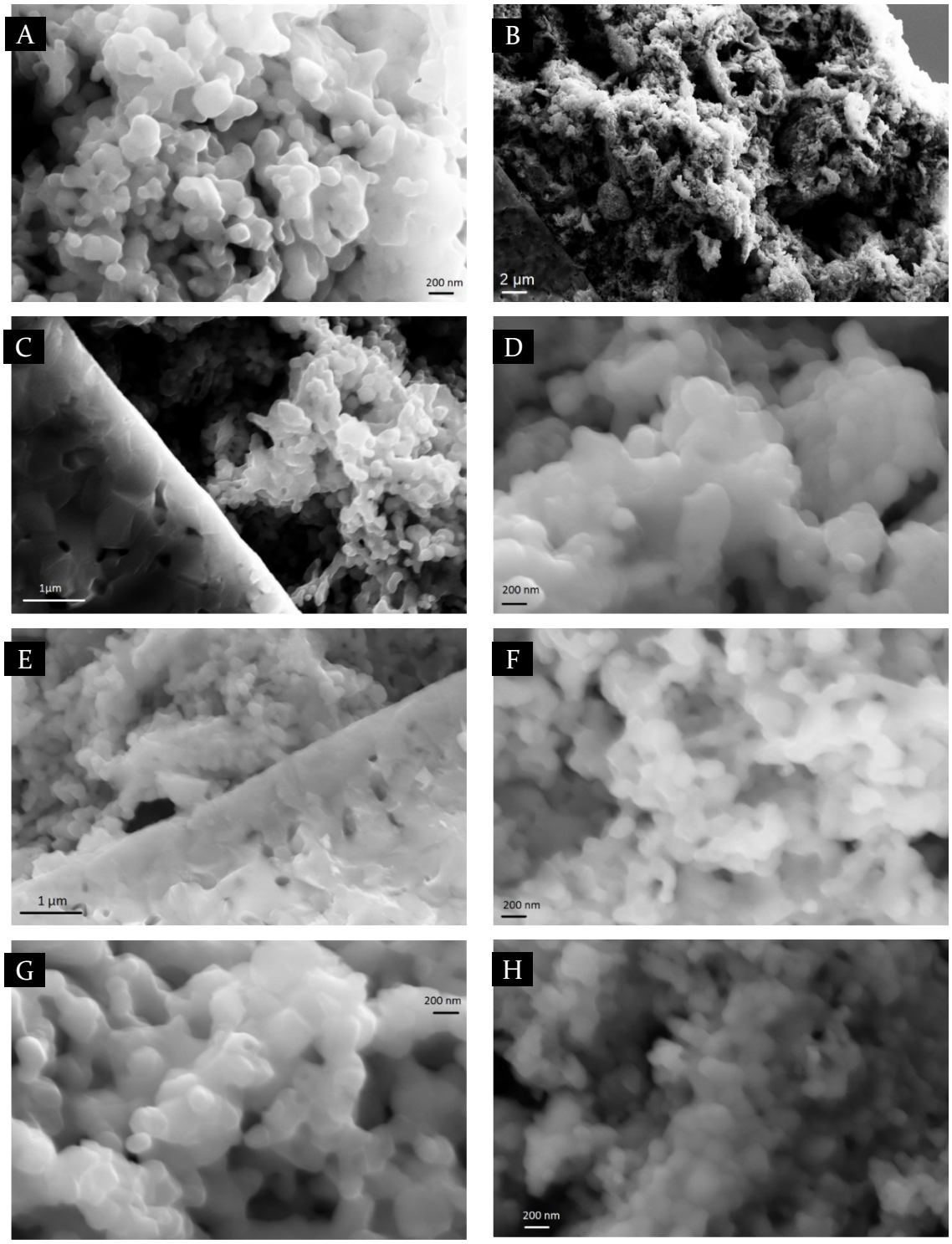

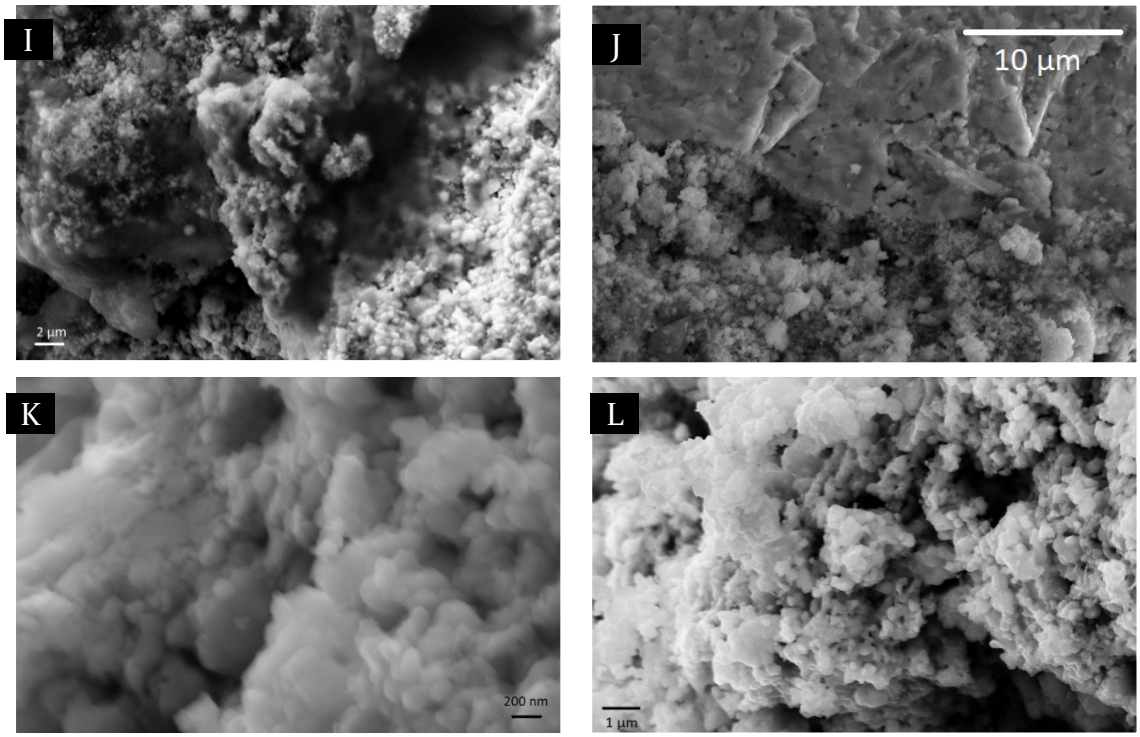

Figure 3.15 SEM images of sections of symmetrical cells on CGO. A and B: LSGF cell treated 1000°C, electrode; C: LSGF cell treated at 1000°C, interface electrode/electrolyte; D: LSGF cell treated at 1100°C, electrode; E: LSGF cell treated at 1100°C, interface electrode/electrolyte, F: LSGF + MnO_x cell treated at 1000°C, electrode; G: LSGF + MnO_x cell treated at 1100°C, electrode; H and I: LSGF + FeO_x cell treated at 1000°C, electrode, J: LSGF + FeO_x cell treated at 1000°C, interface electrode/electrolyte, K: LSGF + FeO_x cell treated at 1100°C, electrode, L: LSGF + FeO_x cell treated at 1100°C under 10% O_2 atmosphere.

Images of sections of cells show the stability of the electrode morphology: no substantial variation is observed after the thermal treatments, apart from a more compact arrangement of the particles (Figure 3.15 A and D). The electrode/electrolyte contact at the interface seems poor after a thermal treatment at 1000°C, although on a macroscopical scale no detachment was observed (even after the application of some mechanical stress - Figure 3.15 C); the treatment at 1100°C induces a much better connection between the two layers (Figure 3.15 E). The deposition of Mn oxide on the powders and subsequent treatment at 1000 and 1100°C during cell curing does not lead to any modification of the morphology and structure of the electrodes, that resemble the non-impregnated LSGF ones (Figure 3.15 F and G vs A and C). Significant differences are observed, in contrast, in the LSGF + FeO_x case. The electrode obtained after the deposition of Fe oxide followed by the same treatment at 1000°C is shown in Figure 3.15 H. The morphology, on a nanometres scale is maintained but on a micron scale the formation of some foils that wrap the LSGF particles is evident (Figure 3.15, compare I with B). These structures are probably thin, as it is possible to observe blurred images of the LSGF particles beneath; moreover, they improve the connection

with the electrolyte (Figure 3.15 J), that seems better than in the case of the pure LSGF. This phase possibly is also responsible for the reductions at 600°C-700°C shown by TPR measurements. Treatment at 1100°C of the LSGF + FeO_x electrolyte cause the collapse of these foil structures, that are no longer observed; instead, as a consequence, the surface of the particles appears much rougher than the previous case (Figure 3.15 K), probably because of the coverage of the pristine particles with the conglomerated fragments of the 1000°C-foils. During the 1100°C treatment, there is also a chemical degradation of the phase constituting the foils, associated with TPR signals decrease, but the cause of the collapse is thermal rather than chemical: the treatment under 10% O_2 is able to maintain the same TPR profile, but, the wrapping foil with the 1000°C treatment again is not observed (Figure 3.15 L); furthermore, as shown in following paragraphs, the electrochemical performance which derives from the presence of the layer is lost also in this case.

3.3.10 EIS

Impedance measurements have been performed in air, to obtain information concerning the ability of the material to exchange oxygen with the atmosphere and the electrolyte: the results obtained with this setup can be related, in general, to the behaviour as SOFC cathode.

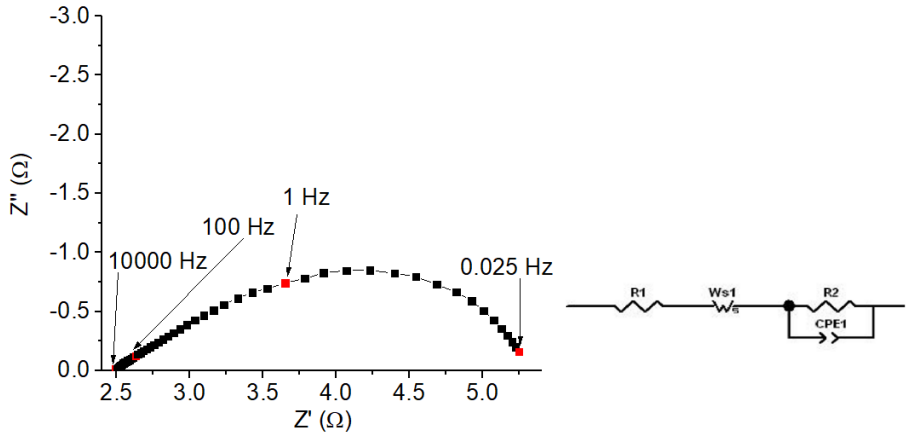

Figure 3.16 Left: Nyquist plot of LSGF 1100°C symmetrical cell at 620°C, all the other samples have the same shape. Right: model circuit used for interpretation, red spots indicate particular frequencies.

The Nyquist plots obtained from measurements in air (see Figure 3.16 as an example) have been fitted using a model circuit (Figure 3.16). The plot of LSGF has the shape of a Warburg-like loop, which is a semicircle with one side appearing as a 45° straight line. To obtain a good fitting it has been necessary to include three

different elements: the R1 resistance, representing the ohmic resistance of the electrolyte, a Warburg element, related with oxygen diffusion, and a R//CPE (resistance in parallel with a Constant Phase Element) element, related to the polarization resistance of the air/perovskite interface during the reduction and uptake of atmospheric oxygen. In the model circuit, chosen in accordance with existing literature[225], the Warburg element is W_{s1}, and the polarization process is represented by in parallel R2 and CPE1. ASR (Area Specific Resistance) is calculated as the sum of the resistances associated to R2 and W_{s1}. The apex frequencies of the two observed processes are very similar, around 10^{-1}-10^{-2} Hz, and the curves are almost overlapped. Because of this, the uncertainty derived from the fitting, relative to the quantification of the respective contributions to overall resistance, is high. Therefore, when resistance changes it is extremely difficult to identify which process is responsible for it.

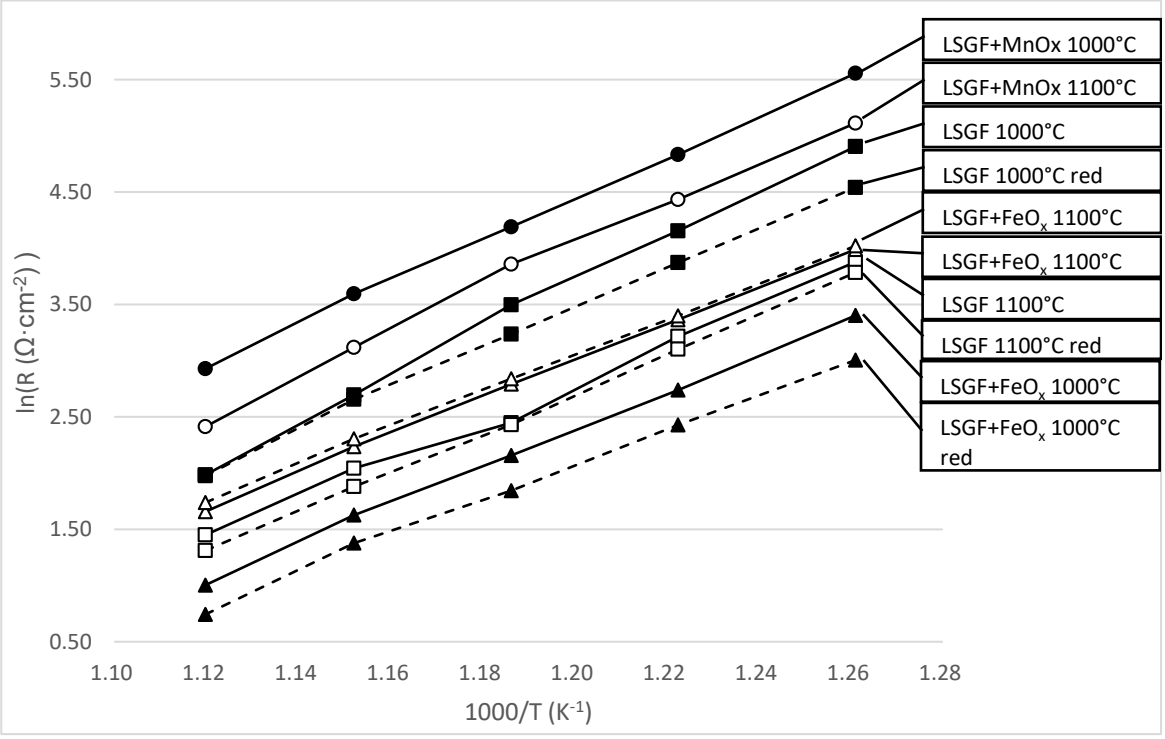

Figure 3.17 ASR measured at different temperatures for all the samples tested. Tag "red" designates second measurements after methane reducing treatment.

The performances of the tested materials are summarized in Figure 3.17, and have been evaluated on the basis of literature[226]. At temperatures of about 600°C state-of-the-art materials have ASR below 2Ω·cm², so materials with similar performances can be considered suitable for application as electrodes. Compared with this ASR

value, the LSGF perovskite has only modest conductivity: its ASR at 600°C is 7.3Ω·cm² after 1000°C treatment and 4.3Ω·cm² after 1100°C treatment. This decrease of the resistance is expected, because higher temperatures improve electrical contact between particles, so a better conduction is obtained. The second measurement in air, after the reducing treatment, shows a small decrease of the resistance in the order of 10%. Previously, it has already been mentioned the tight relation between ionic conduction and Fe^{3+}/Fe^{4+} species: the reduction of Fe^{4+} atoms in the crystalline lattice leads to the creation of oxygen vacancies to maintain the electroneutrality, and a higher amount of vacancies is related, in these materials, to an improvement of ionic conductivity. The atmosphere has an effect also on the superficial sites of the material than can be reduced by it, this is a second possible explanation for the resistance decrease. The capacitance associated with W_{s1} and CPE1 are high: W_{s1} is around 10^{-1}-10^{0}F/cm², and this is consistent with bulk oxygen diffusion[227]; CPE1 is close to 10^{-1}F/cm², which is unusually high for this kind of processes. Capacitances of this size are called chemical capacitances, because they necessarily involve some kind of chemical reaction, as for example the oxidation/reduction of cations when O^{2-} ions move. In fact, only the bulk of a material, by means of its oxygen vacancies, is able to uptake amounts of electrical charge high enough to generate such high apparent capacitances. Thus, chemical capacitances are in general characteristic of a bulk limited process[95], and not of the electrochemical reduction of oxygen that the R//CPE generally represents. It is possible that the dominant limiting process here is bulk oxygen transport, which shades a second underlying process represented by the R//CPE; due to this overlapping the fitting of the CPE could inherit an apparent higher capacitance than its actual one. Some impedance test of a complete fuel cell in chapter 4, which is limited only by the LSGF cathode, can be optimally fitted by a single Warburg element, and this suggests bulk diffusion is the dominant process. Though, this is not true for all the curves. Another possibility is the effective presence of a limiting process, which is related in some way with the bulk so it really has a high capacitance associated, but that is different from diffusion, which is modelled by the Warburg element and is observed aside.

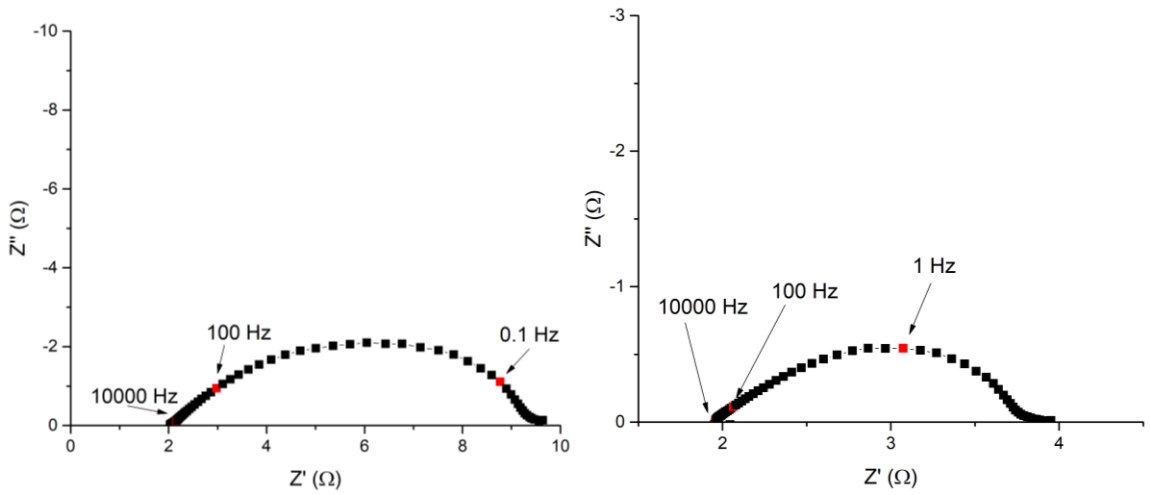

Figure 3.18 Left: Nyquist plot of LSGF + MnO_x cell treated at 1100°C, measured at 620°C. Right: Nyquist plot of LSGF + FeO_x cell treated at 1000°C, measured at 620°C.

A higher resistance is measured in LSGF + MnO_x when compared to the bare perovskite, and the shape of the Nyquist plot is more rounded (Figure 3.18), so in this case the presence of the R//CPE seems obvious. Still, its capacitance is very high, having the same magnitude of LSGF case. The increase is, above all, in the polarization resistance, whereas the increase in the Warburg element seems only modest. The loss of iron atoms on the surface, the only active sites for LSGF, can be responsible for the increased polarization resistance. This highlights also how much iron is important for the activity related to the surface of LSGF. The inclusion of some Mn in the perovskitic lattice, already suggested by the TPR results, can have also modified the conduction properties of the material. According to TPR results, it appears that the 1000°C treated sample included a noticeable amount of manganese in the perovskitic structure, while the 1100°C treated sample has a lower Mn concentration inside the perovskite. This "lost" fraction of manganese could have migrated to grain boundaries as Mn^{2+}, as explained in paragraph 3.3.6 TPR, where it would be still able to influence the materials properties, in terms of oxygen desorption. The amount of desorbed oxygen decreased more with increasing treatment temperatures, and this could be a consequence of the movements of manganese atoms. It can be shown that for ionic conduction in these materials the Warburg resistance can be expressed as[225], [228]:

$$R_W = \frac{RT}{4F^2}\frac{\varepsilon}{CD}$$

Where R is the universal gas constant, F is the Faraday constant, T is the absolute temperature, ε is the diffusion length, C is the vacancies concentration and D is the diffusion coefficient. So, in the same material, a decrease of the vacancies concentration increases Warburg resistance. O_2 TPD clearly indicates that exchange of oxygen, and therefore also the vacancies concentration, is reduced in LSGF + MnO_x samples, and this is consistent with EIS results that show LSGF electrodes having a lower ASR than LSGF + MnO_x ones. In particular β oxygen, the only component related to the bulk, is observed to be decreased from LSGF and similar for both the 1000°C and the 1100°C treatments.

Results of measurements carried out after reducing treatments on LSGF + MnO_x have not been reported. The treatment practically implied the removal of the cell from the setup and then the re-application of the gold current collector including treatment at 850°C, but every time this procedure was performed measured ASR resulted in twice the original value. XRD measurement on 30% MnO_x powder evidenced that at temperatures lower than 1000°C the formation of a Mn_2O_3 phase happens, interrupting the continuity between particles and modifying the active surface. A similar process could easily have happened also during first curing of gold collector, so actually measured performances are probably already affected by this process.

The perovskite impregnated with iron shows the best performances among all the samples (Figure 3.18); it is also peculiar that LSGF + FeO_x are the only samples whose ASR increases if the thermal treatment is carried out at 1100°C instead of 1000°C. After the treatment at 1000°C, only a Warburg element is necessary to fit the data, and the iron oxide deposition is able to reduce the resistance at only 30% of LSGF treated at the same conditions. Capacitance is compatible with bulk limited diffusion, close to 1F/cm². Nonetheless, after the treatment at 1100°C the resistance is slightly worse than that of the supporting LSGF perovskite alone treated at the same temperature. For this sample, the Warburg resistance is a little increased compared to the bare perovskite and polarization resistance is 1.6 times bare perovskite's one.

As mentioned, unlike LSGF and LSGF + MnO_x, the treatment at higher temperatures does not improve the performances of LSGF + FeO_x. TPR results showed

that LSGF + FeO_x sample retains the same curve after treatments at 1000°C and 1100°C only if latter is carried out under controlled 10% O_2 atmosphere; so, a LSGF + FeO_x cell has been treated under these same conditions (10% O_2) to verify if the changes in TPR profile were responsible for the loss of electrochemical activity: the obtained performances are compatible with the ones obtained with the treatment in air, so it can be concluded that variations in TPRs were not linked with electrocatalytic activity. As already mentioned, no significant differences were observed in the XRD patterns.

The comparison of all data collected as a function of temperature, suggests that the explanation of the different performances of LSGF + FeO_x treated at 1000°C is morphological. As evidenced by SEM measurements, this sample shows some thin foil wrapping perovskite particles. This foil collapses at 1100°C, even in controlled 10% O_2 atmosphere. The formation of this layers is probably linked to the movement of iron atoms of the deposited phase: note that in this sample the XPS iron concentration among only cations (hence, excluding oxygen) is 32%, instead of the 23% of pure LSGF at the same temperature (see Table 3.3). This difference is not observed in the same sample treated at 1100°C nor in LSGF + MnO_x samples, and indicates that there still is some prevalence of iron atoms at the surface. Experimental data show a disappearance of polarization resistance and a strong decrease Warburg resistance, so the observed structure is able to assist both the reduction of oxygen molecules and the diffusion of the atoms to the electrolyte. Such a structure could easily provide a number of new iron sites, some apt for the interaction with oxygen, and this explains why polarization resistance decreases. It is not clear, however, what the observed structures exactly are. Some combined data from XRP and TPR suggested the formation of a $SrFeO_3$-like phase, but, as a perovskite, it should not form such extended structures, so this explanation does not give the entire picture. Given the ubiquitous nature of these foils, they could also be able to assist the movement of oxygen ions, especially at the grain borders; however, the exact cause of the easier oxygen conduction is difficult to assess precisely without a deeper knowledge of the nature of the observed structure.

3.4 Conclusions

The work described in this article allows a deep understanding of processes taking place when a perovskite substrate interacts with a deposited oxide phase, and some of them appeared not trivial at all. The presence of the deposited phase triggered some non-linear behaviour: the perovskite influences phase and oxidation state of the deposited oxides (FeO and Mn_3O_4 instead of Fe_2O_3 and Mn_2O_3), and dynamically interacts with them at different temperatures. An interesting behaviour was observed for the $LaSrGa_3O_7$ impurity phase in relation to the impregnated oxides, and its presence in form of a discrete structure within LSGF particles has been proposed, but further data is needed to confirm this interpretation. LSGF is able to absorb manganese during heating until 1000°C, but releases it at 1100°C and during cooling. It has been demonstrated that deposition of a proper oxide and subsequent temperature treatment can modify superficial segregation of selected elements: both manganese and iron heavily influenced La/Sr ratio, and Mn triggers Ga segregation at the surface. The consequences of this interactions have been studied in depth, and have been related with oxygen mobility and catalytic and electrocatalytic activities. The importance of Fe species for the functionality of ferrites is highlighted. Redox couple Fe^{4+} and Fe^{3+} has proven to be fundamental in oxygen mobility, and the ability of the material to form Fe^{4+} centres has been related to the formation of oxygen vacancies and ionic conduction, in accordance with existing literature. Fe sites have also been proven to be fundamental during electrocatalysis: polarization resistance has been found to increase/decrease depending on their superficial concentration. During impedance analysis, an ambiguous response of impedance with anomalously high capacitance has been identified, but no clear explanation was found. Materials and composites have been studied for application as SOFC cathodes, and an excellent improvement of performances has been observed for LSGF + FeO_x materials treated at 1000°C. The origin of this improvement has been examined, and finally related to the formation of thin layers that probably act as a connection between particles. These structures have been found to collapse with treatments at temperatures above 1000°C. The good results found with these materials suggest their application as SOFC electrode should be taken in consideration, given their chemical stability that has already been proven superior to common state-of-the-art cathodes. The

consequences of a deposited phase on catalytic activities have been studied: the presence of the oxide phase has proven to be in general detrimental from this point of view. An interesting interaction between LSGF and MnO_x has been observed, comprising the formation of a passivating layer only in response to the onset of catalytic activity.

4 LSGF/LSGM symmetrical reversible fuel cells

LSGF GOES TO ANODE

A STRANGE *AFFAIR* BETWEEN LSGF AND GOLD

IMPREGNATION WITH NOBLE METALS

REVERSIBLE FUEL CELL/ELECTROLYSER TESTS, WITH THE SAME MATERIALS, THEM AGAIN

4.1 Introduction

In chapter 1 it was outlined how some cells can operate reversibly, as a secondary battery, so they can both store and produce electrical energy. As it is described in this thesis, LSGF ($La_{0.6}Sr_{0.4}Ga_{0.3}Fe_{0.7}O_3$) has been successfully tested as a suitable platform with high stability for custom functionalization, and it was able to develop decent cathodic (see chapter 3) or anodic (see chapter 5) activity depending on the deposited phase. The tests shown here extend its application to the whole category of the solid oxide cells, including also electrolysers; so that a fully reversible cell made with LSGF electrodes can be fabricated. While it is the first time LSGF is used to prepare a SOEC electrode, similar materials as LSF have already been tested with promising results[229]. The aim of this series of experiments was to test the feasibility and the performances of a LSGX based symmetrical reversible cell, with X being Mg for the electrolyte and Fe for the electrodes. LSGM ($La_{0.9}Sr_{0.1}Ga_{0.8}Mg_{0.2}O_3$) is a consolidated electrolyte material; it shows good conductivities at intermediate temperatures, and recently has been tested also for SOECs[230], [231]. Unfortunately, LSGM was proven to be not fully compatible with some other common materials for SOECs, as Ni, ceria[232] and cobalt containing perovskites[233]. In fact, degradation of components is a major issue for SOECs, that found their industrial application to be limited by a fast loss of performances due to a variety of reasons, including: formation of insulating phases at the interfaces, physical degradation of the electrodes/electrolytes, migration of impurities across the components[234]. Reversible operation is

successful in slowing the cell degradation, but it is not able to eliminate it completely. Hence, our primary focus is on stability, rather than cell power, hopeful that providing a stable backbone for cells, whose performance can be enhanced by proper coupling with other phases, can help toward the economical sustainability of these devices. The very similar composition of the two LSGF and LSGM should avoid the formation of any insulating phases with long term depleting effects, and in any case the elimination of nickel from the anode makes impossible the appearance of the insulating $LaNiO_3$, which affects the LSGM/Ni interfaces. The assumed compatibility between LSGF and LSGM has been verified by means of an appropriate XRD test. The first fuel cell tests were conducted on a cell with both the electrodes made of pure LSGF. Then, a second cell was prepared, in an attempt to obtain better performances, trying to solve the most severe issues that affected the first tested cell. The second cell differs at the anodic side, which is not made of simple LSGF; rather, LSGF underwent a dry impregnation with CGO (mixed oxide of Ce 90% and Gd 10%) and Pd. In this kind of electrode, LSGF provides only conductivity, ionic and electronic, mechanical support and contact with the electrolyte. The so-obtained cell was then tested in fuel cell operation, and performances have been compared with the simple non-impregnated cell. Impedance spectroscopies and polarization curves were collected during the cell operation, impedance data were fitted on an appropriate equivalent circuit to retrieve cell Area Specific Resistance (ASR). Both the electrodes, LSGF and LSGF impregnated with CGO/Pd, have been examined by means of Scanning Electron Microscopy (SEM), to identify the structures formed during the impregnation. SEM, along with XRD, has also been employed on a tested cell to find the cause of a performance decrease of non-impregnated LSGF anode above 800°C. Following the good performance of the Pd/CGO impregnated electrode, the same device was tested as an electrolyser for steam electrolysis, and also in this case EIS data and polarization curves were collected. At the end of this work, it was possible to obtain a fair indication about how LSGF can behave in a reversible SOFC.

4.2 Experimental

The cells studied in this work are supported on thick electrolyte, prepared pressing a LSGM powder (commercial LSGM9182, Kceracell) into pellets and then

firing them at 1400°C for 6 hours: thickness of the pellet is around 1.2 mm with a 2 cm diameter. The LSGF powder used for electrodes was synthesized via a solid-combustion route, with the same procedure as explained in chapter 2. Two different inks were prepared for the screen printing of the electrodes on LSGM: a composite LSGF 50%/LSGM 50% and pure LSGF ink. Ink preparation involved grinding of the powders and mixing them with proper amounts of α-terpineol and PVA. Cells were fabricated by screen printing two layers on both sides of the electrolyte, first layer is LSGF/LSGM composite to improve electrolyte/electrode contact and second is pure LSGF, the mask used for printing is a circle of area 1.110 cm^2. Cells were then fired at 1100°C. At this point, electrodes were ready for impregnation: some drops of a solution of $Ce(NO_3)_3$, $Gd(NO_3)_3$ and CTAB (1-hexadecyl trimethyl ammonium bromide) were deposited on the electrode with a pipette until it wetted the whole surface, the cell was then treated at 750°C for 30 minutes. This procedure was repeated until the electrode gained 10-15% extra mass in addition to its original weight. After the CGO deposition, a single drop of $[Pd(NH_3)_4](NO_3)$ was used to impregnate palladium, another treatment at 750°C for 30 minutes followed, to reach a Pd content of around 1 wt%. Only the negative electrode is impregnated (i.e. the anode in fuel cell mode and cathode in electrolyser mode), the positive pole is always made of non-impregnated LSGF. Finally, a gold grid was painted by hand with a brush from a gold paste on both the electrodes and the cell was treated at 750°C for 30 minutes a last time.

SEM images of the electrodes have been taken. Samples have been subjected to gold sputtering prior to analysis to increase conductivity.

Compatibility test between LSGF and LSGM consisted in finely grinding the two powders in a mortar (50/50 weight ratio) and in treating them at 1100°C for 8 hours. XRD analysis has been then performed.

Fuel cell measurements were performed sealing the cell on an alumina tube with a specific ceramic paste (Aremco Ceramabond 552 VFG), with the negative electrode downwards. An inner tube provided gas feeding and kept in place a thermocouple at a few millimetres from the cell surface; an O-ring-sealed electrode with a platinum wire core placed inside the inner feeding tube provided electrical contact between the

anode and the measuring instrument. A symmetric, analogous sample holder was placed on the upper positive electrode, no sealing was applied at this side since positive electrodes have been always fed only with air. In electrolyser measurements, instrumental setup was similar, except for the contacts on the electrodes: the support did not provide any accommodation for a through contact tube, so contacts were ensured by gold wires glued to each electrode with the gold paste. The gold wires passed through the ceramic sealing to the external side of the tube, where they were connected to the measuring instrument. The electrodes impedance measurements and polarization curves were collected with a Solartron Frequency Response Analyser/Electrochemical Interface (1287/1255 for fuel cell testing and 1252/1470 for electrolysis). In fuel cell measurements, negative electrodes could be fed with 5% H_2 in N_2 or pure H_2 fuel mixtures. Fuel could either be directly sent to the cell (dry) or made passing through a bubbler (wet); in these experiments wet 5% H_2, dry 5% H_2 and wet 100% H_2 fuel mixtures were used at a flow rate of 50ml/min. Air was fed to the cathode at 100ml/min. Pure LSGF cell was tested with dry 5% H_2 and wet 100% H_2 fuel mixtures only at 750°C; due to the sensitivity of LSGF to reducing atmospheres at high temperature only the less aggressive mixture was used. During electrolyser measurements, negative electrode was fed with steam in N_2 with concentrations 5% (500ml/min) and 10% (250ml/min); these flows are the minimum necessary to obtain the desired steam concentration with the available flowmeters, and in any case are surely enough to guarantee a good sweeping of the electrode surface.

4.3 Results and discussion

Results of the compatibility tests are shown in Figure 4.1. LSGF and LSGM are both perovskites and all the reflections overlap, so it is difficult to notice structural modifications because the direct reaction between them would produce a phase with the same reflections. All the reflections of the perovskites are observed, as well as a number of minor peaks relative to a $LaSrGa_3O_7$ phase that was already present in the LSGF powder. The intensity of $LaSrGa_3O_7$ peaks after the treatment at 1100°C for 8h in the compatibility test is half the one it has in simple LSGF: this result is consistent with the hypothesis that it only originates from LSGF powder (LSGF and LSGM were mixed in equal amounts). The $LaSrGa_3O_7$ phase is a common product of the

degradation of LSGM due to migration of atoms through the electrode/electrolyte interface[235], [236] and it is of particular relevance that, in the present system, this is not observed to be favoured by the thermal treatment. In general, no new signal is observed to appear.

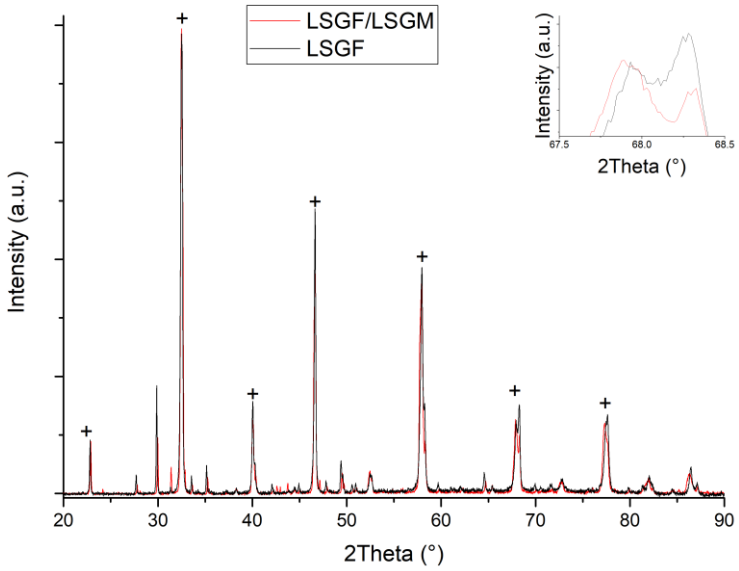

Figure 4.1 XRD pattern of calcined LSGF and LSGM powders, compared to pristine LSGF. + signs mark perovskite peaks, that are in common between LSGF and LSGM.

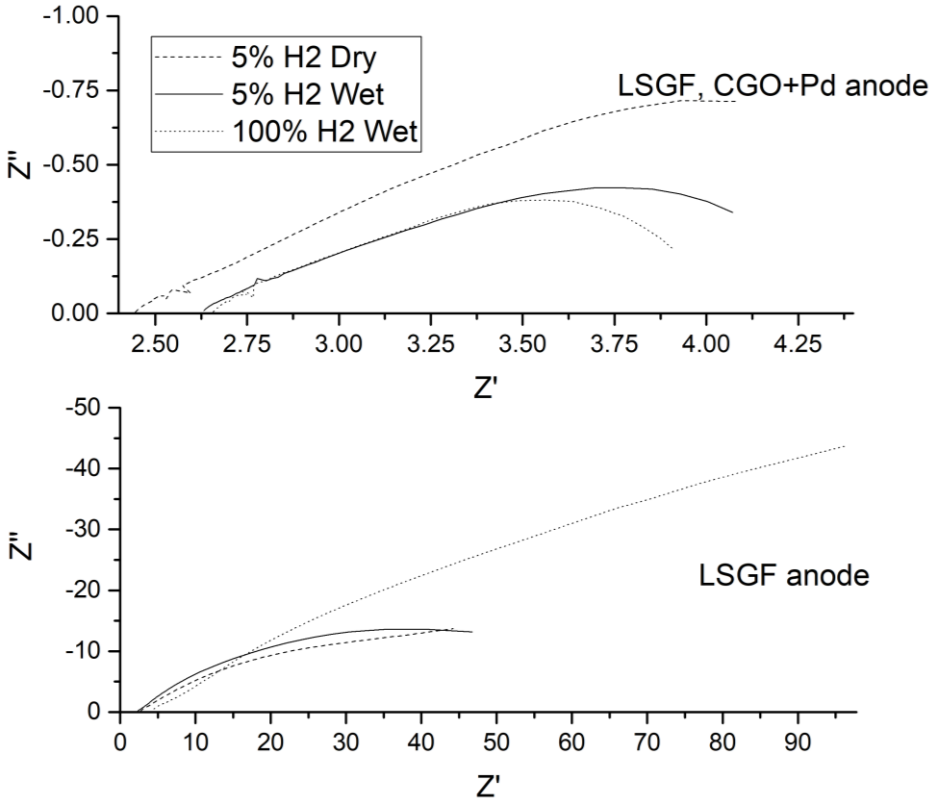

Figure 4.2 Comparison between Nyquist plots of impedance spectra of cells with LSGF anode (below) and LSGF impregnated CGO/Pd (above), with different fuels at 750°C. Electrolyte is LSGM and cathode LSGF.

The main difference between XRD patterns of LSGM and LSGF is the splitting of some LSGF peaks, due to the rhombohedral distortion. The splitting is observed also after the thermal treatment as evidenced for the peak at 68° in upper-right corner of Figure 4.1. The change in relative intensities of the two components is probably caused by the underlying LSGM reflection: it is closer to the lower-angle component of the LSGF doublet, so it unbalances the ratio between the two components in favour of the lower-angle one. The permanence of the splitting after the treatment excludes major breakdown of LSGF phase, but minor modifications cannot be excluded as they would result in reflections overlapping pristine phases' ones.

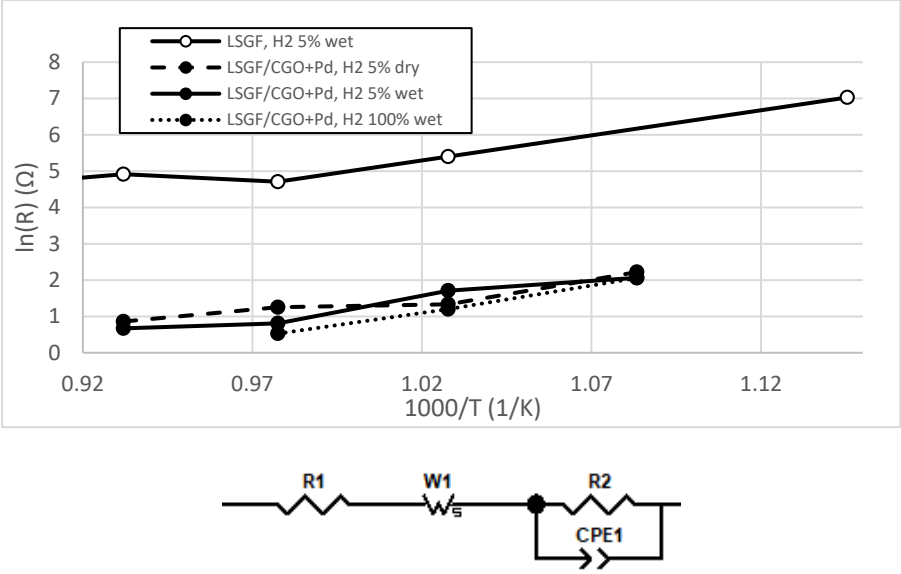

Figure 4.3 Above: Electrode resistance (Ω·cm²) of the samples as calculated from EIS. Anode is indicated in legend, electrolyte is LSGM, cathode is LSGF. Below: equivalent circuit used for ASR calculation from EIS data.

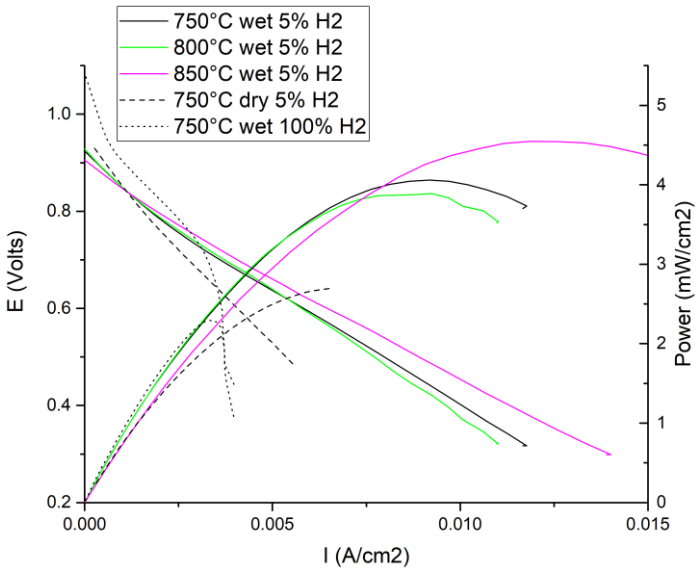

Figure 4.4 Polarization curves and power of symmetrical pure LSGF cells.

Results of test on LSGF cells indicates that the cell works, as it produces the expected polarization curves (Figure 4.4), the EIS response is compatible with fuel cell processes; the OCV, close to 0.9V for 5% H_2 (average/low value), increases to 1.05V (a good value) with pure hydrogen feeding. Nonetheless, the low power produced is not sufficient to make this cell interesting for practical applications (common cells, in fact, are able to produce hundreds of mW/cm^2). In any case, with the present work we have demonstrated the possibility to realize LSGF-based symmetrical cells. Figure 4.2 shows impedance curves with different fuels and reveals that electrode resistances are very high; at the same time ohmic resistance is around $2\text{-}3\Omega \cdot cm^2$, which can be considered a fair value given the thickness of the electrolyte, although further improvement is possible[237].

The large variations depending on fuel suggest the process can be anode (negative pole) controlled, and large part of the resistance evidenced by EIS is attributed to anode, also following some previous measurements that assigned to a LSGF cathode (positive pole) an ASR lower than $10\Omega \cdot cm^2$ (corresponding data are shown in chapter 3). Electrodes' resistance (sum of Warburg resistance and polarization resistance) is reported in Figure 4.3, with the equivalent circuit used for fitting. The CPE in parallel with a resistance accounts for charge transfer processes at the electrode. In addition, a Warburg element has been included because of some diffusion-limited processes already observed in this class of materials[225]. Only one electrode is considered in the model circuit, the other electrode can be neglected if its resistance is much smaller (i.e. if only one electrode kinetically controls the process).

In fact, for the LSGF symmetrical cell the Warburg element has proven to be redundant as a simplified Randles circuit (same circuit as shown but without Warburg element) was able to satisfyingly fit the curve. This means that there is only one limiting step, which consist in the polarization of one electrode. This process is very strongly dependent on hydrogen concentration, and behaves more efficiently if a lower hydrogen concentration is used. Some assumptions can be deduced from this. The limiting electrode is the anode, otherwise there would not be such a great variation depending on the fuel. The limiting process is surely influenced by hydrogen, given the high ASR variations depending on its concentration in the

mixture. Hydrogen oxidation on perovskite anodes is radically different from the same reaction on Ni cermets, as the phase which provides hydrogen adsorption, electrons and oxygen ions is the same and therefore there is no Triple Phase Boundary. Zhu et al.[238] have analysed impedance response of iron-based perovskite anodes under hydrogen, and concluded that the main limiting process is hydrogen dissociative adsorption. Fu et al. reached the same conclusion for $(La,Sr)(Ti,Mn)O_3$ perovskites[239]. The decreased performance of the cell with pure H_2 feeding is due to a very low limiting current, well indicated by the sudden decrease of the i/V curve and corresponding to 0.0037 A/cm^2. Following Zhu's model, such a limitation could be ascribed to a very low oxygen coverage of the surface that limits available sites for hydrogen adsorption. The further small increase of current at voltage under 0.5V was described in the same paper as a change in surface oxygen coverage induced by the decreasing potential, and confirms the proposed interpretation. At lower pH_2 (hydrogen partial pressure), a better oxygen coverage removes the strict limit observed with pure hydrogen, this implies a very high dependence of oxygen superficial sites concentration on pH_2 for LSGF.

A fuel cell can be modelled as a circuit, and this is exactly what it is done during EIS fitting. In this perspective, every part of the cell is represented by one or more circuital elements, and when an electrode is defined by a high Area Specific Resistance, it means the resistance of the circuital element associated is high. When the circuit is closed, i.e. when the cell works, the resistance of the electrodes concurs in determining the current flowing, and consequently also the power. In the case of a pure LSGF anode, we observe a very high electrode resistance (see Figure 4.2 and Figure 4.3, ASR of common anodes is around $10^{-1}\Omega\cdot cm^2$), and power output is very low, as shown in Figure 4.4. Among all the mixtures, the feeding with wet 5% H_2 gives the best results. Consistently, the performance improvement observed with only 5% of hydrogen is symptomatic of a preference of the material for less reducing environments.

Contrary to expectations, at 800°C polarization resistance is higher than at 750°C, and consequently also power output decreases. This could be caused by some degradation effect happening at the electrode: as reported in chapter 2, LSGF starts

to degrade in reducing atmospheres at 800°C, but probably this is not the primary cause of the performance decrease. Indeed, at 850°C, in a condition that should degrade LSGF more rapidly, power increases again, and the resistance decreases again. This degradation appears irreversible, as cooling at 750° does not allow full recovery of the performances previously observed. A second heating over 750°C causes another loss of performances, thus it seems it is not a simple thermal induced degradation, which would increasingly jeopardize performances at higher temperature. Instead, it is heating passing over this temperature threshold that damages the cell.

A visual analysis of the electrode after the measurements evidences an apparent melting of the painted gold collector, indeed, the surface of the electrode seemed covered by some kind of goldish glaze. The anode condition was deeply examined by means of SEM (Figure 4.8). Image B, compared to the electrode before the measurements (image A) evidences a more compact structure and a variety of new features formed on the material, probably following the LSGF deterioration expected at these high temperatures. The surface of the electrode appears covered by a thick layer coming from gold collector, somewhere (images C and D) it is still possible to observe the LSGF particles below the newly formed covering, and to appreciate the crystallization of gold that followed the cooling. A molten gold layer above the electrode surface is able to block porosities and to prevent LSGF contact with gases. If the melting happened between 750°C and 800°C, it could explain the performance decrease observed between these temperatures: each time gold melts it further degrades the cell, and further increase of temperature would improve performances of the non-passivated by gold surface, as it is observed. Nonetheless, gold normally melts over 1050°C, so an intervention of LSGF in promoting gold melting has to be supposed. At the same time, nothing similar happened on the cathode side, so probably LSGF manifests this effect only under reducing atmospheres. The XRD pattern of the electrode (Figure 4.5) is not helpful in explaining the situation, it shows a great amount of gold (* peaks) and that perovskite is still present (+ peaks), in addition the formation of a large number of oxides, resulting in all the minor peaks of the pattern, is observed. Regrettably, the crowding of minor reflections makes impossible to identify the oxide phases with precision. In any case, gold alloys or

formation of any compound with gold is excluded, and some degradation of the LSGF is confirmed.

Therefore, over 750°C two distinct degradation processes are identified: a gold melting over active electrode surface and chemical electrode LSGF degradation due to the reduction of the cations of the perovskite. The gold melting causes a sudden depletion of the power output and has been clearly observed; the LSGF degradation produces a progressive loss of performances on the medium term, and a continued measurement, not included in this work, would be needed to assess it directly.

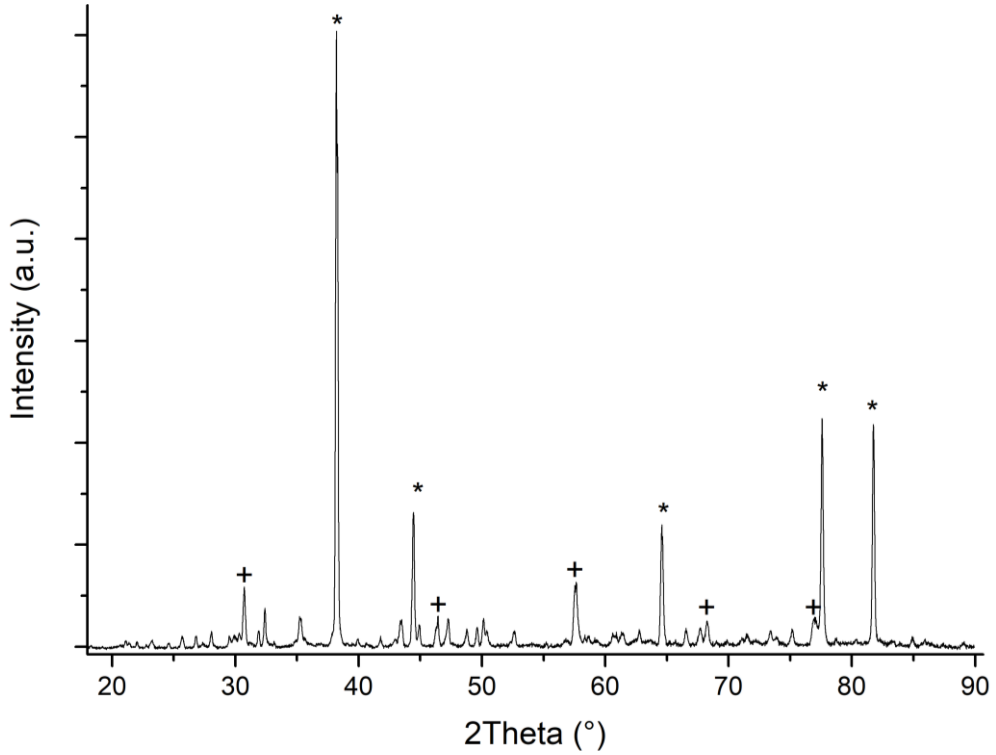

*Figure 4.5 XRD pattern of LSGF anode after test as fuel cell. *: gold reflections, +: LSGF/LSGM reflections.*

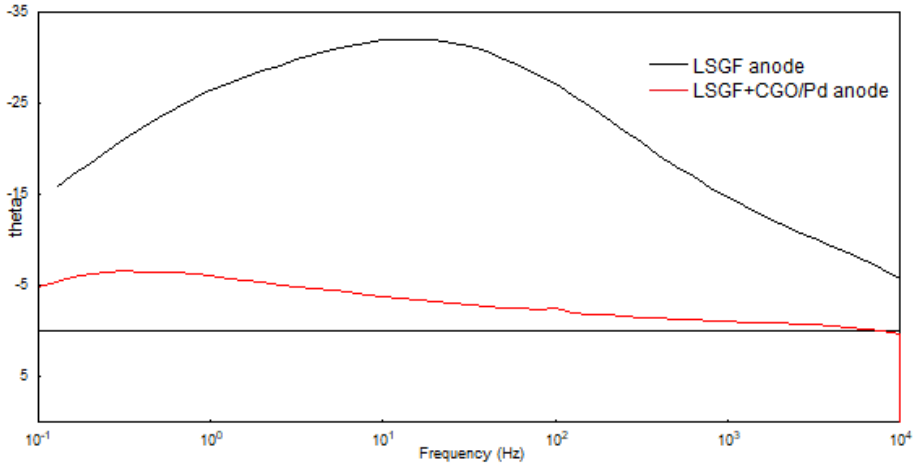

Figure 4.6 Bode plot of impedance phase comparing LSGF based fuel cells at 750°C with 5% H_2 wet fuel.

The impregnation of the anode (negative pole) with CGO/Pd decreases the electrode resistance of more than one order of magnitude (Figure 4.2 and Figure 4.3). Palladium, a noble metal, provides an excellent catalytic activity for these reaction, and the extreme improvement it brings confirms that a poor electrocatalytic performance at the anode was responsible for the low power output of the pure LSGF cell. Ohmic resistance is comparable to the pure LSGF cell: the impregnation did not affect the electrolyte or the LSGF/electrolyte interface so no variation was expected. Variations in hydrogen concentration do not affect performances at the same extent noticed for the non-impregnated cell, but there is some dependency of the ASRs from the fuel used, so anode could be still involved.

The Nyquist plot shows a Warburg-like loop, a shape different from the LSGF symmetrical cells, and the ASR is reduced as well. The shape of curve in Nyquist resembles what already observed for LSGF cathodes in terms of both shape and resistance magnitude (described in chapter 3). The fitting of these curve indicates both a limited diffusion (represented by the Warburg element) and a polarization resistance (represented by the R//CPE) concur in limiting the process, but at 750°C and 800°C a decent fitting quality can be obtained with the only Warburg element. A comparison between Bode plots of phase of the two cells (with and without CGO/Pd in the anode - see Figure 4.6) confirms limiting process for the pure LSGF and the impregnated cells are radically different: apart from the different magnitude, the apex frequency has shifted by a factor 10^{-2}, reaching the same values observed for LSGF cathodes. Altogether, this means that now the main limiting process is ionic conduction of LSGF, probably at both electrodes: ASR is similar to cathodic contribution measured in chapter 3 and the R//CPE has analogous behaviour, but the variations depending on fuel require also the participation of the anode. With pure hydrogen the resistance is lower, as observed in Figure 4.3, because the vacancies of anodic LSGF have higher concentration. The lower importance of the polarization process represented by the R//CPE element in the impregnated LSGF cell is probably linked to the duplication of the resistance related to bulk diffusion: bulk diffusion is limiting in both the electrodes, but the polarization process is relevant only at the cathode, so its relative contribution to total resistance is reduced. Problems highlighted in chapter 3, relative to the discrimination of the two diffusion and

polarization contribution are still present, and have not been solved; also, the high capacitance of the CPE is still observed. The complete disappearance of the hydrogen dissociative adsorption confirms LSGF is not involved in this process, which is carried out by impregnated palladium.

A posteriori, the initial assumption to consider only one electrode during fitting with model circuit has proven to be correct: non-impregnated cell is anode limited, while impregnated cell is probably limited by the same process happening at both electrodes, that is modelled by only one Warburg element. The cell power output reaches 60-70mWcm^{-2}, with only little dependence on the fuel (Figure 4.7). The OCV is very good, being extremely close to the thermodynamic potential in particular with pure H_2 feeding, this suggests the cell probably could be able to reach good efficiencies.

Interestingly, the detrimental effects of heating over 750°C observed with the pure-LSGF cells does not affect this cell: it seems that CGO was able to coat and to prevent contact between LSGF and gold, and this could be an ulterior confirmation that the problem arose due to the interaction between these two phases. CGO avoids also an extensive contact between LSGF and hydrogen fuel potentially allowing operation at temperatures higher than 750°C, but it is not clear at this point if CGO effectively passivates all the LSGF surface. It must be underlined also that the influence of the atmosphere does not necessarily mean that LSGF is exposed, as there is an equilibrium between LSGF and CGO, if the latter is reduced it could drain LSGF's oxygen as well. However, if the passivation is not completely effective, some contact between LSGF and hydrogen happens and the certain outcome is a medium/long term degradation of the electrode. To precisely assess this matter, appropriate stability test should be performed.

On the basis of the shown results, a precautionary temperature of 750°C must be considered as the maximum allowed; this limit, in any case, is well above the safe temperature to avoid gallium evaporation from LSGM, so anode stability should not be an issue. It becomes gradually clearer that the materials under examination are promising, but must be dedicated to Intermediate Temperature operation and should be never heated over 700°C, at least when in fuel cell mode. The good coverage of the

impregnated in CGO is easily visible in SEM images (Figure 4.8 E), CGO coated all the surface of the LSGF particles forming a smooth layer above them. In Figure 4.8 F it is possible also to observe the active palladium nanoparticles and to measure their size, that is around few tens of nanometres. The palladium dispersion is optimal, as well as its stabilization by the CGO substrate.

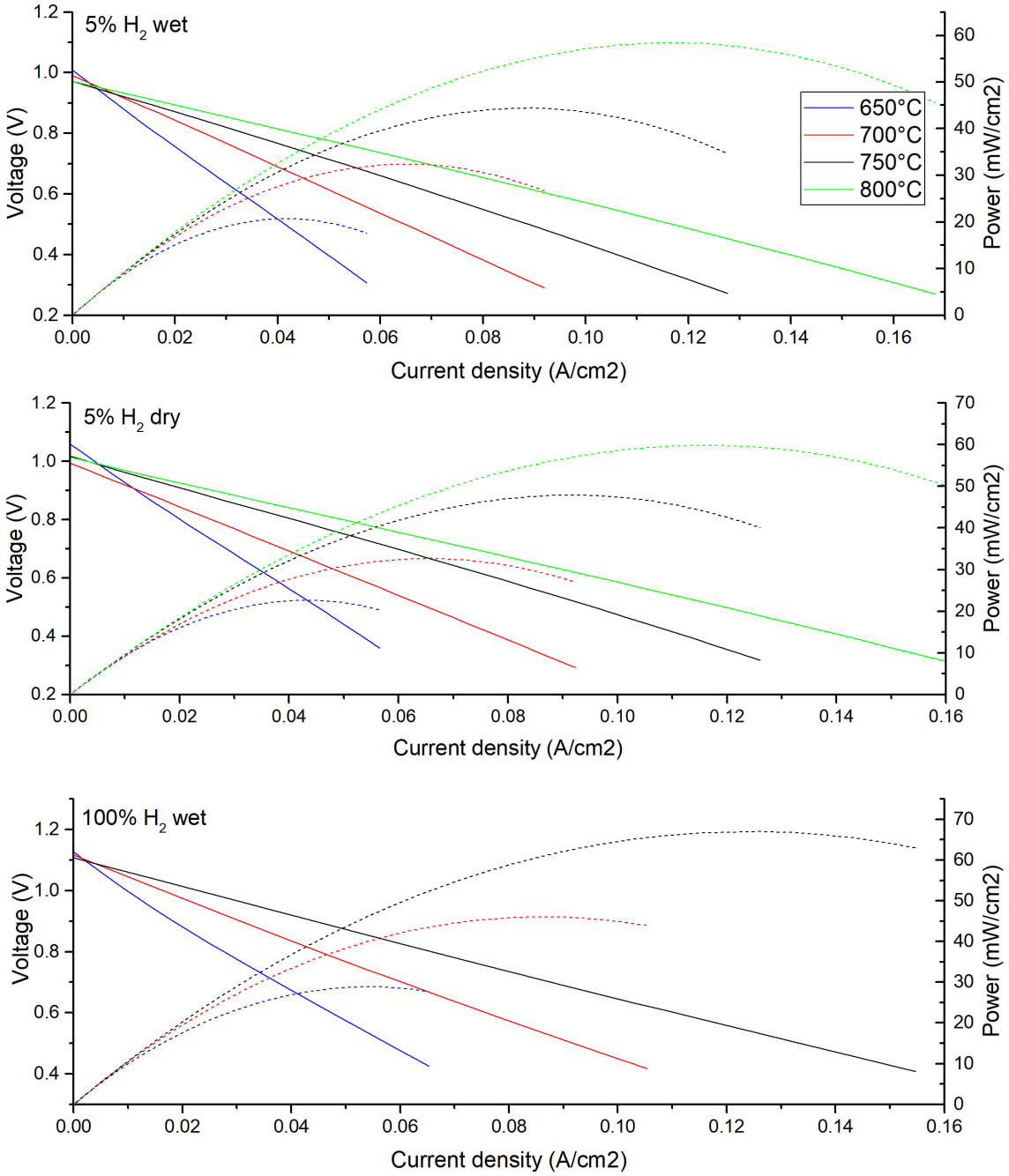

Figure 4.7 Polarization curves and power of fuel cell with impregnated anode with different fuels. Above: wet 5% H_2, in the middle: dry 5% H_2, below: wet 100% H_2.

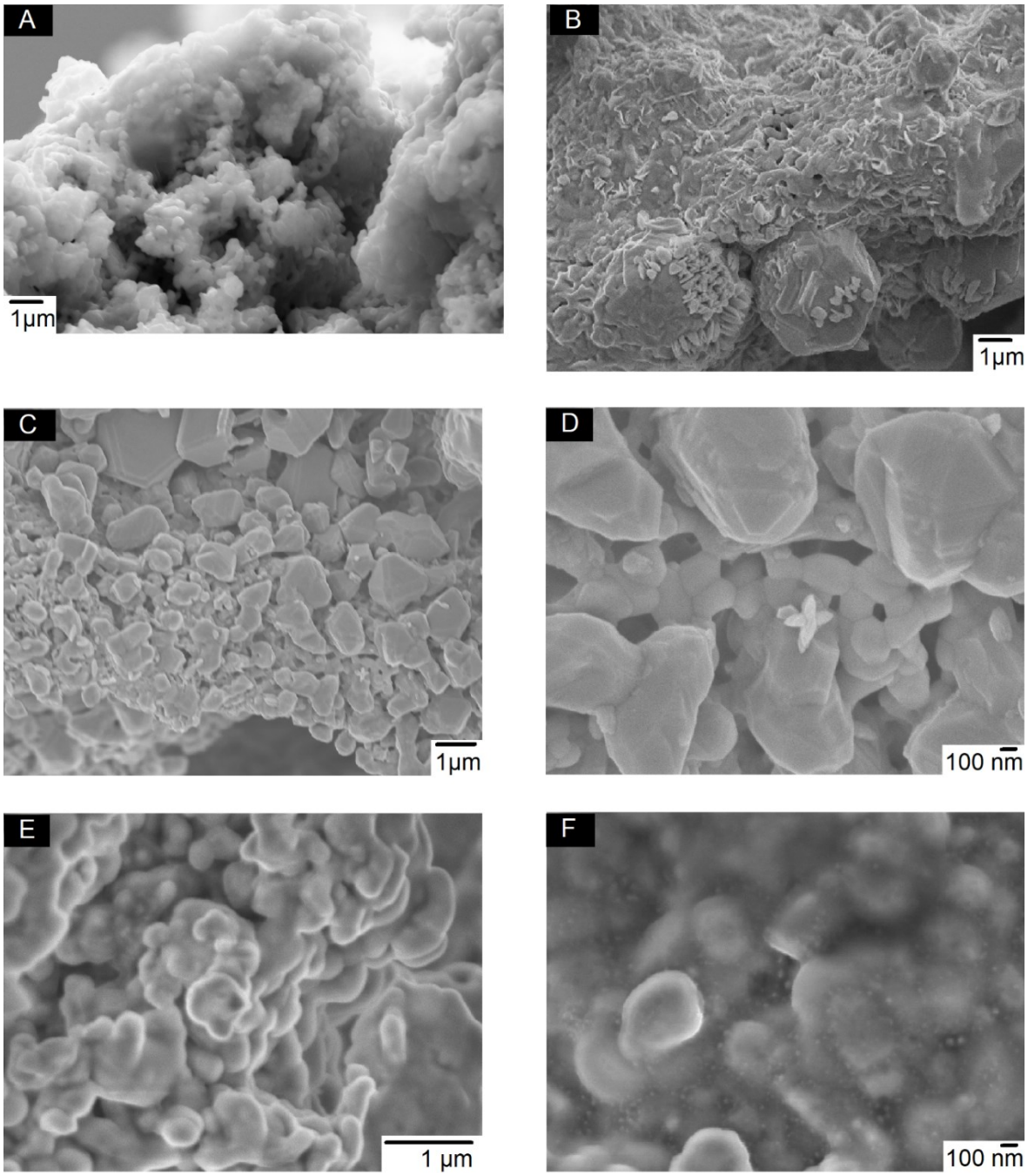

Figure 4.8 SEM images of tested cells. A: cross section of a LSGF electrode. B: cross section of LSGF anode after test as fuel cell. C and D: surface of LSGF anode after test as fuel cell. E and F: surface of a LSGF electrode impregnated with CGO/Pd.

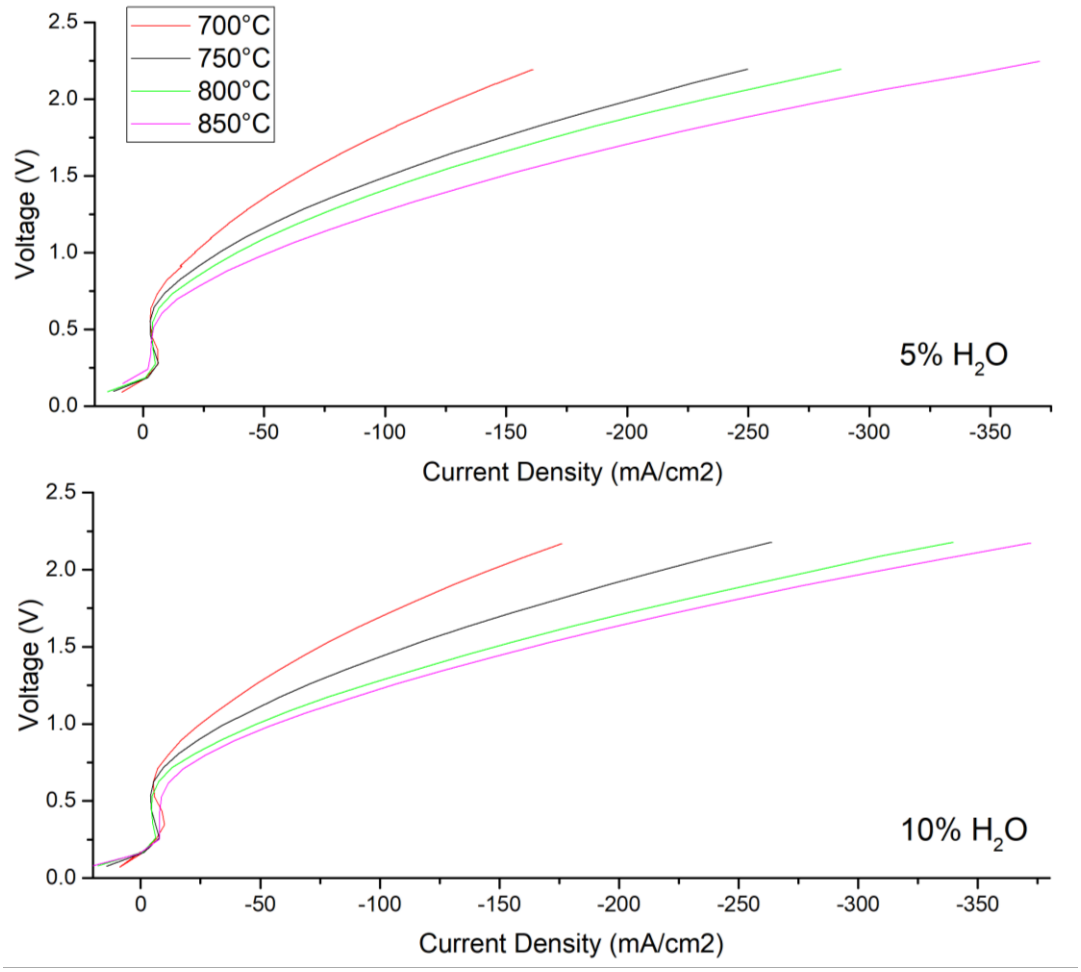

Figure 4.9 Polarization curves of cell with impregnated negative electrode as electrolyser at different temperatures. Electrode is fed with 5% steam in N_2 (above) and 10% steam in N_2 (below).

Polarization curves of the CGO/Pd impregnated cell in electrolysis mode are shown in Figure 4.9; they have in general an "S" shape and maintain it throughout the sampled temperature interval. Overall performance is slightly lower than state of the art materials and comparable with similar materials[240], and in general is fair considering the thick electrolyte employed. Curves begin at OCV with a very steep slope that continuously increases until 0.5V even reversing curve direction, at the point that between 0.3V and 0.5V an increase of voltage corresponds to a decrease of the measured current. Then, over 0.7V slope changes abruptly towards a higher production of current; temperature seems to have no influence on this onset potential. No other transition is observed in the sampled interval.

Impedance spectra show huge polarization resistances at potentials close to OCV, then they suddenly decrease between 0.5V and 1V, the same voltage that induces polarization curves' slope change. Polarization resistance at 800°C is around 2.5Ω·cm²

with 1.0V and 0.6Ω·cm² with 1.5V, and at 850°C is around 2Ω·cm² with 1.0V and 0.4Ω·cm² with 1.5V. There is only little variation between 5% or 10% H_2O feeding. Ohmic resistance trend is interesting: at OCV is at its lowest, and it increases with increasing voltage until 0.5V. A further increase in potential then decreases also ohmic resistance, although the variation has not the same magnitude of the polarization resistance's one.

The behaviour of this cell can be related to some chemical transition leading the cell to activate only at a potential higher than 0.7V[241], the decrease of resistance (polarization and ohmic) and the increase of the current are both coherent with this explanation. Conversely, up to 0.7V some highly resistive phenomenon prevents an efficient electrolyzation of steam. Figure 4.11 shows a comparison between a polarization curve of a cell as the one previously described and a second electrolyser with a pure-LSGF cathode at 600°C, the difference in the examined temperatures from previously shown data is due to impossibility to complete the respective sets of experiments. Apart from poor activity of the cell without impregnation, it is relevant that the activation happens at the same potential, this is even more evident looking at the second derivatives of the I vs V curves: they both cross zero at 0.7V, and this means that the change of slope (or, in other terms, the activation of the electrolysis process) happens at the very same point. This proves again that activation is not temperature dependent, and that impregnated CGO/Pd is not involved. At the cathode (negative pole), LSGF has only a secondary role, providing only mechanical support and connection between the electrolyte and the active phase, so probably the cause of the high resistance at potentials close to OCV could be related to some phenomenon happening at the anode (positive pole).

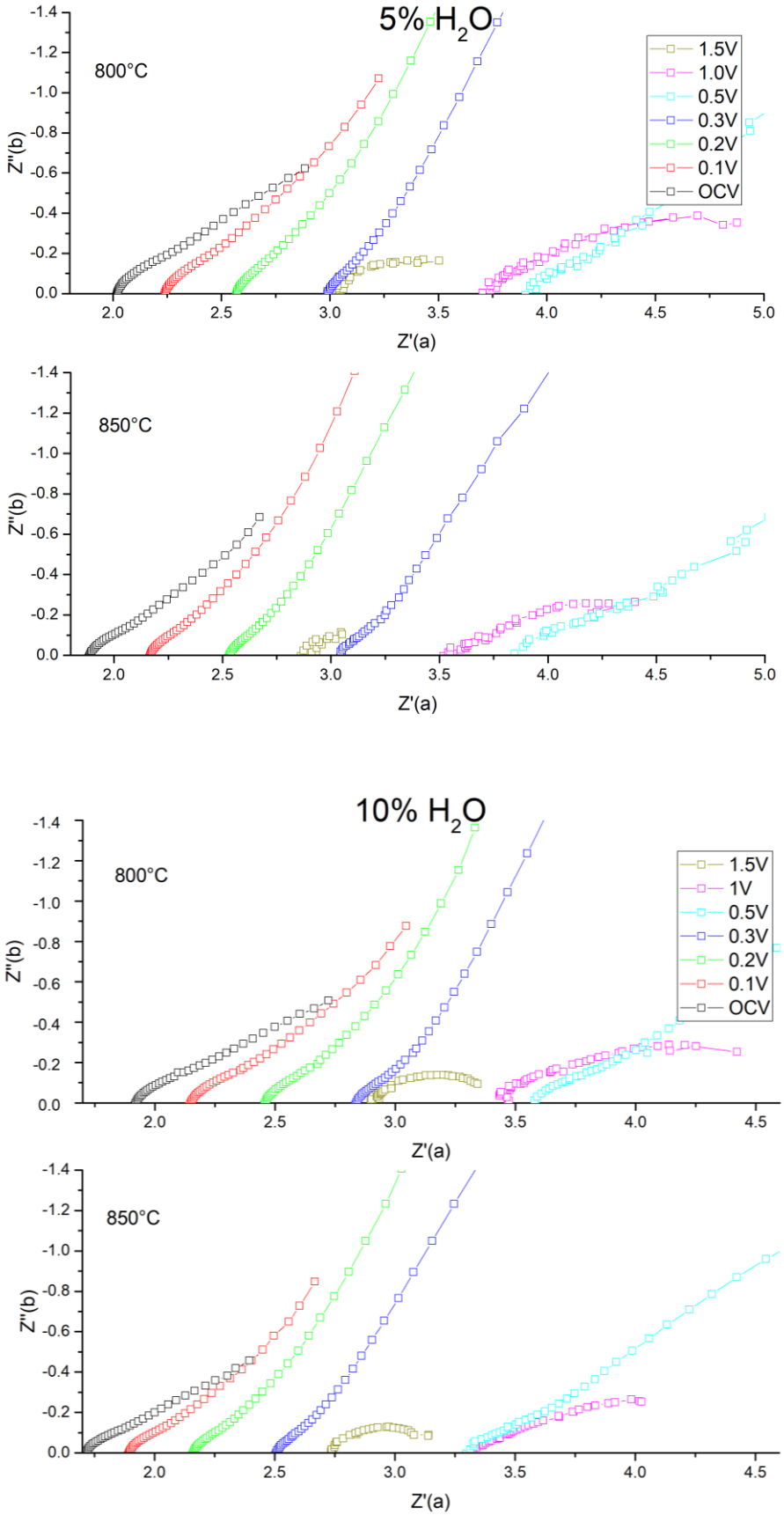

Figure 4.10 Impedances in electrolysis mode at 800°C (above) and 850°C (below) with 5% (left) and 10% steam (right).

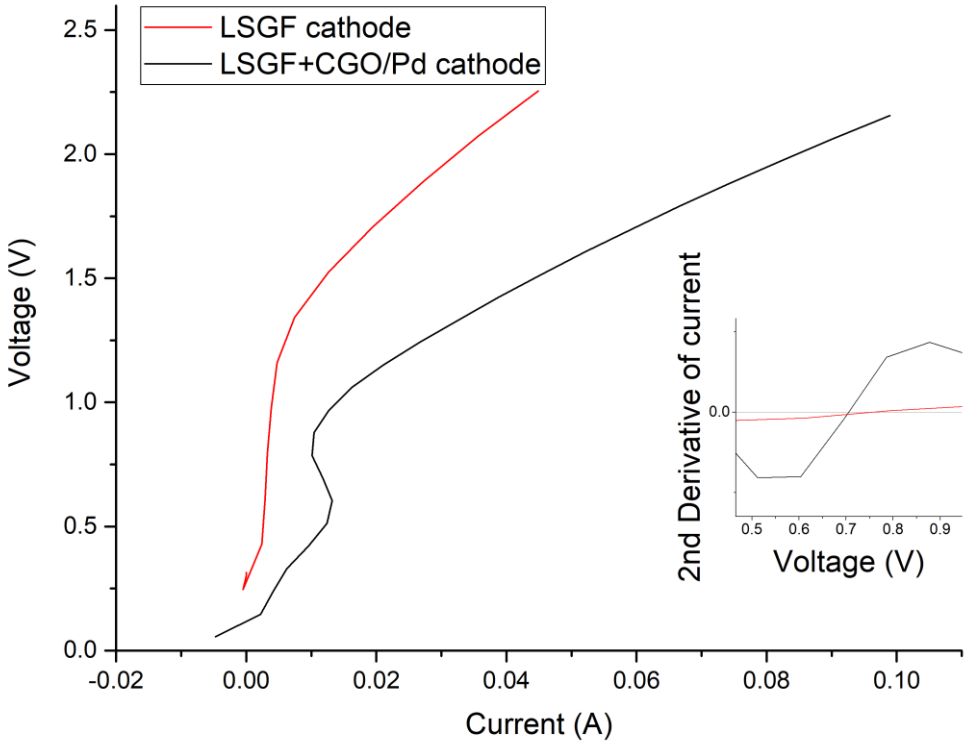

Figure 4.11 Comparison between polarization curves at 600°C of electrolysers with anode LSGF, electrolyte LSGM and cathode as indicated in legend, cathode is fed with 50% H_2O in N_2 and anode is fed with air.

4.4 Conclusions

In this work a symmetrical all-perovskite solid oxide fuel cell has been tested, and some critical flaw has been detected at the anodic compartment; in particular, a very high anodic polarization resistance led to a low power output. In addition, LSGF in reducing environment promoted gold contacts melting hence covering its own active surface; this curious effect compromises the anode in a short time, and probably deserves more attention as, to our knowledge, it has never been reported before. In order to enhance electrocatalytic activity and to avoid contact between LSGF and gold, the anode was impregnated with CGO and nanoparticles of Pd, and this allowed to reach both the prefixed goals. Notably, after impregnation power density with anode impregnation was improved from 4mW/cm² to 60mW/cm², limited this time mainly by cathode performance. The CGO layer was able to avoid contact between LSGF and gold hence preventing gold melting, but it is unclear if it is able to passivate LSGF towards reduction in the long term. The same cell with an impregnated negative electrode was then tested as steam electrolyser in a non-reducing environment and promising performances were observed. A high resistance mechanism was found to

impede electrolyser operativity under 0.7V, this was also found to be independent on temperature, Pd/CGO presence and cathodic gas composition. More investigation is required to precisely assess the cause of this resistive phenomenon, but data at our disposal suggest the anode (positive pole) is probably involved.

5 Highly homogeneous SOFCs with LSGF based electrodes

LSGF + MnO_x was disappointing as cathode, but as anode, not at all

EIS tests on LSGF + MnO_x anodes

The fabrication of a cell with electrolyte LSGM and LSGF + MnO_x/FeO_x

Fuel cell tests in a variety of different fuels

5.1 Introduction

Nickel is the most used catalyst for SOFC anodes, and the performances it allows to reach are very good. Nonetheless, as mentioned in the introduction, it implies some problems that make its substitution desirable, if other candidates are found. Unfortunately, it is not easy to find a good substitute for nickel, because of the several different features that are required at the same time. The anode material must be stable under reducing environment at high temperatures, which is easy for metallic phases that already have a 0 oxidation state, but poses more problems when oxides are used, as frequently required for advanced functional materials design. A good anode must have also a good catalytic activity, a feature that often conflicts with stability, and must be cheap. Research on good substitutes for nickel is currently ongoing, and several different materials have been proposed[130]. Until now, nickel is still the best choice, because of its extreme cheapness and its high activity, but its presence in SOFCs is widely considered as one of the limiting factors of the technology. Nickel obsolescence is particularly evident when planning the use of carbon based fuels, which are completely incompatible with Ni because the catalyst quickly passivates itself with a layer of carbon[127]. Moreover, nickel is highly vulnerable to sulphur poisoning[242], and sulphur is often present as impurity in fuels; so the use of nickel implies expensive purification of the fuel before use.

The approach proposed here is the same outlined in the introduction: the combination of a MIEC substrate with a catalytically active phase. The

nanocomposite proposed as anode material is LSGF + MnO_x, which was already studied in chapter 3, and ruled out as a possible cathode material. For this reason, we refer to chapter 3 for all the information about the synthesis and the characterization of LSGF + MnO_x. To study the performance of LSGF + MnO_x as anode, a cell has been prepared with thick LSGM electrolyte support, LSGF + MnO_x anode and commercial LSCF cathode (the latter was chosen in order to minimise cathode contribution to impedance measurement). This cell was tested by means of EIS (Electrochemical Impedance Spectroscopy) at different temperatures, under hydrogen flows characterized by different hydrogen concentration. Then, complete fuel cells entirely with La Sr Ga based materials have been prepared, on a LSGM thick electrolyte; anode was LSGF + MnO_x nanocomposite, and cathode the LSGF + FeO_x nanocomposite. Both the electrodes are original materials firstly investigated in this work, and have never been used in SOFC technology before. As explained in chapter 4, very similar chemical composition between the electrolyte and the electrodes should allow a great long-term stability, thus avoiding the formation of insulating phases at the interfaces. The fabricated cells have been tested with hydrogen, methane and propane as fuels, and their impedance spectra and polarization curves have been recorded.

5.2 Experimental

The cells presented in this work are all electrolyte supported on LSGM thick electrolyte, prepared pressing a LSGM powder (commercial LSGM8282, Treibacher) into pellets and then firing them at 1500°C for 10 hours, thickness of the pellet is around 1.2 mm, 2 cm is the diameter. The LSGF + MnO_x powder used for anodes and the LSGF + FeO_x powder used for cathode of all-LSG cells were synthesized via a wet chemistry solid-combustion route, with the same procedure explained in chapter 3. LSCF used in EIS measurements on LSGF + MnO_x is commercial (Treibacher). All the electrodes were prepared via slurry coating. Inks were prepared from the respective powder by adding a proper amount of vehicle and thinner. Then inks are spread in two layers with a razor blade over the sintered electrolyte, a mask made of adhesive tape was used to obtain electrodes with circular shape. LSGF + MnO_x/LSCF cells were deposited from inks prepared only by adding α-terpineol, electrodes have areas 0.1256 cm^2. LSGF + MnO_x/LSGF + FeO_x cells were deposited from inks prepared with vehicle

V400 and thinner 404 (commercial, ESL), electrodes had area 1.074 cm^2. LSGF + MnO_x and LSGF electrodes were fired at 1100° for 6 hours, and LSGF + FeO_x cathodes at 1000°C for 6 hours.

For testing, anodes were sealed to an alumina tube with Flexitallic Thermiculite gaskets. An inner pipe close to the anode surface provided fuel feeding. A thermocouple was placed close to the anode surface to monitor directly cell temperature. The cathode was not sealed, and left exposed to air.

Cell for EIS tests of LSGF + MnO_x anode has LSCF cathode. The anode was fed with a H_2 and inert mixture with concentration ranging from 1% to 50%. The studied temperature range was from 550°C to 750°C, with sampling every 50°C. Electrochemical Impedance data were collected with an Autolab PGSTAT302N and fitted with an appropriate model circuit to examine the observed processes. ASR (Area Specific Resistance) were derived from fitting.

The complete La Sr Ga based cells, with LSGF + MnO_x anode and LSGF + FeO_x cathode was tested in hydrogen, then propane, then hydrogen again to verify if propane was beneficial to the cell, then methane and finally hydrogen a last time. During the tests, EIS spectra and polarization curves were taken with an AMEL 7050 potentiostat and an AMEL 7200 frequency response analyser. Finally, the short-term stability under diluted hydrogen has been assessed after one night of operation.

5.3 Results and discussion

5.3.1 Cell with LSGF + MnO_x anode and LSCF cathode

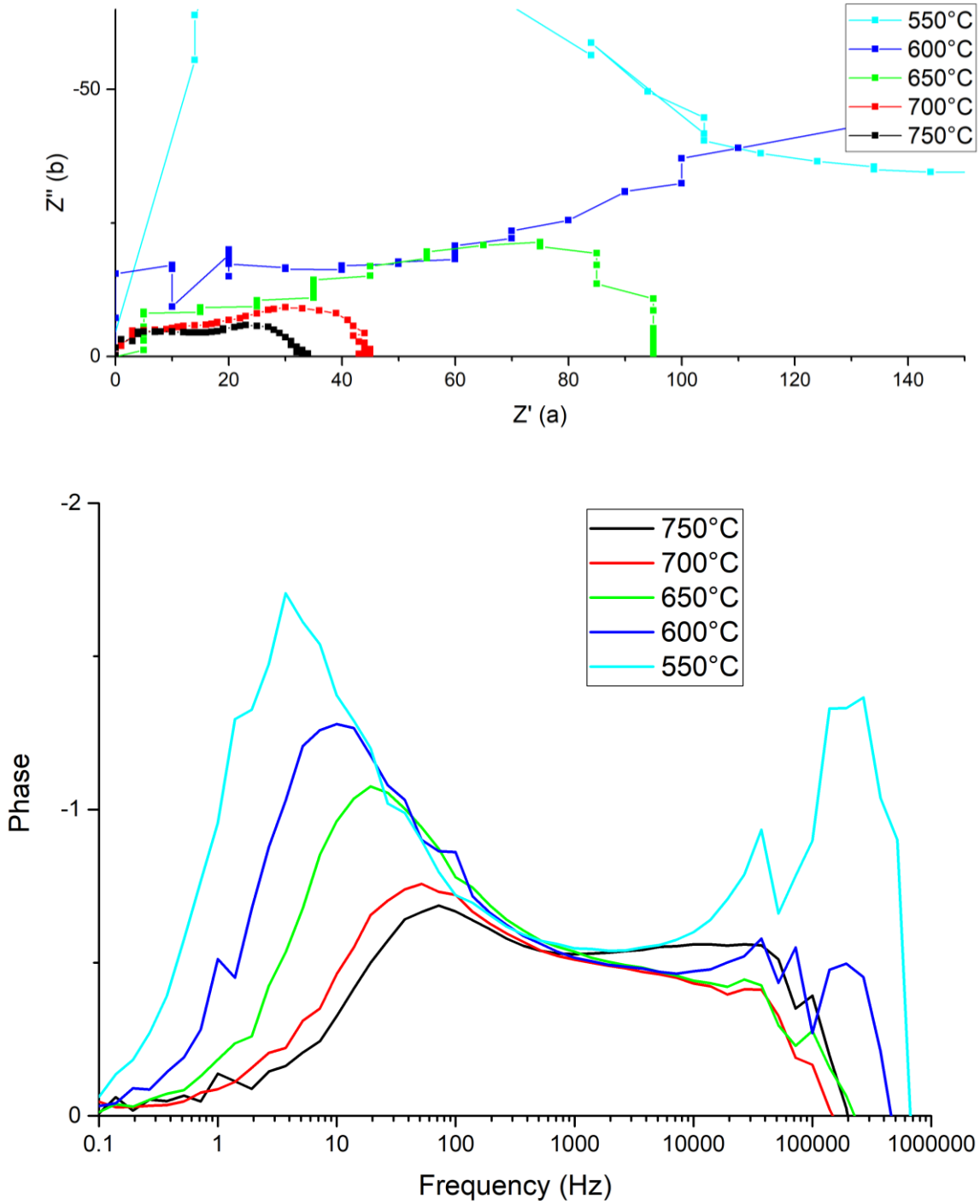

Figure 5.1 Cell electrolyte LSGM, cathode LSCF and anode LSGF + MnO_x. Plots of impedance with 40% hydrogen concentration at the anode at different temperatures. Above: Nyquist plot. Below: Bode phase plot.

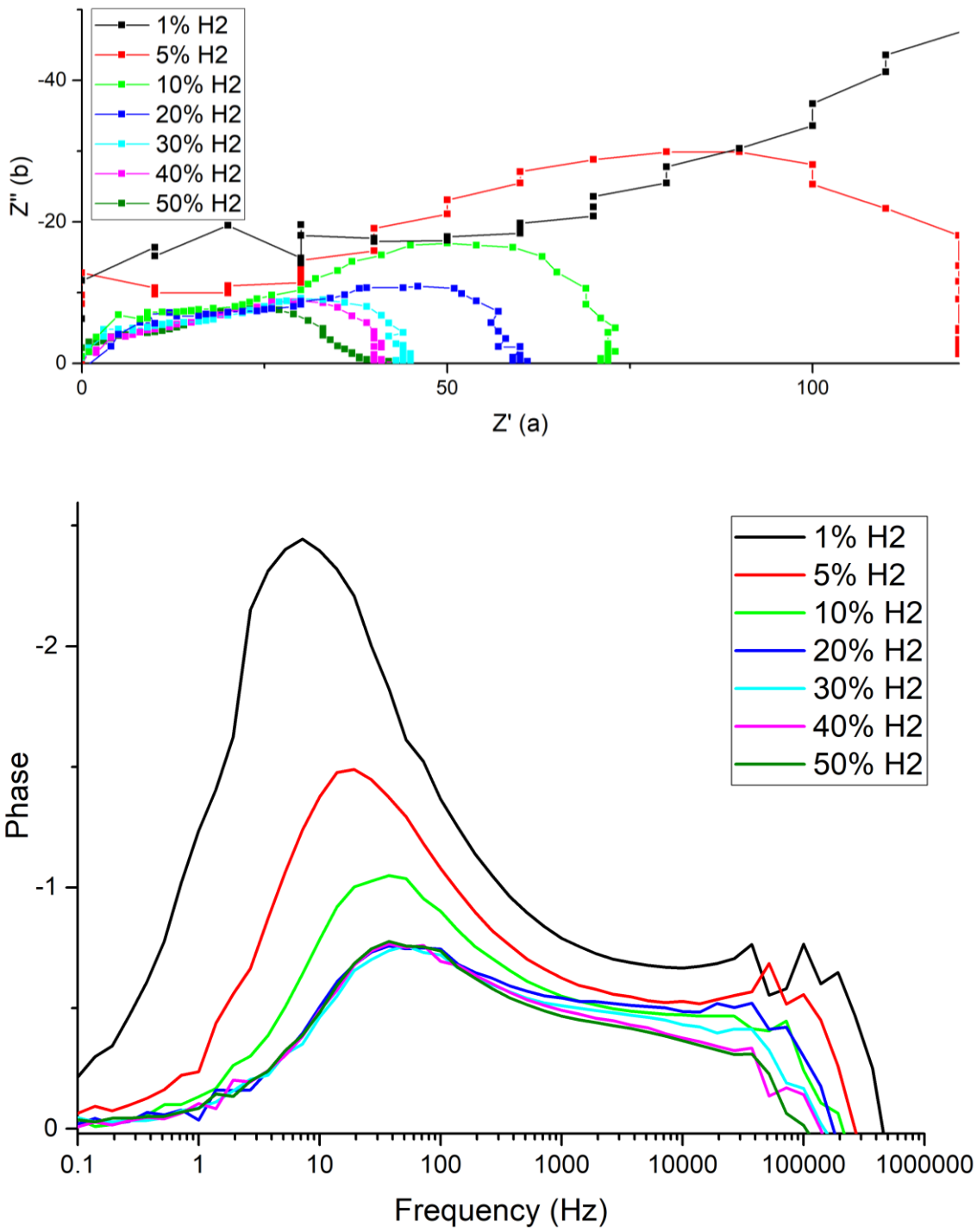

Figure 5.2 Cell electrolyte LSGM, cathode LSCF and anode LSGF + MnO_x. Plots of impedance at 700°C with different hydrogen concentrations at the anode. Above: Nyquist plot. Below: Bode phase plot

The EIS response for the cell anode LSGF + MnO_x cathode LSCF is shown in Figure 5.1, where variations depending on temperature are evidenced, and Figure 5.2, which is focused on hydrogen concentration. Two processes are well distinguishable, named High Frequency (HF) and Low Frequency (LF) depending on their characteristic

frequencies. Both processes are well fitted by a resistance in parallel with a CPE, the CPE is necessary to take in account the depression of the semicircles, in particular, the HF process is markedly depressed. Both of the processes are observed to be influenced by pH_2, so they are related with the anodic compartment. This was expected, as LSCF has negligible ASR compared to the arcs observed in these measurements, thus its arcs are hidden under the ones of the anode. At lower temperatures and at a lower pH_2 some scattering of the signals is noticeable. The behaviour of the HF process is not completely linear. With increasing temperature, it shifts towards lower frequencies and is more and more depressed in a tendency to disappear in the adjacent peak. But at 750°C its peak phase increases again, with the relaxation frequency continuing the trend towards lower frequencies. With increases of pH_2, again the frequency decreases. The prominence of the peak decreases too, apart 20% H_2 which is higher than 10% H_2. The capacitance of this process is around 10^{-6} – 10^{-7}F/cm², close to the double layer-capacitance[243], the process is thermally activated, and its apex frequency is between 10^4-10^5 Hz; all of this matches with a charge transfer process at the anode electrolyte interface[239]. The dependence on pH_2 is not always observed for this process, and when it is, it is in general associated to chemical modifications on the interface induced by pH_2 and local formation of new phases[95]. The LF process is thermally activated, favoured by a higher pH_2, and its relaxation frequency increases with temperature and pH_2. All of these features match for the dissociative adsorption of hydrogen[238], which is favoured by both temperature and high pressure of hydrogen. This process was already described in chapter 4 as it was already observed in an anode made of pure LSGF, but in this case the resistance associated to it is greatly reduced. Since it is not entirely clear how the surface of LSGF + MnO_x is (see the discussion in chapter 3), it is difficult to define precisely how this material works. In any case, manganese is certainly involved. The great decrease of the resistance means the sites responsible for the hydrogen adsorption differ from those of pure LSGF, and are probably based on manganese. ASR values obtained by fitting are shown in Figure 5.3 as logarithms. Results regarding resistance at lower temperatures are not shown in Figure because of an excessive scattering of data at lower frequencies, that makes impossible to obtain accurate calculations from fittings. The plots are linear up to 700°C, but for all the

concentrations of hydrogen, at 750°C, the pendency changes. This indicates a noticeable variation in the activation energy towards lower values, from 117kJ/mol below 750°C to 46kJ/mol above that temperature. Such changes are often correlated with chemical modification of the catalyst, for example phase transitions[244], or radical changes in limiting steps of the process, and it could be interesting to find if it is possible to extend the low activation energy regime also to lower temperatures.

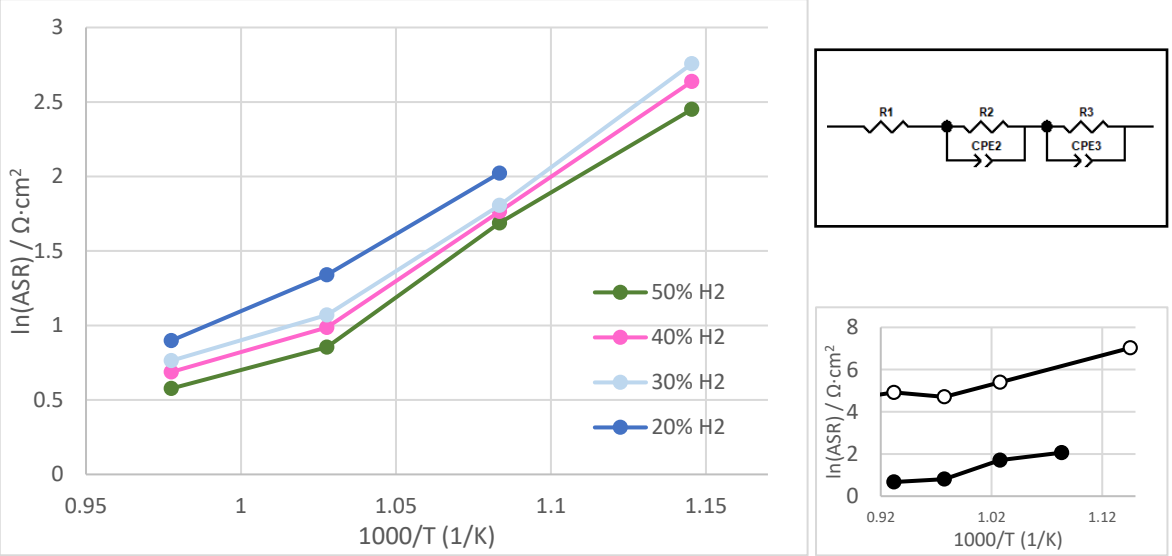

Figure 5.3 Left: model circuit used for data interpretation. Right, above: Arrhenius plot of ASR variation depending on temperature and concentration of hydrogen. Right below: ASR of cell with both electrodes of pure LSGF (empty circles) and with cathode of pure LSGF and anode of LSGF impregnated with CGO/Pd (full circles).

5.3.2 Cell with LSGF + MnO_x anode and LSGF + FeO_x cathode

Compared to the pure LSGF anode, performances with MnO_x impregnated anodes are greatly improved. As shown in Figure 5.4, the cell power output is more than 10 times the one of the cell with pure LSGF anode, and is similar to one of the cell with anode impregnated with palladium. The cell with palladium impregnated anode had a pure LSGF cathode and was limited mainly by it, while the cell studied in this chapter has a cathode impregnated with FeO_x, which, according to chapter 3, has an ASR only 30% of LSGF's one. So, theoretically this cell should be able to obtain better performances because cathode is not as limiting as in the previous case.

Though, this does not give the whole picture, because the processes evidenced by EIS (Figure 5.5) are different from both the pure LSGF anode and the LSGF impregnated Pd cells. At higher frequencies a quite large arc appears, it can be related to charge transfer processes at the electrolyte/electrode interface. When current

flows, the resistance associated at both the arcs increases, this behaviour is in general related to problems at the interface electrode/electrolyte, and suggests performance can be enhanced improving this contact.

The low frequency arc is originated by cathode, and it is the Warburg-like loop well described in chapter 3. This arc is related only to cathode: it is observed that with changes of gas flows at the anode it is not altered, and cathode processes are not affected by changes of flows at the other electrode. The high frequency arc, on the contrary, is reduced if higher gas flows at the anode are used. The observed limiting processes are different from both the pure LSGF cell and the cell with Pd impregnated LSGF anode. The impedance spectrum of the cell with pure LSGF anode showed a very large resistance associated to the hydrogen dissociative adsorption, a feature that is not observed at all here. This is a considerable achievement, it means that with the addition of a very small amount of manganese we were able to completely change the activity of the material. The impregnated moles of manganese atoms are 10% compared to the moles of perovskite, but only 5% compared to the amount of cations (a perovskite is ABO_3, so each mole of it contains two moles of A and B cations); nonetheless, the behaviour of the material has changed so much, that now it is the interfacial charge transfer that limits the performance of the anode. The cell with Pd impregnated LSGF was co-limited by the anode and the cathode. The cathode contribution, the Warburg-like loop, is still present at the low frequency arc of the curve, but the anode contribution is not observed (the low frequency arc has been related only to cathode). This limitation was related to bulk ionic conduction in the material, and its disappearance is a clue that hydrogen oxidation is carried out differently than pure LSGF.

In O_2-TPD measurements shown in chapter 3, a decrease of the amount of vacancies in LSGF impregnated with manganese was described, hence ionic conductivity is not improved for sure. The fact that ionic conduction is not limiting, albeit it has probably worsened, suggests a different mechanism is at work, for whom the ionic conductivity is not as important as in pure LSGF.

Compared to the EIS results of the LSGF + MnO_x/LSCF described previously, the lack of the dissociative adsorption is surprising, because the anode fabrication

treatments are the same. It is possible that this difference is caused by some parameter that was not accounted in the present analysis: data in chapter 3 indicate that LSGF + MnO_x composite is very susceptible, also the XRD reflections change swiftly and unpredictably with small temperature variations, so this anode can be prone to such a behaviour.

Unfortunately, after one hour of operation the maximum power decreases from 70mW/cm² to 35mW/cm². The OCV is very good, around 1.10V, and it appears not to be affected by the decrease of performances from the first to the second hour. After the testing of several cells based on LSGF, it can be easily noticed that optimal OCVs have always been recorded, it is probably a feature of this material the ability to carry on this reaction with only minimal voltage losses. This is promising, as cells with high OCVs tend to be more efficient.

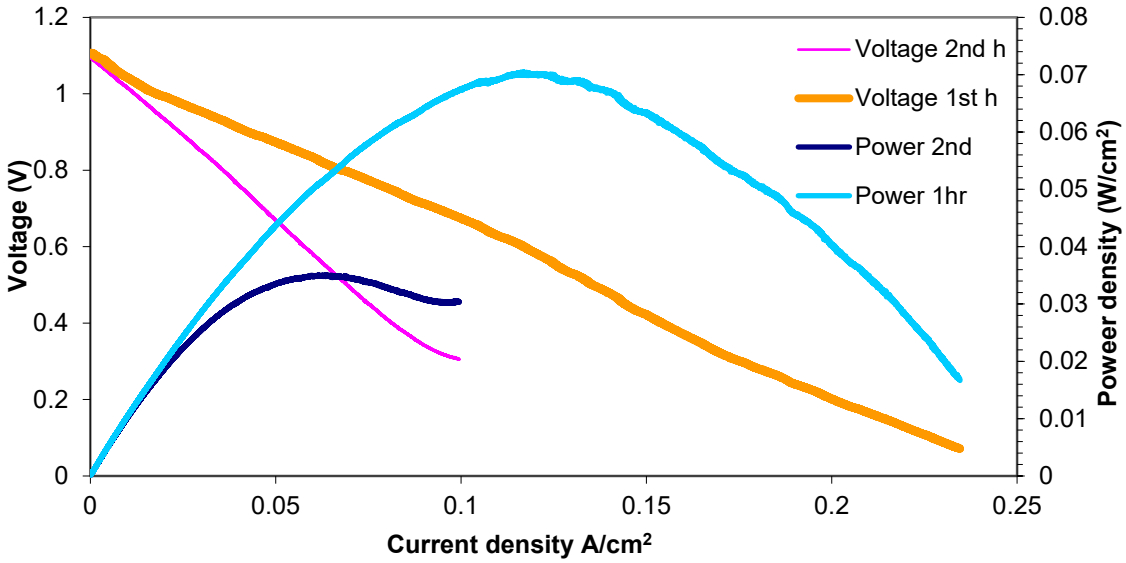

Figure 5.4 Cell polarization curves after switch-on (1st hour) and after 1 hour of operation (2nd hour) at 744°C. Anode is fed with pure H_2, 53 sccm.

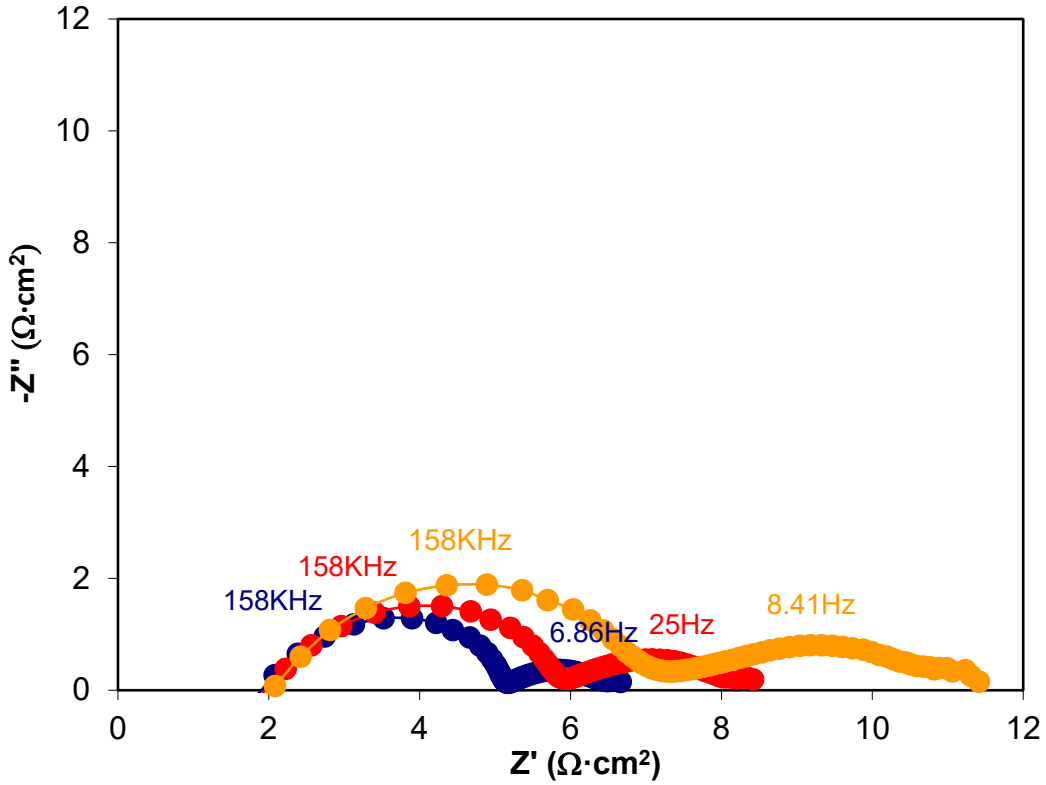

Figure 5.5 Nyquist plots of LSGF + MnO_x / LSGF + FeO_x cell at 744°C, anode fed with pure hydrogen, flow 53 sccm. Blue = OCV, Red = 0.6 V, Yellow = 0 V.

Feeding of the cell with propane gives very interesting results. As shown in Figure 5.6, current and power increase, compared to hydrogen feeding, and an output of 67mW/cm² is reached again. The OCV has even increased from hydrogen feeding, and has reached 1.13 V. No short-term performance depletion is observed when propane is used as a fuel. Impedance spectra (Figure 5.7) are composed of the same arcs of hydrogen feeding, plus a large signal at very low frequencies, which stands for a high gas-diffusion resistance[245]. Its magnitude suggests that a better optimization of porosity of the electrode could greatly improve the performances with this fuel. Performances under propane are interesting because the difficulty to use hydrocarbon based fuel with common nickel based anodes is one of the biggest flaws of current SOFCs[246]. The finding of an efficient anode material, able to work smoothly also with carbon containing fuel, would open considerable opportunities for the SOFC market. This result suggests LSGF + MnO_x could be an interesting candidate for this task.

Propane does not only induce good performances, but also proves to be beneficial for the electrode. When hydrogen is fed again at the cell, the maximum power output

is more than doubled, and reached 75mW/cm² at 0.55V. Comparing between impedance spectra before and after propane, it is evident that the change is mainly due to the high frequency component, that was related to electrode/electrolyte interfacial charge transfer, while the low frequency arc is unaffected (Figure 5.8). As previously explained, changes in interfacial charge transfer depending on the atmosphere are possible; they often have been related to the local formation at the interface of specific phases, able to impede, in case they are insulators, the passage of O^{2-} ions from the anode to the electrolyte. It is possible that something similar has happened also in this case, but specific analysis on the interface should be carried out to assess it. The cause of the improved connection between anode and electrolyte is reversible (and this is coherent with the formation of new phases and interface) as this effect is partially lost after some hours of operation. As it is shown in Figure 5.9, the relative impedance arc regains a larger magnitude, the maximum power is 55mW/cm². Again, the low frequency arc is not affected.

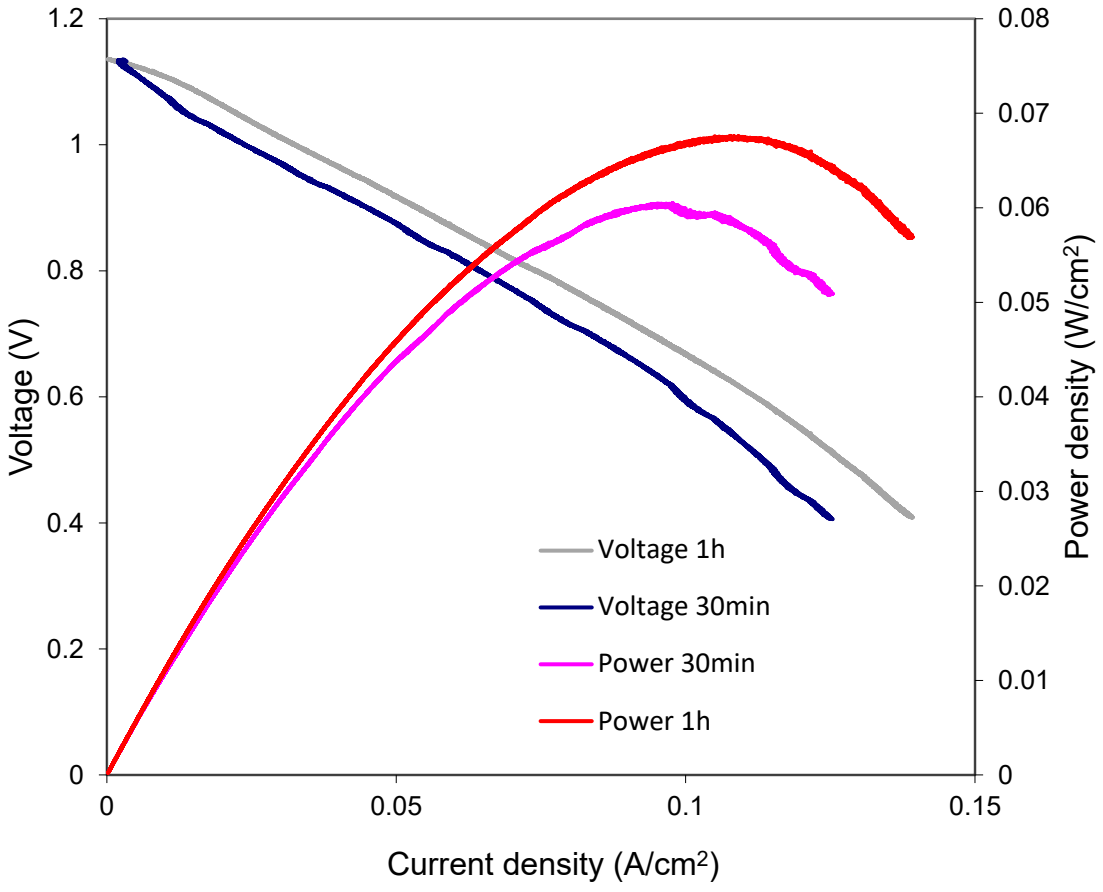

Figure 5.6 Polarization curves and power of the cell fed with propane at the anode. Results after 30 minutes and one ore of operation are reported. Temperature is 744°C and gas flow at the anode is 50sccm.

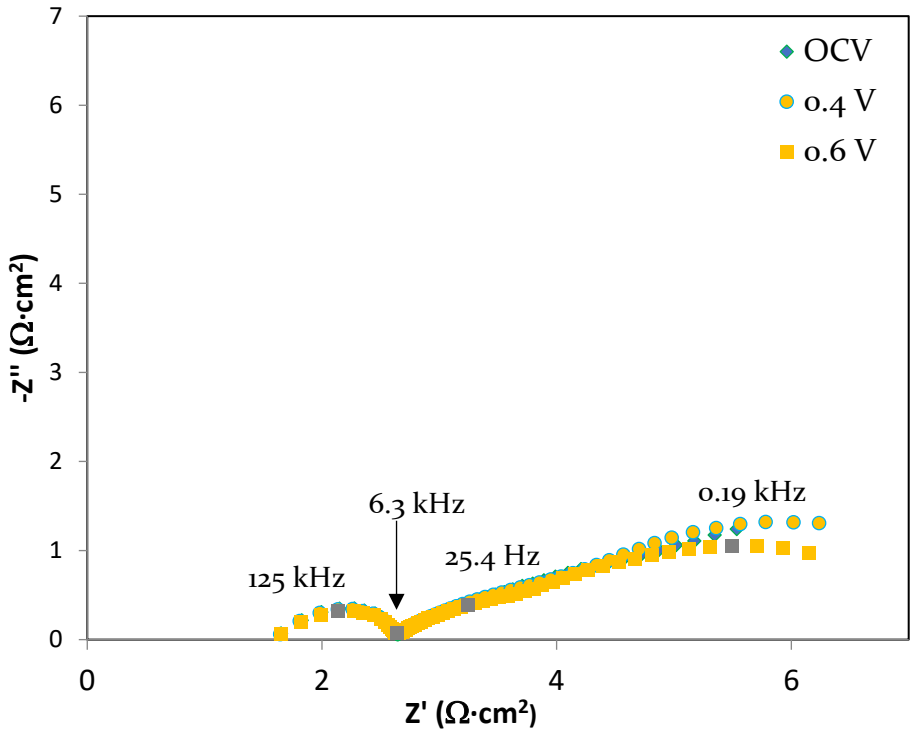

Figure 5.7 Impedance spectra of cell fed with propane at different voltages, after 1 hour of operation. Temperature is 744°C, propane flow is 50sccm.

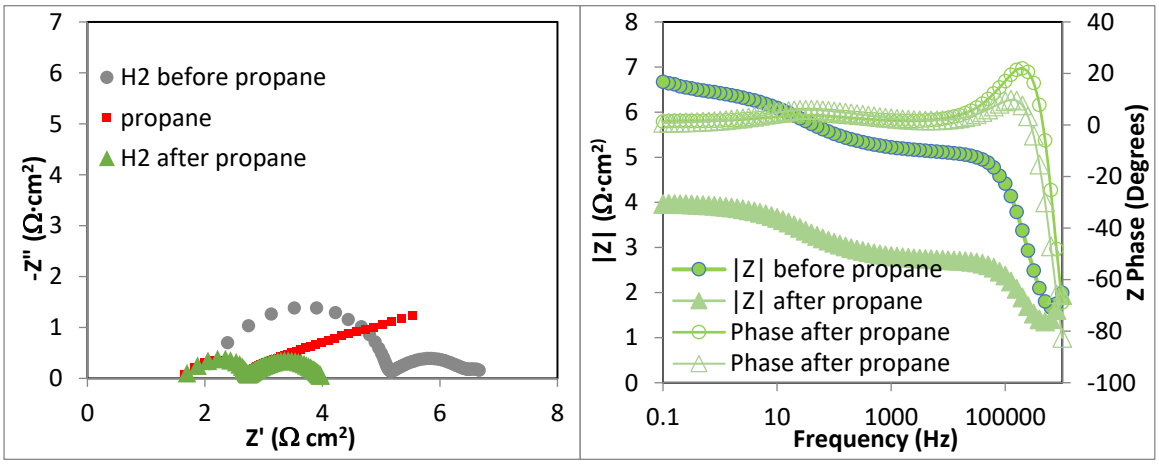

Figure 5.8 Comparison between impedance spectra before, during and after propane feeding. Left: Nyquist plots. Right: Bode plots.

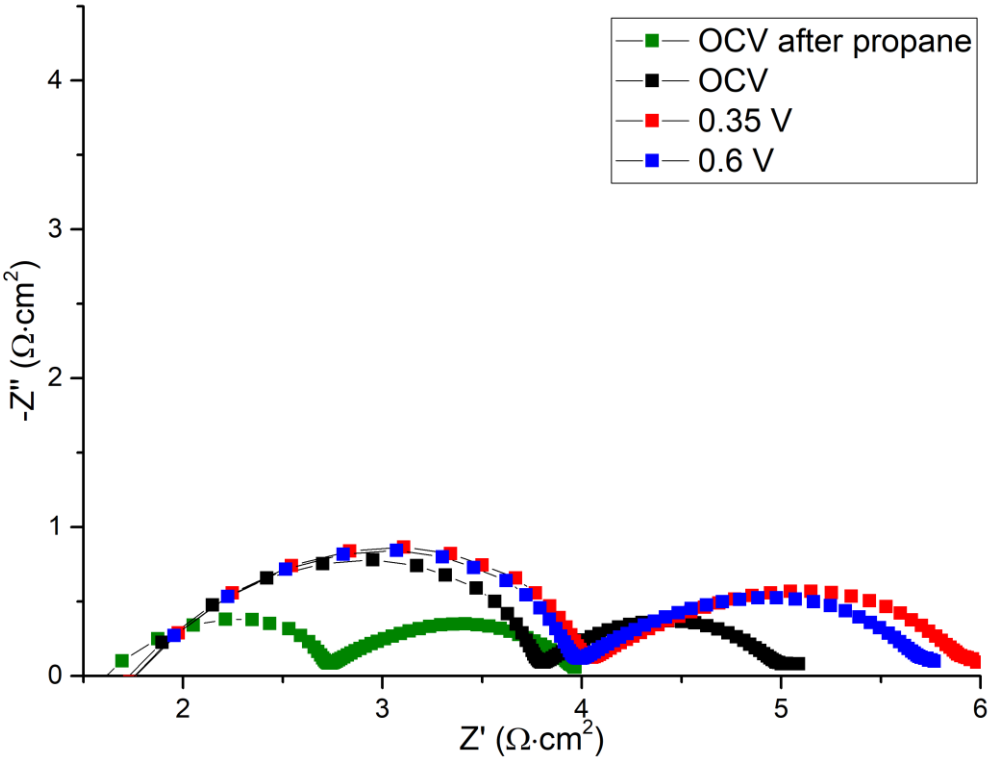

Figure 5.9 Nyquist plots of cell under hydrogen, after some our of operation since change of fuel from propane. Curve at OCV measured immediately after propane/hydrogen change is shown for comparison.

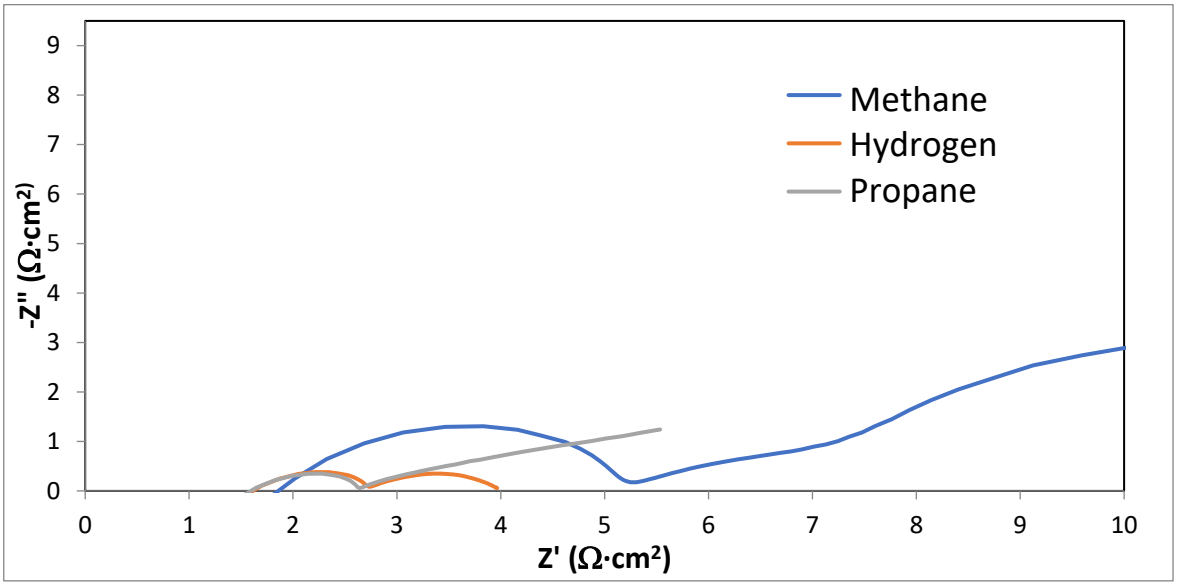

Figure 5.10 Comparison of Nyquist plots with different fuels.

As a third fuel, also methane has been tested. After 90 minutes of operation, the performance severely decreases: OCV is limited at 0.79V and power output is 13mW/cm². The variations are reflected also on impedance spectra, the arcs observed under methane are greatly expanded compared to other fuels (Figure 5.10). The

performances under hydrogen after methane are slightly decreased, as a power of only 50mW/cm² is obtained. The OCV is still good, around 1.07V.

A last test involved the measurement of power output during a night under diluted 5% hydrogen. Performances were recorded before and after, and while power was only slightly decreased (from 35mW/cm² to 33mW/cm²), the OCV remained stable at 1.01V. No significant variation is observed in the impedance response, as shown in Figure 5.11 (the expansion of the high frequency arc, compared to other plots, is only due to dilution of fuel). The absence of major degradation of the cell confirms a fair stability of the materials under the tested conditions. In any case, a full assessment of the long-term stability of the studied materials would necessarily involve tests over thousands hour of operation. They are clearly beyond the scope of this work, and are usually carried out at a later stage of development of the material.

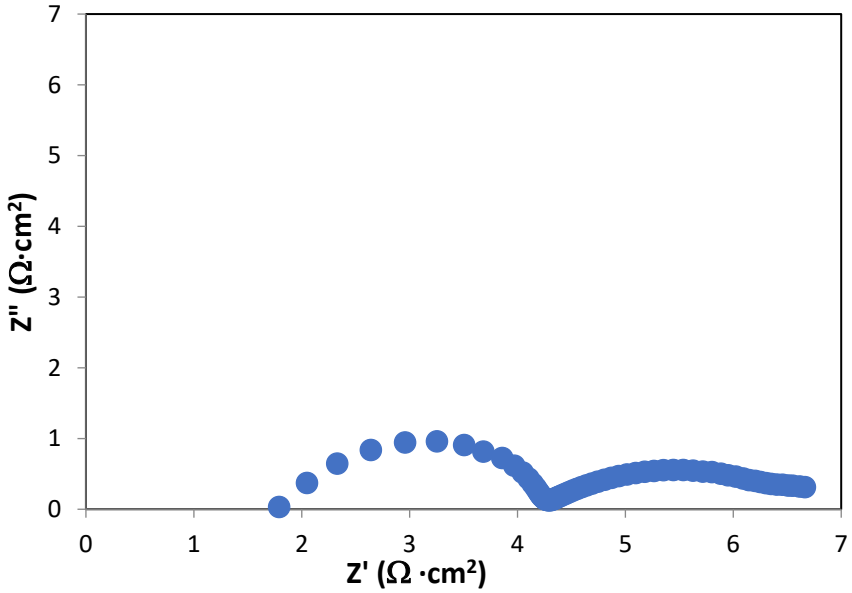

Figure 5.11 Nyquist plot of cell under 5% hydrogen, after one night of operation. Temperature is 750°C, fuel flow is 10 sccm.

5.4 Conclusions

A new anode material, LSGF + MnO_x, has been tested for fuel cells operation. Its performances confirm a great improvement from the simple LSGF anode, by over 10 times in terms of power output. A cell entirely based on La Sr Ga perovskites, designed to attain a great chemical stability, has been tested in a variety of fuels, and shows an interesting performance, considering that all the electrode materials have been entirely designed during this work. Different strategies to improve performances have

been outlined. In general, the cell showed optimal OCVs and very promising performances under propane. This makes the LSGF + MnO_x an interesting candidate for operation with carbon containing fuels. The strategy of coupling a substrate with an active deposited phase at the end has been successful: starting from LSGF, a material which was not particularly active neither as cathode or anode, by means of an appropriate deposition of a cheap non-noble metal oxide, it has been possible to obtain a cathode and an anode with a decent catalytic activity.

6 $Ca_2FeAl_{0.95}Mg_{0.05}O_5$ based materials for highly selective Single Chamber SOFC cathodes

SC-SOFCs, CELLS THAT WITHOUT PROPER MATERIALS WASTE HUGE AMOUNT OF FUELS
THE DESIGN OF A CATHODE SPECIFIC FOR SC-SOFCS
SOME PROMISING EIS TESTS ON A VERY CHEAP CA FE AL BASED ELECTRODE
AND A VERY PROMISING SELECTIVITY TEST ON A SC-SOFC

6.1 Introduction

Solid Oxide Fuel Cell technology is in a period of great development. The increasing possibility to employ, in a short time, sustainable methods to obtain hydrogen and other fuels has shifted the attention on these devices, that are able to supply electrical energy with extreme efficiencies. SOFCs have since now been reserved to stationary applications, due to their size and their thermomechanical fragility.

During the last twenty years a particular type of SOFC has been proposed and studied, but without being able to attract considerable industrial interest: the Single Chamber SOFC (SC-SOFC). A SC-SOFC[87], [247] resolves most of the flaws of a traditional SOFC and in principle would have several advantages[97], as it has been also described in chapter 1. But, no material turned out to have the appropriate selectivity for this application, so the most important prerequisite for this cell was in fact lacking. Regrettably, despite a considerable attention devoted to the SC-SOFCs especially from 2005 to 2013, no effort has been dedicated to the design and optimization of selective materials specific for SC-SOFCs, at the end only a maximum 8% efficiency has been reached[98]. Instead, great advancements were accomplished under the point of view of the cell design, also with indisputably good results in terms of cell power[248].

The great flexibility of these devices led to the study of different geometries, other than the classical planar cell electrolyte or anode supported, with the electrodes at the opposite sides of an electrolyte[98]. Coplanar cells are electrolyte plates in which both the electrodes are printed on the same side, with an interdigitated geometry[249], [250]. Also flow-through cells are possible, in which the gas mixture is forced through repeated porous layers of cathode, electrolyte and anode[251], these devices are called *Mixed Reactant Cells*.

An interesting theoretical work on SC-SOFCs has been carried out by Riess[99], [252]–[254], who stressed the importance of the selectivity of the materials and correctly foresaw the decline of these devices if the right attention was not devoted to it. A SC-SOFC is operated in an anomalous way compared to other cells. There is a strong imbalance in fuel (methane)/oxygen ratio, which should be 0.5 to have complete fuel consumption, but is set between 1 and 2 depending on the author[255], [256]. In addition, a high gas flow is used, so a large fraction of the fuel passes through the cell unreacted. There are precise reasons under these choices.

The oxygen poor mixture is necessary to promote only methane partial oxidation to syngas at the anode. The anode is nickel based, so it catalyses hydrocarbons oxidation, that would proceed to carbon dioxide if a stoichiometric mixture were used[99]. Moreover, the cathode should not be able to catalyse methane oxidation, and hardly methane can be used directly for electrochemical oxidation. The syngas produced by partial oxidation is the real fuel used in the electrochemical reaction, so feeding this mixture of methane and oxygen is a way to actually feed fuel only at the anode. Otherwise, feeding directly with syngas would lead to loss of performances, because the cathode is able to electrocatalyse its oxidation.

The high flow is needed to reduce molecules residence times, i.e. the time each molecule stays in contact with the catalyst; residence times are influenced by materials porosity, cell geometry and gas flows. In general, in a fuel cell, it is possible to distinguish between electrochemical desired reactions and chemical reactions between gas components that reduce efficiency. This distinction exists in all SOFCs, for example a common SOFC with hydrocarbon fuel can reform it internally and use the obtained hydrogen as effective fuel. This is not necessarily an undesired reaction,

a cell could be designed to work with internal reforming so all chemical reactions are planned and included in the cell mechanism; but, some fraction of the total reaction energy would be certainly lost for them. In SC-SOFCs, the distinction between chemical and electrochemical reactions is particularly important, because fuel and oxidant are physically in the same place; so, a direct reaction between them is possible and must be avoided. Electrochemical reactions require only limited residence times, while chemical reactions, that should be suppressed in a SC-SOFC, take longer times; as a reference, 10ms is a suitable time for electrocatalysis reactions while being low enough to avoid catalytic effect[254]. Thus, high flow is a mean to decrease residence times and to avoid the catalytic effect of the used materials, but that entails a very low fuel utilization.

Summarizing, a SC-SOFC requires anode and cathode selectivity. At the anode it is possible to create a fake but effective selectivity with a fuel rich mixture, but the cathode must be selective by itself. In other words, a single chamber cell with an efficient cathode could operate with low flows and reach high fuel utilization efficiencies, up to 25% each cell and to $1-(3/4)^n$ for a stack of n cells[99].

The problem of selectivity is not restricted only to the cathode, as at high temperatures also electrolytes can catalyse to some degree direct oxidation of hydrocarbon. Accurate assessment led to the conclusion that for a truly efficient SC-SOFC only YSZ can be used, at a maximum temperature of 600°C[99]. Above that temperature, also YSZ is active for methane oxidation, with a catalytic activity small but able to induce noticeable losses of fuel. Other electrolytes are active also below 600°C, so they should be avoided in commercial cells. In this thesis, cells are based on CGO because it allowed to minimise ohmic reactions, and it provided an efficient framework we already had experience with.

Anode, compared to cathode, is the electrode that less needs improvement, at least at this stage; but this does not mean it is optimal for this application. Its activation must be carried out carefully[257], and there is some concern about its stability, in particular regarding reduction/oxidation cycles that would have most severe effect than in double chamber cells, due to direct contact with oxygen in the mixed atmosphere[94], [258].

In this part of the thesis, a cathode material for SC-SOFCs is designed and prepared, in order to fabricate a cell with a proper selectivity and therefore a high efficiency. Since in catalysis selectivity is often opposed to high speed reaction, for these tests it has been decided to choose a material potentially able to carry on the cathodic reaction, but with a supposed low activity. The aim is to demonstrate that it is possible, by adopting this strategy, to operate a SC-SOFC with high efficiencies.

All materials used as SOFC cathodes are Mixed Ionic Electronic Conductive (MIEC) oxides or composites of MIEC materials[149], hence the choice has been restricted to MIEC materials with a relatively low conductivity. At the end, the Ca_2FeAlO_5 (CFA) brownmillerite was chosen[139]. Moreover, to improve conductivity, a small amount of magnesium was inserted, so the actual formula of CFA is $Ca_2FeAl_{0.95}Mg_{0.05}O_5$[259]. After its synthesis, CFA has been characterized by means of XRD, TPR, SEM, XPS, EDX and N_2 adsorption isotherms; its catalytic activity towards methane oxidation has been measured. Following the good results of iron oxide impregnation on LSGF for the cathodic compartment, a portion of the synthesized powder has been impregnated as well and characterized following the same protocol mentioned above. We refer to this second material as CFA + FeO_x.

To assess the effects of the firing of the electrode to the impregnated phase, CFA + FeO_x in powder form has been treated at 1050°C, and characterized again by means of XRD, XPS, SEM and EDX. Then, symmetrical cells on a CGO electrolyte have been prepared with both CFA and CFA + FeO_x for EIS tests, firing temperature has been optimized. CGO has been chosen for these preliminary tests, even if it is not the most fitting electrolyte for SC-SOFCs, for the reasons explained above. Then, complete cells with a Ni/CGO anode have been fabricated and their polarization curves have been measured. Finally, the selectivity of the cathodes under reaction conditions has been tested.

6.2 Synthesis and characterization

CFA has been synthesized with a solid combustion synthesis. Precursors $CaCO_3$, Fe, $Al(NO_3)_3$ and $Mg(OH)_2$ were dissolved in water with the help of HNO_3 when needed. Citric acid in amount 1.9 times the cations in solution was then added. The solution was neutralized adding drop-by-drop NH_4OH and water was eliminated by

mildly heating on hot plate, gel formation happens at the end of this step. Increasing of hot-plate heating over 250°C triggers gel self-combustion. The obtained powder was grinded and calcined at 1050°C for 6h.

Iron oxide was deposited via a wet impregnation procedure. An aqueous solution of $Fe(NO_3)_3$ was prepared, and CFA was added to it. The suspension was covered and kept under stirring for one day. Mild heating on a hot plate was employed to evaporate water. The obtained powder was finally treated at 550°C for 6 hours.

Cells for EIS and polarization measurements are electrolyte supported and prepared by screen printing the material to be tested on both sides of a CGO pellet (diameter 20mm, thickness 1.4mm). The pellet was prepared by pressing the CGO powder (GDC10-TC, Fuel Cell Materials) and treating the so-obtained pellet at 1350°C for two hours. An ink was prepared by mixing the electrode (CFA or NiO) powder with a fraction of CGO powder, and adding binder V400 (ESL, commercial) and solvent T404 (ESL, commercial) to adjust viscosity. The ink deposition is carried out with a screen printing machine. The layer is then dried in an oven at 100°C for 15 minutes. For symmetrical cells two layers on each side of the CGO pellets were printed this way, for complete cells cathode was printed with two CFA layers and anode with four NiO layers. Anodes were treated at 1200°C and cathodes were treated at 1000°C and 1100°C, to ensure a good electrical contact between the electrolyte and the electrodes. While different symmetrical cells were prepared for each temperature for each material, cathodes of complete cells were treated only at the temperature that gave the best performance as a symmetric cell. Treatments at temperatures lower than 1000°C have been found not to be sufficient to ensure enough mechanical adhesion on the electrodic layer. Finally, a gold grid is printed from a gold ink (8880-H, ESL, commercial) on both the electrodes, and the cell is treated a last time at 850°C for two hours.

In order to evaluate the performances of the materials for SOFC operation, Electrochemical Impedance Spectroscopy tests were performed on the following symmetrical cells: two CFA/CGO/CFA cells and two CFA+FeO_x/CGO/CFA+FeO_x cells, each cell treated at a different temperature (1000°C or 1100°C). Impedance of the cells was measured under air (normal operating condition for a double cell SOFC

cathode), under a 20% CH_4 10% O_2 atmosphere and then a second time under air. Data were collected with Solartron 1286 Electrochemical Interface and Solartron 1255 Frequency Response Analyzer devices. Prior to test, complete cells require anode activation, consisting in a reduction of NiO to Ni, carried out with a 5 minutes treatment under CH_4 10% in N_2 at 600°C, then cell measurements were carried out under a 20% CH_4 10% O_2 atmosphere. For the collection of polarization curves of complete single chamber fuel cells, a Keithley 2400 SourceMeter was used. Selectivity tests of the cathodes were performed by sealing two alumina tubes at both sides of a complete cell with a commercial cement (Aremco Ceramabond 571). An inner tube with outlet close to the cell provided gas feeding at each side, and pushed a nickel wire on the electrodes to ensure contact. An Autolab PGSTAT204 was used to keep the cell working during the test, voltage was set at 0.4V to obtain the maximum power. A thermocouple each side measured the actual cell temperature. An ESS Evolution quadrupole was used to measure composition of the cathode exhaust gas, the instrument was calibrated with a CO_2 standard to obtain quantitative data. Each cathode was flushed with a 140sccm flow of a 20% CH_4 and 10% O_2 gas mixture.

The XPS measurements were carried out with a Perkin Elmer Φ 5600ci Multi Technique System. The spectrometer was calibrated by assuming the binding energy (BE) of the Au 4f7/2 line to be 84.0eV with respect to the Fermi level. Both extended spectra (survey - 187.85eV pass energy, 0.5eV·step^{-1}, 0.05 s·step^{-1}) and detailed spectra (for La 3d, Fe 2p, Ga 2p, Sr 3d, O 1s and C 1s – 23.50eV pass energy, 0.1eV·step^{-1}, 0.1s·step^{-1}) were collected with a standard Al Kα source working at 250W. The standard deviation in the BE values of the XPS line is 0.10eV. The atomic percentage, after a Shirley-type background subtraction[161], was evaluated by using the PHI sensitivity factors[162]. The peak positions were corrected for the charging effects by considering the C 1s peak at 285.0eV and evaluating the BE differences[200].

The XRD analyses were performed with a Bruker D8 Advance diffractometer with Bragg-Brentano geometry using a Cu Kα radiation (40kV, 40mA, λ = 0.154nm). The data were collected at 0.03° at a counting time of 10s/step in the (2θ) range from 10° to 90°. The crystalline phases were identified by the search-match method using the JCPDS database.

Temperature Programmed Reduction (TPR) was performed with an Autochem II 2920 Micromeritics, equipped with a Thermal Conductivity Detector (TCD). The TPR measurements were carried out in a quartz reactor by using 50mg of sample and heating from RT to 900°C at 10°C min^{-1} under a constant flow of H_2 5% in Ar (50ml·min^{-1}). TPR samples were previously outgased with He (50ml·min^{-1}) at room temperature.

Nitrogen adsorption isotherms were measured at 77K with a Micromeritics ASAP 2020 plus instrument. Superficial area by BET model has been calculated from adsorption curves. DFT calculations were carried out with built-in software of the instrument.

Field emission-scanning electron microscopy and EDX measures were carried on a Zeiss SUPRA 40VP. Morphological and EDX analysis were carried out setting the acceleration voltages at 20kV.

The catalytic activity was measured placing 100mg of CFA in the middle of a vertical quartz tube, with a 7% O_2, 14% CH_4 gas mixture flowing upside, with a 100sccm flow. The exhaust composition was measured with a GC.

6.3 Results and discussion

6.3.1 XRD

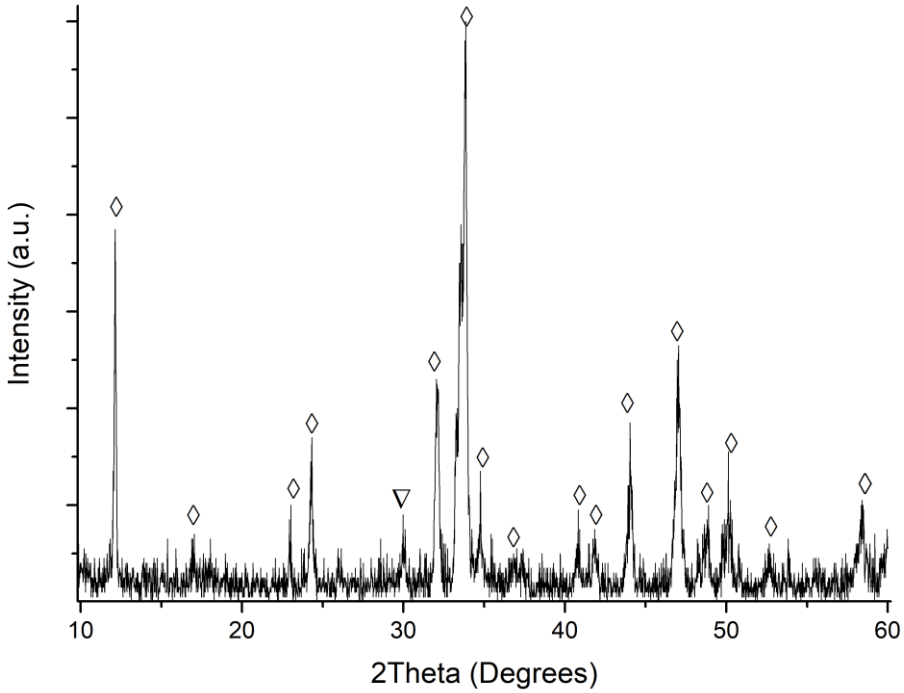

Figure 6.1 XRD pattern of CFA. ◊: Brownmillerite Ca_2FeAlO_5 peaks (JCPDS 00-030-0226), ∇: Krotite $CaAl_2O_2$ peaks (JCPDS 00-062-0217).

CFA has a good crystallinity; as shown in Figure 6.1, the signal/noise ratio is good. The observed peaks match with a brownmillerite phase Ca_2FeAlO_5, so the synthesis can be considered successful: the magnesium concentration is only minimal, and, whereas it certainly causes a shrinkage of the crystalline cell, its extent is insufficient to produce significant deviations from parent Ca_2FeAlO_5 structure. Brownmillerite's crystal structure is similar to perovskite's one, from which it can be obtained with the ordered removal of one oxygen atom every six[141]. With this transformation, each layer every two of the perovskite becomes a layer of tetrahedra[260], and symmetry changes from cubic to orthorhombic. Other than the brownmillerite, in the XRD pattern a peak related to a small krotite impurity is also present, but can be neglected due to is small intensity.

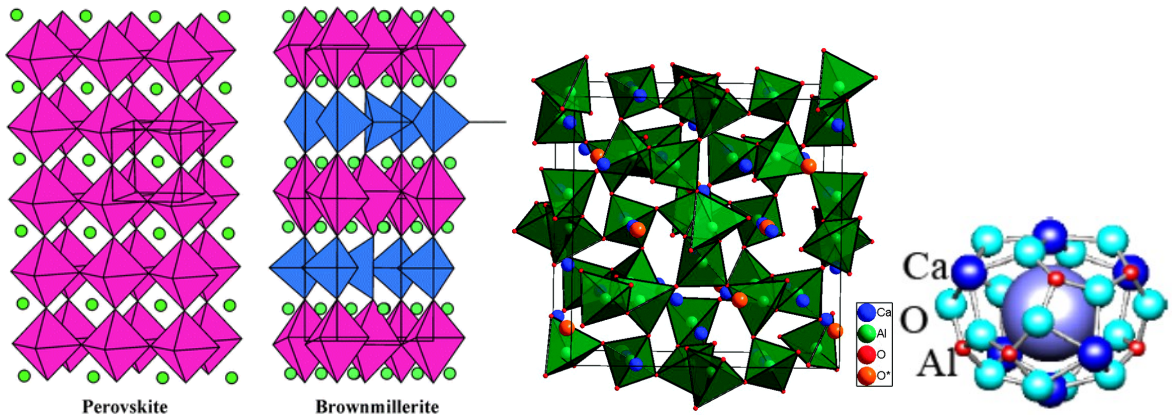

Figure 6.2 Left: comparison between perovskite and brownmillerite crystalline structure (from [261]). Middle: mayenite unit cell (from [262]), O are the cage centre oxygen ions. Left: mayenite cage, twelve of them form a unit cell (from [263]).*

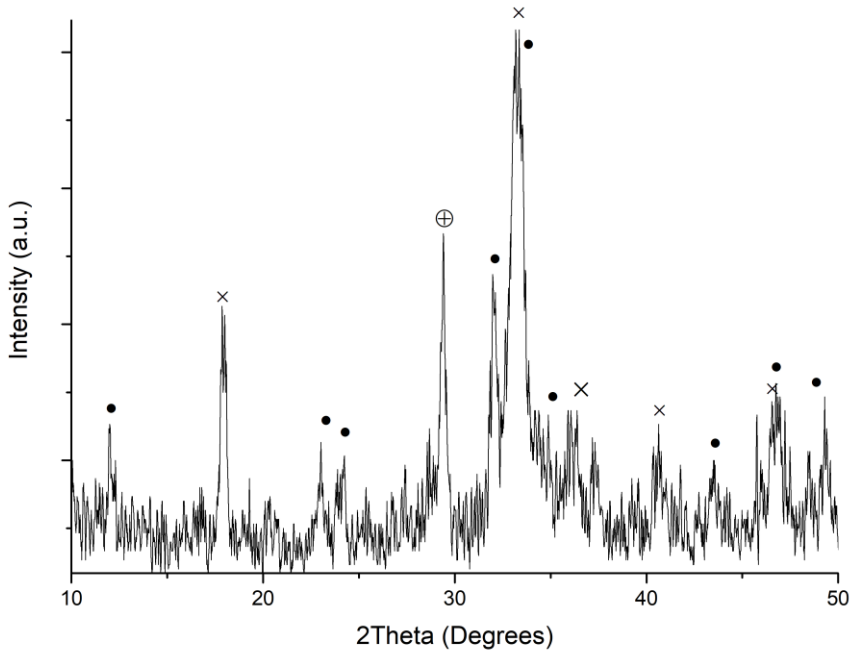

Figure 6.3 CFA + FeO_x XRD. ●: Srebrodolskite $Ca_2Fe_2O_5$ peaks (JCPDS 00-047-1744), ⊕: Calcite $CaCO_3$ peaks (JCPDS 00-047-1743), ×: Mayenite $Ca_{12}Al_{14}O_{33}$ peaks (JCPDS 00-048-1882).

After the deposition of FeO_x the phase composition is much different from the pristine one (Figure 6.3). The sample is much less uniform than the previous case, the signal/noise ratio is worse and the pattern has changed completely. There is no more brownmillerite; instead three new phases appeared, all of them containing calcium, oxygen and one other element. They probably formed following the decomposition of the brownmillerite, with Fe and Al cations separating in two different phases.

The $Ca_2Fe_2O_5$ phase is very similar to the original brownmillerite and has its same structure, in fact srebrodolskite is the name of a mineral with composition $Ca_2Fe_2O_5$

and the brownmillerite crystalline structure. The mayenite, despite its formula similar to the brownmillerite (that would be $Ca_{14}Al_{14}O_{35}$, against mayenite $Ca_{12}Al_{14}O_{33}$), has a very different crystalline structure. Its unit cell is very large (see Figure 6.2), made of 12 cages as shown in the figure, crystalline structure is cubic. $Ca_{12}Al_{14}O_{33}$, also called C12A7, is commonly known as an intermediate product in Portland cements, it is an electric insulator and a very good ionic conductor[264]. In any case, the composition close to the brownmillerite is consistent with the hypothesis of the brownmillerite splitting into Fe-only and Al-only phases. The formation of the carbonate cation is less straightforward to explain because there was no organic fraction in the synthesis mixture and no carbon atom, probably some uptake of atmospheric CO_2 was involved in this process.

The extent of the drastic changes the mild treatments used for iron impregnation determined in the sample structure is surprising, as nothing of the original crystalline structure is found successively. The brownmillerite is a ceramic phase stable at high temperatures, but has been entirely degraded by a simple impregnation of iron and a treatment at 550°C. Previous experiments in our laboratory (not published) reported that at room temperature the brownmillerite is completely disrupted by immersion at room temperature in a simple solution of Fe(II) acetate, so it is possible to suspect that this crystalline structure is affected by the presence of iron species in solution.

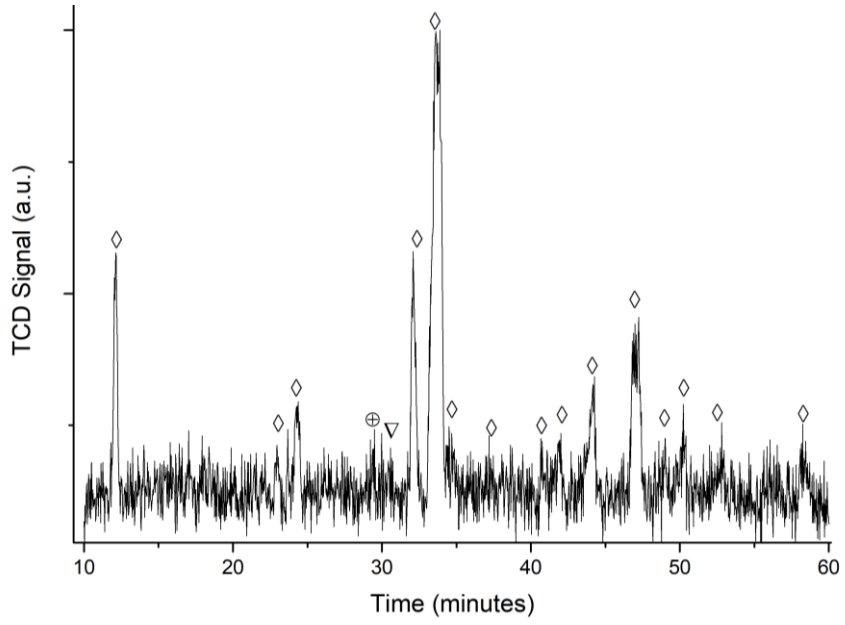

Figure 6.4 CFA+FeO_x treated at 1050°C XRD. ◊: Brownmillerite Ca_2FeAlO_5 peaks (JCPDS 00-030-0226), ∇: Krotite $CaAl_2O_2$ peaks (JCPDS 00-062-0217), ⊕: Calcice $CaCO_3$ peaks (JCPDS 00-047-1743).

A treatment at 1050°C, which replicates the firing of the electrodes to make them adhere to the electrolyte, restores the original brownmillerite phase (Figure 6.4). This means that when preparing a cell with the iron impregnated powder, the electrode is deposited as a mixture of $Ca_{12}Al_{14}O_{33}$, $Ca_2Fe_2O_5$ $CaCO_3$, and then reverts to the pristine brownmillerite during the firing. Traces of $CaAl_2O_2$ are again observed, and there still is some trace of calcite, close to the detection limit. In general, signal/noise ratio is worse than as-synthesized brownmillerites so probably the phases are less defined than immediately after CFA synthesis.

6.3.2 TPR

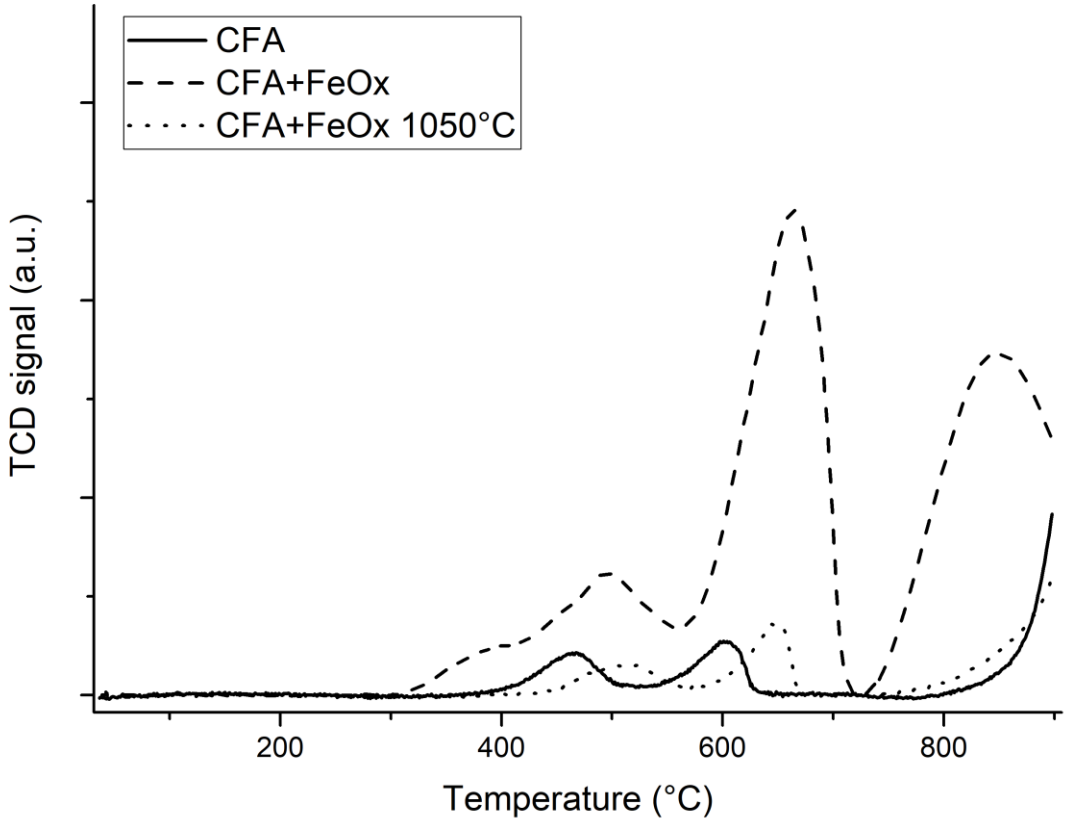

Figure 6.5 TPR profiles of synthesized powders.

	450°C	650°C
CFA	0.010	0.012
CFA + FeO_x	0.005+0.045	0.172
CFA + FeO_x 1050°C	0.009	0.016

Table 6.1 Area in mol of H_2/mol of CFA of the TPR peaks shown in Figure 6.5.CFA + FeO_x peaks has been obtained by fitting and deconvolution.

The TPR curves are shown in Figure 6.5, and the area of the peaks are summarized in Table 6.1. TPR profile of CFA reveals only two very small peaks at 450°C and 600°C. The only species that can be reduced is iron: the reduction of the other cations (Ca^{2+}, Al^{3+}, Mg^{2+}) happens well above 1000°C. If all the signals are assigned to iron, the area of the peaks is way too small to account even for a Fe(III)→Fe(II) reduction; this probably means that the observed signals correspond only to the reduction of the small amount of Fe^{4+}. The presence of Fe^{4+} in this brownmillerite is not unexpected[265] and probably the inserted Mg atoms in the Ca_2FeAlO_5 structure are involved in their formation. Moreover, quantitatively the amount of Fe^{4+} atoms as determined by these measurements roughly corresponds to the amount of magnesium, so probably iron atoms were oxidized to 4+ to balance magnesium 2+ charge, in accordance with literature[259]. TPR profiles of Ca_2FeAlO_5 report only one small reduction peak at 700-800°C[266], so it is possible that of the two peaks observed for $Ca_2FeAl_{0.95}Mg_{0.05}O_5$ the one at higher temperature is Fe^{4+} normally present inside the material, and the one at lower temperature is the Fe^{4+} generated by magnesium insertion. The reduction of Fe^{3+} is shifted at higher temperatures, it is possible to see only the beginning of the curve above 800°C, a temperature corresponding to the one observed for LSGF perovskites during the TPR measurements described in chapter 2. The impregnation with iron modifies heavily the shape of the TPR profile, more signals characterized by a higher intensity appear, coherently with the phase transitions observed by XRD. $Ca_2Fe_2O_5$ is the phase to be related with the TPR response as it is the only containing iron one; indeed, observed peaks are compatible with what described in literature about this phase[267]: both the 650°C and 800°C peaks are Fe^{3+}→Fe^{2+} reduction of two types of Fe^{3+}. The two peaks between 300°C and 600°C are compatible with the presence of Fe_2O_3, that according to literature[268] would be reduced with two non-resolved peaks having area ratio 1:8, as observed here. After the treatment at 1050°C a shape similar to pristine CFA is obtained again, this is coherent with XRD results that described a restore of the original structure. The peaks are shifted at higher temperature, this phenomenon is generally associated with an increase of the crystallite size as reduction of larger particles is more difficult; in this case the second treatment at 1050°C is very likely to have induced an increase of the particle size.

6.3.3 N_2 isotherms and superficial area

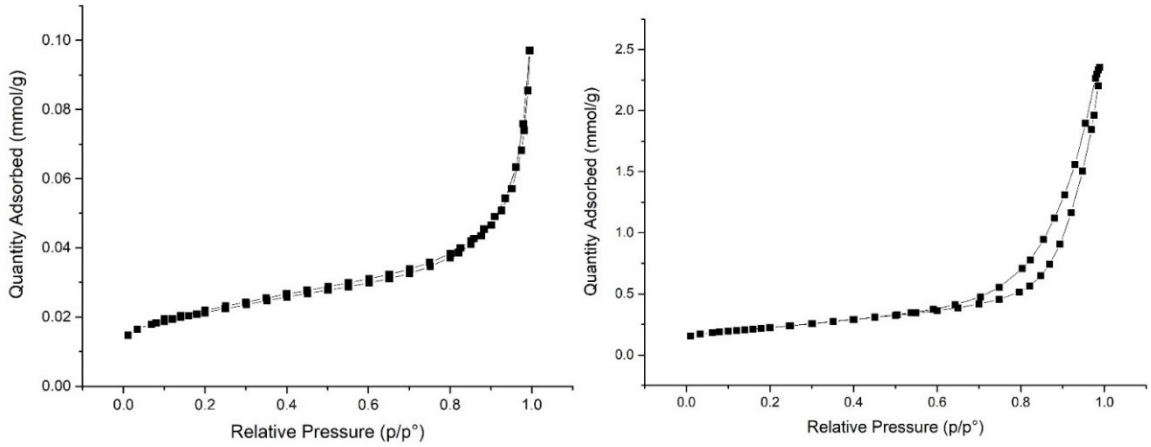

Figure 6.6 N_2 adsorption isotherm of CFA (left) and CFA + FeO_x (right).

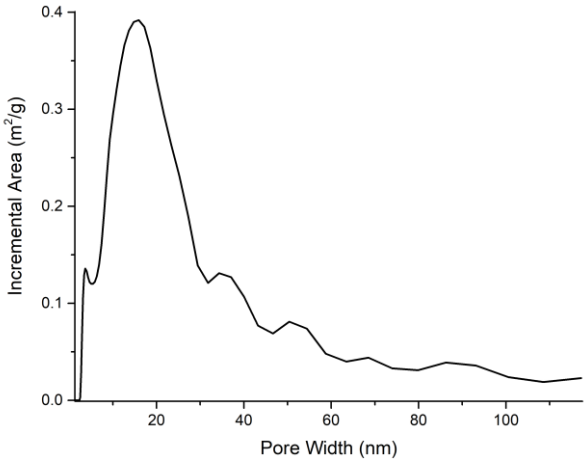

Figure 6.7 Pores distribution after FeO_x deposition, as calculated by DFT.

The surface area of CFA is low, 1.7m²/g, the calcination temperature is a clear limit to obtaining higher superficial areas. The employment of other specific techniques to increase superficial area, as ball milling and pore formers during synthesis, would be useful, but have been excluded for the moment, given the exploratory nature of this work. In any case, they would be certainly considered if tests on this material continue. The CFA isotherm (shown in Figure 6.7) is type II, although the pressure interval in which a monolayer is exclusively formed is very short, and multilayer formation happens early, at p/p°=0.05. The absence of any hysteresis loop means there is no mesoporosity. On the whole, this isotherm shape indicates there is no micro- or meso- porosity and pore distribution is irregular; this is in accordance with the low superficial area, and means there was no ordinated process to govern surface formation.

The result of adsorption on CFA + FeO_x (Figure 6.7) are quite different, the material has a higher surface area, 17.1m²/g, and the isotherm is type V. At low pressures, there is no change in curve slope, as it happened with CFA, and this means there is no monolayer formation; instead, nitrogen forms directly multilayers. Mono or multilayer formation is determined by heat of adsorption of nitrogen on the surface and heat of liquefaction of nitrogen; if the first is higher, monolayer formation proceeds until completion, if the latter is higher molecules find energetically convenient to adsorb on already formed layers instead of covering the whole surface. In this case, the extent of monolayer formation was not considerable even in CFA, but the fact that it did not happen at all means the surface has changed. This fact is consistent with the phase modifications observed by means of XRD and TPR, and also with the different shape of the surface observed by SEM and described in the following paragraph. Other than the different curve shape, in CFA + FeO_x also a hysteresis loop appeared. Loops in adsorption measurements form due to capillary forces during pore filling with adsorbates when a mesoporosity is present; this loop shape, of type H3, is associated to slit-like pores.

From adsorption curves it is possible to perform DFT calculations to analyse the CFA + FeO_x pore distribution. Such procedure reveals a porosity distribution with D_{50}=22nm, the complete result of the procedure is shown in Figure 6.7. In this case, a more defined surface structure is possible: the deposition of iron from the surface is not a violent process as the combustion required for CFA synthesis, so an ordered surface with defined pores can form.

6.3.4 SEM

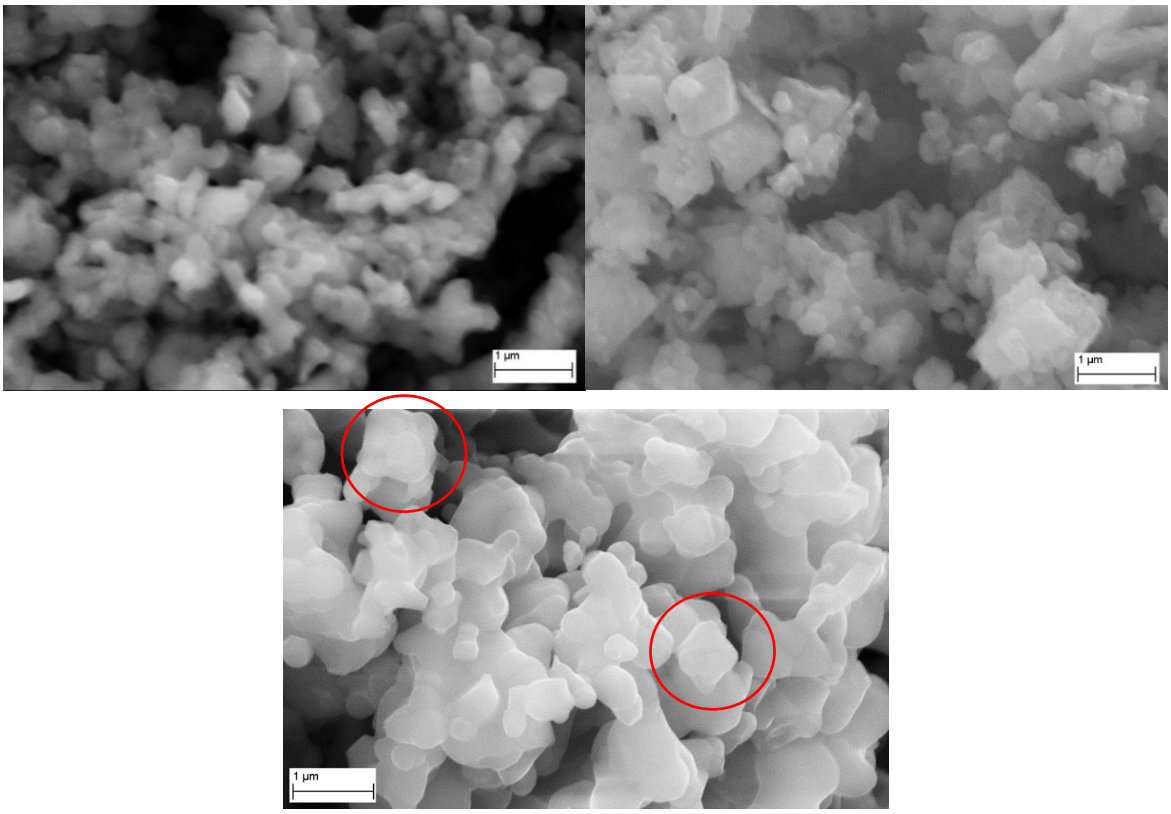

Figure 6.8 SEM images of CFA (above, left), CFA + FeO_x (above, right) and CFA + FeO_x (below) treated at 1050°C.

CFA powder, as seen by SEM (Figure 6.8), is in form of conglomerated particles of size around 200nm; the shape of the particle appears smooth and irregular, no particular feature is observed. In the image of CFA + FeO_x powder, some crystals with an octahedral shape and 1µm size are mixed with smaller and less defined particles. The octahedra formed as a result of the creation of a new phase, and among the two new phases identified by XRD ($Ca_2Fe_2O_5$ and $Ca_{12}Al_{14}O_{33}$) an octahedral crystal appears more compatible with the orthorhombic crystalline system of the $Ca_2Fe_2O_5$ phase. After the 1050°C thermal treatment the new phases are not observed anymore, consequently also octahedra disappears. Basically, the constituent phases of CFA and CFA + FeO_x after the 1050°C treatment are the same, although the latter, due to a small excess of iron due to the impregnation, has some iron based impurity that accommodates the extra iron in an amount not sufficient to be revealed by XRD. In spite of the very similar bulk composition, morphology is completely different. After the thermal treatment, CFA + FeO_x is an agglomerate of very different sizes of particles, from around 200nm to more than 1µm. This size distribution can be a consequence of the phase separation before the treatment, in which large octahedral

$Ca_2Fe_2O_5$ crystals were surrounded by smaller particles, supposedly of $Ca_{12}Al_{14}O_{33}$. During the treatment, probably the atoms moved along the existing structures, and recombined maintaining the shape of the bigger particles. Thus, it could be not fortuitous that the final structure (evidenced in Figure 6.8) has a shape that reminds an octahedron with some rough coating around.

6.3.5 XPS and EDX

	NOMINAL		XPS			EDX		
	CFA	CFA+FeO_x	CFA	CFA + FeO_x	CFA+FeO_x 1050°C	CFA	CFA + FeO_x	CFA + FeO_x 1050°C
CA	22.2 (50.0)	22.0 (48. 8)	18.0 (66.4)	15.9 (56.6)	17.4 (61.3)	15.6 (49.1)	14.8 (51.2)	17.5 (47.8)
FE	11.1 (25.0)	12.1 (26.8)	2.9 (10.7)	3.1 (11.0)	3.2 (11.3)	7.1 (22.3)	7.1 (24.6)	9.0 (24.6)
AL	10.6 (23.7)	10.4 (23.2)	5.0 (18.5)	8.0 (28.5)	6.9 (24.2)	8.6 (27.0)	7.0 (24.2)	9.8 (26.8)
MG	0.6 (1.3)	0.6 (1.2)	1.2 (4.4)	1.1 (3.9)	0.9 (3.2)	0.5 (1.6)	0	0.3 (0.81)
O	55.6	55.0	72.9	71.9	71.6	68.2	71.2	63.5

Table 6.2 Summary of quantitative analysis by means of XPS and EDX on powders. Abundances are indicated as atomic % relative concentrations. Numbers in brackets refer to calculation considering only cations.

Quantitative analysis is shown in Table 6.2. In general, XPS reveals a superficial segregation of Ca at expense of B site cations, and between B cations there is a relative abundance of Al compared to Fe instead of the nominal 1:1 ratio. Traces of Mg have been detected, and, even if the values are near to the XPS experimental error, the observed values seem slightly higher than the nominals. The deposition of iron oxide, unexpectedly, favours the surface segregation of Al and this situation is not significantly cancelled by the following treatment at 1050°C. After the Fe deposition, there is a slight re-equilibration of the Fe/Al ratio, which is not modified after the 1050°C treatment. EDX results on CFA and its composites are in accordance to nominal composition within experimental error. The Mg abundance is close to the detectability limit also for these measurements, and in all the cases it has been very difficult to identify the relative peaks. In the CFA + FeO_x case this has not been possible at all.

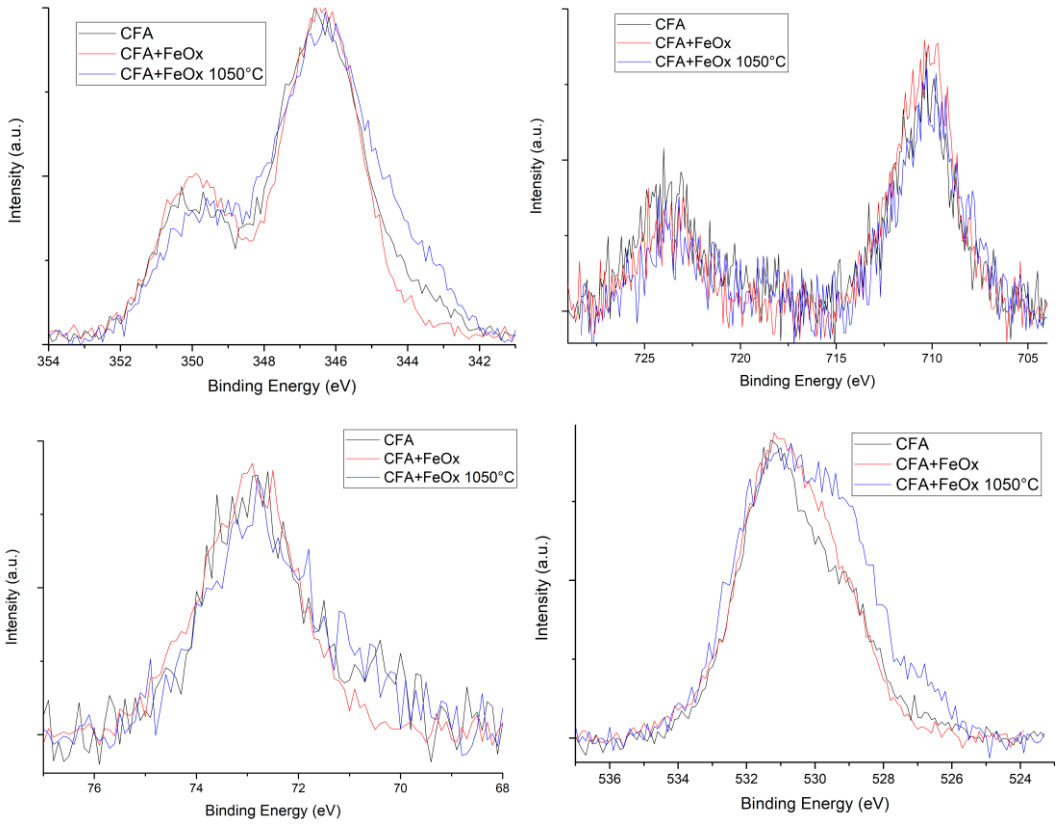

Figure 6.9 XPS spectra of CFA, CFA + FeO_x, CFA + FeO_x treated at 1050°C.

Figure 6.9 shows the results of the XPS measurements, each elemental peak is shown in a separate graph in order to compare differences between the samples. The binding energy of calcium XPS peaks does not variate significantly depending on the chemical compound, so only limited information can be deduced from calcium spectrum. The position of the experimental calcium peaks corresponds to the expected values for a calcium oxide, and this is consistent with expectations, as the brownmillerite is a calcium oxide. All the $2p_{3/2}$ peaks maintain the same position at 346.4eV; $2p_{1/2}$ peaks of CFA and CFA + FeO_x are both at 349.9eV while the peak of CFA + FeO_x treated at 1050°C is slightly shifted at lower energies at 349.4eV. Iron XPS peaks can be completely overlapped for all the three samples, seemingly iron does not see its chemical surrounding change during any of the transition the material experiences. This could be expected, in both Ca_2FeAlO_5 and $Ca_2Fe_2O_5$ iron coordination does not change and each iron atom is surrounded by the same arrangement of oxygen atoms. The lack of changes even in the CFA + FeO_x profile indicates also that the iron deposition and the mild thermal treatment did not produce an iron layer covering the material, but initiated the $Ca_2FeAl_{0.95}Mg_{0.05}O_5$

phase decomposition and all iron became part of the newly formed phase. Also for the Al 2p peaks there are very modest differences as a consequence of iron oxide deposition of thermal treatment. The progression of the composition of the samples, as described by XRD and neglecting Mg, can be summarized as:

$$Ca_2FeAlO_5 \xrightarrow{+\,FeO_x,\ 550°C} Ca_2Fe_2O_5 + Ca_{12}Al_{14}O_{33} \xrightarrow{1050°C} Ca_2FeAlO_5$$

The only minimal variation of the Al XPS peaks between the samples means that, in spite of the radically different structure of $Ca_{12}Al_{14}O_{33}$, the surrounding of each aluminium atom is not so different from Ca_2FeAlO_5, and this could explain why precisely this particular structure has formed from brownmillerite. In effect, under the point of view of the B cations there is some similarity between the two structures Ca_2FeAlO_5 and $Ca_{12}Al_{14}O_{33}$. In Ca_2FeAlO_5 B cations occupy both octahedral and tetrahedral sites inside the oxygen atoms framework, in $Ca_{12}Al_{14}O_{33}$ Al is at the centre of oxygen tetrahedra organised in the complexed arrangement that composes the wide unit cell of this phase. Finally, oxygen peaks are similar between CFA and CFA + FeO_x, but CFA + FeO_x treated at 1050°C is broader towards lower binding energies. This shoulder can be related to the presence of simple iron oxide of composition Fe_2O_3; this phase was already observed in the corresponding TPR profile, so the considered shape of the O1s peaks is a confirmation of its presence. In this discussion magnesium has been deliberately neglected, because, due to its low concentration, it is difficult to consider significant the eventual shape and position variations.

6.3.6 Catalytic activity

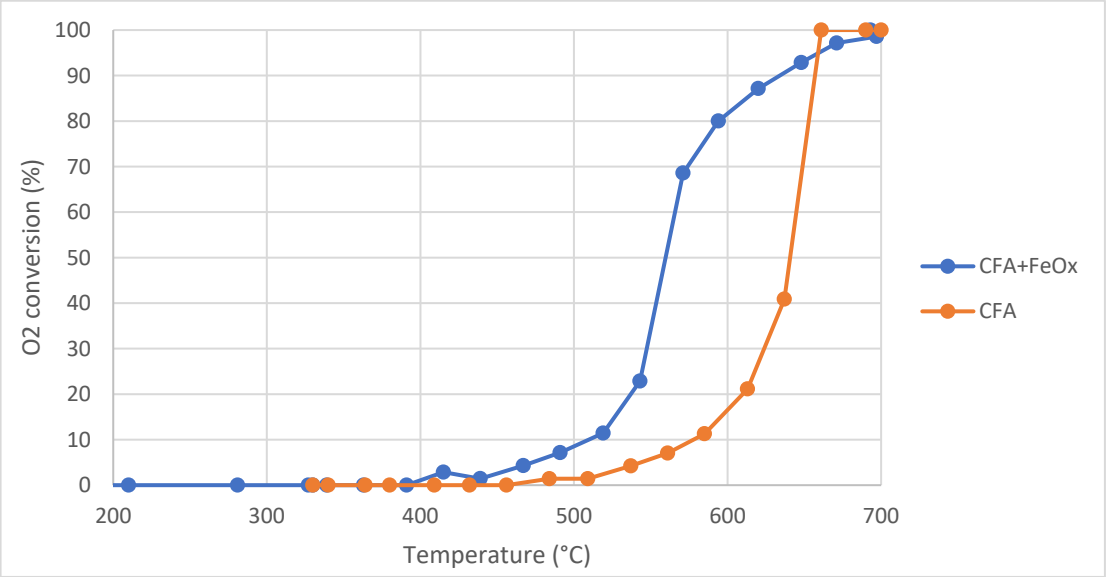

Figure 6.10 Oxygen conversion of CFA and CFA + FeO_x, in fuel rich mixture (CH_4:O_2=2). flow 100sccm, CH_4=14%, O_2=7%.

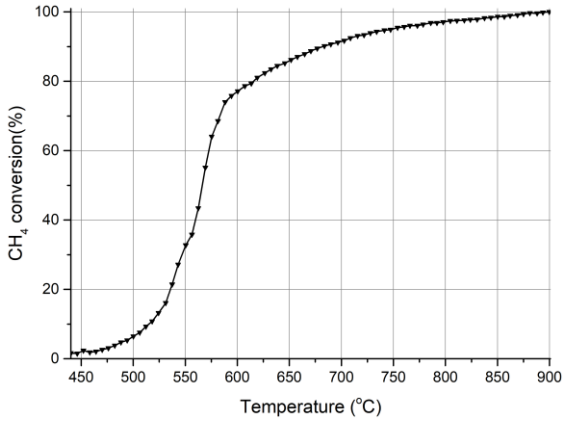

Figure 6.11 Methane conversion of CGO in stoichiometric mixture, from [269].

The catalytic activity of the electrodes used in SC-SOFCs is very important, as it has been mentioned in the introduction. For the efficiency's sake it is important to use materials with the lowest catalytic activity for methane oxidation as possible, so this ability for the synthesized materials has been measured. To obtain a result as close as possible to real cell operation, the same fuel/oxygen ratio used in SC-SOFCs has been used, the results are shown in Figure 6.10. The activity of CFA towards methane oxidation is low. Onset temperature is around 500°C, then activity increases slowly with temperature, and at 600°C it is only modest (around 15% of oxygen conversion). The reaction reaches completion at 660°C. The composite CFA + FeO_x has a much higher activity. Onset happens 100°C earlier, around 400°C, and at 600°C

the conversion is at 80%. Then, complete conversion is reached after CFA, at 700°C. The higher catalytic activity of the composite phase could be due to the presence of $Ca_2Fe_2O_5$, which is a MIEC with a higher conduction than CFA. This confirms the previous assumption that often a higher mixed conductivity is linked to higher catalytic activity towards oxidation. From these data, it appears CFA + FeO_x should not be suitable for operation in SC-SOFCs, because of a quite high catalytic activity that would deplete excessive fraction of the reactants. Nonetheless, as indicated by XRD, after the electrode firing the $Ca_2Fe_2O_5$ disappears leaving its place again to a mixed brownmillerite of iron and aluminium, hence it is expected the catalytic activity of the cathode after firing to be described better by the CFA curve, rather than the one of CFA + FeO_x. The results of cells selectivity, shown in the following paragraph, confirm this expectation. For comparison purposes, it is also shown a conversion curve for methane oxidation catalysed by CGO measured with the same experimental setup, in Figure 6.11.

6.3.7 EIS and fuel cell performances

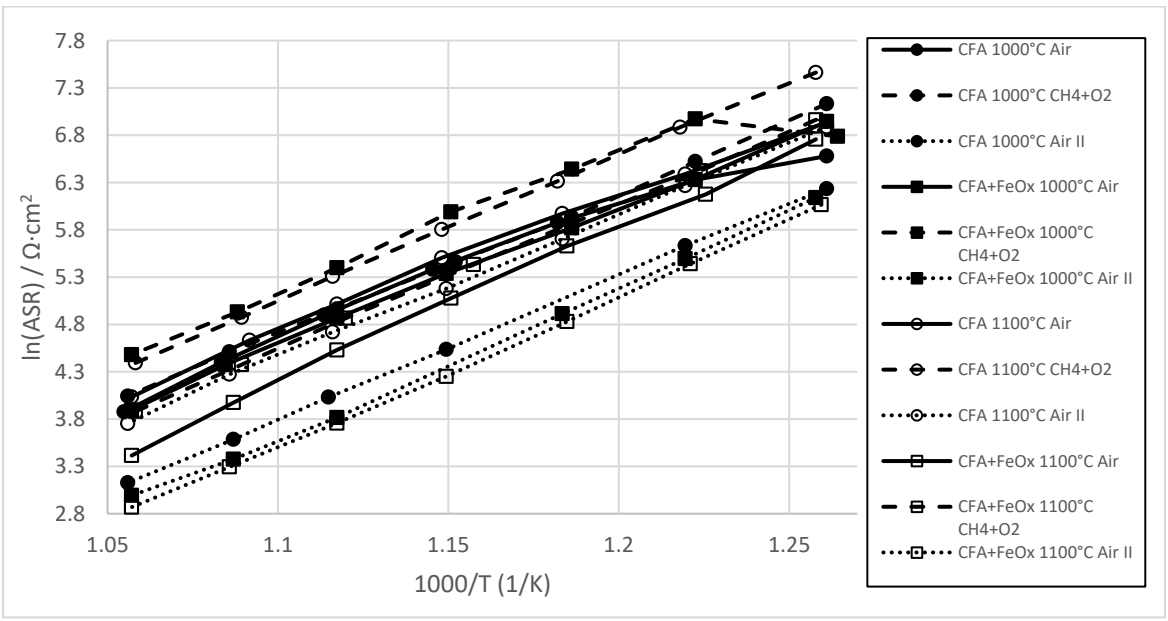

Figure 6.12 Above: model circuit used for EIS data fitting. Below: ASR of tested samples.

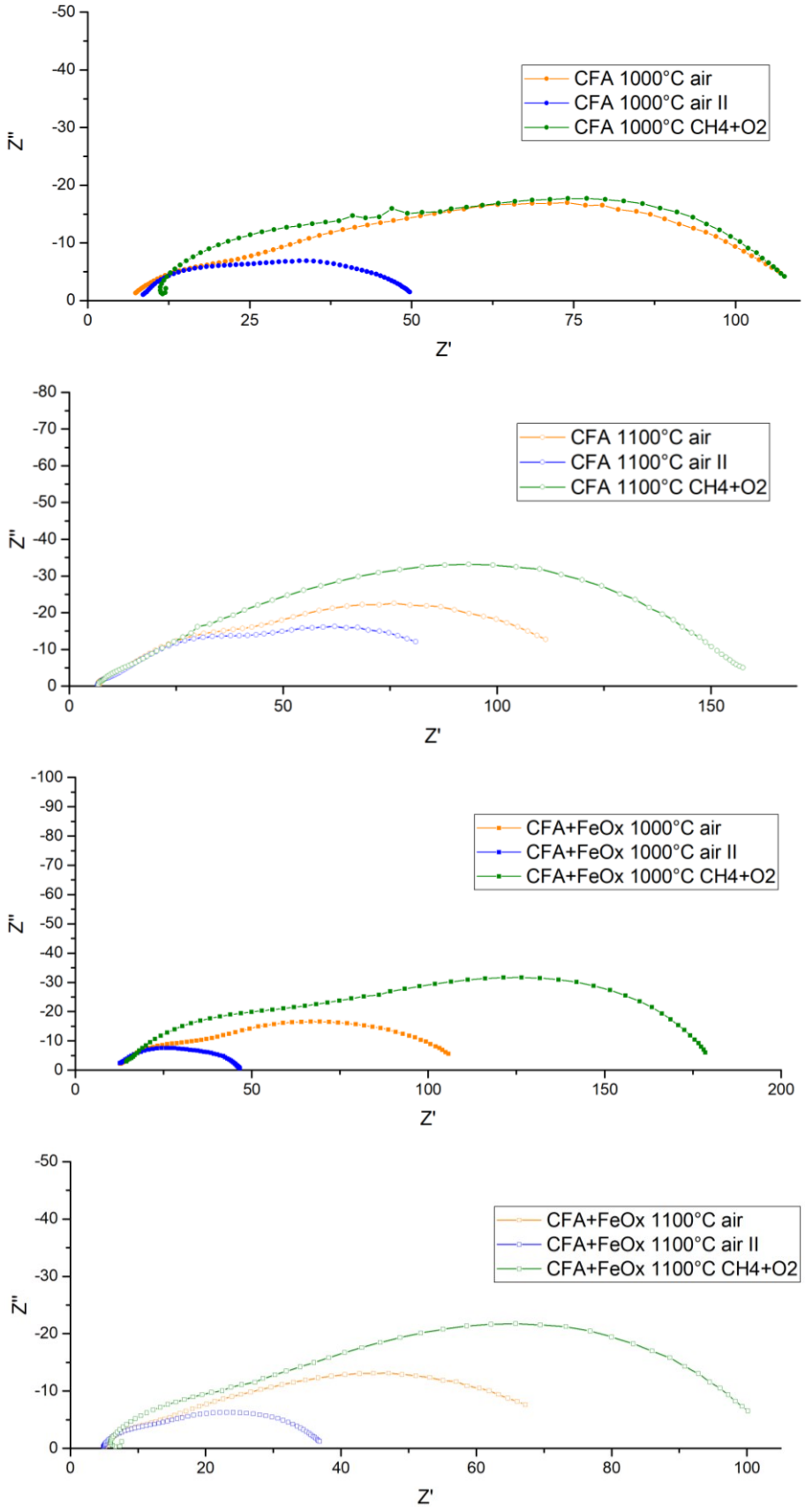

Figure 6.13 Nyquist plot of impedance spectra of symmetric cells at 620°C.

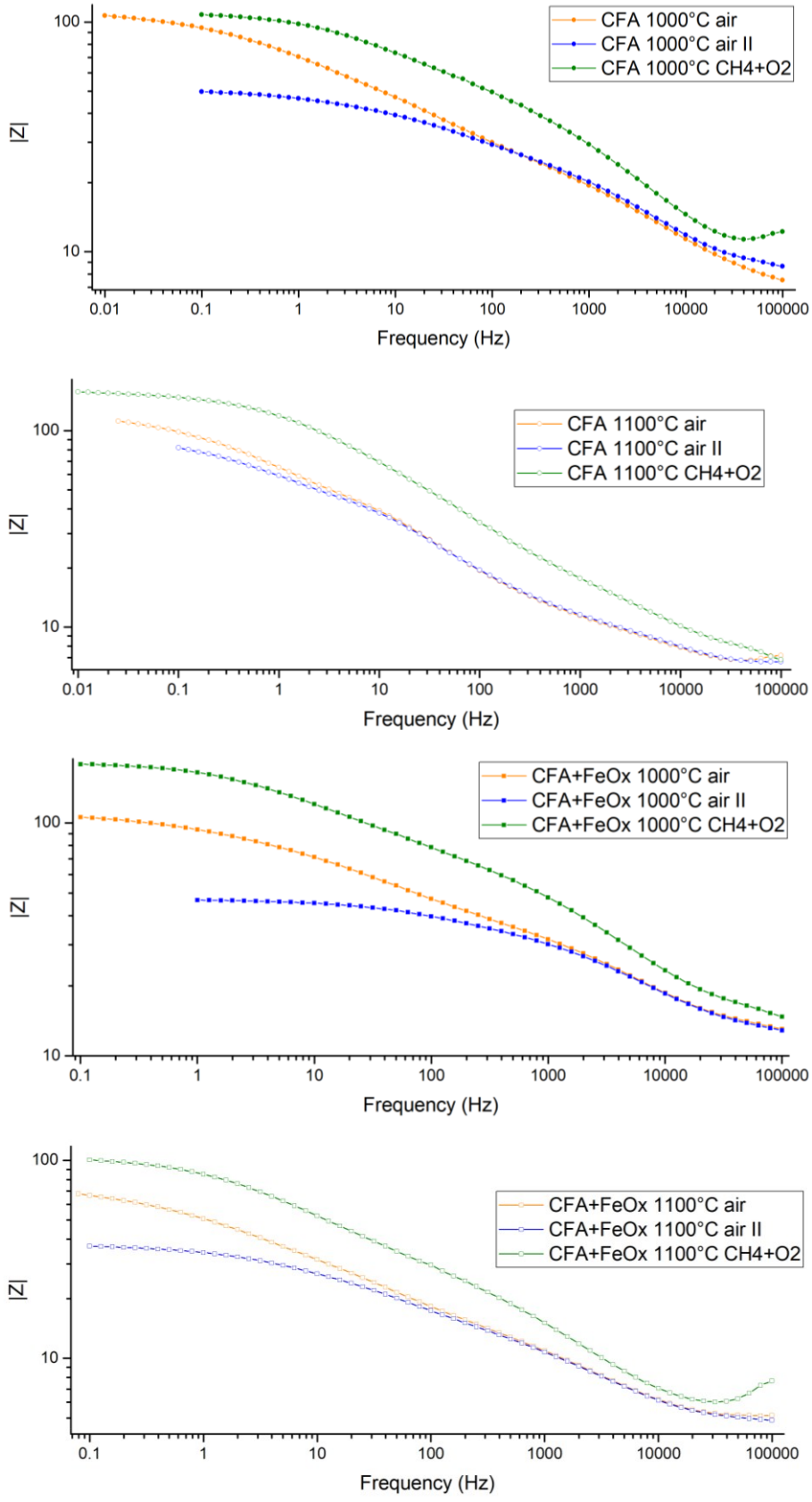

Figure 6.14 Bode plots of impedance magnitude of symmetric cells at 620°C.

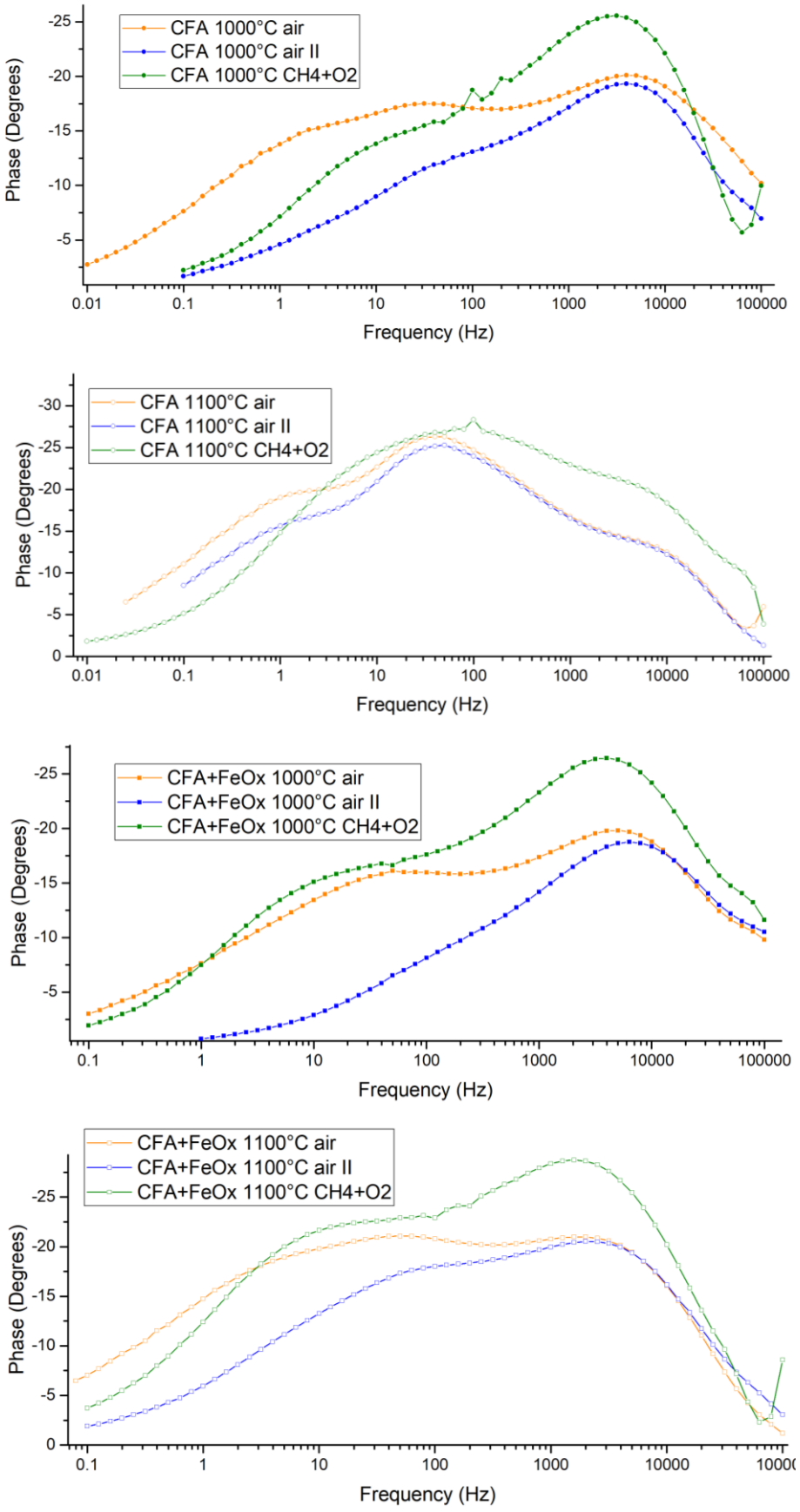

Figure 6.15 Bode plots of impedance phase of symmetric cells at 620°C.

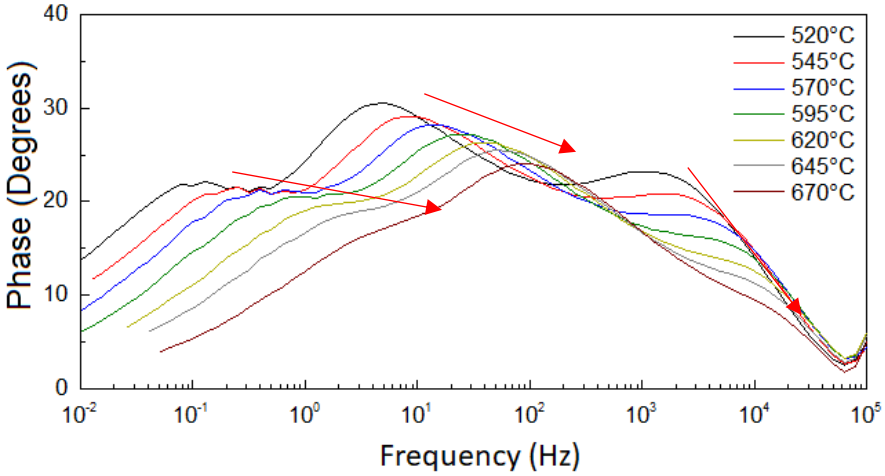

Figure 6.16 Bode plot of the impedance phase of CFA treated at 1100°C under air (first measurement), showing the frequency shifts of the resistive processes depending on temperature.

The differences between the cathodes CFA and CFA + FeO_x are small but significant. CFA is entirely composed by $Ca_2FeAl_{0.95}Mg_{0.05}O_5$ brownmillerite. CFA + FeO_x originally was $Ca_2FeAl_{0.95}Mg_{0.05}O_5$, then the FeO_x induced the decomposition into at least 4 phases: srebrodolskite, mayenite and calcite evidenced by XRD and also iron oxide shown by TPR. Then the thermal treatment during electrode firing synthesized again $Ca_2FeAl_{0.95}Mg_{0.05}O_5$, but crystallinity is different from as-synthesized sample. While some amorphous fraction is excluded as the XRD baseline is flat, more secondary non-identified species are present and determine the poor signal to noise ratio of the XRD plot. Such phases are small in amount, but they certainly bring an important contribution, because impedance spectra differ significantly, as well as the shape of the curves. For the sake of brevity, only 620°C EIS spectra have been reported.

Figure 6.13 shows the Nyquist plots, Figure 6.14 and Figure 6.15 are the Bode plots respectively of magnitude and phase, and Figure 6.16 shows the frequency shifts depending on temperature of the observed processes. The interpretation of these spectra is not easy, but it is possible to get some insight about the actual mechanisms, or at least to make some hypothesis. The way oxygen goes from molecular in gas phase to ion in the electrolyte depends heavily on cathode characteristics; including geometrical ones as porosity, tortuosity, thickness, and chemical ones as catalytic activity, ionic and electronic conductivity. An exhaustive decryption of the processes

at place and of their kinetics of a cathode never tested before is beyond the scope of this thesis.

The different atmospheres the sample experiences in this series of tests have not only effects on the ongoing process, but can also modify the sample. When changing from air to oxygen/methane mixture, it is possible that under the new conditions some site is reduced, or the amount of vacancies in the material can change. These effects sum with the consequences of carrying out the process under different conditions, and it is not always clear which variation is caused by what. This sum of effects is certain, because when reverting to oxygen after measurements under $CH_4 + O_2$, equal results are never obtained. Instead, a second measurement under $CH_4 + O_2$ always gives the same results of the first one. Second measurements under $CH_4 + O_2$ are not reported here, because they were done only as spot checks. So, the material tested during first air measurement is not exactly the same of the one under $CH_4 + O_2$.

Under air, up to three different resistive processes can be distinguished, on the basis of their frequency they can be labelled as High Frequency (HF), Medium Frequency (MF) and Low Frequency (LF); the latter is observed only in some samples and conditions. The resistance of the HF process is highly dependent on oxygen concentration in all the samples, and its apex frequency is dependent on the temperature. It is fitted with a R//CPE element. The frequency close to 10^4Hz in SOFCs can be attributed to the O^{2-} transfer at the electrode/electrolyte interface[270], the observed capacitance around 10^{-5}F/cm^2, compatible with a double layer, is consistent with this interpretation[271]. Such a process would be influenced by which phases really compose the interface, these phases could be different from the bulk ones, and their formation would be influenced by the atmosphere (hence pO_2)[95]. This phenomenon has already been observed in other cases, as for YSZ/LSM interfaces[272], and related to changes of the impedance response[273], so could be involved also in the present case.

The MF process depends on the atmosphere, its apex frequency is strongly influenced by the temperature and is well fitted be a R//CPE. It is the main contribution to resistance, and probably represents the oxygen reduction process; its

resistance slightly increases from air to CH_4+O_2 and strongly decreases when going back to air, something analogous of what was observed on LSGF (Chapter 3). The reduction of some superficial sites, carried out by methane, can potentially modify catalytic activity permanently, and could be at the base of the changes of the resistance.

The LF process is very well fitted by a Warburg element, the change of atmosphere from air to CH_4+O_2 make it disappear, and only in the samples treated at 1100°C it is observed again during the second measurement in air. CFA + FeO_x never features it. Diffusive processes at very low frequencies can be associated to oxygen diffusion in the gas phase inside the porosities of the electrode[245], but in this case the decrease of resistance when pO_2 decreases excludes this interpretation (diffusion of oxygen is easier when it is more concentrated, not the opposite). So, this process could be related to the electrode diffusion of oxygen ions, either superficial or bulk, depending on which path is preferred for this material. If the bulk path is preferred, a decrease of pO_2 can induce an increase of vacancies of CFA and speeds up ionic conduction; on the other hand, diffusion of O^{2-} in bulk electrode is in general observed ad higher frequencies (see Chapter 3 and [225]). If the surface path is preferred, superficial sites are influenced by atmosphere and the mobility of adsorbed oxygen could vary depending on pO_2.

It is possible also that the reason the LF process is observed only in some case is that it is related to a specific path that is chosen depending on the conditions; consistently, its presence indicates that only during those particular measurements oxygen was moved via the path the LF semicircle is associated with. The process is very temperature sensitive (Figure 6.16), and tends to shift at higher frequency and disappear at increasing temperature; such a remarkable change can be associated to a change, depending on temperature, of the limiting phenomenon. Such a result would be in accordance with a surface diffusion. In general, overall resistance is higher when the atmosphere is changed to CH_4+O_2, because of a significant increase of the resistances associated to the HF and MF processes.

The disappearance of the LF process could be also linked to the increase of the resistance of the others two, in case the LF phenomenon was able to affect the HF

and MF ones. An example could better explain what this means, clarifying that it is only a hypothesis and there is no data to support it. We consider a scenario in which for CFA it is very difficult to move oxygen across its interface, both from atmosphere to its crystalline structure and from its crystalline structure to the electrolyte. If the oxygen transport is carried out through the surface, as it has been suggested, the whole cathode mechanism is composed of: reduction of oxygen from O_2 to ion (MF process), transport of the ion to the electrolyte (LF process) and exchange of the oxygen ion with the electrolyte (HF process). This way, the cathode avoids the incorporation of oxygen, which would be difficult for it. But, a different atmosphere, as the CH_4+O_2 instead of air, can change the superficial sites and make unavailable the superficial ionic conduction path. In this case, the Warburg element (LF), that is related to the superficial conduction, disappears, the oxygen reduction (MF) increases because of the difficult incorporation into the lattice and the ionic exchange (HF) increases too. The bulk diffusion of oxygen would not be evident as it would be less limiting than the other two processes. This is what is observed when atmosphere is changed from air to methane: LF disappears, MF and HF increase. Note that HF in Bode plots (Figure 6.15) was always found at the same frequency and always had the same shape, while MF is more variable, so it could be that time to time MF represents a different limiting step of the oxygen reduction depending on the material. The atmosphere influences superficial sites and could determine the availability of superficial diffusion. In any case, the increase of resistance under CH_4+O_2 atmosphere is significant, in spite of the disappearance of the LF resistance. The measurement in air after CH_4+O_2 reduces the resistance at about one half the first measurement in air, mainly due to the decrease in MF: the reduction of some metallic centres was probably able to improve the materials catalytic activity. After all, considering the performances observed with these measurements, the performance of CFA is mediocre, compared to other materials; its ASR is one order of magnitude higher than state of the art materials.

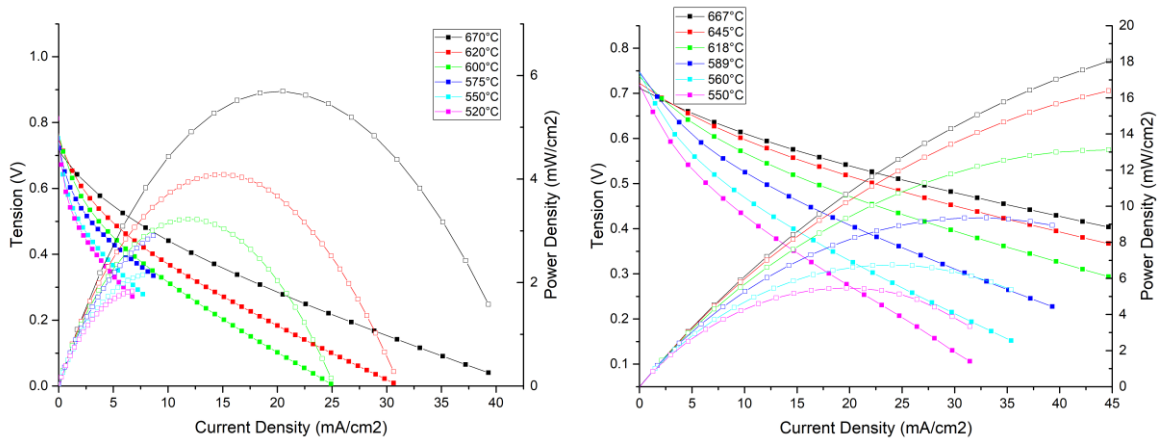

Figure 6.17 Polarization curves and power of cells with CFA treated at 1000°C (left) and CFA+FeO_x (right) treated at 1100°C (right) cathodes. Anode is Ni/CGO and electrolyte is CGO

Figure 6.17 shows the current and power output of complete single chamber fuel cells with CFA based cathodes. Two cells have been tested, one with CFA and one with CFA + FeO_x. Cathodes have been fired at the temperature that allowed to reach the lowest resistance during EIS measurements, so 1000°C for CFA and 1100°C for CFA + FeO_x. The results of these measurements prove that CFA actually work as cathode for single chamber fuel cells. Compared to state-of-the-art cells, the power output is low, as it could be expected from the high ASR from single chamber measurements. In any case, it is remarkable that a material never tested for this application, without any kind of noble, toxic, rare or expensive component, is able to operate a fuel cell. ASRs of CFA and CFA + FeO_x as measured by EIS in symmetric cell were almost similar, nonetheless power obtained from polarization curve are quite different. In fact, CFA + FeO_x is able to produce a power output three times higher than CFA, reaching values close to 20mW/cm².

So, the deposition of the iron oxide, in spite of the devastating effect it had on the brownmillerite, at the end was effectively able to improve the performances of the material. Regrettably, solely with available data, it is not possible to understand which mechanism is involved. No kind of optimization has been carried out on these samples as it was not the aim of this work, so a more accurate study of the deposition should improve the performances at some extent. Power output of a cell with CFA based cathode could be even better in double chamber architecture: as measured by means of EIS, the resistance in air is 1/3 the one under the atmosphere single chamber

cells operate, so better values would be probably obtained under atmospheres richer in oxygen.

As already mentioned, selectivity of the cathode is one of the most difficult and important issues in SC-SOFCs. In order to verify if the selectivity target has been reached, some preliminary test has been performed on the same cathodes tested in complete cells. Ideally, from the outlet of the cathode only oxygen, methane and inert gases should be found, because the only process happening in theory is oxygen transfer to the anode. All the products of a combustion (as CO_2 and CO) are result of parasitic undesired reactions. The results were found to be identical in both the tests of CFA and CFA + FeO_x, this means that the processes involved in the parasitic reactions were only catalytic: if electrocatalysis was involved, it would have had some dependence on the cell power. Furthermore, the catalytic activity of the composite electrode is the same of the simple CFA, so the formation of the $Ca_2FeAl_{0.95}Mg_{0.05}O_5$ phase again avoids the increase of activity of the non-treated sample, as verified in the previous paragraph.

During the selectivity tests, a concentration of 400ppm of CO_2 was detected, and no CO was found. Considering methane Low Heating Value (LHV) as a reference and comparing with the gas flow, this methane conversion corresponds to a power loss of 30mW. This is a very promising result. Electrodes, for adherence reasons, have been made, in fact, of a composite of CFA and CGO. Between the two materials, CGO has a decent catalytic activity towards methane oxidation from 520°C; whereas CFA, as previously shown, at 600°C shows only modest activity. So, a large part of the lost fuel should not to be ascribed to CFA. In any case, even in the current situation, estimating an equal power loss also at the anode side, the cell was able to convert into energy 25% of the consumed fuel. Unfortunately, it is not possible to calculate the actual efficiency of the cell, as the used setup did not allow a proper gas management, which was also beyond our scope.

A possibility to further improve the result is to change the electrolyte to YSZ, which could be the most suitable electrode material for SC-SOFCs[251]; in any case this would require a dedicated study of the treatments for the deposition of the electrodes, that could be different depending on the electrolyte. Then, an

optimization of the electrode deposition would be appropriate, as well as a more accurate gas management. With those described improvements, a SC-SOFC based on CFA has strong chances of attaining the best efficiency ever for a SC-SOFC. On the other hand, as it was in the premises of this work, the power output would not compare with current double chamber SOFC, but this is evidently the price to pay for selectivity.

6.4 Conclusions

A specific material for cathodes of SC-SOFCs has been designed aiming to obtain a material with specific properties in terms of process efficiency. During the material design, the requirement of a final high power output was deliberately dropped in order to maximize the selectivity. CFA and its derivative CFA + FeO_x have been successfully synthesized and completely characterized. Symmetrical cells with CFA and CFA + FeO_x have been fabricated and tested by means of EIS, the respective electrode firing temperatures have been optimized. ASR were calculated, obtaining high overall values, but in line with expectations. Then, complete cells have been prepared and tested as power output and, preliminary, efficiency. Results confirm initial targets were reached, as cell showed an optimal efficiency.

7 LSGF composites as O_2 semi-permeability membranes

LSGF COMPOSITES TESTED ALSO AS PERMEABILITY MEMBRANES
AND IMPLICATIONS OF SEMI-PERMEABILITY RESULTS REGARDING MATERIALS STRUCTURES

7.1 Introduction

As outlined in the introduction, MIEC materials find wide application for oxygen separating membranes, in processes for oxygen purification[133]. In these devices, a mixture of gases is pushed towards a dense MIEC ceramic membrane at high temperature, oxygen is reduced to O^{2-} at the MIEC's surface and incorporated into the crystalline lattice, as in a common SOFC electrode. Oxygen anions then flow to the other side of the membrane thanks to the ionic conductivity of the material, while a movement of electrons in the other direction keeps electrical neutrality. The driving force of the whole process is the difference in the partial pressure of oxygen between the two sides of the membrane[135]–[137]. In effect, features allowing a material to operate as a SOFC cathode or an oxygen membrane are very similar, for example, the mixed conductivity is required in both the cases, and the process is similar.

There are, as well, some important differences. In SOFC anodes the ionic conductivity is important, but not fundamental, as the reaction can be restricted to the areas close to interface with the electrolyte. Depending on the distance the ions are supposed to travel, the material can change its type of ionic conduction (for example bulk or superficial). For membranes ionic conduction is fundamental, and being in general a slow process, it is the one which determines the performance in case of thick membranes[139]; on the other hand, it has been determined that also superficial processes can have an influence[151]. The identification of the steps is different for cathodes, where more factors are involved, including the presence of an electrical potential and of processes related to the electrochemistry of the interfaces. Membranes, in addition, must be able to catalyse also oxygen re-oxidation and

desorption to atmosphere. In any case, good cathode materials tend to be good membrane materials, and vice-versa. Stability with low pO_2 is very important in oxygen separation membranes: on the side where oxygen is released pO_2 is inevitably low (otherwise there would be no driving force to push the purification). For these reasons, the synthesized materials LSGF, LSGF + MnO_x and LSGF + FeO_x have been tested also for oxygen separation.

In oxygen semi-permeability measurements, a dense pellet of the MIEC material is heated at high temperature. On one side, oxygen concentration is kept constant with a continuous flow of air. The other side is gas-sealed, and a flow of argon sweeps the surface on the pellet and collects the permeated oxygen, which is measured by an appropriate detector. Oxygen flow is finally related to the surface of the pellet.

7.2 Experimental

LSGF, LSGF + MnO_x and LSGF + FeO_x were synthesized as indicated in chapters 2 and 3. Powders were finely grinded and pressed into dense pellets, which were fired at 900°C. After the firing, the pellet thickness is 1 mm. The fired pellet was attached to a MACOR tube with Aremco Ceramabond 571 cement. The tube was sealed with Arexons Seal 5661 silicone on a flat base. A pipe under the pellet provided argon feeding and kept a thermocouple in position close to the surface. The tube with the pellet was placed inside a chamber with outlet open to the atmosphere, a pipe close to the upper pellet surface was used to flush synthetic air. A resistance outside the chamber heated the membrane, and a ESS Evolution quadrupole mass spectrometer was used to analyse the composition of the gas from the lower side of the pellet. Quantitative concentration data of oxygen were calculated on the basis of calibration with standard gases. The contribution to the oxygen signal of the leakages were calculated through the nitrogen signal and subtracted to the total oxygen concentration.

7.3 Results and discussion

The results of the measurements are shown in Figure 7.1. In general, all the curves are similar, and the presence of MnO_x of FeO_x seems to have not affected extensively the process. This proves that ionic conductivity is the real limiting step of the process,

because the impregnated oxides cover some fraction of the surface but this does not seem to have any influence on the oxygen flux. Measurements in chapter 3 indicates the presence of the impregnated oxides modified LSGF oxygen transport properties, but nothing of that effect is found again in semi-permeation measurements. There are two possible explanation to this fact. First, the calcination temperature is different (only 900°C for membranes and 1000°C or higher for cathodes), and this can influence how the impregnated phases interact with the LSGF substrate. Second, the examined conduction mechanism could be different, as mentioned in the introduction, so the impregnated phases were able to impact (positively for FeO_x, negatively for MnO_x) on transport of oxygen if there is an electrolyte in the close range, both are not effective for the transport mechanism used to reach long distances.

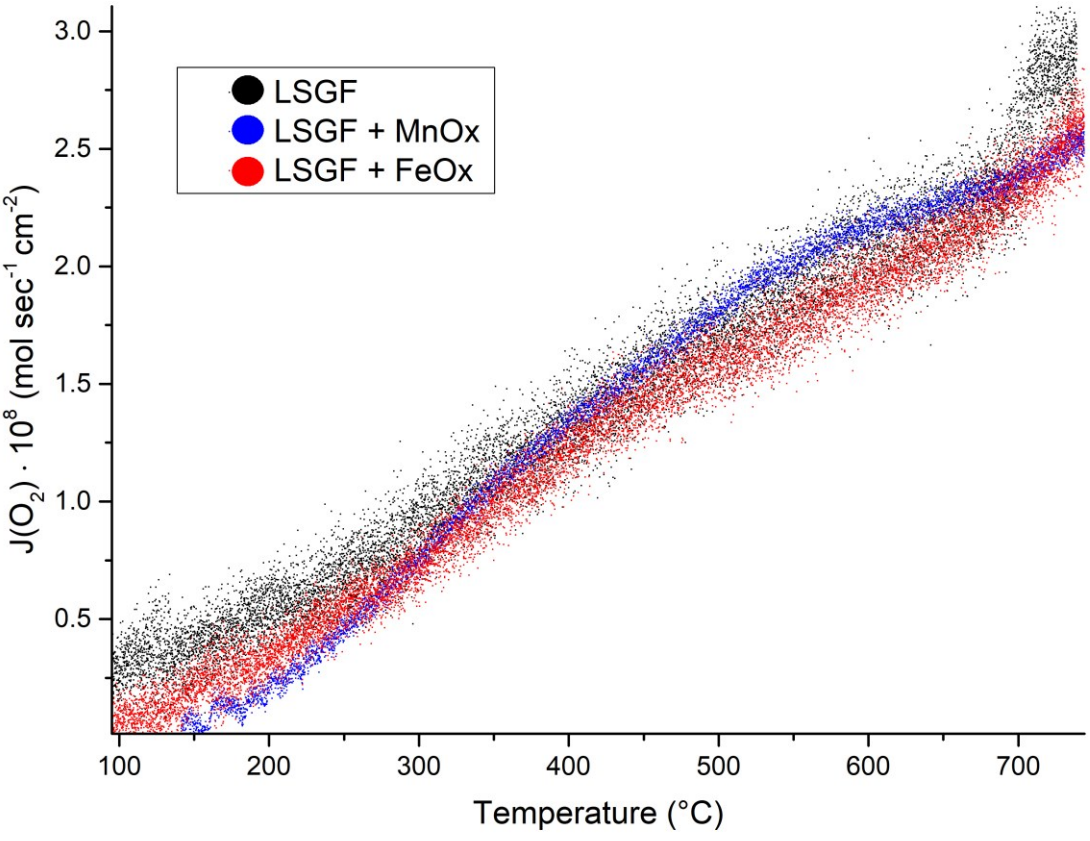

Figure 7.1 Results of oxygen semi-permeation measurements on pellets made of LSGF and LSGF based nanocomposites.

Compared to existing literature, the results obtained in this work are similar to values reported elsewhere. Ishihara et al.[274] found higher permeation rates, around $40{\cdot}10^{-8}$mol·s^{-1}·cm^{-2}, for materials with a higher Ga content, but they did not quantify

the effect of leakages, that are always present. Etchegoyen et al.[152] worked on $La_{0.6}Sr_{0.4}Fe_{0.9}Ga_{0.1}O_3$ membranes laminated from tape casted thick layers, the powder was prepared by means of solid-state synthesis, and found in general lower fluxes than the one reported here. In any case, according to Vivet et al.[151], a higher amount of Ga is beneficial for oxygen semi-permeation. Kharton's group worked on membranes pressed from solid-state synthesized powders, and has reported several measurements on LSGF membranes with different compositions. In general, their results are similar to what found in our measurements [260], [275]. There is no wide accordance about the rate limiting step for oxygen semi-permeation in LSGF-type materials. Some authors suggest a clear limitation by surface exchange mechanisms[151], [276], while others report fluxes controlled by bulk processes[152]. From our data, a bulk control appears more probable, because the surface of the three membranes is significantly different, due to the presence of the deposited oxide, and no important variation is observed between the three curves.

8 Conclusions

During this thesis, an innovative approach for the development of functional materials has been elaborated. All the materials have been designed attempting to find a positive synergy between a substrate and a deposited phase, that would allow to reach superior performances, while limiting the use of noble metals or expensive elements in general. The aim of this work was the design of novel materials for high temperature ceramic cells. The main focus was in particular on two innovative devices: the reversible Solid Oxide Fuel Cells, able to work both as fuel cells and electrolysers, and the Single Chamber Fuel Cells, which work without any separation between anodic and cathodic compartment.

First, a suitable substrate material has been searched in existing literature. Required properties were the resistance at high temperature in both oxidizing and reducing conditions, a good mixed conductivity (so, both ionic and electronic), the total avoidance of noble metals and in general the limitation of the materials considered critical by the European Union, or the too expensive ones. A perovskite named LSGF with composition $La_{0.6}Sr_{0.4}Ga_{0.3}Fe_{0.7}O_3$ was identified as the material best matching the outlined requirements. The synthesis of LSGF, by means of a wet-chemistry procedure, has been studied in depth. This route, compared to conventional solid state synthesis, uses only moderately high temperatures and only for limited times, hence is simpler, faster and cheaper. LSGF, as a perovskite, has a good resistance under air atmosphere, even at high temperature. On the other hand, chemical stability in environments characterized by low oxygen partial pressure is a concern, because the reduction of metallic cations is able to disrupt the crystalline structure. So, resistance of LSGF under 5% H_2 atmosphere has been fully assessed. During measurements, 750°C has been identified as the maximum prudential safe temperature. In addition, the reversibility of the perovskite degradation with reduction treatments up to 1000°C has been demonstrated to be possible with a simple 6 hours oxidation under air at 900°C.

LSGF has been then impregnated with selected cheap metals in order to obtain the desired properties. Among all the simple oxides, the ones of Fe and Mn have been chosen. The presence of redox couples for both of them should push the development of an electrocatalytic activity when coupled with LSGF. The composite electrode materials were obtained with a wet impregnation synthesis. These materials have been fully characterized, and in general complex interactions between the deposited phases and LSGF were encountered. Then, they were tested as SOFC cathodes in EIS tests. The LSGF + FeO_x showed promising performances, and was able to reduce the LSGF ASR by a factor of 0.3. This improvement has been attributed to the formation of thin foils that connect LSGF particles and in some way speed up the oxygen reduction and transport processes. Regrettably, the impregnation with MnO_x was not able to bring any improvement compared to a pure LSGF cathode.

After the fair performances of LSGF as a substrate for SOFCs, its employment in reversible symmetric solid oxide cells has been tested as well. The electrolyte used was LSGM, because its composition similar to LSGF should guarantee a higher chemical stability of the device. After a very slow reaction rate was detected for the negative pole when only LSGF was used, the electrode has been impregnated by means of a dry impregnation procedure with CGO and Pd. The formation of Pd nanoparticles on a CGO compact layer was verified, and performances in fact were greatly improved for both the fuel cell and the electrolyser mode. LSGF has confirmed its suitability for this application. In addition, an interesting interaction between LSGF and gold was found, with the perovskite being able to induce gold melting at 800°C under a reducing atmosphere.

The LSGF + MnO_x nanocomposite, after the poor performances as a cathode, was tested as an anode material. The presence of manganese is able to boost the performances of the electrode by a factor 10, compared to the pure LSGF. A cell supported on a LSGM electrolyte, with LSGF + FeO_x as cathode and LSGF + MnO_x as anode has been prepared, and has shown promising performances with very high OCV values. In particular, operation under propane gave very interesting results.

A particular geometry of SOFC, the Single Chamber Cell, has been considered in this work has well. Such cells offer significant advantages compared to conventional

SOFCs for small application, but their efficiency is heavily dependent on the selectivity of the used materials. With the same approach outlined before, a specific cathode material for SC-SOFCs has been designed and synthesized. As substrate, the $Ca_2FeAl_{0.95}Mg_{0.05}O_5$ (CFA) brownmillerite has been synthesized and characterized. Then, it has been attempted to replicate LSGF improvements with an impregnation with iron oxide. Both CFA and CFA + FeO_x were tested in symmetric cells for EIS measurements and in complete cells with a state-of-the-art anode. Both the materials were able to carry out cathodic reaction, although simple CFA gave an extremely low power output, OCV was decent for a SC-SOFC, around 0.75V. CFA + FeO_x cathode produced a 20mW/cm² power output, low compared to conventional SOFCs, but promising considering the cheapness of the materials used. The selectivity, the crucial feature targeted in this part of the work, was tested by means of a preliminary efficiency test of the cells. Both CFA and CFA + FeO_x showed considerably low losses of fuel due to parasitic reactions, that were mainly attributed to factors external to the cathode material. Hence, CFA-based compounds should be considered as an interesting starting point for the development of truly efficient SC-SOFCs.

Finally, LSGF composites have also been tested as oxygen semi-permeability membranes. The obtained results are good, although it is not possible to find significant effect of the impregnation in these cases.

8.1 Outlook

The explorative nature of this thesis opens different possibilities for further development. The materials, in particular the composite electrodes, can be optimized towards higher performances. The deposition protocol leaves room for advances, so higher power could be easily reached. For example, the implementation of a ball milling step in the powders' fabrication could be a first quick improvement, this has not been possible until now because of the low amount of powders being synthesized. An exhaustive study of the behaviour of the composites of LSGF and the deposited oxides could be interesting, in particular the nature of the foil arising from FeO_x presence is not satisfyingly explained yet, and the interaction between LSGF and MnO_x is still not clear. It is also possible that the positive effect of FeO_x can be replicated for different ferrites and other perovskites. With the LSGF + MnO_x anode

operated with propane a high diffusion limited resistance is reported, this could be eliminated with a higher attention to porosity and electrode's morphology. This, joint to a full assessment of the stability of the anode towards deactivation by carbon deposition, could present LSGF + MnO_x as a good candidate for direct carbon SOFCs.

The study of LSGF-based reversible cells was only preliminary, and a deeper assessment would be required. In particular, the stability of the device over long times of operation must be examined, and the resistive process impeding operation of the electrolyser below 0.7V must be identified. The study of a reversible cell with composite electrodes, avoiding the palladium presence, could give good results.

CFA-based cathodes have good perspectives towards the development of a truly selective SC-SOFC, but their selectivity must be measured comprehensively with the examination of a device, based on YSZ electrolyte, on a scale larger than the laboratory level this thesis corresponds to. It has to be underlined that a simple Single Chamber device, with YSZ electrolyte, Ni-YSZ anode and CFA + FeO_x cathode would be extremely cheap, because it would be sufficient to connect electrically the electrodes, place it in a sealed chamber with gases flowing and heat it to obtain electrical power. This perspective deserves some attention, even if current powers are still low.

Acknowledgements

This work would be certainly worse without the invaluable help of many people. First of all, my supervisor Prof. Antonella Glisenti, who guided my faltering steps through the first experiences of scientific research. She supported me with great kindliness and understanding all along these three years, I would not have enjoyed my PhD so much without her.

Most parts of this thesis would not have been possible without the kindness and the help of our colleagues from the École des Mines of Saint-Étienne, Dr. Mathilde Rieu and Prof. Jean-Paul Viricelle. They introduced me to the EIS for the first time, chapter 3 and 6 have been developed in their laboratories. My gratitude is not only professional, but sincerely personal, because they made me my stay *chez eux* a real pleasure, I never had a single occasion where I felt uncomfortable. I must not forget also all the staff and the PhD students of the École des Mines, you are too many and I cannot name everybody, but I had a very great time with you.

Chapter 4 has been entirely conceived and carried out in the facilities of the School of Chemistry of the University of St Andrews, Scotland, under the supervision of Dr. Cristian Savaniu and prof. John Irvine. It has been a period of great professional growth for me, and I thank them sincerely for their invaluable suggestions and their hospitality.

Chapter 5 is part of a joint project between us, the University of Udine (prof. Marta Boaro) and the University of Genova (prof. Antonio Barbucci and Dr. Davide Clematis), who willingly accepted to try to build a complete cell from the materials we developed in Padova. Dr. Davide Clematis has my gratitude also for its patience in introducing me to the secrets of EIS interpretation.

My research group, IMPACT, small but fierce, has made this work a real fun, I think we have done great things in these years. Above all I want to mention our saint Michael Pacella, may he guide us from the Zoppas, the Mega-Director Alberto and

the ever-ready uber-efficient Giovanno, thanks for the wonderful time we spent together.

Life is not only work, rather, one does not make good jobs if he is not content with his life beyond work. So, I reckon I have to mention also somebody that contributed indirectly, but whose contribution has been fundamental.

So, I want to thank my family, which has sustained me (literally and economically) during this years, I would not have reached this goal without them.

And last but not least, a huge thank to Lorenza, who always cared about me also in the most difficult moments and is not fed up with me yet.

References

[1] M. Grätzel, "Photoelectrochemical cells," *Nature*, vol. 414, no. 6861, pp. 338–344, Nov. 2001.

[2] British Petroleum, "BP Statistical Review of World Energy 2017," 2017.

[3] K. Bleich and R. D. Guimaraes, "Renewable Infrastructure Investment Handbook: A Guide for Institutional Investors," 2016.

[4] D. M. Chapin, C. S. Fuller, and G. L. Pearson, "A New Silicon p-n Junction Photocell for Converting Solar Radiation into Electrical Power," *J. Appl. Phys.*, vol. 25, no. 5, pp. 676–677, May 1954.

[5] M. L. McKinney and R. M. Schoch, *Environmental Science: Systems and Solutions*. Jones & Bartlett Learning, 2003.

[6] V. Smil, "World History and Energy," in *Encyclopedia of Energy*, vol. 6, Elsevier, 2004, pp. 549–561.

[7] P. Brimblecombe, "Attitudes and Responses Towards Air Pollution in Medieval England," *J. Air Pollut. Control Assoc.*, vol. 26, no. 10, pp. 941–945, Oct. 1976.

[8] C. Uglietti, P. Gabrielli, C. A. Cooke, P. Vallelonga, and L. G. Thompson, "Widespread pollution of the South American atmosphere predates the industrial revolution by 240 y," *Proc. Natl. Acad. Sci.*, vol. 112, no. 8, pp. 2349–2354, Feb. 2015.

[9] S. Hong, J.-P. Candelone, C. C. Patterson, and C. F. Boutron, "Greenland Ice Evidence of Hemispheric Lead Pollution Two Millennia Ago by Greek and Roman Civilizations," *Science (80-.).*, vol. 265, no. 5180, pp. 1841–1843, Sep. 1994.

[10] U.S. Energy Information Administration, "International Energy Outlook 2017 Overview," *Int. Energy Outlook*, vol. IEO2017, no. September 14, 2017.

[11] F. Barbir, T. N. Veziroğlu, and H. J. Plass, "Environmental damage due to fossil fuels use," *Int. J. Hydrogen Energy*, vol. 15, no. 10, pp. 739–749, 1990.

[12] C. Olson and F. Lenzmann, "The social and economic consequences of the fossil fuel supply chain," *MRS Energy Sustain.*, vol. 3, p. E6, 2016.

[13] B. Pandey, M. Agrawal, and S. Singh, "Assessment of air pollution around coal mining area: Emphasizing on spatial distributions, seasonal variations and heavy metals, using cluster and principal component analysis," *Atmos. Pollut. Res.*, vol. 5, no. 1, pp. 79–86, 2014.

[14] V. K. Mishra, A. R. Upadhyaya, S. K. Pandey, and B. D. Tripathi, "Heavy metal pollution induced due to coal mining effluent on surrounding aquatic ecosystem and its management through naturally occurring aquatic macrophytes," *Bioresour. Technol.*, vol. 99, no. 5, pp. 930–936, 2008.

[15] R. B. Finkelman, "Potential health impacts of burning coal beds and waste banks," *Int. J. Coal Geol.*, vol. 59, no. 1–2, pp. 19–24, 2004.

[16] P. R. Epstein, J. J. Buonocore, K. Eckerle, M. Hendryx, B. M. Stout III, R. Heinberg, R. W. Clapp, B. May, N. L. Reinhart, M. M. Ahern, S. K. Doshi, and L. Glustrom, "Full cost accounting for the life cycle of coal," *Ann. N. Y. Acad. Sci.*, vol. 1219, no. 1, pp. 73–98, Feb. 2011.

[17] R. W. Howarth, R. Santoro, and A. Ingraffea, "Methane and the greenhouse-gas footprint of natural gas from shale formations," *Clim. Change*, vol. 106, no. 4, pp. 679–690, 2011.

[18] D. Hughes, *Will natural gas fuel America in the 21st Century?* 2011.

[19] T. Bakke, J. Klungsøyr, and S. Sanni, "Environmental impacts of produced water and drilling waste discharges from the Norwegian offshore petroleum industry," *Mar. Environ. Res.*, vol. 92, pp. 154–169, Dec. 2013.

[20] C. Corden, R. Whiting, D. Luscombe, O. Power, A. Ma, J. Price, Mi. Sharman, and J. Shorthose, "Study on the assessment and management of environmental impacts and risks resulting from the exploration and production of hydrocarbons Final Report," 2016.

[21] N. Butt, H. L. Beyer, J. R. Bennett, D. Biggs, R. Maggini, M. Mills, A. R. Renwick, L. M. Seabrook, and H. P. Possingham, "Biodiversity Risks from Fossil Fuel Extraction," *Science.*, vol. 342, no. 6157, pp. 425–426, 2013.

[22] Oao "Taneco," "Environmental and Social Impact Assesssment (ESIA) for the Oil Refinery (Stage 1) of the TANECO Oil Refining and Petrochemical Complex, Nizhnekamsk, Republic of Tatarstan, Russian Federation," 2009.

[23] M. R. Narimisa and N. E. A. Basri, "A case study for environmental impact assessment of oil refinery in Iran with emphasis of Environmental and Social Action Plan (ESAP)," *2nd Int. Conf. Environ. Sci. Technol.*, vol. 6, pp. 334–337, 2011.

[24] H. Wake, "Oil refineries: a review of their ecological impacts on the aquatic environment," *Estuar. Coast. Shelf Sci.*, vol. 62, no. 1–2, pp. 131–140, Jan. 2005.

[25] J. S. Alshammari, F. K. Gad, A. a M. Elgibaly, A. R. Khan, and R. Engineering, "Solid Waste Management in Petroleum Refineries 1," *Am. J. Environ. Sci.*, vol. 4, no. 4, pp. 353–361, 2008.

[26] R. A. Alvarez, S. W. Pacala, J. J. Winebrake, W. L. Chameides, and S. P. Hamburg, "Greater focus needed on methane leakage from natural gas infrastructure," *Proc. Natl. Acad. Sci.*, vol. 109, no. 17, pp. 6435–6440, 2012.

[27] J. Tollefson, "Methane leaks erode green credentials of natural gas.," *Nature*, vol. 493, p. 12, 2013.

[28] EPA, "Methane and Nitrous Oxide Emissions from Natural Sources, a review." 2010.

[29] Greenpeace, "Silent Killers: Why Europe must replace coal power with green energy," no. June, p. 56, 2013.

[30] J. L. Mumford, X. Z. He, R. S. Chapman, S. R. Cao, D. B. Harris, X. M. Li, Y. L. Xian, W. Z. Jiang, C. W. Xu, and J. C. Chuang, "Lung cancer and indoor air pollution in Xuan Wei, China.," *Science*, vol. 235, no. 4785, pp. 217–220, 1987.

[31] M. Ando, M. Tadano, S. Asanuma, K. Tamura, S. Matsushima, T. Watanabe, T. Kondo, S. Sakurai, R. Ji, C. Liang, and S. Cao, "Health effects of indoor fluoride pollution from coal burning in China," *Environ. Health Perspect.*, vol. 106, no. 5, pp. 239–244, 1998.

[32] R. Chandrappa and U. Chandra Kulshrestha, *Sustainable Air Pollution Management*. Cham: Springer International Publishing, 2016.

[33] M. Kampa and E. Castanas, "Human health effects of air pollution," *Environ. Pollut.*, vol. 151, no. 2, pp. 362–367, 2008.

[34] C. A. Pope and D. W. Dockery, "Health effects of fine particulate air pollution: Lines that connect," *J. Air Waste Manag. Assoc.*, vol. 56, no. 6, pp. 709–742, 2006.

[35] S. Solomon, G.-K. Plattner, R. Knutti, and P. Friedlingstein, "Irreversible climate change due to carbon dioxide emissions.," *Proc. Natl. Acad. Sci. U. S. A.*, vol. 106, no. 6, pp. 1704–9, 2009.

[36] S. Arrhenius, "On theInfluence of Carbonic Acid in the Air upon the Temperature of the Ground," *Philos. Mag. J. Sci.*, vol. 41, no. 251, pp. 237–279, 1896.

[37] N. Ekholm, "on the Variations of the Climate of the Geological and Historical Past and Their Causes," *Q. J. R. Meteorol. Soc.*, vol. 27, no. 117, pp. 1–62, 1901.

[38] M. C. MacCracken and F. M. Luther, "Projecting the climatic effects of increasing carbon

dioxide," 1985.

[39] V. Ramanathan and Y. Feng, "Air pollution, greenhouse gases and climate change: Global and regional perspectives," *Atmos. Environ.*, vol. 43, no. 1, pp. 37–50, 2009.

[40] P. M. Cox, R. a Betts, C. D. Jones, S. a Spall, and I. J. Totterdell, "Acceleration of global warming due to carbon-cycle feedbacks in a coupled climate model.," *Nature*, vol. 408, no. 6809, pp. 184–187, 2000.

[41] B. J. Soden, A. J. Broccoli, and R. S. Hemler, "On the use of cloud forcing to estimate cloud feedback," *J. Clim.*, vol. 17, no. 19, pp. 3661–3665, 2004.

[42] A. C. Clement, R. Burgman, and J. R. Norris, "Observational and Model Evidence for Positive Low-Level Cloud Feedback," *Science (80-.).*, vol. 325, no. 5939, pp. 460–464, Jul. 2009.

[43] R. D. Cess, M. H. Zhang, W. J. Ingram, G. L. Potter, V. Alekseev, H. W. Barker, E. Cohen-Solal, R. a Colman, D. a Dazlich, a D. DelGenio, M. R. Dix, V. Dymnikov, M. Esch, L. D. Fowler, J. R. Fraser, V. Galin, W. L. Gates, J. J. Hack, J. T. Kiehl, and H. LeTreut, "Cloud Feedback in Atmospheric General Circulation Models: An Update," *J. Geophys. Res.*, vol. 101, no. D8, pp. 12791–12794, 1996.

[44] J. Hansen, A. Lacis, D. Rind, G. Russel, P. Stone, I. Fung, R. Ruedy, and J. Lerner, "Climate Sensitivity: Analysis of Feedback Mechanisms," *Clim. Process. Clim. Sensit.*, vol. 29, pp. 130–163, 1984.

[45] I. M. Held and B. J. Soden, "Water Vapor Feedback and Global Warming," *Annu. Rev. Energy Environ.*, vol. 25, no. 1, pp. 441–475, Nov. 2000.

[46] J. a. Curry, J. L. Schramm, and E. E. Ebert, "Sea Ice-Albedo Climate Feedback Mechanism," *J. Clim.*, vol. 8, no. 2, pp. 240–247, Feb. 1995.

[47] D. K. Perovich, B. Light, H. Eicken, K. F. Jones, K. Runciman, and S. V. Nghiem, "Increasing solar heating of the Arctic Ocean and adjacent seas, 1979-2005: Attribution and role in the ice-albedo feedback," *Geophys. Res. Lett.*, vol. 34, no. 19, pp. 1–5, 2007.

[48] M. Winton, "Sea Ice-Albedo Feedback and Nonlinear Arctic Climate Change," in *Arctic Sea Ice Decline: Observations, Projections, Mechanisms, and Implications*, 2013, pp. 111–131.

[49] J. A. Screen and I. Simmonds, "The central role of diminishing sea ice in recent Arctic temperature amplification," *Nature*, vol. 464, no. 7293, pp. 1334–1337, 2010.

[50] S. Vijayavenkataraman, S. Iniyan, and R. Goic, "A review of climate change, mitigation and adaptation," *Renew. Sustain. Energy Rev.*, vol. 16, no. 1, pp. 878–897, 2012.

[51] M. McNutt, "Climate Change Impacts," *Science (80-.).*, vol. 341, no. 6145, pp. 435–435, 2013.

[52] N. Oreskes, "BEYOND THE IVORY TOWER: The Scientific Consensus on Climate Change," *Science (80-.).*, vol. 306, no. 5702, pp. 1686–1686, Dec. 2004.

[53] W. R. L. Anderegg, J. W. P. Prall, J. Harold, and S. H. Schneider, "Expert credibility in climate change," *Pacific Conserv. Biol.*, vol. 17, no. 3, pp. 166–167, 2011.

[54] S. L. D. Van Linden, A. A. Leiserowitz, G. D. Feinberg, and E. W. Maibach, "The scientific consensus on climate change as a gateway belief: Experimental evidence," *PLoS One*, vol. 10, no. 2, pp. 2–9, 2015.

[55] S. C. Moser, "Communicating climate change: history, challenges, processes and future directions," *WIREs Clim. Chang.*, vol. 1, pp. 31–53, 2010.

[56] J. Besley and A. Dudo, "Scientists' Views about Public Engagement and Science Communication in the Context of Climate Change," vol. 1, no. October, pp. 1–19, 2017.

[57] "Average Operating Heat Rate for Selected Energy Sources." [Online]. Available: https://www.eia.gov/electricity/annual/html/epa_08_01.html. [Accessed: 05-Oct-2017].

[58] "Mazda Announces Long-Term Vision for Technology Development, 'Sustainable Zoom-Zoom 2030.'" [Online]. Available: http://www2.mazda.com/en/publicity/release/2017/201708/170808a.html. [Accessed: 05-Oct-2017].

[59] L. Carrette, K. A. Friedrich, and U. Stimming, "Fuel Cells - Fundamentals and Applications," *Fuel Cells*, vol. 1, no. 1, pp. 5–39, 2001.

[60] "Alkaline Fuel Cells (AFC)," in *Electrochemical Power Sources*, Hoboken, NJ, USA: John Wiley & Sons, Inc., 2015, pp. 229–237.

[61] E. Baur and H. Preis, "Uber brennstoff-ketten mit festleitern.," *Berichte der Bunsengesellschaft für Phys. Chemie*, vol. 43, no. 9, pp. 727–732, 1937.

[62] G. McLean, "An assessment of alkaline fuel cell technology," *Int. J. Hydrogen Energy*, vol. 27, no. 5, pp. 507–526, May 2002.

[63] M. Cifrain and K. Kordesch, "Hydrogen/oxygen (air) fuel cells with alkaline electrolytes," in *Handbook of Fuel Cells*, vol. 1, no. December 2010, Chichester, UK: John Wiley & Sons, Ltd, 2010, pp. 267–280.

[64] M. Warshay and P. R. Prokopius, "The fuel cell in space: yesterday, today and tomorrow," *J. Power Sources*, vol. 29, no. 1–2, pp. 193–200, 1990.

[65] W. T. Grubb, "Batteries with Solid Ion Exchange Electrolytes .1. Secondary Cells Employing Metal Electrodes," *J. Electrochem. Soc.*, vol. 106, no. 4, pp. 275–278, 1959.

[66] W. T. Grubb and L. W. Niedrach, "Batteries with Solid Ion-Exchange Membrane Electrolytes," *J. Electrochem. Soc.*, vol. 107, no. 2, p. 131, 1960.

[67] E. B. Yeager, "4. Solid polymer electrolyte fuel cells (SPEFCs)," *Energy*, vol. 11, no. 1–2, pp. 137–152, 1986.

[68] J. Weissbart and R. Ruka, "A Solid Electrolyte Fuel Cell," *J. Electrochem. Soc.*, vol. 109, no. 8, p. 723, 1962.

[69] J. M. Andújar and F. Segura, "Fuel cells: History and updating. A walk along two centuries," *Renew. Sustain. Energy Rev.*, vol. 13, no. 9, pp. 2309–2322, 2009.

[70] M. Ji and Z. Wei, "A review of water management in polymer electrolyte membrane fuel cells," *Energies*, vol. 2, no. 4, pp. 1057–1106, 2009.

[71] V. Mehta and J. S. Cooper, "Review and analysis of PEM fuel cell design and manufacturing," *J. Power Sources*, vol. 114, no. 1, pp. 32–53, Feb. 2003.

[72] J. J. Baschuk and X. Li, "Carbon monoxide poisoning of proton exchange membrane fuel cells," *Int. J. Energy Res.*, vol. 25, no. 8, pp. 695–713, 2001.

[73] M. Ni, D. Y. C. Leung, M. K. H. Leung, and K. Sumathy, "An overview of hydrogen production from biomass," *Fuel Process. Technol.*, vol. 87, no. 5, pp. 461–472, 2006.

[74] C. Sealy, "The problem with platinum," *Mater. Today*, vol. 11, no. 12, pp. 65–68, 2008.

[75] E. Antolini, S. C. Zignani, S. F. Santos, and E. R. Gonzalez, "Palladium-based electrodes: A way to reduce platinum content in polymer electrolyte membrane fuel cells," *Electrochim. Acta*, vol. 56, no. 5, pp. 2299–2305, 2011.

[76] O. T. Holton and J. W. Stevenson, "The Role of Platinum in Proton Exchange Membrane Fuel Cells," *Platin. Met. Rev.*, vol. 57, no. 4, pp. 259–271, Oct. 2013.

[77] E. Gulzow and E. Giilzow, "Alkaline fuel cells: A critical view," *J. Power Sources*, vol. 61, no. 1–2, pp. 99–104, 1996.

[78] A. L. Dicks, "Molten carbonate fuel cells," *Curr. Opin. Solid State Mater. Sci.*, vol. 8, no. 5, pp. 379–383, 2004.

[79] I. Rexed, *Applications for Molten Carbonate Fuel Cells*. 2014.

[80] M. Andersson and B. Sundèn, "Technology Review - Solid Oxide Fuel Cells," Jul. 2017.

[81] Y. Tanaka, T. Terayama, A. Momma, and T. Kato, "Numerical Simulation of SOFC System Performance at 90% Fuel Utilization with or without Anode Off-Gas Recycle for Enhancing Efficiency," *ECS Trans.*, vol. 68, no. 1, pp. 293–300, Jul. 2015.

[82] A. Evans, A. Bieberle-Hütter, H. Galinski, J. L. M. Rupp, T. Ryll, B. Scherrer, R. Tölke, and L. J. Gauckler, "Micro-solid oxide fuel cells: status, challenges, and chances," *Monatshefte für Chemie - Chem. Mon.*, vol. 140, no. 9, pp. 975–983, Sep. 2009.

[83] A. Evans, A. Bieberle-hütter, J. L. M. Rupp, and L. J. Gauckler, "Review on microfabricated micro-solid oxide fuel cell membranes," vol. 194, pp. 119–129, 2009.

[84] M.-F. Han, H.-Y. Yin, W.-T. Miao, and S. Zhou, "Fabrication and properties of anode-supported solid oxide fuel cell," *Solid State Ionics*, vol. 179, no. 27–32, pp. 1545–1548, 2008.

[85] H. Huang, C. H. Hsieh, N. Kim, J. Stebbins, and F. Prinz, "Structure, local environment, and ionic conduction in scandia stabilized zirconia," *Solid State Ionics*, vol. 179, no. 27–32, pp. 1442–1445, 2008.

[86] T. Ishihara, N. M. Sammes, and O. Yamamoto, "Electrolytes," in *High Temperature and Solid Oxide Fuel Cells*, Elsevier, 2003, pp. 83–117.

[87] D. J. L. Brett, A. Atkinson, N. P. Brandon, and S. J. Skinner, "Intermediate temperature solid oxide fuel cells," *Chem. Soc. Rev.*, vol. 37, no. 8, p. 1568, 2008.

[88] K. Yamaji, T. Horita, M. Ishikawa, N. Sakai, and H. Yokokawa, "Chemical stability of the La0.9Sr0.1Ga0.8Mg0.2O2.85 electrolyte in a reducing atmosphere," *Solid State Ionics*, vol. 121, no. 1, pp. 217–224, 1999.

[89] J. Y. Yi and G. M. Choi, "The effect of reduction atmosphere on the LaGaO3-based solid oxide fuel cell," *J. Eur. Ceram. Soc.*, vol. 25, no. 12 SPEC. ISS., pp. 2655–2659, 2005.

[90] N. P. Brandon and D. Thompsett, *Fuel Cells Compendium*. Elsevier, 2005.

[91] J. Fergus, R. Hui, X. Li, D. P. Wilkinson, and J. Zhang, *Solid Oxide Fuel Cells*. CRC Press, 2016.

[92] F. C. Nix and D. MacNair, "The thermal expansion of pure metals: Copper, gold, aluminum, nickel, and iron," *Phys. Rev.*, vol. 60, no. 8, pp. 597–605, Oct. 2004.

[93] H. Hayashi, T. Saitou, N. Maruyama, H. Inaba, K. Kawamura, and M. Mori, "Thermal expansion coefficient of yttria stabilized zirconia for various yttria contents," *Solid State Ionics*, vol. 176, no. 5–6, pp. 613–619, 2005.

[94] A. Faes, A. Hessler-Wyser, A. Zryd, and J. Van Herle, "A review of RedOx cycling of solid oxide fuel cells anode," *Membranes (Basel).*, vol. 2, no. 3, pp. 585–664, 2012.

[95] S. B. Adler, "Factors governing oxygen reduction in solid oxide fuel cell cathodes," *Chem. Rev. Rev.*, vol. 104, no. 10, pp. 4791–4843, 2004.

[96] S. Jung-Hoon, M. G. Jung, H. W. Park, and H.-T. Lim, "The Effect of Fabrication Conditions for GDC Buffer Layer on Electrochemical Performance of Solid Oxide Fuel Cells," *Nano-Micro Lett.*, vol. 5, no. 3, pp. 151–158, 2013.

[97] M. Yano, A. Tomita, M. Sano, and T. Hibino, "Recent advances in single-chamber solid oxide fuel cells : A review," vol. 177, pp. 3351–3359, 2007.

[98] M. Kuhn and T. W. Napporn, "Single-Chamber Solid Oxide Fuel Cell Technology—From Its Origins to Today's State of the Art," *Energies*, vol. 3, no. 1, pp. 57–134, Jan. 2010.

[99] I. Riess, "On the single chamber solid oxide fuel cells," *J. Power Sources*, vol. 175, no. 1, pp. 325–337, 2008.

[100] J. Richter, P. Holtappels, T. Graule, T. Nakamura, and L. J. Gauckler, "Materials design for perovskite SOFC cathodes," *Monatshefte für Chemie - Chem. Mon.*, vol. 140, no. 9, pp. 985–999, Sep. 2009.

[101] K. Zhang, J. Sunarso, Z. Shao, W. Zhou, C. Sun, S. Wang, and S. Liu, "Research progress and materials selection guidelines on mixed conducting perovskite-type ceramic membranes for oxygen production," *RSC Adv.*, vol. 1, no. 9, p. 1661, 2011.

[102] M. a. Peña and J. L. G. Fierro, "Chemical structures and performance of perovskite oxides," *Chem. Rev.*, vol. 101, no. 7, pp. 1981–2017, 2001.

[103] "Mitsubishi Electric Delivers High-capacity Energy-storage System to Kyushu Electric Power's Buzen Substation." [Online]. Available: http://www.mitsubishielectric.com/news/2016/0303-b.html. [Accessed: 04-Oct-2017].

[104] "Tesla Powerpack to Enable Large Scale Sustainable Energy to South Australia." [Online]. Available: https://www.tesla.com/it_IT/blog/tesla-powerpack-enable-large-scale-sustainable-energy-south-australia?redirect=no. [Accessed: 04-Oct-2017].

[105] L. Bertuccioli, A. Chan, D. Hart, F. Lehner, B. Madden, and E. Standen, "Study on development of water electrolysis in the EU," *Fuel Cells Hydrog. Jt. Undert.*, no. February, pp. 1–160, 2014.

[106] B. Kruse, S. Grinna, and C. Buch, *Hydrogen: Status and Possibilities*, no. 6. 2002.

[107] J. Schefold, A. Brisse, and M. Zahid, "Electronic Conduction of Yttria-Stabilized Zirconia Electrolyte in Solid Oxide Cells Operated in High Temperature Water Electrolysis," *J. Electrochem. Soc.*, vol. 156, no. 8, p. B897, 2009.

[108] A. Brisse, J. Schefold, and M. Zahid, "High temperature water electrolysis in solid oxide cells," *Int. J. Hydrogen Energy*, vol. 33, no. 20, pp. 5375–5382, 2008.

[109] Y. Zheng, J. Wang, B. Yu, W. Zhang, J. Chen, J. Qiao, and J. Zhang, "A review of high temperature co-electrolysis of H_2O and CO_2 to produce sustainable fuels using solid oxide electrolysis cells (SOECs): advanced materials and technology," *Chem. Soc. Rev.*, vol. 46, no. 5, pp. 1427–1463, 2017.

[110] A. Serrano-Lotina, A. J. Martin, M. A. Folgado, and L. Daza, "Dry reforming of methane to syngas over La-promoted hydrotalcite clay-derived catalysts," *Int. J. Hydrogen Energy*, vol. 37, no. 17, pp. 12342–12350, 2012.

[111] D. Pakhare and J. Spivey, "A review of dry (CO_2) reforming of methane over noble metal catalysts," *Chem. Soc. Rev.*, vol. 43, no. 22, pp. 7813–7837, 2014.

[112] S. Arora and R. Prasad, "An overview on dry reforming of methane: strategies to reduce carbonaceous deactivation of catalysts," *RSC Adv.*, vol. 6, no. 110, pp. 108668–108688, 2016.

[113] J.-M. Lavoie, "Review on dry reforming of methane, a potentially more environmentally-friendly approach to the increasing natural gas exploitation," *Front. Chem.*, vol. 2, no. November, pp. 1–17, 2014.

[114] J. W. Han, C. Kim, J. S. Park, and H. Lee, "Highly coke-resistant Ni nanoparticle catalysts with minimal sintering in dry reforming of methane," *ChemSusChem*, vol. 7, no. 2, pp. 451–456, 2014.

[115] O. Boucher and G. A. Folberth, "New Directions: Atmospheric methane removal as a way to mitigate climate change?," *Atmos. Environ.*, vol. 44, no. 27, pp. 3343–3345, 2010.

[116] M. E. Dry, "Practical and theoretical aspects of the catalytic Fischer-Tropsch process," *Appl. Catal. A Gen.*, vol. 138, no. 2, pp. 319–344, 1996.

[117] M. E. Dry, "The Fischer-Tropsch process: 1950-2000," *Catal. Today*, vol. 71, no. 3–4, pp. 227–241, 2002.

[118] I. Helms, *Solar Driven Chemistry. A vision for a sustainable chemistry production.* Euchems, 2016.

[119] C. Bessou, F. Ferchaud, B. Gabrielle, and B. Mary, "Biofuels, greenhouse gases and climate change. A review," *Agron. Sustain. Dev.*, vol. 31, no. 1, pp. 1–79, 2011.

[120] Q. Li, Y. Zheng, W. Guan, L. Jin, C. Xu, and W. G. Wang, "Achieving high-efficiency hydrogen production using planar solid-oxide electrolysis stacks," *Int. J. Hydrogen Energy*, vol. 39, no. 21, pp. 10833–10842, 2014.

[121] M. A. Laguna-Bercero, R. Campana, A. Larrea, J. A. Kilner, and V. M. Orera, "Electrolyte degradation in anode supported microtubular yttria stabilized zirconia-based solid oxide steam electrolysis cells at high voltages of operation," *J. Power Sources*, vol. 196, no. 21, pp. 8942–8947, 2011.

[122] P. Di Giorgio and U. Desideri, "Potential of reversible solid oxide cells as electricity storage system," *Energies*, vol. 9, no. 8, 2016.

[123] C. Graves, S. D. Ebbesen, S. H. Jensen, S. B. Simonsen, and M. B. Mogensen, "Eliminating degradation in solid oxide electrochemical cells by reversible operation," *Nat. Mater.*, vol. 14, no. 2, pp. 239–244, 2014.

[124] Q. Cai, D. J. L. Brett, D. Browning, and N. P. Brandon, "A sizing-design methodology for hybrid fuel cell power systems and its application to an unmanned underwater vehicle," *J. Power Sources*, vol. 195, no. 19, pp. 6559–6569, Oct. 2010.

[125] W. C. Chueh and S. M. Haile, "Electrochemistry of Mixed Oxygen Ion and Electron Conducting Electrodes in Solid Electrolyte Cells," *Annu. Rev. Chem. Biomol. Eng.*, vol. 3, no. 1, pp. 313–341, Jul. 2012.

[126] A. Manthiram, J.-H. Kim, Y. N. Kim, and K.-T. Lee, "Crystal chemistry and properties of mixed ionic-electronic conductors," *J. Electroceramics*, vol. 27, no. 2, pp. 93–107, Oct. 2011.

[127] J. B. Goodenough and Y.-H. Huang, "Alternative anode materials for solid oxide fuel cells," *J. Power Sources*, vol. 173, no. 1, pp. 1–10, 2007.

[128] T. Carraro, J. Joos, B. Rüger, A. Weber, and E. Ivers-Tiffée, "3D finite element model for reconstructed mixed-conducting cathodes: I. Performance quantification," *Electrochim. Acta*, vol. 77, pp. 315–323, Aug. 2012.

[129] S. Giddey, A. Kulkarni, C. Munnings, and S. P. S. Badwal, "Composite anodes for improved performance of a direct carbon fuel cell," *J. Power Sources*, vol. 284, pp. 122–129, Jun. 2015.

[130] W. H. Kan and V. Thangadurai, "Challenges and prospects of anodes for solid oxide fuel cells (SOFCs)," *Ionics (Kiel).*, vol. 21, no. 2, pp. 301–318, Feb. 2015.

[131] J. Sunarso, S. Baumann, J. M. Serra, W. A. Meulenberg, S. Liu, Y. S. Lin, and J. C. Diniz da Costa, "Mixed ionic–electronic conducting (MIEC) ceramic-based membranes for oxygen separation," *J. Memb. Sci.*, vol. 320, no. 1–2, pp. 13–41, Jul. 2008.

[132] W. Li, X. Zhu, Z. Cao, W. Wang, and W. Yang, "Mixed ionic-electronic conducting (MIEC) membranes for hydrogen production from water splitting," *Int. J. Hydrogen Energy*, vol. 40, no. 8, pp. 3452–3461, Mar. 2015.

[133] S. Engels, T. Markus, M. Modigell, and L. Singheiser, "Oxygen permeation and stability investigations on MIEC membrane materials under operating conditions for power plant processes," *J. Memb. Sci.*, vol. 370, no. 1–2, pp. 58–69, 2011.

[134] H. Bouwmeester, H. Kruidhof, and A. Burggraaf, "Importance of the surface exchange kinetics as rate limiting step in oxygen permeation through mixed-conducting oxides," *Solid State Ionics*, vol. 72, pp. 185–194, Sep. 1994.

[135] L. Heyne, *Solid Electrolytes*. Springer, 1977.

[136] C. Wagner, "Equations for transport in solid oxides and sulfides of transition metals," *Prog. Solid State Chem.*, vol. 10, pp. 3–16, 1975.

[137] A. V. Virkar, "Theoretical analysis of the role of interfaces in transport through oxygen ion and electron conducting membranes," *J. Power Sources*, vol. 147, no. 1–2, pp. 8–31, Sep. 2005.

[138] I. Riess, "Mixed ionic–electronic conductors—material properties and applications," *Solid State Ionics*, vol. 157, no. 1–4, pp. 1–17, 2003.

[139] P.-M. Geffroy, J. Fouletier, N. Richet, and T. Chartier, "Rational selection of MIEC materials in energy production processes," *Chem. Eng. Sci.*, vol. 87, pp. 408–433, Jan. 2013.

[140] V. V. Kharton, F. M. B. Marques, and a. Atkinson, "Transport properties of solid oxide electrolyte ceramics: A brief review," *Solid State Ionics*, vol. 174, no. 1–4, pp. 135–149, 2004.

[141] M. Johnsson and P. Lemmens, "Crystallography and Chemistry of Perovskites," in *Handbook of Magnetism and Advanced Magnetic Materials*, Chichester, UK: John Wiley & Sons, Ltd, 2007, p. 11.

[142] B. Saparov and D. B. Mitzi, "Organic–Inorganic Perovskites: Structural Versatility for Functional Materials Design," *Chem. Rev.*, vol. 116, no. 7, pp. 4558–4596, Apr. 2016.

[143] K. Uchino, "Glory of piezoelectric perovskites," *Sci. Technol. Adv. Mater.*, vol. 16, no. 4, p. 46001, Jul. 2015.

[144] H. Kozuka, K. Ohbayashi, and K. Koumoto, "Electronic conduction in La-based perovskite-type oxides," *Sci. Technol. Adv. Mater.*, vol. 16, no. 2, p. 26001, Apr. 2015.

[145] A. Jun, J. Kim, J. Shin, and G. Kim, "Perovskite as a Cathode Material: A Review of its Role in Solid-Oxide Fuel Cell Technology," *ChemElectroChem*, vol. 3, no. 4, pp. 511–530, Apr. 2016.

[146] N. Labhasetwar, G. Saravanan, S. Kumar Megarajan, N. Manwar, R. Khobragade, P. Doggali, and F. Grasset, "Perovskite-type catalytic materials for environmental applications," *Sci. Technol. Adv. Mater.*, vol. 16, no. 3, p. 36002, Jun. 2015.

[147] C. Niedrig, S. F. Wagner, W. Menesklou, and E. Ivers-Tiffée, "Characterization of oxygen-dependent stability of selected mixed-conducting perovskite oxides," *Solid State Ionics*, vol. 273, pp. 41–45, May 2015.

[148] S. P. Jiang, "Development of lanthanum strontium manganite perovskite cathode materials of solid oxide fuel cells: a review," *J. Mater. Sci.*, vol. 43, no. 21, pp. 6799–6833, Nov. 2008.

[149] C. Sun, R. Hui, and J. Roller, "Cathode materials for solid oxide fuel cells: a review," *J. Solid State Electrochem.*, vol. 14, no. 7, pp. 1125–1144, Jul. 2010.

[150] E. Juste, A. Julian, G. Etchegoyen, P. Geffroy, T. Chartier, N. Richet, and P. Delgallo, "Oxygen permeation, thermal and chemical expansion of (La, Sr)(Fe, Ga)O3–δ perovskite membranes," *J. Memb. Sci.*, vol. 319, no. 1–2, pp. 185–191, Jul. 2008.

[151] a. Vivet, P. M. Geffroy, T. Chartier, P. Del Gallo, and N. Richet, "La(1–x)SrxFe(1–y)GayO3–δ perovskite membrane: Oxygen semi-permeation, thermal expansion coefficient and chemical stability under reducing conditions," *J. Memb. Sci.*, vol. 372, no. 1–2, pp. 373–379, Apr. 2011.

[152] G. Etchegoyen, T. Chartier, A. Julian, and P. Del-Gallo, "Microstructure and oxygen permeability of a Lao.6Sro.4Feo.9Gao.1O3–δ membrane containing magnesia as dispersed second phase particles," *J. Memb. Sci.*, vol. 268, no. 1, pp. 86–95, Jan. 2006.

[153] A. C. Bose, *Inorganic Membranes for Energy and Environmental Applications*. New York: Springer Science & Business Media, 2008.

[154] M. P. Pechini, "Method of preparing lead and alkaline earth titanates and niobates and coating method using the same to form a capacitor," US 3330697 A, 1967.

[155] C. Marcilly, P. Courty, and B. Delmon, "Preparation of Highly Dispersed Mixed Oxides and Oxide Solid Solutions by Pyrolysis of Amorphous Organic Precursors," *J. Am. Ceram. Soc.*, vol. 53, no. 1, pp. 56–57, Jan. 1970.

[156] M. S. G. Baythoun and F. R. Sale, "Production of strontium-substituted lanthanum manganite perovskite powder by the amorphous citrate process," *J. Mater. Sci.*, vol. 17, no. 9, pp. 2757–2769, Sep. 1982.

[157] Q. Xu, "Citrate method synthesis, characterization and mixed electronic–ionic conduction properties of Lao.6Sro.4Coo.8Feo.2O3 perovskite-type complex oxides," *Scr. Mater.*, vol. 50, no. 1, pp. 165–170, Jan. 2004.

[158] F. Deganello, G. Marcì, and G. Deganello, "Citrate–nitrate auto-combustion synthesis of perovskite-type nanopowders: A systematic approach," *J. Eur. Ceram. Soc.*, vol. 29, no. 3, pp. 439–450, Feb. 2009.

[159] K. Kammer Hansen and M. Mogensen, "Evaluation of LSF based SOFC Cathodes using Cone-shaped Electrodes," in *ECS Transactions*, 2008, pp. 153–160.

[160] S. Tantayanon, J. Yeyongchaiwat, J. Lou, and Y. Ma, "Synthesis and characterization of Sr and Fe substituted LaGaO 3 perovskites and membranes," *Sep. Purif. Technol.*, vol. 32, pp. 319–326, 2003.

[161] D. A. Shirley, "High-resolution x-ray photoemission spectrum of the valence bands of gold," *Phys. Rev. B*, vol. 5, no. 12, pp. 4709–4714, 1972.

[162] D. Briggs, "Handbook of X-ray Photoelectron Spectroscopy C. D. Wanger, W. M. Riggs, L. E. Davis, J. F. Moulder and G. E.Muilenberg Perkin-Elmer Corp., Physical Electronics Division, Eden Prairie, Minnesota, USA, 1979. 190 pp. $195," *Surf. Interface Anal.*, vol. 3, no. 4, pp. v–v, Aug. 1981.

[163] D. Briggs and J. C. Riviere, *Practical Surface Analysis*. New York: John Wiley & Sons, Inc., 1983.

[164] H. R. Wenk, S. Matthies, and L. Lutterotti, "Texture Analysis from Diffraction Spectra," *Mater. Sci. Forum*, vol. 157–162, pp. 473–480, 1994.

[165] M. Ferrari and L. Lutterotti, "Method for the simultaneous determination of anisotropic residual stresses and texture by x-ray diffraction," *J. Appl. Phys.*, vol. 76, no. 11, pp. 7246–7255, 1994.

[166] "Inorganic Crystal Structure Database, version 2007, Fachinformationszentrum, Karlsruhe, Germany." .

[167] F. A. Cotton and G. Wilkinson, *Advanced Inorganic Chemistry 3rd ed.* New York: Interscience Publishers, 1972.

[168] H. Wang, W. Yang, Y. Cong, X. Zhu, and Y. Lin, "Structure and oxygen permeability of a dual-phase membrane," *J. Memb. Sci.*, vol. 224, no. 1–2, pp. 107–115, 2003.

[169] P. Datta, P. Majewski, and F. Aldinger, "LaGaO3-based cermet for solid oxide fuel cell cathodes," *J. Eur. Ceram. Soc.*, vol. 29, no. 8, pp. 1469–1476, 2009.

[170] L. A. Isupova, I. S. Yakovleva, G. M. Alikina, V. A. Rogov, and V. A. Sadykov, "Reactivity of La1 – x Sr x FeO3 – y (x = 0–1) Perovskites in Oxidation Reactions," *Kinet. Catal.*, vol. 46, no. 5, pp. 729–735, Sep. 2005.

[171] M. M. Natile, A. Ponzoni, I. Concina, A. Glisenti, F. Marzolo, S. Chimiche, U. Padova, and F. Marzolo, "Chemical Tuning versus Microstructure Features in Solid-State Gas Sensors: LaFe 1 -," 2014.

[172] S. Furfori, S. Bensaid, N. Russo, and D. Fino, "Towards practical application of lanthanum ferrite catalysts for NO reduction with H 2," vol. 154, pp. 348–354, 2009.

[173] A. Galenda, M. M. Natile, and A. Glisenti, "La 0.6 Sr 0.4 Co 0.8 Fe 0.2 O 3-δ and Fe 2 O 3 /La 0.6 Sr 0.4 Co 0.8 Fe 0.2 O 3-δ Powders: XPS Characterization," *Surf. Sci. Spectra*, vol. 13, no. 1, pp. 31–47, Dec. 2006.

[174] A. Galenda, M. M. Natile, L. Nodari, and A. Glisenti, "Lao.8Sro.2Gao.8Feo.2O3–δ: Influence of

the preparation procedure on reactivity toward methanol and ethanol," *Appl. Catal. B Environ.*, vol. 97, no. 3–4, pp. 307–322, Jun. 2010.

[175] J. Yuenyongchaiwat, S. Tantayanon, J. Lou, and Y. H. Ma, "Synthesis of Sr- and Fe-doped LaGaO 3 perovskites by the modified citrate method," *J. Mater. Sci.*, vol. 39, no. 23, pp. 7067–7074, Dec. 2004.

[176] E. Echeverri and O. Arnache, "Structural and impedance analysis of Co-doped SrTiO3 perovskite," *J. Phys. Conf. Ser.*, vol. 687, p. 12040, Feb. 2016.

[177] A. Aguadero, D. Pérez-Coll, J. A. Alonso, S. J. Skinner, and J. Kilner, "A New Family of Mo-Doped SrCoO 3–δ Perovskites for Application in Reversible Solid State Electrochemical Cells," *Chem. Mater.*, vol. 24, no. 14, pp. 2655–2663, Jul. 2012.

[178] P. Zeng, R. Ran, Z. Chen, W. Zhou, H. Gu, Z. Shao, and S. Liu, "Efficient stabilization of cubic perovskite SrCoO3–δ by B-site low concentration scandium doping combined with sol–gel synthesis," *J. Alloys Compd.*, vol. 455, no. 1–2, pp. 465–470, May 2008.

[179] T. Tian, M. Zhan, W. Wang, and C. Chen, "Surface properties and catalytic performance in methane combustion of La0.7Sr0.3Fe1–yGayO3–δ perovskite-type oxides," *Catal. Commun.*, vol. 10, no. 5, pp. 513–517, Jan. 2009.

[180] H. Falcón, J. A. Barbero, J. A. Alonso, M. J. Martínez-Lope, and J. L. G. Fierro, "SrFeO 3 - δ Perovskite Oxides: Chemical Features and Performance for Methane Combustion," *Chem. Mater.*, vol. 14, no. 5, pp. 2325–2333, May 2002.

[181] Q. Ming, "Combustion synthesis and characterization of Sr and Ga doped LaFeO3," *Solid State Ionics*, vol. 122, no. 1–4, pp. 113–121, Jul. 1999.

[182] Q. Fu, X. Xu, D. Peng, X. Liu, and G. Meng, "Preparation and electrochemical characterization of Sr- and Mn-doped LaGaO3 as anode materials for LSGM-based SOFCs," *J. Mater. Sci.*, vol. 38, no. 13, pp. 2901–2906, 2003.

[183] S. Koutcheiko, P. Whitfield, and I. Davidson, "Electrical and thermal properties of La0.7Sr0.3Ga0.6Fe0.4O3 ceramics," *Ceram. Int.*, vol. 32, no. 3, pp. 339–344, 2006.

[184] S. N. Shkerin, A. V. Kyz'min, O. I. Gyrdasova, A. Y. Stroeva, and A. V. Nikonov, "Electrical conductivity and thermal expansion of La1 – x Sr x Fe1 – y Ga y O3 – δ (x = 0.2–0.5; y = 0–0.4)," *Russ. J. Electrochem.*, vol. 53, no. 2, pp. 154–160, 2017.

[185] J. A. Schwarz, C. Contescu, and A. Contescu, "Methods for Preparation of Catalytic Materials," *Chem. Rev.*, vol. 95, no. 3, pp. 477–510, 1995.

[186] M. Shelef and R. . McCabe, "Twenty-five years after introduction of automotive catalysts: what next?," *Catal. Today*, vol. 62, no. 1, pp. 35–50, Sep. 2000.

[187] H. S. Gandhi, G. W. Graham, and R. W. McCabe, "Automotive exhaust catalysis," *J. Catal.*, vol. 216, no. 1–2, pp. 433–442, May 2003.

[188] A. Glisenti, M. Pacella, M. Guiotto, M. M. Natile, and P. Canu, "Largely Cu-doped LaCo 1–x Cu x O 3 perovskites for TWC: Toward new PGM-free catalysts," *Appl. Catal. B Environ.*, vol. 180, pp. 94–105, Jan. 2016.

[189] S. Keav, S. Matam, D. Ferri, and A. Weidenkaff, "Structured Perovskite-Based Catalysts and Their Application as Three-Way Catalytic Converters—A Review," *Catalysts*, vol. 4, no. 3, pp. 226–255, Jul. 2014.

[190] P. Munnik, P. E. De Jongh, and K. P. De Jong, "Recent Developments in the Synthesis of Supported Catalysts," *Chem. Rev.*, vol. 115, no. 14, pp. 6687–6718, 2015.

[191] European Commission, "On the review of the list of critical raw materials for the EU and the implementation of the Raw Materials Initiative," 2014.

[192] P. Xu, G. M. Zeng, D. L. Huang, C. L. Feng, S. Hu, M. H. Zhao, C. Lai, Z. Wei, C. Huang, G. X.

Xie, and Z. F. Liu, "Use of iron oxide nanomaterials in wastewater treatment: A review," *Sci. Total Environ.*, vol. 424, pp. 1–10, May 2012.

[193] S. Rahim Pouran, A. A. Abdul Raman, and W. M. A. Wan Daud, "Review on the application of modified iron oxides as heterogeneous catalysts in Fenton reactions," *J. Clean. Prod.*, vol. 64, pp. 24–35, Feb. 2014.

[194] S.-S. Lin and M. D. Gurol, "Catalytic Decomposition of Hydrogen Peroxide on Iron Oxide: Kinetics, Mechanism, and Implications," *Environ. Sci. Technol.*, vol. 32, no. 10, pp. 1417–1423, May 1998.

[195] S. L. Brock, N. Duan, Z. R. Tian, O. Giraldo, H. Zhou, and S. L. Suib, "A Review of Porous Manganese Oxide Materials," *Chem. Mater.*, vol. 10, no. 10, pp. 2619–2628, 1998.

[196] P. G. Smirniotis, P. M. Sreekanth, D. A. Peña, and R. G. Jenkins, "Manganese Oxide Catalysts Supported on TiO 2 , Al 2 O 3 , and SiO 2 : A Comparison for Low-Temperature SCR of NO with NH 3," *Ind. Eng. Chem. Res.*, vol. 45, no. 19, pp. 6436–6443, Sep. 2006.

[197] T. S. Park, S. K. Jeong, S. H. Hong, and S. C. Hong, "Selective Catalytic Reduction of Nitrogen Oxides with NH 3 over Natural Manganese Ore at Low Temperature," pp. 4491–4495, 2001.

[198] J. J. Spivey and J. B. Butt, "Literature review: deactivation of catalysts in the oxidation of volatile organic compounds," *Catal. Today*, vol. 11, no. 4, pp. 465–500, Jan. 1992.

[199] A. Bedon, M. M. Natile, and A. Glisenti, "On the synthesis and stability of La0.6Sr0.4Ga0.3Fe0.7O3," *J. Eur. Ceram. Soc.*, vol. 37, no. 3, pp. 1049–1058, Mar. 2017.

[200] N. S. McIntyre and in D. Briggs and M. P. Seah (eds.), "Practical Surface Analysis in Auger and X-ray Photoelectron Spectroscopy," *John Wiley Sons, New York*, vol. 1, pp. 397–427, 1983.

[201] O. Mn, J. Pike, J. Hanson, L. Zhang, and S. Chan, "Synthesis and Redox Behavior of Nanocrystalline Hausmannite," *Society*, vol. 42, no. 11, pp. 5609–5616, 2007.

[202] S. C. Kim and W. G. Shim, "Catalytic combustion of VOCs over a series of manganese oxide catalysts," *Appl. Catal. B Environ.*, vol. 98, no. 3–4, pp. 180–185, 2010.

[203] Gregg S J and K. S. W. Sing, "Adsorption, Surface Area and Porosity," *New York, Academic Press*. 1999.

[204] Z. A. Alothman, "A review: Fundamental aspects of silicate mesoporous materials," *Materials (Basel).*, vol. 5, no. 12, pp. 2874–2902, 2012.

[205] E. R. Stobbe, B. A. de Boer, and J. W. Geus, "The reduction and oxidation behaviour of manganese oxides," *Catal. Today*, vol. 47, no. 1–4, pp. 161–167, Jan. 1999.

[206] F. Kapteijn, L. Singoredjo, A. Andreini, and J. A. Moulijn, "Activity and selectivity of pure manganese oxides in the selective catalytic reduction of nitric oxide with ammonia," *Appl. Catal. B Environ.*, vol. 3, no. 2–3, pp. 173–189, Feb. 1994.

[207] F. C. Buciuman, F. Patcas, and J. Zsakó, "TPR-study of Substitution Effects on Reducibility and Oxidative Non-stoichiometry of La0.8A'0.2MnO3+δ Perovskites," *J. Therm. Anal. Calorim.*, vol. 61, no. 3, pp. 819–825, 2000.

[208] H. Yang, P. G. Kotula, Y. Sato, M. Chi, Y. Ikuhara, and N. D. Browning, "Segregation of Mn2+ dopants as interstitials in SrTiO3 grain boundaries," *Mater. Res. Lett.*, vol. 2, no. 1, pp. 16–22, 2014.

[209] J. Requies, M. B. Güemez, S. Perez Gil, V. L. Barrio, J. F. Cambra, U. Izquierdo, and P. L. Arias, "Natural and synthetic iron oxides for hydrogen storage and purification," *J. Mater. Sci.*, vol. 48, no. 14, pp. 4813–4822, 2013.

[210] H.-Y. Lin, Y.-W. Chen, and C. Li, "The mechanism of reduction of iron oxide by hydrogen," *Thermochim. Acta*, vol. 400, no. 1, pp. 61–67, 2003.

[211] G. Xiao, Q. Liu, S. Wang, V. G. Komvokis, M. D. Amiridis, A. Heyden, S. Ma, and F. Chen, "Synthesis and characterization of Mo-doped SrFeO 3-δ as cathode materials for solid oxide fuel cells," *J. Power Sources*, vol. 202, pp. 63–69, 2012.

[212] Y. Niu, J. Sunarso, F. Liang, W. Zhou, Z. Zhu, and Z. Shao, "A Comparative Study of Oxygen Reduction Reaction on Bi- and La-Doped SrFeO3 – δ Perovskite Cathodes," *J. Electrochem. Soc.*, vol. 158, no. 2, pp. B132–B138, 2011.

[213] S. Q. Chen, H. Wang, and Y. Liu, "Perovskite La-St-Fe-O (St=Ca, Sr) supported nickel catalysts for steam reforming of ethanol: The effect of the A site substitution," *Int. J. Hydrogen Energy*, vol. 34, no. 19, pp. 7995–8005, 2009.

[214] G. Pecchi, M. G. Jiliberto, A. Buljan, and E. J. Delgado, "Relation between defects and catalytic activity of calcium doped LaFeO 3 perovskite," *Solid State Ionics*, vol. 187, no. 1, pp. 27–32, 2011.

[215] H. Xian, F.-L. Li, X.-G. Li, X.-W. Zhang, M. Meng, T.-Y. Zhang, and N. Tsubaki, "Influence of preparation conditions to structure property, NOx and SO2 sorption behavior of the BaFeO3–x perovskite catalyst," *Fuel Process. Technol.*, vol. 92, no. 9, pp. 1718–1724, 2011.

[216] F. Dong, D. Chen, Y. Chen, Q. Zhao, and Z. Shao, "La-doped BaFeO3-δ perovskite as a cobalt-free oxygen reduction electrode for solid oxide fuel cells with oxygen-ion conducting electrolyte," *J. Mater. Chem.*, vol. 22, no. 30, pp. 15071–15079, 2012.

[217] N. Li, A. Boréave, J. P. Deloume, and F. Gaillard, "Catalytic combustion of toluene over a Sr and Fe substituted LaCoO3 perovskite," *Solid State Ionics*, vol. 179, no. 27–32, pp. 1396–1400, 2008.

[218] R. Zhang, A. Villanueva, H. Alamdari, and S. Kaliaguine, "Crystal structure, redox properties and catalytic performance of Ga-based mixed oxides for NO reduction by C3H6," *Catal. Commun.*, vol. 9, no. 1, pp. 111–116, 2008.

[219] A. A. Leontiou, A. K. Ladavos, T. V. Bakas, T. C. Vaimakis, and P. J. Pomonis, "Reverse uptake of oxygen from La1–xSrx (Fe3+/Fe4+)O3±δ perovskite-type mixed oxides (x = 0.00, 0.15, 0.30, 0.40, 0.60, 0.70, 0.80, 0.90)," *Appl. Catal. A Gen.*, vol. 241, no. 1, pp. 143–154, 2003.

[220] T. Seiyama, N. Yamazoe, and K. Eguchi, "Characterization and activity of some mixed metal oxide catalysts," *Ind. Eng. Chem. Prod. Res. Dev.*, vol. 24, no. 1, pp. 19–27, 1985.

[221] T. Nitadori and M. Misono, "Catalytic properties of La1 – xA′xFeO3(A′ = Sr,Ce) and La1 – xCexCoO3," *J. Catal.*, vol. 93, no. 2, pp. 459–466, Jun. 1985.

[222] B. P. Barbero, J. A. Gamboa, and L. E. Cadús, "Synthesis and characterisation of La1–xCaxFeO3 perovskite-type oxide catalysts for total oxidation of volatile organic compounds," *Appl. Catal. B Environ.*, vol. 65, no. 1–2, pp. 21–30, May 2006.

[223] M. I. Zaki, M. A. Hasan, L. Pasupulety, N. E. Fouad, and H. Knözinger, "CO and CH4 total oxidation over manganese oxide supported on ZrO2, TiO2, TiO2–Al2O3 and SiO2–Al2O3 catalysts," *New J. Chem.*, vol. 23, no. 12, pp. 1197–1202, 1999.

[224] Y. Han, K. Ramesh, L. Chen, E. Widjaja, and S. Chilukoti, "Observation of the Reversible Phase-Transformation of r -Mn 2 O 3 Nanocrystals during the Catalytic Combustion of Methane by in Situ Raman Spectroscopy," *J. Phys. Chem. C Lett.*, vol. 3, pp. 2830–2833, 2007.

[225] N. Grunbaum, L. Dessemond, J. Fouletier, F. Prado, L. Mogni, and A. Caneiro, "Rate limiting steps of the porous La0.6Sr0.4Co0.8Fe0.2O3–δ electrode material," *Solid State Ionics*, vol. 180, no. 28–31, pp. 1448–1452, Nov. 2009.

[226] D. Rembelski, J. P. Viricelle, L. Combemale, and M. Rieu, "Characterization and Comparison of Different Cathode Materials for SC-SOFC: LSM, BSCF, SSC, and LSCF," *Fuel Cells*, vol. 12, no. 2, pp. 256–264, Apr. 2012.

[227] F. S. Baumann, J. Maier, and J. Fleig, "The polarization resistance of mixed conducting SOFC cathodes: A comparative study using thin film model electrodes," *Solid State Ionics*, vol. 179, no. 21–26, pp. 1198–1204, 2008.

[228] E. Siebert, A. Hammouche, and M. Kleitz, "Impedance spectroscopy analysis of La1-xSrxMnO3-yttria-stabilized zirconia electrode kinetics," *Electrochim. Acta*, vol. 40, no. 11, pp. 1741–1753, 1995.

[229] T. Ishihara, "Solid oxide reversible cells (SORCs) using LaGaO3-based oxide electrolyte and oxide fuel electrode," vol. 20001, p. 20001, 2017.

[230] C. Yang, Z. Yang, C. Jin, M. Liu, and F. Chen, "High performance solid oxide electrolysis cells using Pro.8Sr1.2(Co,Fe)0.8Nb0.2O4+δ–Co–Fe alloy hydrogen electrodes," *Int. J. Hydrogen Energy*, vol. 38, no. 26, pp. 11202–11208, Aug. 2013.

[231] T. H. Shin, J.-H. Myung, M. Verbraeken, G. Kim, and J. T. S. Irvine, "Oxygen deficient layered double perovskite as an active cathode for CO ₂ electrolysis using a solid oxide conductor," *Faraday Discuss.*, vol. 182, pp. 227–239, 2015.

[232] X. Zhang, S. Ohara, R. Maric, H. Okawa, T. Fukui, H. Yoshida, T. Inagaki, and K. Miura, "Interface reactions in the NiO-SDC-LSGM system," *Solid State Ionics*, vol. 133, no. 3, pp. 153–160, 2000.

[233] A. T. Duong and D. R. Mumm, "On the interaction of SSC and LSGM in composite SOFC electrodes," *J. Power Sources*, vol. 241, pp. 281–287, 2013.

[234] K. Chen and S. P. Jiang, "Review—Materials Degradation of Solid Oxide Electrolysis Cells," *J. Electrochem. Soc.*, vol. 163, no. 11, pp. F3070–F3083, 2016.

[235] K. Huang, J.-H. Wan, and J. B. Goodenough, "Increasing Power Density of LSGM-Based Solid Oxide Fuel Cells Using New Anode Materials," *J. Electrochem. Soc.*, vol. 148, no. 7, p. A788, 2001.

[236] R. Polini, A. Falsetti, and E. Traversa, "Sol-gel synthesis and characterization of Co-doped LSGM perovskites," *J. Eur. Ceram. Soc.*, vol. 25, no. 12 SPEC. ISS., pp. 2593–2598, 2005.

[237] K. Bin Yoo and G. M. Choi, "Performance of La-doped strontium titanate (LST) anode on LaGaO3-based SOFC," *Solid State Ionics*, vol. 180, no. 11–13, pp. 867–871, 2009.

[238] T. Zhu, D. E. Fowler, K. R. Poeppelmeier, M. Han, and S. A. Barnett, "Hydrogen Oxidation Mechanisms on Perovskite Solid Oxide Fuel Cell Anodes," *J. Electrochem. Soc.*, vol. 163, no. 8, pp. F952–F961, 2016.

[239] Q. X. Fu, F. Tietz, and D. Stöver, "La[sub 0.4]Sr[sub 0.6]Ti[sub 1–x]Mn[sub x]O[sub 3–δ] Perovskites as Anode Materials for Solid Oxide Fuel Cells," *J. Electrochem. Soc.*, vol. 153, no. 4, p. D74, 2006.

[240] K. Hosoi, H. Hagiwara, S. Ida, and T. Ishihara, "La 0.8 Sr 0.2 FeO 3–δ as Fuel Electrode for Solid Oxide Reversible Cells Using LaGaO 3 -Based Oxide Electrolyte," *J. Phys. Chem. C*, vol. 120, no. 29, pp. 16110–16117, Jul. 2016.

[241] X. Yang and J. T. S. Irvine, "(La0.75Sr0.25)0.95Mn0.5Cr0.5O3 as the cathode of solid oxide electrolysis cells for high temperature hydrogen production from steam," *J. Mater. Chem.*, vol. 18, no. 20, p. 2349, 2008.

[242] M. Gong, X. Liu, J. Trembly, and C. Johnson, "Sulfur-tolerant anode materials for solid oxide fuel cell application," *J. Power Sources*, vol. 168, no. 2, pp. 289–298, 2007.

[243] X. Ge, C. Fu, and S. H. Chan, "Double layer capacitance of anode/solid-electrolyte interfaces," *Phys. Chem. Chem. Phys.*, vol. 13, no. 33, p. 15134, 2011.

[244] J. Nielsen and J. Hjelm, "Impedance of SOFC electrodes: A review and a comprehensive case study on the impedance of LSM:YSZ cathodes," *Electrochim. Acta*, vol. 115, pp. 31–45, 2014.

[245] A. Flura, C. Nicollet, S. Fourcade, V. Vibhu, A. Rougier, J.-M. Bassat, and J.-C. Grenier, "Identification and modelling of the oxygen gas diffusion impedance in SOFC porous electrodes: application to Pr2NiO4+δ," *Electrochim. Acta*, vol. 174, pp. 1030–1040, Aug. 2015.

[246] C. Sun and U. Stimming, "Recent anode advances in solid oxide fuel cells," *J. Power Sources*,

vol. 171, no. 2, pp. 247–260, 2007.

[247] T. Hibino and H. Iwahara, "Simplification of Solid Oxide Fuel Cell System Using Partial Oxidation of Methane," *Chemistry Letters*, vol. 22, no. 7. pp. 1131–1134, 1993.

[248] Z. Shao, S. M. Haile, J. Ahn, P. D. Ronney, Z. Zhan, and S. a Barnett, "A thermally self-sustained micro solid-oxide fuel-cell stack with high power density.," *Nature*, vol. 435, no. 7043, pp. 795–798, 2005.

[249] M. Kuhn, T. W. Napporn, M. Meunier, S. Vengallatore, and D. Therriault, "Miniaturization limits for single-chamber micro-solid oxide fuel cells with coplanar electrodes," *J. Power Sources*, vol. 194, pp. 941–949, 2009.

[250] M. Kuhn, T. W. Napporn, M. Meunier, and D. Therriault, "Single-chamber micro solid oxide fuel cells : Study of anode and cathode materials in coplanar electrode design," *Solid State Ionics*, vol. 181, no. 5–7, pp. 332–337, 2010.

[251] I. Riess, "Catalytic Requirements for Mixed Reactant Fuel Cells," *Funct. Mater. Lett.*, vol. 1, no. 2, pp. 105–113, 2008.

[252] I. Riess, "Significance of impeded reactions in solid state electrochemistry–Conspicuous examples," *Solid State Ionics*, vol. 177, no. 19–25, pp. 1591–1596, Oct. 2006.

[253] I. Riess, "The significance of impeded reactions in solid state electrochemistry," *Solid State Ion. BT - 7th Int. Symp. Syst. with Fast Ion. Transp.*, vol. 176, no. 19–22, pp. 1667–1674, 2004.

[254] I. Riess, "Catalysis of electrochemical processes and the suppression of chemical ones are needed in mixed reactant fuel cells — Can this be achieved?," *Solid State Ionics*, vol. 181, no. 17–18, pp. 790–795, Jun. 2010.

[255] D. Rembelski, M. Rieu, L. Combemale, and J. P. Viricelle, "In situ reduction and evaluation of anode supported single chamber solid oxide fuel cells," *J. Power Sources*, vol. 242, pp. 811–816, 2013.

[256] B. Morel, R. Roberge, S. Savoie, T. W. Napporn, and M. Meunier, "Temperature and performance variations along single chamber solid oxide fuel cells," *J. Power Sources*, vol. 186, no. 1, pp. 89–95, Jan. 2009.

[257] G. Yang, C. Su, W. Wang, R. Ran, M. O. Tadé, and Z. Shao, "Single-chamber solid oxide fuel cells with nanocatalyst-modified anodes capable of in situ activation," *J. Power Sources*, vol. 264, pp. 220–228, Oct. 2014.

[258] Z. H. Wang, Z. Lü, K. F. Chen, B. Wei, X. B. Zhu, X. Q. Huang, and W. H. Su, "Redox Tolerance of Thin and Thick Ni/YSZ Anodes of Electrolyte-Supported Single-Chamber Solid Oxide Fuel Cells under Methane Oxidation Conditions," *Fuel Cells*, vol. 13, no. 6, pp. 1109–1115, Dec. 2013.

[259] J. Malveiro, T. Ramos, L. P. Ferreira, J. C. Waerenborgh, M. R. Nunes, M. Godinho, and M. D. Carvalho, "Magnesium doping on brownmillerite Ca2FeAlO5," *J. Solid State Chem.*, vol. 180, no. 6, pp. 1863–1874, 2007.

[260] A. Shaula, Y. Pivak, J. Waerenborgh, P. Gaczynski, A. Yaremchenko, and V. Kharton, "Ionic conductivity of brownmillerite-type calcium ferrite under oxidizing conditions," *Solid State Ionics*, vol. 177, no. 33–34, pp. 2923–2930, Nov. 2006.

[261] F. Ramezanipour, J. E. Greedan, L. M. D. Cranswick, V. O. Garlea, J. Siewenie, G. King, A. Llobet, and R. L. Donaberger, "The effect of the B-site cation and oxygen stoichiometry on the local and average crystal and magnetic structures of Sr2Fe1.9M0.1O5+y (M = Mn, Cr, Co; y = 0, 0.5)," *J. Mater. Chem.*, vol. 22, no. 19, p. 9522, 2012.

[262] J.-P. Eufinger, A. Schmidt, M. Lerch, and J. Janek, "Novel anion conductors – conductivity, thermodynamic stability and hydration of anion-substituted mayenite-type cage compounds $C_{12}A_7$:X (X = O, OH, Cl, F, CN, S, N)," *Phys. Chem. Chem. Phys.*, vol. 17, no. 10, pp. 6844–6857, 2015.

[263] H. Hosono, K. Hayashi, T. Kamiya, T. Atou, and T. Susaki, "New functionalities in abundant element oxides: ubiquitous element strategy," *Sci. Technol. Adv. Mater.*, vol. 12, no. 3, p. 34303, 2011.

[264] J. T. S. Irvine, M. Lacerda, and A. R. West, "Oxide ion conductivity in Ca12Al14O33," *Mater. Res. Bull.*, vol. 23, no. 7, pp. 1033–1038, 1988.

[265] J. C. Waerenborgh, D. P. Rojas, N. P. Vyshatko, A. L. Shaula, V. V. Kharton, I. P. Marozau, and E. N. Naumovich, "Fe4+ formation in brownmillerite CaAlo.5Feo.5O2.5+δ," *Mater. Lett.*, vol. 57, no. 28, pp. 4388–4393, Oct. 2003.

[266] S. Tian, J. Jiang, D. Hosseini, A. M. Kierzkowska, Q. Imtiaz, M. Broda, and C. R. Müller, "Development of a Steel-Slag-Based, Iron-Functionalized Sorbent for an Autothermal Carbon Dioxide Capture Process - Supporting Information," *ChemSusChem*, vol. 8, no. 22, pp. 3839–3846, 2015.

[267] D. Hirabayashi, T. Yoshikawa, K. Mochizuki, K. Suzuki, and Y. Sakai, "Formation of brownmillerite type calcium ferrite (Ca2Fe 2O5) and catalytic properties in propylene combustion," *Catal. Letters*, vol. 110, no. 3–4, pp. 269–274, 2006.

[268] M. Liang, W. Kang, and K. Xie, "Comparison of reduction behavior of Fe2O3, ZnO and ZnFe2O4 by TPR technique," *J. Nat. Gas Chem.*, vol. 18, no. 1, pp. 110–113, Mar. 2009.

[269] G. Carollo, A. Garbujo, D. Ferri, M. M. Natile, and A. Glisenti, "Cu/CGO Cermet Based Electrodes for Symmetric and Reversible Solid Oxide Fuel Cells," in *Hydrogen and Fuel Cells*, pp. 53–64.

[270] A. Ringuedé and J. Fouletier, "Oxygen reaction on strontium-doped lanthanum cobaltite dense electrodes at intermediate temperatures," *Solid State Ionics*, vol. 139, no. 3–4, pp. 167–177, 2001.

[271] Y. L. Yang, A. J. Jacobson, C. L. Chen, G. P. Luo, K. D. Ross, and C. W. Chu, "Oxygen exchange kinetics on a highly oriented La0.5Sr0.5CoO3-?? thin film prepared by pulsed-laser deposition," *Appl. Phys. Lett.*, vol. 79, no. 6, pp. 776–778, 2001.

[272] T. Kawada, N. Sakai, H. Yokokawa, M. Dokiya, and I. Anzai, "Reaction Between Solid Oxide Fuel-Cell Materials," *Solid State Ionics*, vol. 50, no. 3–4, pp. 189–196, 1992.

[273] M. Liu, "Significance of interfaces in solid-state cells with porous electrodes of mixed ionic–electronic conductors," *Solid State Ionics*, vol. 107, no. 1–2, pp. 105–110, 1998.

[274] T. Ishihara, T. Yamada, H. Arikawa, H. Nishiguchi, and Y. Takita, "Mixed electronic – oxide ionic conductivity and oxygen permeating property of Fe- , Co- or Ni-doped LaGaO 3 perovskite oxide," *Solid State Ionics*, vol. 135, pp. 631–636, 2000.

[275] V. V. Kharton, A. L. Shaulo, A. P. Viskup, M. Avdeev, A. A. Yaremchenko, M. V. Patrakeev, A. I. Kurbakov, E. N. Naumovich, and F. M. B. Marques, "Perovskite-like system (Sr,La)(Fe,Ga)O3-δ: Structure and ionic transport under oxidizing conditions," *Solid State Ionics*, vol. 150, no. 3–4, pp. 229–243, 2002.

[276] S. Kim, S. Wang, X. Chen, Y. L. Yang, N. Wu, A. Ignatiev, A. J. Jacobson, and B. Abeles, "Oxygen surface exchange in mixed ionic electronic conductors: Application La0.5Sr0.5Fe0.8Ga0.2O3-delta," *J. Electrochem. Soc.*, vol. 147, no. 6, pp. 2398–2406, 2000.